

Robust Control Techniques for DFIG Driven WECS with Improved Efficiency

by
Ifte Khairul Amin

A thesis submitted in partial fulfilment of the requirement for the degree of
Doctor of Philosophy at
Department of Electrical Engineering
Lakehead University
Thunder Bay, Ontario, Canada
July 2019

Abstract

Wind energy has emerged as one of the fastest growing renewable energy sources since mid-80's due to its low cost and environmentally friendly nature compared to conventional fossil fuel based power generation. Current technologies for the design and implementation of wind energy conversion systems (WECSs) include induction generator and synchronous generator based units. The doubly fed induction generator (DFIG) is chosen in this thesis because of its economic operation, ability to regulate in sub-synchronous or super-synchronous speed and decoupled control of active and reactive powers. Among the major challenges of wind energy conversion system, extraction of maximum power from intermittent generation and supervision on nonlinear system dynamics of DFIG-WECS are of critical importance. Maximization of the power produced by wind turbine is possible by optimizing tip-speed ratio (TSR), turbine rotor speed or torque and blade angle. The literature reports that a vast number of investigations have been conducted on the maximum power point tracking (MPPT) of wind turbines. Among the reported MPPT control algorithms, the hill climb search (HCS) method is typically preferred because of its simple implementation and turbine parameter-independent scheme. Since the conventional HCS algorithm has few drawbacks such as power fluctuation and speed-efficiency trade-off, a new adaptive step size based HCS controller is developed in this thesis to mitigate its deficiencies by incorporating wind speed measurement in the controller. In addition, a common practice of using linear state-feedback controllers is prevalent in speed and current control of DFIG-based WECS. Traditional feedback linearization controllers are sensitive to system parameter variations and disturbances on grid-connected WECS, which demands advanced control techniques for stable and efficient performance considering the nonlinear system dynamics. An adaptive backstepping based nonlinear control (ABNC) scheme with iron-loss minimization algorithm for RSC control of

DFIG is developed in this research work to obtain improved dynamic performance and reduced power loss. The performance of the proposed controller is tested and compared with the benchmark tuned proportional-integral (PI) controller under different operating conditions including variable wind speed, grid voltage disturbance and parameter uncertainties. Test results demonstrate that the proposed method exhibits excellent performance on the rotor side and grid side converter control. In addition, the compliance with the modern grid-code requirements is achieved by featuring a novel controller with disturbance rejection mechanism. In order to reduce the dependency on system's mathematical model, a low computational adaptive network fuzzy interference system (ANFIS) based neuro-fuzzy logic controller (NFC) scheme is developed for DFIG based WECS. The performance of the proposed NFC based DFIG-WECS is tested in simulation to regulate both grid and rotor side converters under normal and voltage dip conditions. Furthermore, a new optimization technique known as grey wolf optimization (GWO) is also designed to regulate the battery power for DFIG driven wind energy system operating in standalone mode.

In order to verify the effectiveness of the proposed control schemes, simulation models are designed using Matlab/Simulink. The proposed model for MPPT and nonlinear control of grid-connected mode and GWO based power control of standalone DFIG-WECS has been successfully implemented in the real-time environment using DSP controller board DS1104 for a laboratory 480 VA DFIG. The comparison among different controllers suggests that each control technique has its own specialty in wind power control application with specific merits and shortcomings. However, the PI controller provides fast convergence, the ANFIS based NFC controller has better adaptability under grid disturbances and ABNC has moderate performance. Overall, the thesis provides a detailed overview of different robust control techniques for DFIG driven WECS in grid-connected and standalone operation mode with practical implementation.

Acknowledgements

I would like to express my sincere gratitude to those people who have supported me in completion of PhD degree. I thank my supervisor, Dr. M. Nasir Uddin for his support, guidance and advices. His constant encouragement gave me the confidence to carry out my work.

I wish to thank the members of my supervisory committee-Dr. K. Natarajan, Dr. Xiaoping Liu, Dr. Saleh Saleh and Dr. A. Tayebi. This thesis might remain incomplete without their valuable feedbacks and insightful suggestions. My special thanks go to the professors and the staffs of Lakehead University who help me a lot in numerous occasions during my study period.

I want to thank my mother and my wife as well as other family members and friends who have always been patient and supportive to me. Their encouragement and optimism have allowed me to overcome the obstacles that I face in my life.

Numerous people and innumerable instances, which I cannot enumerate in a single page, have helped me to finish my degree. Finally, I express my sincere appreciation to my fellow lab-mates, graduate fellows, and people from the community of Thunder Bay for their unconditional help and cooperation.

List of Publications

Journal:

- [1] M.N. Uddin, I.K. Amin, "Adaptive step size based hill-climb search algorithm for MPPT control of DFIG-WECS with reduced power fluctuation and improved tracking performance", Electric Power Components and Systems, vol. 46, no. 19-20, pp. 2203-2214, 2018.
- [2] M. N. Uddin, Z. Zhai, I. Amin, "Development and implementation of a port controlled hamilton with dissipation based high precision speed control of IPMSM drive", IEEE Transactions on Power Electronics (Early Access), pp. 1-10, May 2019.

Conditional Acceptance (2nd revision):

- [3] I. K. Amin, M. N. Uddin, "Nonlinear control operation of DFIG based WECS incorporated with machine loss reduction scheme", IEEE Transactions on Power Electronics, 2019.

Conference:

- [4] I.K. Amin, M.N. Uddin, "MPPT based efficiently controlled DFIG for wind energy conversion system," IEEE International Electric Machines and Drives Conference (IEMDC), Miami, FL, USA, May 2017.
- [5] I.K. Amin, M.N. Uddin, "Nonlinear control operation of DFIG based WECS with stability analysis", IEEE Industry Applications Society Annual Meeting, pp.1 – 8, Cincinnati, OH, USA, Oct. 2017.
- [6] I.K. Amin, M.N. Uddin, N. Rezaei, M. Marsadek, "Grey wolf optimization based power management strategy for battery storage of DFIG-WECS in standalone operating mode", IEEE Industry Applications Society Annual Meeting, Portland, OR, USA, Sep. 2018.
- [7] I.K. Amin, M.N. Uddin, M.A. Hannan , AHM. Z. Alam, "Adaptive neuro-fuzzy controller for grid voltage dip compensations of grid connected DFIG-WECS", presented at International Electric Machines & Drives Conference (IEMDC), San Diego, USA, May 2019.
- [8] I.K. Amin, M.N. Uddin,, M. Marsadek, "ANFIS Based Neuro-Fuzzy Control of DFIG for Wind Power Generation in Standalone Mode", presented at International Electric Machines & Drives Conference (IEMDC), San Diego, USA, May 2019.

Table of Contents

Chapter 1 Introduction	1
1.1 General Background.....	1
1.2 Historical Aspect of Wind Power Generation.....	3
1.3 Literature Review	6
1.3.1 Maximum Power Point Tracking Algorithm	8
1.3.2 Adaptive Nonlinear Control of WECS	12
1.3.3 Intelligent Control of WECS.....	14
1.4 Research Motivation.....	18
1.5 Objectives of the Thesis	21
1.6 Organization of the Chapters.....	22
Chapter 2 The Structure and Modeling of Wind Energy Conversion Systems.....	24
2.1 Wind Model.....	24
2.2 Wind Turbine Structure.....	26
2.2.1 Turbine Blade.....	28
2.2.2 Tower and Foundation	28
2.2.3 Nacelle	28
2.2.4 Gearbox.....	29
2.2.5 Coupling and Mechanical Brake.....	29
2.2.6 Yaw Drive	29
2.2.7 Sensors	29
2.3 Power Characteristics Equations of Wind Turbine	30
2.4 Wind Turbine Conversion System Topologies	31
2.4.1 Fixed Speed Wind Turbines.....	32

2.4.2	Variable Speed Wind Turbine with Limited Speed Control	32
2.4.3	Variable Speed Wind Turbine with Partial Scale Frequency Converter	33
2.4.4	Full Capacity Converter Operated WECS	34
2.5	Electrical Generators in Wind Turbine	35
2.5.1	Synchronous Generators	35
2.5.2	Permanent Magnet Synchronous Generator	35
2.5.3	Wound Rotor Synchronous Generator.....	36
2.5.4	Asynchronous Generators	36
2.5.5	Doubly Fed Induction Generator	37
2.6	Power Converters	44
2.6.1	Soft Starter	44
2.6.2	Diode Rectifier.....	44
2.6.3	The Back-to-Back PWM-VSI.....	44
2.6.4	Matrix Converter.....	45
2.6.5	Multilevel Converter	45
2.6.6	Neutral Point Clamped Converter (NPCC).....	46
2.7	Summary	47
	Chapter 3 Development and Performance Analysis of an Adaptive Step-Size Based HCS MPPT Controller	48
3.1	Overview of MPPT Algorithm.....	48
3.1.1	Hill-Climb Search Control.....	52
3.2	Description of the Overall Wind Power Control System	56
3.2.1	Design of the Proposed Adaptive Step Size HCS-MPPT Controller.....	57
3.3	Description of the Grid Side and Rotor Side Converter Control of DFIG.....	63
3.3.1	Grid-Side Power Converter Control	63

3.3.2	Rotor Side Converter Control	64
3.4	Simulation Performance of the Proposed Adaptive Step-Size Based MPPT Control of DFIG-WECS.....	66
3.5	Real-Time Implementation and Results	73
3.6	Summary	78
Chapter 4	Design of an Adaptive Backstepping Based Nonlinear Controller for DFIG Based WECS	80
4.1	Overview of Adaptive Backstepping Control	81
4.2	Dynamic Model of DFIG for Nonlinear Control	81
4.3	Description of the System with Control Blocks.....	84
4.3.1	Lyapunov Based Controller for Grid Side Converter Control.....	85
4.3.2	Rotor Side Converter Control for Backstepping Based Nonlinear Control Approach	88
4.4	Adaptive Backstepping Based Rotor Side Converter Control with Adaptation of Magnetizing Inductance	94
4.5	Development of Loss Minimization Algorithm	101
4.6	Simulation Results.....	104
4.6.1	Rotor Side Converter (RSC) Control Performance.....	104
4.6.2	Grid Side Converter (GSC) Control Performance	105
4.7	Real-Time Implementation and Results	112
4.8	Summary	114
Chapter 5	ANFIS based Control of DFIG-WECS in Grid Connected Mode	116
5.1	Description of the ANFIS Based Control Operation.....	116
5.1.1	ANFIS Network	117
5.1.2	Online Self-tuning Algorithm.....	120
5.1.3	Tuning of Pre-Condition and Consequent Parameters.....	120
5.2	Control of Grid-Connected DFIG in Normal Condition	121

5.2.1	RSC Control by ANFIS Method for Grid-Connected Mode	121
5.2.2	GSC control in Grid-Connected Mode	122
5.2.3	Control Performance in Grid-Connected Mode for Normal Grid Condition.....	123
5.3	Performance Comparison among Controllers for Grid-Connected DFIG-WECS.....	126
5.4	Control of Grid-Connected DFIG Under Voltage Dip Conditions	129
5.5	Converter Control in Voltage Dip Conditions	133
5.6	Simulation Results for Voltage Dip Conditions.....	138
5.7	Summary	143
Chapter 6 Intelligent Control of DFIG Driven WECS in Standalone Mode		145
6.1	Description of the ANFIS Based Control of DFIG-WECS in Standalone Mode	147
6.1.1	ANFIS Based Converter Control Operation in SA Mode.....	149
6.1.1.1	Proposed ANFIS Based LSC Control for SA Mode.....	150
6.1.1.2	PI Control of RSC in SA Mode	151
6.1.2	Simulation Results of the ANFIS Controller in SA Mode.....	152
6.2	GWO Based Battery Power Management in Standalone Mode.....	155
6.2.1	Description of the Control Operation.....	158
6.2.1.1	Boost Converter Control Operation	158
6.2.1.2	RSC Control Operation in Standalone Mode.....	159
6.2.2	Grey Wolf Optimization	161
6.2.2.1	Inspiration	161
6.2.2.1	Encircling Pattern.....	161
6.2.2.2	Position Update Mechanism	163
6.2.3	Power Management Strategy for Battery Storage.....	165
6.2.4	Dumping Power Control	166
6.3	Simulation Results.....	167

6.4	Real-Time Implementation and Results	171
6.5	Discussion	173
Chapter 7	Conclusion	175
7.1	Summary	175
7.2	Major Contributions of the Thesis.....	176
7.3	Future Scopes of Work.....	178
7.4	Concluding Remarks	179
References.....		180
Appendix -A		190
Appendix –B.....		191
Appendix –C.....		199
Appendix –D.....		203

List of Figures

Fig. 1.1. Cumulative installed wind capacity in all over the world over the last decade	2
Fig. 1.2. Country-wise shares in cumulative wind generation capacity until April 2018: (a) New onshore installation in 2018 (b) Total onshore wind power installation till 2018	5
Fig. 1.3. The generation of electric power by source: (a) All over Canada (b) In Ontario	5
Fig. 1.4. A typical turbine power output curve.	8
Fig. 2.1. Main components of a horizontal-axis wind turbine	27
Fig. 2.2. Fixed speed wind turbine power conversion system with SCIG.....	32
Fig. 2.3. Variable speed wind power conversion system using WRIG with limited speed control.....	33
Fig. 2.4. Variable speed wind power conversion system using DFIG with speed control	34
Fig. 2.5. Typical variable speed wind power system with full-scale power conversion	34
Fig. 2.6. Power flow direction in DFIG based wind power conversion system	38
Fig. 2.7. Steady-state equivalent circuit of the DFIG	38
Fig. 2.8. Space vector equivalent circuit of an induction generator in the arbitrary reference frame....	40
Fig. 2.9. d-q axis equivalent circuits of DFIG in a reference frame with rotational speed ω : (a) d-axis, (b) q-axis	43
Fig. 2.10. Configuration of back to back PWM-VSI converter topology.....	45
Fig. 2.11. Configuration of multilevel converter topology.....	46
Fig. 3.1. (a) Power coefficient versus tip-speed ratio ($C_p\lambda$) of wind turbine for various blade pitch angle (β), (b) Optimum tip speed ratio versus pitch angle at corresponding maximum value of power coefficients.....	49
Fig. 3.2. Mechanical power-speed ($P_m\omega_m$) characteristics and the maximum power point curve (dashed curve) attained at each wind speed, for a blade pitch angle of $\beta = 0^\circ$ and radius = 42 m.	51
Fig. 3.3. Method of MPP tracking in hill climb search method.....	53
Fig. 3.4. Flow chart of the conventional HCS algorithm for WECS.....	56
Fig. 3.5. Configuration of the MPPT based converter controlled WECS.....	57
Fig. 3.6. Flow chart of the proposed adaptive step size based MPPT algorithm	58

Fig. 3.7. Performance analysis of fixed step size based HCS controller for maximum power tracking: (a) Small step size based tracking with slow convergence, (b) Large step size based tracking led to wrong direction of perturbation, (c) Fixed step size based HCS controller steered to wrong track under drastic change in wind speed, (d) Adaptive step size variation with respect to the change in wind speed and turbine power.....	59
Fig. 3.8. Block diagram of the grid side converter control for the proposed system.....	64
Fig. 3.9. Block diagram of the rotor side converter control.....	65
Fig. 3.10. Matlab-Simulink block diagram of overall structure of DFIG-WECS.	67
Fig. 3.11. Matlab-Simulink block diagram of GSC control pulse generator.....	67
Fig. 3.12. Matlab-Simulink block diagram of RSC control pulse generator.	69
Fig. 3.13. Comparison of turbine output power at constant wind speed 10 m/s: (a) Turbine output power for conventional fixed-step HCS controller; (b) Turbine output power for the proposed controller; (c) Zoom-in view of Fig. (a); (d) Zoom-in view of Fig. (b); (e) Turbine output power for Constant TSR controller; (f) Zoom-in view of Fig. (e).....	70
Fig. 3.14. Performance of the proposed and constant TSR controller for random variation in wind speed: (a) Arbitrary wind speed, (b) Generator rotor speed tracking by the proposed controller to maintain MPPT, (c) Adaptation in step size, (d) Random wind profile, (e) Generator rotor speed for constant TSR controller, (f) Deviation of actual rotor speed from reference speed.	71
Fig. 3.15. Performance of the DFIG under randomly varied wind speed: (a) Arbitrary variation in wind speed from 10 m/s to 12 m/s, (b) Corresponding variation in generator speed, (c) Change in generator torque, (d) DC-link voltage level.	72
Fig. 3.16. Experimental setup for the proposed DFIG based WECS.....	75
Fig. 3.17. Real-time α phase stator voltage and current for the proposed control at super-synchronous mode.....	75
Fig. 3.18. MPPT controller performance for incremental wind speed.	76
Fig. 3.19. MPPT control action along with GSC and RSC controls of DFIG while wind speed declines.	77
Fig. 3.20. DC-link voltage tracking performance.	78
Fig. 4.1. d-q axis equivalent circuits of DFIG in synchronous reference frame referred to stator side with core loss resistance: (a) d-axis and, (b) q-axis.	82

Fig. 4.2. Configuration of the proposed nonlinear controller based DFIG-WECS.	85
Fig. 4.3. Comparative simulation results between PI controller and the proposed nonlinear controller for RSC control of DFIG under variable wind speed: (a) Variation in wind speed, (b) Rotor speed error, (c) d-axis rotor current error, (d) q-axis rotor current error.	105
Fig. 4.4. Comparative simulation results between PI controller and proposed nonlinear controller for GSC control of DFIG under variable wind speed: (a) dc-link voltage error , (b) d-axis grid converter current error , (c) q-axis grid converter current error	106
Fig. 4.5. Control input performance comparison between the proposed nonlinear controller and PI controller for GSC and RSC control under variable wind speed: (a) Nonlinear rotor control voltages (Volt), (b) PI controlled rotor control voltages for RSC, (c) Nonlinear grid converter control voltages, (d) Control voltages for grid side converter under PI control	107
Fig. 4.6. Generator output performance for a momentary change in grid voltage for wind speed of 10 m/s: (a) 10% increase in grid voltage between t=2 to 2.5 sec, (b) Corresponding change in rotor speed , (c) Stator power output in p.u., (d) 10% dip in grid voltage between t=2 to 2.5 sec, (e) Corresponding change in rotor speed , (f) Stator power output in p.u.	108
Fig. 4.7. Performance of the online parameter estimation Estimated value of magnetizing inductance under rated condition	109
Fig. 4.8. Effect of machine loss minimization scheme: (a) Overall machine loss when loss reduction model is activated at t=2.5 sec, (b) Corresponding change in reference d-axis rotor current, (c) Reference q-axis rotor current, (d) Power loss comparison with and without activation of the loss reduction model for variable rotor speed.	110
Fig. 4.9. Parameter sensitivity analysis for proposed loss minimization scheme: (a) Increment of rotor resistance by 50% during simulation at t=14.65 sec, (b) Overall machine loss when loss reduction model is activated at t=5.5 sec, (c) Zoom-in view for power loss at the instant of the change in rotor resistance.	111
Fig. 4.10. Experimental performance of the proposed nonlinear controller based DFIG-WECS: (a) variation in wind speed generated by the turbine emulator (b) Corresponding power produced by the DFIG, (c) reference speed generation, and (d) rotor speed error.	112
Fig. 4.11. Experimental performance of the proposed nonlinear controller based RSC of DFIG: (a) d-axis rotor currents and errors,(b) q-axis rotor currents and error dynamics under varying wind speed.	113

Fig. 4.12. Experimental performance of the machine loss reduction model (a) Total power loss before and after the activation of loss reduction algorithm, (b) Corresponding change in d-axis rotor current of DFIG 114

Fig. 5.1. Schematic of typical ANFIS architecture.....	117
Fig. 5.2. Membership function for input data x	118
Fig. 5.3. ANFIS architecture based RSC control for grid-connected mode of DFIG.....	122
Fig. 5.4. ANFIS architecture based GSC control of DFIG.....	123
Fig. 5.5. Performance of the ANFIS based RSC control: (a) Variation in wind speed, (b) Corresponding change in generator speed, (c) Reference and actual d-axis rotor current, (d) Reference and actual q-axis rotor current.....	124
Fig. 5.6. Performance of the ANFIS based GSC control: (a) DC-link voltage, (b) d-axis grid current component, (c) q-axis grid current component	125
Fig. 5.7. ANFIS based controller performance for step change in reactive power: (a) Variation in reference value of reactive power, (b) Corresponding change in reference and actual d-axis rotor currents, (c) Three phase rotor currents.....	126
Fig. 5.8. Comparative rotor speed response for a step increase in wind speed: (a) PI, (b) Nonlinear, (c) ANFIS.....	127
Fig. 5.9. Comparative dc-link voltage tracking performance at variable wind speed: (a) PI, (b) Nonlinear, (c) ANFIS.....	128
Fig. 5.10. Comparative d-axis rotor current tracking response for a step change in reactive power demand at $t=2$ sec : (a) PI, (b) Nonlinear, (c) ANFIS.....	128
Fig. 5.11. Change of stator flux when three phase dip starts at the end of the first quarter of a voltage cycle.....	131
Fig. 5.12. Effect of voltage dip (a) Natural flux due to symmetrical dip, (b) Negative sequence stator flux due to asymmetrical dip, (c) Sudden rise in induced emf at rotor windings.....	132
Fig. 5.13. Overall configuration of the DFIG-WECS with ANFIS controller for voltage dip condition.....	133
Fig. 5.14. Overall Configuration for the ANFIS based DFIG-WECS control in voltage dip.....	134
Fig. 5.15. (a) MATLAB-Simulink block diagram for ANFIS based GSC control during voltage dip, (b) Block diagram for sequence decomposition.....	135

Fig. 5.16. (a) Simulink configuration for ANFIS based RSC control during voltage dip. (b) Block diagram for rotor current sequence decomposition.....	137
Fig. 5.17. Performance of the proposed ANFIS based DFIG-WECS for 90% three-phase symmetrical voltage dip: (a) Grid voltage, (b) Positive sequence d-axis rotor currents, (c) Reference and actual rotor speed, (d) Electromechanical Torque, (e) Positive sequence q-axis rotor current, (f) d-q axis stator flux.	139
Fig. 5.18. Performance of the proposed ANFIS for 90% three phase symmetrical voltage dip: (a) dc-link voltage, (b) Positive sequence d-axis grid current, (c) Three phase grid currents.....	140
Fig. 5.19. Performance of the proposed ANFIS based DFIG-WECS for phase-to-phase 40% voltage dip: (a) Grid voltage, (b) Reference and actual rotor speed, (c) Positive sequence q-axis rotor current, (d) Electromechanical torque, (e) Positive sequence d-axis rotor currents, (f)Three phase rotor current.	141
Fig. 5.20. Performance of the proposed ANFIS based GSC control for phase-to-phase 40% voltage dip: (a) dc-link voltage, (d)Positive sequence d-q axis grid current, (c) Positive sequence stator flux, (d) Three phase rotor voltage, (e) Negative sequence d-q axis rotor current, (f) Negative sequence d-q axis stator flux.	142
Fig. 5.21. Updated value of the membership function parameters and consequent parameters: (a-d) For variable wind speed at normal grid voltage, (e-h) For grid voltage dip condition:(a) a_3 , (b) b_2 , (c) b_3 , (d) β_0 , (e) a_3 , (f) b_2 , (g) b_3 , (h) β_0	143
Fig. 6.1. Overall configuration of the SA-WECS with ANFIS based NFC control.	148
Fig. 6.2. Gaussian membership functions for input data.	149
Fig. 6.3. Proposed ANFIS based LSC control for SA mode of DFIG.....	150
Fig. 6.4. RSC control scheme for SA mode of DFIG.	152
Fig. 6.5. Performance of the proposed ANFIS on SA mode for step increase in load demand: (a) Demand load power, (b) 3-phase voltage across load end, (c) \underline{a}' phase load current.	153
Fig. 6.6. Performance of the control system in SA mode under variable wind speed: (a) Wind speed, (b) Generator speed in rad/sec, (c) DC bus voltage, (d) Grid voltage of phase-c, (e) Frequency of load voltage.....	155
Fig. 6.7. Overall configuration of the DFIG-WECS at standalone mode with battery storage power management.	156

Fig. 6.8. Boost converter control for different operational mode of DFIG.....	158
Fig. 6.9. RSC control for SA mode of DFIG.	160
Fig. 6.10. Position update pattern of wolves using random vectors.	163
Fig. 6.11. Flow chart of GWO algorithm.....	164
Fig. 6.12. Battery power control with bidirectional buck-boost converter.	165
Fig. 6.13. Performance in the proposed standalone DFIG for wind speed variation: (a) Step changes in wind speed, (b) Variation in rotor speed, (c) Corresponding change in reference power generation from GWO block.	167
Fig. 6.14. Boost converter and bidirectional controller control performance for the proposed standalone DFIG under variation of wind power: (a) Variation in turbine power, (b) Reference and actual input current of the boost converter, (c) Reference and actual current at the output of the bidirectional buck-boost converter.	168
Fig. 6.15. Performance of RSC and battery control unit for step variation in wind speed: (a) Zoomed in load voltage (b) Load frequency (Hz), (c) DC link voltage, (d) Corresponding output voltage of 3-phase rectifier, (e) Battery voltage , (f) Battery current variation.....	169
Fig. 6.16. Performance of RSC and converter controllers for variation in load: (a) rms terminal voltage, (b) Load frequency, (c) Difference between reference and actual frequency, (d) Reference power generated by GWO block,(e) Corresponding output current of bidirectional buck-boost converter (f) Zoom-in view of (a), (g) Zoom-in view of (b), (h) Zoom-in view of (c), (i) Zoom-in view of (d), (j) Zoom-in view of (e).	170
Fig. 6.17. Performance of the GWO algorithm: (a) Variation in turbine power, (b) Reference power generated by GWO block, (c) Reference and actual current of bidirectional converter, (d) Convergence curve for the objective function (in \log_{10} scale).....	171
Fig. 6.18. Experimental setup for the proposed standalone DFIG-WECS.	172
Fig. 6.19. Voltage output for the standalone system at wind speed 6 m/s and 600 Ω load.	172
Fig. 6.20. Performance of the boost converter controller with MPPT scheme.....	173
Fig. 6.21. Performance of the proposed GWO based power flow control using bidirectional buck-boost converter.....	173

List of Tables

Table 3.1 Function types used for adaptive step determination.....	62
Table 3.2 Range of coefficients and constants for functional expression of adaptive step size calculation	63
Table 3.3 Wind turbine and DFIG parameters.....	66
Table 3.4 PI controller constants for GSC and RSC control pulse generator.....	69
Table 4.1 Simulation parameters for PI and nonlinear controller.....	104
Table 5.1 PI controller constants for comparative analysis	127
Table 5.2 Performance comparison among the proposed controllers.....	129
Table 6.1 Wind turbine, DFIG, battery and load parameters.....	157
Table 6.2 Boost and bidirectional buck-boost converter parameters.....	162

List of Symbols

v_{wind}, v_w	Wind speed
v_{base}	Base wind velocity
v_{gust}	Gust wind velocity
v_{ramp}	Ramp wind velocity
v_{noise}	Background noise wind velocity
R	Turbine radius
ρ	Air density
C_p	Power coefficient of the blade
A	Swept area of the air flow
λ_{opt}	Optimal tip speed ratio
β	Turbine pitch angle
P_m	Mechanical power of the turbine
ω_m	Speed of the turbine
i_{ms}	Magnetization current of DFIG
L_m	Magnetizing inductance
L_s, L_r	Stator and rotor leakage reactance
$v_{ds}, v_{qs}, v_{dr}, v_{qr}, v_{dg}, v_{qg}$	d-q axis stator, rotor, grid converter voltages
$i_{ds}, i_{qs}, i_{dr}, i_{qr}, i_{dg}, i_{qg}$	d-q axis stator, rotor, grid current components
$i_{dfe}, i_{qfe}, i_{dm}, i_{qm}$	d-q axis core resistance and magnetization current components
$\psi_{ds}, \psi_{qs}, \psi_{dr}, \psi_{qr}$	d-q axis stator and rotor flux-linkages
R_s, R_r, R_{fe}	Stator, rotor and core loss resistances

P	Number of pole pairs
ω_s, ω_r	Synchronous and rotor electrical angular speed
$L_{\sigma s}, L_{\sigma r}$	Stator and rotor leakage inductances
T_e, T_{em}	Electromagnetic developed torque
T_t	Turbine torque
\hat{x}	Estimated value of the variable x .
x^*, x_{ref}	Reference value or set point of the variable x .
\dot{x}	First derivative of the variable x .
s	Machine slip
V_{bus}	Bus voltage
V_{dc}	dc-link voltage
J	Machine inertia
i_{cd}, i_{cq}	d-q axis grid converter current components
V_{cd}, V_{cq}	d-q axis grid converter voltage components
L_g, R_g	Grid line inductance and resistance
Q_s	Reactive power of the stator
V_{load}, V_t	Load and terminal voltage
V_{dl}, V_{ql}	d-q axis load voltage
i_{dl}, i_{ql}	d-q axis load current
$V_{bat}, I_{bat}, P_{bat}$	Battery voltage, current and power
$P_s, P_r, P_{tur}, P_{load}$	Stator, rotor, turbine and load power
I_{rec}	Rectifier current
P_{dump}	Dumped power

List of Acronyms

ABNC	Adaptive backstepping based nonlinear controller
ANFIS	Adaptive network fuzzy interference system
ANN	Artificial neural network
DFIG	Doubly fed induction generator
DSP	Digital signal processor
EMF	Electromagnetic force
FACTS	Flexible AC transmission system
FLC	Fuzzy logic controller
GSC	Grid side converter
GWO	Grey wolf optimization
HCS	Hill climb search
LSC	Load side converter
LMA	Loss minimization algorithm
LMC	Loss minimization controller
LUT	Look-up table
LVRT	Low voltage ride-through
MPP	Maximum power point

MPPT	Maximum power point tracking
MRAS	Model reference adaptive system
NFC	Neuro-fuzzy controller
NN	Neural network
OT	Optimal torque
PI	Proportional integral
PID	Proportional integral derivative
PMSG	Permanent magnet synchronous generator
P&O	Perturbation and observe
PSF	Power signal feedback
PSO	Particle swarm optimization
PWM	Pulse width modulation
RSC	Rotor side converter
SA	Standalone
SCIG	Squirrel-cage induction generator
TSR	Tip-speed ratio
WECS	Wind energy conversion system
WRIG	Wound rotor induction generator
WT	Wind turbine

Chapter 1

Introduction

1.1 General Background

—As yet, the wind is an untamed and unharnessed force; and quite possibly one of the greatest discoveries hereafter to be made, will be the taming and harnessing of it.”

Abraham Lincoln, Lecture- 'Discoveries and Inventions' (1860)

The demands for energy sources are increasing day by day with the increasing global population and developmental activities. Every nation in today’s world is looking forward to alternative sources of energy other than the prevailing one to meet future energy requirements. According to the report of the US Department of Energy, based on current consumption and population growth, projected crude oil and natural gas would come near an end around the year 2075 and 2181 respectively [1]. Apart from the issue of imminent depletion, environmental ill effects of fossil fuel based power plants have intensified the ecological imbalance of nature. Fossil fuel based power plants load the atmosphere with greenhouse gases (GHG), and it is proved that generation and consumption of energy are responsible for 50 to 60 percent of GHG released into the atmosphere on a global basis [2]. In the year 2013, annual global energy and process-related GHG emissions rose to the level of 37.5 Giga-tonnes of carbon-dioxide equivalent and will keep increasing henceforth [3]. Rising Global concern caused by the harmful effect of fossil fuel based plants and scarcity of the diminishing non-renewable energy sources enforces a gigantic drift towards the renewable energy sources in the power sector. Nuclear energy had been often anticipated as one of the major contributors to fulfill the future energy demand, but the risks associated with nuclear power plants are immense. Especially, after the

colossal damages and fatalities caused by the few accidents in nuclear power plants like the one in Fukushima, Japan on March 2011, people started to raise their voice publicly against the establishment of nuclear plants.

Eventually, solar power and wind power is supposed to dominate as potential renewable energy sources in all over the world. In many countries, the potential generation of wind power exceeds by far the local consumption. Economically attractive features and environment-friendly power production led the incorporation of this weather-dependent power source into existing power systems. The global wind energy council recently released an outlining scenario where it predicts that wind could supply 20% of global electricity by 2030. Fig. 1.1 shows the global trend towards increasing demand in wind energy production [4].

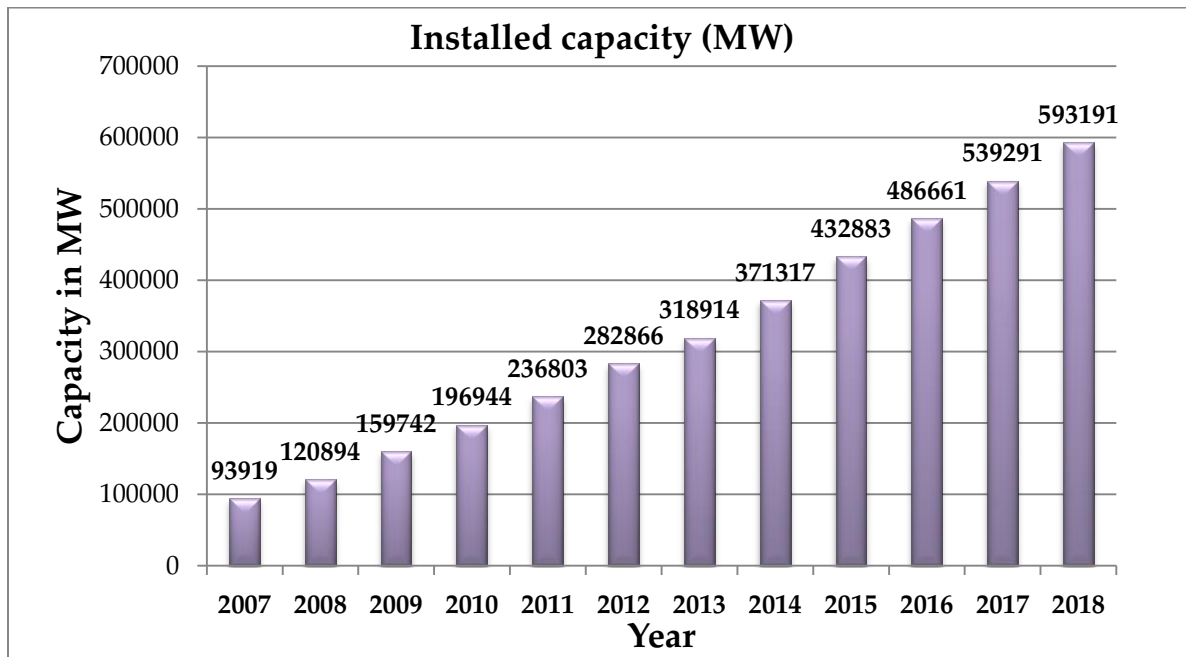


Fig. 1.1. Cumulative installed wind capacity in all over the world over the last decade [4].

In the near future, many countries around the world are likely to experience a higher penetration level because of its economic advantage in areas with appropriate wind speed. It is technically possible

to develop a power system with a very high wind peak penetration of up to 70% in isolated wind-diesel systems [5]. The integration of bigger share of wind energy into power system was initially designed for large-scale synchronous generator. Now-a-days the advancements with state-of-the-art generators and converter topologies have opened up doors for researchers to achieve higher efficiency and better power quality in wind energy conversion system (WECS).

1.2 Historical Aspect of Wind Power Generation

The earliest documented design of windmill dates back to 200 B.C. People used vertical axis windmills for grinding grains during this period. At early age, Europeans led the innovation and development of windmills. The French adopted grain grinding mills by 1105 A.D. and the English by 1191 A.D. By the 13th century, the Dutch were the pioneers in making horizontal axis wind farms [2]. The rotor made with crude airfoil profile and the protection against high winds by turning the rotor out of the wind had incredibly improved the efficiency of these wind mills. By 1800 about 20,000 modern European windmills were in operation in France alone and 90% of the energy used in industries was produced by wind farms across the Netherlands. These windmills reached America through the Dutch settlers by mid-1700. The so-called American multi-bladed wind turbine appeared in the wind energy history by the mid-1800. These windmills were self-regulated which offered better field performance as water-pumpers. Over six million such units were installed in the US alone, between 1850 and 1930.

The era of wind electric generators began close to the 1900's. In 1891, Dane Poul Lacour designed a wind turbine that could generate electricity. A large wind electric generator with 'picket fence' rotor was built in Cleveland, Ohio during the same period. The development continued during world wars I and II to overcome energy shortages. Some interesting designs of wind turbine had been experimented during this period. G.J.M Darrieus put forth the design of Darrieus turbine in 1920 [6]. In contrast with

the popular horizontal axis rotors, Darrieus turbines had narrow curved blades rotating about its vertical axis. Another major improvement in turbine design was led by S.J. Savonius in Finland. The Savonius rotor, which was made with two halves of a cylinder split longitudinally and arranged radially on a vertical shaft [7] was driven by the difference in drag forces acting on its concave and convex halves by the wind. By about 1925, wind electric generators with a capacity of 0.2 to 3 kW became commercially available in America, have two and three bladed propeller turbines. The Russians built a 100kW turbine in 1931 which worked for two years. The Danish company F.L. Smidh is considered as forerunner to build the first modern wind turbine generators in 1941-42 which used modern airfoils. Intensive research on the behavior of wind turbines occurred during 1950's. Johan Juul developed the Danish design philosophy further during 1960's by installing Wind turbines in Gedser, Denmark which remains operational over decades. German scientist Hutter designed highly efficient turbines comprised of two slender fibreglass blades. In the later years, cheaper and more reliable electricity, generated from fossil fuel based plants became available. Thus, the interest in wind energy declined gradually by 1970. Only small scale wind turbines for remote area power systems or for battery charging received some interest.

The oil crisis in 1973 caused the revival of interest in wind energy. A series of horizontal axis turbines named MOD-0, MOD-1, MOD-2 and MOD-5 were developed by NASA in early 80's. Research and development on wind energy have been intensified in the later years. By the end of the twentieth century, 20 years after the unsuccessful testing of megawatt wind turbines, the 2 MW wind turbines had become the technical state-of-the-art of that time. Figs. 1.2 depict the share of installed wind power till 2018 by the top wind power generating countries (capacity-wise) worldwide. It would be worthy of mentioning here that the Vestas V164, has a rated capacity of 9.5 MW with 164 m rotor

diameter and an overall height of 220 m, is the world's largest-capacity wind turbine till date since its introduction in 2014.

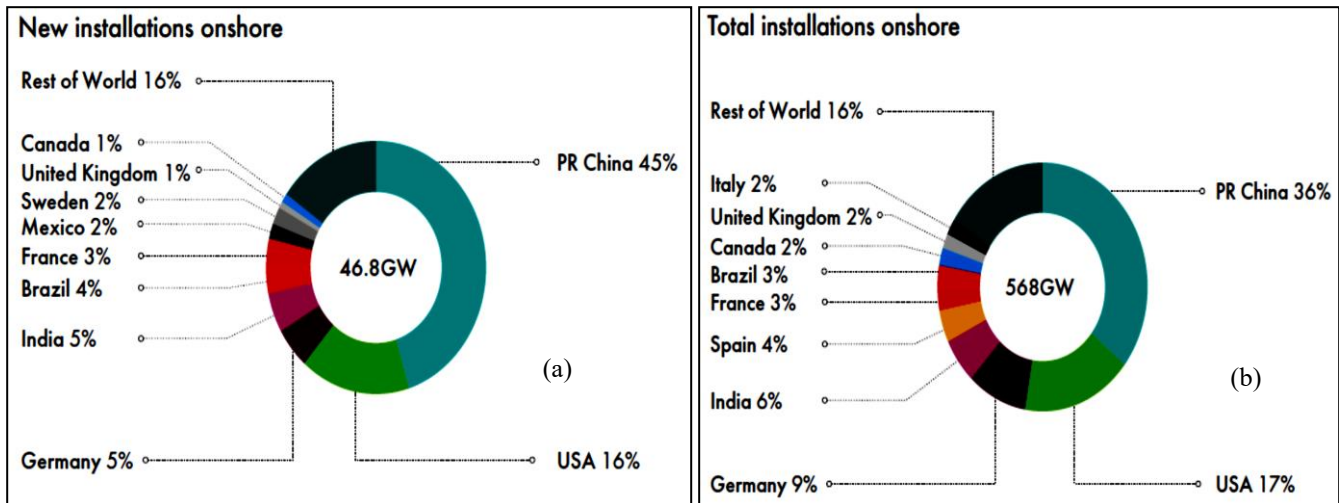


Fig. 1.2. Country-wise shares in cumulative wind generation capacity until April 2018: (a) New onshore installation in 2018 (b) Total onshore wind power installation till 2018 [4].

In Canada, the share of wind energy in total energy generation is burgeoning. The major portion of the energy demand in Canada is met by hydropower generation.

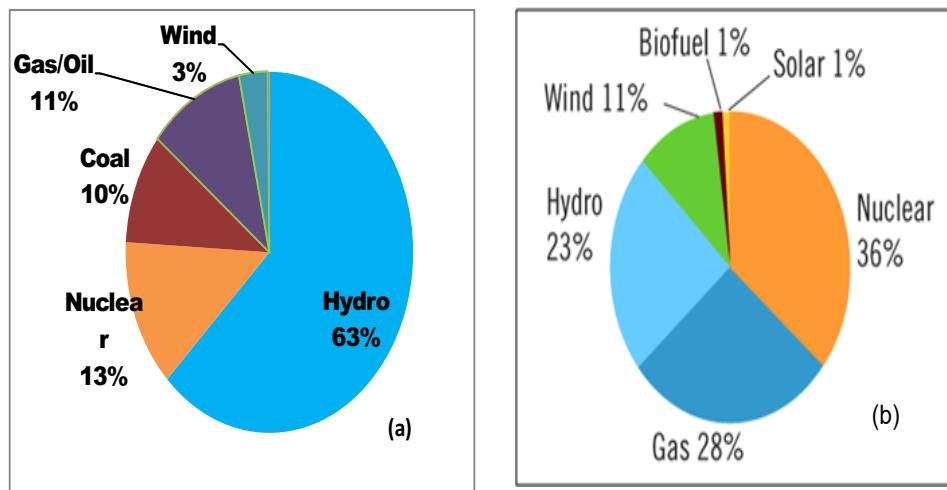


Fig. 1.3. The generation of electric power by source: (a) All over Canada (b) In Ontario [120].

According to the report of the Canadian wind energy association (CanWEA), the current installed capacity in Canada has reached to 12816 MW (as of December 2018) while it was only 114 MW across the country in 2000. The five-year annual growth rate for wind energy is 23% (1348 MW/year). In 2018, Canada has become 8th in the world for total onshore installed wind energy capacity [4]. Fig. 1.3(a) and (b) show the participation of wind power in total power installed capacity nationwide and in Ontario, respectively. Considering the increased demand for green energy, there are immense scopes of expansion in wind power generation in all over Canada, particularly in Ontario.

1.3 Literature Review

Nowadays, the wind turbine market mixes and matches a variety of innovative concepts with proven technology. One of the design criteria of a modern wind turbine is its mechanical structure of the blades that influences the power extraction efficiency of the turbine. Modern wind turbines are predominantly based on the aerodynamic lift. This type of turbine utilizes the incoming wind to create the necessary driving torque [8]. Wind turbines that utilize aerodynamic lift, are divided into two groups according to the orientation of the spin axis- vertical axis and horizontal axis turbines. Horizontal axis (HA) wind turbine is commercially used in modern turbines since 1980 and nowadays three bladed HA wind turbines dominate the grid-connected wind power conversion system because the turbines have better visual aesthetics and lower noise level [9].

The aerodynamic operating principle of the blade of the wind turbine can be explained by Bernoulli's principle on the flow of fluids. The extracted power by the wind turbines can be regulated by controlling the lift force created by the wind on the blades. The important parameter that characterizes the lift force of the blade is the wind's angle of attack. The angle of attack is the angle between the chord of the blade and the direction of the wind blow. The angle of attack can be changed

by pitch mechanism, which enables the rotation of the blade along the longitudinal axis. Thereby, the pitch control of the turbine blade provides a degree of control on the extracted power and protection of the turbine. There are three aerodynamic methods of control for turbine blades in modern large-scale wind turbine: passive stall control, active stall control and pitch control. In passive stall control, the blade is fixed on the rotor-hub at an optimal angle of attack and the wind turbine operates at constant rotational speed with fixed-pitch blade. In the active stall method, the wind turbine rotates at a particular speed with adjustable pitch blade. On the other hand, the pitch control mechanism can either be hydraulic or electric [10]. Pitch control is very important for the protection of wind turbine at high-speed wind. When the wind speed exceeds the maximum limit of tolerance, the blades are fully stalled or fully pitched to stop power capturing by the turbine. Also, the aerodynamic control provides tight control over the power generation while the turbine operates above rated speed.

For turbine connected squirrel cage induction machines, the generator runs at near-synchronous speed by consuming reactive power from the grid. This mode of operation is denoted as constant speed constant frequency (CSCF) mode. In this mode, the system delivers the rated power to the grid only at given wind speed, leading to low energy conversion efficiency at other wind speeds. However, if there is the flexibility of altering the rotor speed, the energy capture due to intermittent wind velocities can be increased significantly [11,12] that can be implemented in variable-speed constant frequency (VSCF) mode. The requirement for VSCF mode of operation leads to several developments in the generator control. Irrespective of the generator used for a variable-speed WECS, the output power depends on the method of tracking the peak power points on the turbine characteristics because of the variation in wind velocity.

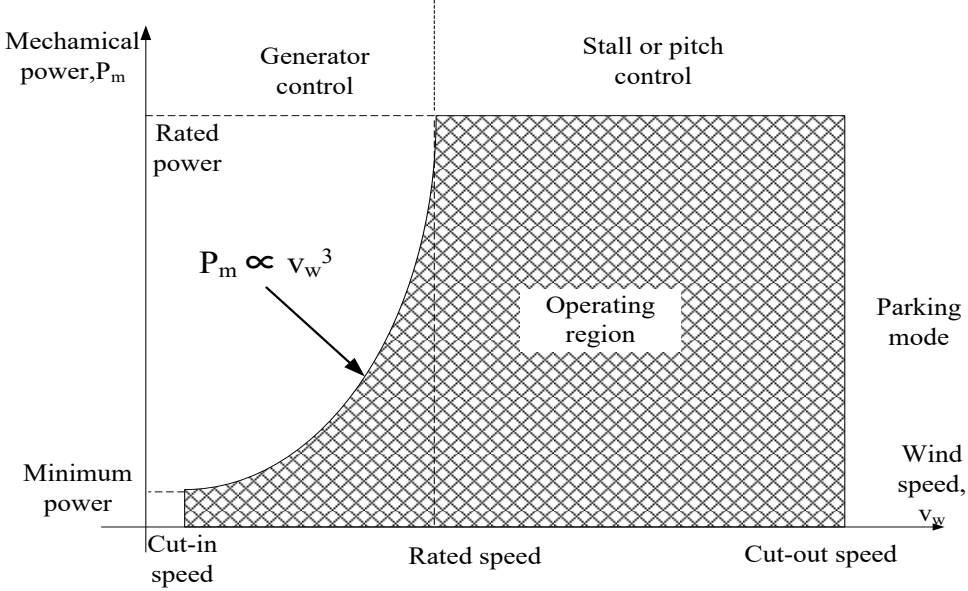


Fig. 1.4. A typical turbine power output curve.

The power captured by the blades is a cubic function of wind speed as shown in Fig. 1.4 until the wind speed reaches its rated value according to (2.8). In moderate-speed region where wind speed is delimited by the cut-in speed and turbine rated speed, the turbine rotor speed is controlled to extract the available maximum power via variable speed wind turbines through adjustment of rotational speed. The variable speed generators capable to follow the instantaneous variations of wind speed. Therefore, there is an increasing research trend to use maximum power point tracking algorithm to extract maximum power from wind by using variable speed generators over the past decade.

1.3.1 Maximum Power Point Tracking Algorithm

According to the maximization of captured power, the MPPT algorithms are broadly categorized into two types- indirect power controller and direct power controller. The indirect power controller maximizes the captured mechanical wind power whereas the direct power controller exclusively maximizes the generator output power [13]. Three different types of MPPT algorithm are observed in indirect power control method. The first type of MPPT is the tip speed ratio (TSR) algorithm [14]. In

the TSR control algorithm, it is required to keep up the TSR to an optimum value at which extracted power is maximized by regulating the rotational speed of the generator. This requires an anemometer which, however, is inaccurate due to the turbulence on the surface of the turbine blades and the variation of the wind speed along the length of the blade. The other two algorithms are power signal feedback (PSF) [15] and optimal torque MPPT algorithm [16-18] which do not need the anemometer, but still require the specific parameters of wind turbine. PSF control requires the knowledge of the turbine maximum power tracking curve for its control mechanism. The peak power tracking curve can be obtained through simulation or experimental data of individual turbine which is cost ineffective and troublesome. In [16], Abdullah *et al.* compares among the performance of different MPPT algorithms based on various speed responses and ability to achieve the maximum energy yield and concludes that optimum torque control provides the most convincing outcome for wind energy system. Wind speed sensorless control, generator rotor position control, speed sensorless vector control schemes, direct torque and direct power control schemes for a variety of direct-drive permanent magnet synchronous generator (PMSG) based WECS has been reviewed by Y. Zhao *et al.* in [17]. In this paper, authors explored that the inherent motion-sensorless DTC and DPC provide promising and attractive alternatives for speed sensorless control of PMSG-based WECS. An output maximization control is proposed without mechanical sensors such as wind speed sensor and position sensor in [18]. In the proposed MPPT strategy, the generator torque is controlled based on trailing of the optimum torque curve. However, in [16-18], authors suggested TSR or modified TSR method for MPPT control. The first barrier to implement TSR control is the need to obtain the optimal value of TSR, which is different from one wind turbine to another. Also, the method uses look-up table for storing the optimal TSR value for the turbine. Though the optimal values are assumed to be constant, there are various factors, such as, wind density, aging factor, non-constant efficiency of generator and power converters that may

cause drift in the optimal TSR. Therefore, the stored curve or mapping function may not remain valid for MPPT operation [121]. Optimal torque (OT) control adjusts the generator torque to an optimal one at different wind speed. The knowledge of the generator torque curve is needed for this method.

An optimum point search algorithm has been proposed in [18] to find out the peak power generated by the WECS. In the proposed method, the speed control mode with the speed reference is dynamically modified in accordance with the magnitude and direction of change of active power. In another work [19], the authors have proposed a fuzzy logic based variable speed wind power generation system that uses cage type induction generator and double-sided pulse width modulation (PWM) converters. However, identical results can be achieved even without the difficulty of executing a fuzzy controller. Uddin *et al.* developed [20] an adaptive MPPT algorithm incorporating an LMC and rotor speed sensorless schemes to transfer maximum power from WT to the dc link. In this work, optimum reference speed is generated for interior permanent magnet synchronous generator (IPMSG) by adaptive perturbation & observe (P&O) algorithm which is relatively slow to find peak point if the rotational speed is far away from its maximum power point (MPP) value. Hui *et al.* [21] have proposed a sensorless and adaptive parameter independent MPPT algorithm that is robust to wind speed change. A state observer supervisory control requires assisting the search for MPP which makes it complex. In [22], the authors investigated a neural network based control to maximize the extracted power by estimating wind velocity and computing pseudo power curves. This method has the drawbacks of having computational burden and dependency on the experience of the designer. Apart from the aforementioned methods, a number of other MPPT control strategies have additionally been proposed recently in [23,24] to get rid of their drawbacks. The hill climb search (HCS) and optimum relation (OR) based MPPT algorithms are considered under direct power control. These algorithms are also sensorless methods which locate the maximum power point by analyzing the power variation. Between

the two methods, HCS is vastly popular because of its simple implementation and flexibility [14- 16], [19]. This method is also known as perturbation and observe algorithm. The adaptive step HCS and the modified HCS algorithm mitigates the problems of the conventional HCS algorithm while tracing the MPP [25-27]. Researchers have attempted to mitigate the deficiencies of classical HCS algorithm through different complicated methods [28-34]. In [28], the maximum power point is obtained by calculating variable step size from the scaled measure of the slope of power with respect to the perturbed generator speed ($\Delta P/\Delta\omega$). This method might fail under rapidly changing wind speed condition because of the slope $\Delta P/\Delta\omega$ may not provide a correct measure of distance from the maximum point as the operating point shifts from one power curve to another for changing wind velocity. Some authors have proposed a search-remember-reuse based HCS controller introducing look-up table based technique by online training of a memory table [29]. The memory table is trained by comparing current output power at the nearest dc-link voltage and updated if the present peak power is greater than the previously recorded one. However, this update rule can't construct a proper look-up table for MPP. Instead this rule will result in a memory table that generate an output power versus dc-link voltage with highest power occurring at a definite rotor speed. The calculated rotor speed could be different from the optimum turbine speed. Also, the method might create a indecision to decide the direction of perturbation when the sign of change in output power is opposite to sign of change in dc-link voltage. Another approach is discussed in [30] where MPPT control of the wind generator is accomplished by direct adjustment of the dc-dc converter duty cycle. This technique is efficient but only suitable for permanent magnet wind generator and isolated load. Fuzzy logic provides a convenient method of maximum power point tracking as an advanced HCS control technique [31-33]. The adaptation attributes, the capability to achieve specified control objective and robustness under turbine parameter uncertainties make the algorithm appealing. However, the challenge in fuzzy control

is that how to define an optimal set of rules for desired control. In [34], a disturbance injection based HCS algorithm is proposed where a sinusoidal perturbation is employed instead of constant step. The convergence speed is slow in this method and it is capable of working efficiently only at constant or slowly varying wind speed. The combination of rotor speed deviation and corresponding power variation is used in the controller to calculate the step size adjustment. Although wind speed explicitly plays a vital role in peak power point determination, researchers have avoided this parameter in most cases due to the requirement of anemometers and having a tendency to avoid an extra variable in the controller design. However, all the modern wind turbines are usually equipped with high-precision ultrasonic anemometers. In those turbines, the updated wind stream velocity is available for control operation. As the turbine power output and optimum turbine speed both are strong functions of wind velocity, wind speed data should be incorporated in the MPPT control scheme. Apart from the literature mentioned earlier, a number of other MPPT control strategies with hybrid power control scheme have been proposed recently in [35-37]. However, the techniques are too complicated and infeasible for practical implementation.

1.3.2 Adaptive Nonlinear Control of WECS

Various control strategies have been implemented so far by researchers for effective control of grid-connected DFIG. The conventional vector control design of DFIG based wind power system involves cascaded control loops where simple proportional-integral (PI) controllers are executed to regulate the voltage/current. A major drawback of the PI controller is that proper tuning of the proportional and integral constants. The controller may fail to implement proper tracking performance if the constants are not selected appropriately. The PI control loop may lead to the unstable condition due to excessive integral gain if the machine and grid filter parameters are not precisely known in DFIG based WECS. Hence, direct power control (DPC) and direct torque control (DTC) of DFIGs have been introduced as

the alternative of the conventional vector control scheme [38-40]. However, large power or torque ripple and variable switching frequency are the two major drawbacks of these approaches [41]. As feedback linearization method requires the precise value of the model parameters and this technique often cancels out some useful nonlinearity, adaptive nonlinear control techniques have been approached as an efficient method for generator control [42-47]. Most researches have been conducted on nonlinear control operation of PMSG for wind energy applications [42,43]. However, backstepping algorithm based power control strategy of DFIG has been presented by authors in [44] under normal and harmonics in grid voltage to achieve better dynamic performance. A simulation study of adaptive backstepping algorithm for maximum power point tracking (MPPT) control is outlined in [45] which includes grid-connected DFIG-WECS. Azzaoui *et al.* have presented a similar approach to control electromagnetic torque and reactive power by regulating the rotor side and grid side converter utilizing Lyapunov stability criterion [46]. However, in the aforementioned literature, adaptive backstepping based control strategies are studied only in simulation. Also, parameter adaption has not been evaluated in most of these analyses. An observer based online parameter estimation technique for DFIG has been proposed in [47]. In [48], FPGA-based experimentation is presented, where an adaptive pole placement control approach is integrated into an adaptive backstepping based nonlinear control system. The control system utilizes Lyapunov's stability theorem to achieve MPPT along with stable output although the control of grid side converter and regulation of DC-link voltage has not been studied in the paper. Resonance based backstepping direct power control strategy is developed by X. Wang *et al.* [49]. The experimental results suggest better performance in reactive power and current THD control under normal and harmonic grid voltage. But, the system performance is not analyzed under variable wind speed and machine parameter variations. Touhidi *et al.* proposed an active power tracking algorithm by using a nonlinear discrete-time backstepping controller with higher order sliding mode

operation [50]. The offline gain scheduling of this method is turbine parameter dependent and requires precise parameter measurement. The boundedness and stability of a closed-loop DFIG-WECS are investigated in [51] that introduces lumped uncertainty to the system to check the stability. However, the sliding mode MPPT control is confined only to simulation study. The studies only suggest the solutions related to the obstacle in DFIG converter control to a partial extent. Hence, a comprehensive nonlinear adaptive control technique is required to guarantee the global stability of the DFIG-WECS under grid voltage fluctuation and wind speed variation with parameter adaptation incorporating MPPT scheme.

1.3.3 Intelligent Control of WECS

As DFIG based WECS experiences strong nonlinearity and uncertainties originated from the aerodynamics of the wind turbine and magnetic saturation of the DFIG, different adaptive and intelligent control schemes have been proposed in the literature to remedy the issue. Vector control associated with PI controllers has been widely recognized and applied in industry for reliable power regulation of DFIG. However, the performance of the vector control based system depends on the parameter tuning of the PI controllers, voltage condition at the grid end, randomness in wind speed, etc. Furthermore, the performance of the fixed-gain PI controller deteriorates with the variation in machine parameters due to the change in temperature, magnetic saturation and machine-aging. Therefore, the researchers have focused on more sophisticated problems for WECS control, such as backstepping based nonlinear control [44], fuzzy logic control [31], sliding mode control [39] etc. The major drawback of the reported fuzzy inference system is that it is completely based on the knowledge and experience of the designer [22]. On the other hand, intelligent control algorithms such as neural network (NN), neuro-fuzzy control (NFC), adaptive network-based fuzzy inference system (ANFIS), genetic algorithm, particle swarm optimization, artificial bee colony algorithm, grey wolf optimization

have not been thoroughly investigated yet for wind energy conversion system. ANFIS provides adaptability on choosing the membership functions and fast convergence due to its hybrid learning. Moreover, ANFIS architecture has the distinguishing feature of modeling a highly nonlinear system, as it combines the competence of fuzzy reasoning in handling uncertainties and learning aptitude of neural network from complex system [57,117]. Therefore, it has been chosen as the control algorithm for grid-connected and standalone wind power generation in this thesis.

1.3.3.1 Intelligent Control of Grid Connected WECS

Many researchers have focused on fuzzy logic based control of DFIG-WECS to improve the robustness of the controller. In [52], the concept of parallel distributed compensation is employed to design Takagi-Sugeno fuzzy model to stabilize a nonlinear wind power system with parametric uncertainties and disturbance. Model reference adaptive system [53] and sliding mode [54] based fuzzy logic control are used by authors to implement maximum power point tracking. A combined approach is found in [55] where authors have utilized fuzzy-PI controller to achieve the maximum wind energy extraction. An adaptive fuzzy control is introduced by Zhang *et al.* [56] to regulate generator torque and extract maximum power at below rated wind speed. The method exhibits robust control performance for different cases. However, the study is confined to simulation studies only. A vector control method is developed in [57] based on neuro-fuzzy scheme to control the converter that allows independent control of the generated active and reactive power. A data-driven DFIG model with neural network based control is proposed in [58] to compare the advantages of the data-driven modeling approach over the conventional system identification method. However, the models are dependent on fuzzy logic based determination of proportional and integral gains. No online parameter adaptation is introduced in the schemes. Several other advanced DFIG control algorithms, such as model-based predictive control [59], sliding mode control [60] have also been proposed in the literature.

From the design point of view, the reduced power rating of the converter makes DFIG driven WECS economically profitable compared to the full-scale power converter topologies; however, it limits the effective power conversion under voltage dips. Among the major challenges in the grid-connected operation of DFIG-WECS, effective and robust control of the system against grid voltage distortion and harmonic imbalances are of critical importance. Especially, it has been more challenging in the modern power system as different countries have their own grid code to fulfill during voltage dip condition [61-62]. Voltage sag in the grid supply creates three major problems in grid-connected DFIG system. The first one is high per unit rotor current which could exceed the allowable rotor current limit. Secondly, it may cause overvoltage on dc-link that may create an imbalance in grid-side converter control. Thirdly, voltage dip may enforce power saturation at the rotor side converter that could damage the converter itself. Therefore, a sophisticated control scheme is required to overcome the issues related to the voltage-dip condition. So far, various control schemes have been proposed in the literature that often involves hardware-based solutions such as crowbar, energy storage rather than tackling with the problem of appropriate controller design. An H_{∞} robust current controller is proposed by Wang *et al.* [63] to track the unbalanced current components effectively and suppress unwanted harmonics. The problem of the method is the determination of the weighting functions, which is complex and cumbersome. The application of a dynamic voltage restorer (DVR) connected to a wind-DFIG-WECS is investigated in [64] that is a voltage source converter connected in series with the grid to correct the faulty line voltages. The DVR allows uninterruptible fault ride through of voltage dips fulfilling the grid code requirements under transient grid voltage sag condition. This method requires expensive hardware setup apart from the crowbar protection for implementation. A virtual impedance control strategy to enhance the high-voltage ride-through capability of DFIG is investigated in [65]. Although the method is capable of suppressing the rotor current and torque oscillation; three different

parameters, e.g., maximum amplitude ratio of rotor voltage and implied disturbance, resistance inductance ratio and proportion of virtual impedance are required for implementing this scheme. A combination of passive and active compensators is proposed in [66] to improve the low-voltage ride-through (LVRT) capability in wind turbines with DFIGs where passive compensator consists of new crowbar protection. However, because of the limited capacity of the rotor side converter, the proposed method doesn't completely remove the oscillations of stator flux and DFIG transient response during and after clearing the fault. Since ANFIS has the potential to cope with the wind power system uncertainties, such as wind speed variation, the instance of voltage-dip occurrence and bypasses the dependency on system's mathematical model in the design of controller, this method is chosen as the current control scheme for converter control in this thesis.

1.3.3.2 Intelligent Control of Standalone WECS

Remote villages and communities, isolated from the utility grid, have to generate electric power from their own resources. Till now, fossil fuel based generators have prevailed as the primary source of power generation in remote islands and isolated rural areas where grid connections are unavailable. However, fossil-fuel based power supply is comparatively expensive because it involves heavy-vehicle transportation and extra overhead costs for storage in isolated areas. Also, there has been a global concern to reduce the usage of CO₂ emitting fuels. One of the solutions to these issues is to introduce sustainable power sources as standalone units. Wind power is one of the main renewable energy sources that have gained attention for remote-area power generation in the last few decades. Due to the intermittent nature of wind flow, the wind generator can't sustain during isolated operation without the support of additional power sources. Various alternative energy sources such as flywheel based energy storage, turbine driven by water flow, hybrid energy storage supported by diesel engine, photovoltaic panel have been chosen for standalone operation of DFIG driven WECS. However, the battery storage

based standalone wind turbine power system gained popularity because of its ease of control and convenient storage facility [67-69]. Power control techniques such as vector control [70], direct power control [71], direct torque control [72] have been proposed in the literature to regulate the power output of DFIG for standalone mode under balanced and unbalanced condition. Unlike the numerous research attempts on grid-connected DFIG-WECS, only a handful of articles have been found in standalone mode operation of DFIG in wind power islanding mode under variable speed condition [73-75]. A model reference adaptive system (MRAS) observer [76] and signal parameter estimation based approach [77] for the determination of harmonics/ inter-harmonics are proposed by the authors for standalone control of DFIG to solve power quality issues. To the best of the author's knowledge, the only paper that focuses on intelligent control approach for standalone WECS, utilizes particle swarm optimization (PSO) algorithm adopted with PID controller in unified power flow controller [78]. However, this approach is confined to reactive power compensation issue with the help of flexible AC transmission system (FACTS) controller and transient stability analysis in hybrid power system with limited simulation results. Also, the model doesn't show the detail design of the system. Therefore, there is a strong need to develop intelligent algorithm based control techniques to achieve robust and sustainable WECS.

1.4 Research Motivation

Wind is stochastic in nature. Speed and direction of the wind at a location vary randomly with time. Hence, the process of harnessing wind power requires sophisticated techniques. Researchers aim for different goals while designing the controllers for WECS. Extraction of the available maximum power from the wind turbine is one of the primary targets in modern wind power conversion systems. Among different MPPT schemes, the HCS method is the basis of all parameter-independent MPPT algorithms. Although fixed step size based HCS algorithm has several shortcomings such as power

fluctuation near peak power, determination of proper step size, trade-off between controller speed and efficiency, the drawbacks can be overcome by applying mathematical strategies. Hence in this thesis, an adaptive step size MPPT controller based on the HCS algorithm is proposed. The proposed function-based adaptive control scheme evaluates the step size by the variation of the wind speed and turbine-power range and minimizes the steady state power fluctuation with improved tracking. The controller is designed to overcome the drawbacks of the conventional HCS algorithm by incorporating wind speed measurement in the controller design.

Sooner or later, wind turbine will replace the conventional power plant at massive scale and large wind farms will be expected to meet very high technical demands such as strict frequency and voltage control. Although the implementation of the fixed gain PI controller has been successful in DFIG-WECS, proper tuning of the gain constants and lack of robustness are the major deficiencies of this type of controller. Alternative nonlinear control approach are backstepping and adaptive backstepping based control. These controllers are effective when systems are not exactly linearizable and affected by disturbances. DFIG inherits nonlinear magnetization characteristics and the generator parameters may experience variation due to the aging effect and change in temperature. Therefore, in this thesis, a nonlinear controller is designed to deal with the nonlinear coupling among generator currents and the rotor speed and cope with parameter uncertainties. For the adaptation of magnetization inductance of the machine, estimation rule is derived. Furthermore, a loss reduction model is incorporated into the design to achieve enhanced efficiency.

Injection of wind power into an electrical grid affects the power quality in it. Direct connection of a turbine-connected induction generator may result in inrush current that could cause turbulence to the grid and high torque spikes in the drive train. The common impacts of wind farms on the power quality of a power system are voltage fluctuation/flicker, voltage dip, harmonic generation, etc. To maintain

the power quality characteristics specified by IEC 61400-21, these impacts have to be kept within allowable limit; hence, stability must be maintained at the generation side. As discussed in the literature review section, the design of nonlinear controller depends on extensive mathematical model. The control variable sometimes suffers from chattering around steady-state specially in sliding mode control [122]. As an alternative to nonlinear controllers recently researchers paid attention to the application of intelligent algorithms but so far only a few research has been reported on the application of intelligent control techniques for DFIG based wind power system. Intelligent control algorithms such as neuro-fuzzy control (NFC) or adaptive network-based fuzzy inference system (ANFIS) have not been thoroughly investigated yet for grid-connected DFIG. Therefore one of the prime foci of this research work is to develop an efficient, low computational neuro-fuzzy scheme to control the real and reactive power of the DFIG based wind power system.

Modern day grid code requirement demands that the generators need to remain connected to the grid even during voltage dip. The ANFIS based NFC current control technique is also implemented to prevent voltage and current saturation in the rotor converter during symmetric and asymmetric voltage dip. Besides, an offline trained NFC technique is proposed for converter control in standalone operation of DFIG-WECS for improved performance.

Finally, a novel battery storage power optimization technique for DFIG-WECS is also proposed in this thesis. A unique meta-heuristic algorithm known as grey wolf optimization (GWO) is introduced to ensure the optimized power exchange in a battery supported DFIG standalone (SA) system. The proposed optimization algorithm is chosen for its simplistic implementation, fast convergence and superior ability to avoid local optima over other conventional optimization techniques.

To verify the performance of the MPPT, nonlinear and GWO based battery power optimization controller, the proposed schemes are tested both in simulation and experimental environment using

MATLAB-Simulink and dSPACE DS1104 board, respectively for a laboratory 480 VA prototype DFIG.

1.5 Objectives of the Thesis

Wind energy technology itself has moved very fast to a new dimension. Researchers are focusing on innovative control strategies and cutting-edge methodologies that could maximize aerodynamic efficiency, thus, the wind energy capture. In this research work, the target is to focus on maximizing the turbine output power, maintaining stable output produced by DFIG and exploring the option of utilizing back-to-back converter in WECS.

The main objectives of this research are as follows:

- a) To develop and investigate the performance of a new adaptive step size based HCS controller for extraction of peak power from the wind turbine under variable conditions.
- b) To design an adaptive backstepping based nonlinear control scheme incorporated with machine loss reduction and parameter uncertainties.
- c) To develop a loss minimization algorithm (LMA) and incorporate with the nonlinear controller to improve the efficiency of the system
- d) To develop an ANFIS based NFC controller to control the converters both in normal and voltage dip conditions.
- e) To design GWO based intelligent battery power optimization control algorithm for standalone operation of DFIG-WECS.
- f) To implement the controllers in real-time and verify the results obtained from the simulation.

The controllers are designed and verified in simulation. Within the limited resources of the laboratory, the proposed MPPT scheme, nonlinear control scheme and standalone control of DFIG has

been implemented in real-time module using digital signal processor (DSP) processor board for a laboratory prototype DFIG.

1.6 Organization of the Chapters

The chapters of the thesis are organized as follows.

A review of literature on the existing control techniques of DFIG-WECS and objectives of this thesis are presented in this Chapter 1. The historical background on the development of wind power conversion system and the motivation of the thesis is also provided in this chapter.

In Chapter 2, an overview of the wind energy conversion system is portrayed. The description of equipment used in wind turbine is described. The mathematical model of the wind turbine and dynamic model equations of the DFIG are collected in this chapter.

Chapter 3 illustrates the performance of the designed MPPT controller. The simulated response and comparison between the proposed and conventional HCS controller are illustrated in this chapter.

In Chapter 4, adaptive backstepping based nonlinear control is developed for DFIG based WECS. The estimation model of magnetizing inductance is also formulated along with a loss minimization algorithm.

ANFIS based converter control for grid-connected DFIG-WECS is presented in Chapter 5. The performance analysis of the neuro-fuzzy controller for normal and voltage dip conditions of the system is detailed in this chapter. Also, comparative analyses among the designed controllers are presented for grid-connected generator.

Chapter 6 details the analysis of intelligent control algorithm of DFIG-WECS for standalone operation mode. ANFIS and GWO based control for islanded wind power system are presented with results demonstrating the performance of the algorithms through a series of tests carried in the real-time prototype.

Finally, a summary of the thesis and suggestions for future works are highlighted in Chapter 7.

All pertinent references and appendices are listed at the end of the thesis.

Chapter 2

The Structure and Modeling of Wind Energy Conversion Systems

The source of power for wind energy conversion system is the kinetic energy of wind. The turbine converts the kinetic energy of wind into mechanical energy. Then the obtained mechanical energy is transformed into electrical energy with the help of the generator. The WECS system is made up of several components such as, wind turbine, power converters, sensors, gear-box, controller etc. In order to understand the steps of wind energy conversion process, the basic components of a wind turbine system are briefly described here.

2.1 Wind Model

The movement of air masses in the space of the global atmosphere is perceived as wind flow. There are many factors that cause the wind flow. The most important factor is the heating of the earth's surface by the sun. Also the rotation of the earth, the topography of the land, such as the presence of mountain, sea, desert, valley, etc. affect the motion of the wind in the atmosphere. For the purpose of simulation, the wind vector is considered to be composed of a steady state component plus fluctuations about the steady value. A proper wind model should include the spatial effect of wind behavior including rapid changes, gusting and environmental noises. The wind model chosen for the simulation of this thesis has four components and is defined by the following equation [79]:

$$v_{wind} = v_{base} + v_{gust} + v_{ramp} + v_{noise} \quad (2.1)$$

Where, v_{wind} is the total wind speed.

v_{base} is the base wind velocity.

v_{gust} is the gust wind velocity.

v_{ramp} is the ramp wind velocity.

v_{noise} is the background noise velocity.

The base wind speed is defined by the following equation:

$$v_{base} = K \text{ m/s} \quad (2.2)$$

Where, K is a constant. The range of K is selected in between 5 to 12 for simulation purpose.

The gust wind velocity is described by the following equation

$$v_{gust,i} = \begin{cases} 0, & t < t_{gi,start} \\ \frac{v_{gmax,i}}{2} \{1 - \cos(2\pi[(t - t_{gi,start})/t_{gi,per}])\}, & t_{gi,start} < t < t_{gi,per} + t_{gi,start} \\ 0, & t > t_{gi,per} + t_{gi,start} \end{cases} \quad (2.3)$$

Where, $v_{gmax,i}$ is the peak wind gust in m/s for i-th gust velocity.

$t_{gi,start}$ is the starting time of i-th gust (sec).

$t_{gi,per}$ is the i-th gust period (sec).

t is time in sec.

The ramp wind velocity component is expressed by the equation

$$v_{ramp,i} = \begin{cases} 0, & t < t_{ri,start} \\ \frac{v_{ri,peak}}{2} [1 - \frac{t - t_{ri,peak}}{t_{ri,start} - t_{ri,peak}}], & t_{ri,start} < t < t_{ri,peak} \\ 0, & t > t_{ri,peak} \end{cases} \quad (2.4)$$

Where, $v_{ri,peak}$ is the i-th peak ramp speed in m/s.

$t_{ri,start}$ is the i-th ramp start time (sec).

$t_{ri,peak}$ is the i-th maximum ramp time (sec).

The background noise component of wind velocity is completely random. The random number Simulink block is utilized to imitate the background noise of wind velocity with maximum, minimum and sample time of 0.02 m/s,-0.01 m/s and 0.01 sec respectively.

2.2 Wind Turbine Structure

Historically it is evident that the utilization of wind power started at least 3000 years ago. Before the modern era people managed to exploit the wind power to pump water or to grind grains. The early Persian vertical axis wind wheels ran on the drag principle. However, this equipment had very low efficiency. In modern wind turbines, mechanisms are introduced such that aerofoils interacting with the incoming wind produce aerodynamic lift. The lift force acts in the perpendicular direction of the air flow and via the leverage of the rotor blade produces necessary driving torque for the machine. Wind turbines using aerodynamic lift can be further divided into two different types, namely vertical axis and horizontal axis turbine. Horizontal axis wind turbine has become the dominant candidate in today's wind market, especially in large commercial wind farms.

Wind turbines can also be classified into fixed-speed and variable-speed turbines. Regardless of the wind speed, wind turbine's rotor speed is almost constant in fixed speed wind turbine and determined by the gear-ratio of the gear box, supply frequency of the grid and pole number of the generator. This type of turbine is simple, robust and reliable. However, its disadvantages are uncontrollable reactive power consumption, mechanical stress and limited power quality control. The fixed-speed turbine generates highly fluctuating output power to the grid, causing disturbances to the power system.

On the contrary, variable speed wind turbines are designed to achieve maximum aerodynamic efficiency over a wide range of wind speed. With the use of variable speed operation, the rotational speed of the turbine is adapted according to the wind speed. In doing so, the tip speed ratio, which is

the ratio of the blade tip speed to the wind speed, is kept constant at an optimal value that corresponds to the maximum power coefficient. The advantages of variable speed wind turbines are reduced mechanical stress, improved power quality and increased wind energy output. The disadvantages are losses in power electronics and increased manufacturing cost because of the intermediate power converter stages. The typical structure of a horizontal axis wind turbine is shown in Fig. 2.1. A brief description of the parts of a wind turbine are described in the following subsections.

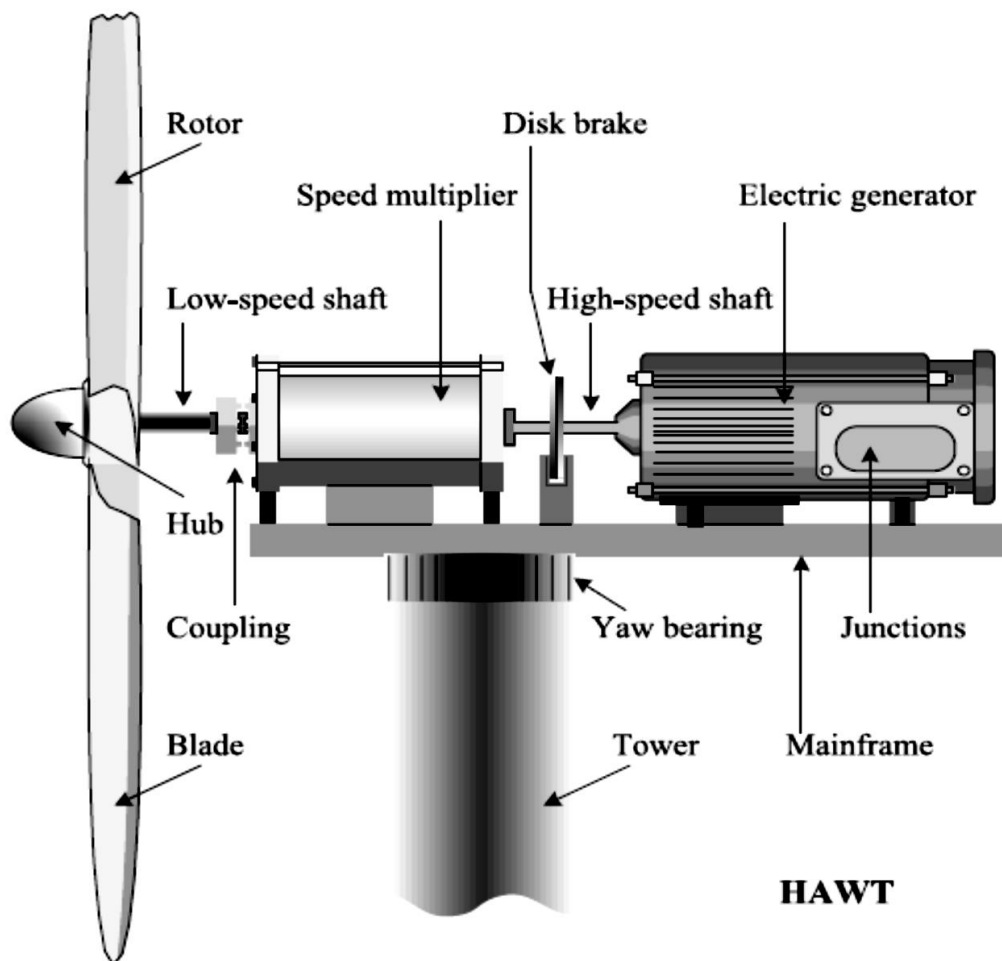


Fig. 2.1. Main components of a horizontal-axis wind turbine [116].

2.2.1 Turbine Blade

Although single and two-bladed wind turbines have found practical applications, the three-blade rotor is considered the industry standard for large wind turbines. Turbines with fewer blades operate at higher rotational speeds. This is an advantage from the drive train point of view since they require a gearbox with a lower gear ratio, which translates into lower cost. Single-blade turbines have an asymmetrical mechanical load distribution. The turbine rotors are aerodynamically unbalanced, which can cause mechanical vibrations. Rotors with more than three blades are not common since they are more expensive. The lagging wind turbulence of one blade can affect the other blades since they are closer to each other in turbines with more than three blades. Hence, the three-blade rotor offers the best trade-off between mechanical vibrations, acoustic noise, cost and rotational speed for large wind turbines [80].

2.2.2 Tower and Foundation

The tower of a wind turbine is made of concrete or steel with tubular or cylindrical structure. The design of the tower and the foundation needs sophisticated calculations and accuracy as it not only carries the weight of the nacelle and the rotor blade but also absorbs the huge static loads caused by the varying power of the wind. Also foundation needs to be grounded against lightning strikes etc. and the calculations for that is quite intense as the soil needs to be prepared for this by copper rings being buried along with additional conductors to keep the voltage from the lightning strike low.

2.2.3 Nacelle

The nacelle holds all the turbine machinery. It is connected to the tower via bearings because it must be able to rotate to follow the wind direction.

2.2.4 Gearbox

The gearbox takes on the task of matching the rotation speeds of the slow-moving rotor and the fast-moving generator and generally has several steps to cover for various wind conditions. The gearbox conversion ratio, also known as the gear ratio, is designed to match the high-speed generator with the low-speed turbine blades. The ratio can be calculated by using the following equation.

$$r_{gb} = \frac{n_g}{n_t} = \frac{(1-s)60f_s}{P \cdot n_t} \quad (2.5)$$

Where, s is the rated slip, f_s is the frequency of the stator in Hz, P is the number of pole pairs of the generator and n_g and n_t are generator and turbine rated speed in rpm.

2.2.5 Coupling and Mechanical Brake

Because of the enormous torque, the coupling between the main shaft and the transmission should be a rigid one. The mechanical brake is normally placed on the high-speed shaft between the gearbox and the generator. The brake is normally used to aid the aerodynamic power control (stall or pitch) to stop the turbine during high-speed winds or to lock the turbine into a parking mode during maintenance.

2.2.6 Yaw Drive

The yaw drive is an important component of the horizontal axis wind turbines yaw system. To ensure the wind turbine in producing the maximal amount of electric energy at all times, the yaw drive is used to keep the rotor facing into the wind as the wind direction changes.

2.2.7 Sensors

The pitch/stall and yaw control systems require wind speed and direction measurements, respectively. Most large wind turbines are equipped with sensors, also referred to as anemometer. The wind speed and direction is measured by a wind vane connected to optoelectronic transducers. In

modern wind turbines, ultrasonic anemometers are used which measure the wind speed by emitting and receiving acoustic signals through air and monitoring the transmission time.

2.3 Power Characteristics Equations of Wind Turbine

Wind speed plays the key role to characterize the output of a wind farm. The wind turbine power characteristics curve provides the necessary insight to explain how the power output of a wind turbine can be regulated by adjusting the blade pitch angle or by controlling the generator's torque or speed. Wind energy conversion systems convert the kinetic energy of the wind into electrical energy. The kinetic energy associated with an object moving at a velocity v can be expressed as,

$$E_k = \frac{1}{2}mv^2 \quad (2.6)$$

The mechanical power of the wind turbine can be related to the kinetic energy of the wind. The total power of air mass flowing at a speed v_w is given by,

$$P_w = \frac{E_k}{t} = \frac{\frac{1}{2}mv_w^2}{t} = \frac{\frac{1}{2}\rho Adv_w^2}{t} = \frac{1}{2}\rho A v_w^3 = \frac{1}{2}\rho\pi R^2 v_w^3 \quad (2.7)$$

Where, ρ is the air density, A is the swept area of the air flow, R is the radius of the turbine and d is the distance traveled by the wind. The wind power captured by the blade and converted into mechanical power can be calculated by,

$$P_m = \frac{1}{2}C_p\rho\pi R^2 v_w^3 \quad (2.8)$$

Where C_p is the power coefficient of the blade. The theoretical optimum for utilizing the power in the wind by reducing its velocity was first discovered by Betz. According to Betz, even if power extraction without any losses were possible, only 59% of the wind power could be utilized by a wind turbine. Hence the maximum value of C_p can be 0.59. The power coefficient of a modern turbine usually ranges

from 0.2 to 0.5, which is a function of the tip-speed ratio (λ) and pitch angle (β). The term tip-speed ratio, defined as

$$\lambda = \frac{\omega R}{v_w} \quad (2.9)$$

Where, ω is the wind turbine rotor speed of rotation (rad/s).

The wind turbine torque can be defined by the following equation

$$T_m = \frac{P_m}{\omega} = \frac{1}{2} \frac{C_p \rho \pi R^3 v_w^2}{\lambda} \quad (2.10)$$

$$P_m = \frac{1}{2} C_p \rho \pi R^2 v_w^3 \quad (2.11)$$

Many different versions of fitted equations for the turbine power coefficient C_p have been discussed in literature. In this thesis, C_p is expressed by the following generic function [118].

$$C_p(\lambda, \beta) = c_1 \left(\frac{c_2}{\lambda_i} - c_3 \beta - c_4 \right) \exp\left(\frac{-c_5}{\lambda_i}\right) \quad (2.12)$$

$$\frac{1}{\lambda_i} = \frac{1}{\lambda + 0.08\beta} - \frac{0.035}{1 + \beta^3} \quad (2.13)$$

and $c_1 = 0.5, c_2 = 116, c_3 = 0.4, c_4 = 5$ and $c_5 = 21$. A three blade horizontal axis wind turbine is chosen for the simulation and the rotor pitch angle (β) is set to zero.

2.4 Wind Turbine Conversion System Topologies

Nowadays, all wind turbines are designed with some sort of power control. As a result, a mix and match of novel concepts with proven technology exist both for generators and power converters in wind energy conversion industry. Different designs and configurations of these two components lead to a wide variety of WECS arrangements, which can be classified into four types:

- I) Fixed speed wind turbine without power converter interface
- II) Variable speed wind turbine with limited speed control
- III) Variable speed wind turbine with partial scale frequency converter

IV) Full capacity converter operated WECS

2.4.1 Fixed Speed Wind Turbines

Fixed-speed wind turbines are equipped with an induction generator that is connected to the grid through a transformer (Fig. 2.2). A squirrel cage induction generator (SCIG) is exclusively used in this type of WECS. This configuration requires a soft starter to limit high inrush currents during system start-up, but the soft starter is bypassed by a switch after the system is started. A capacitor bank is often used for reactive power compensation. Three basic turbine power control configurations may be applied in fixed speed wind turbines, namely, stall control, pitch control and active stall control.

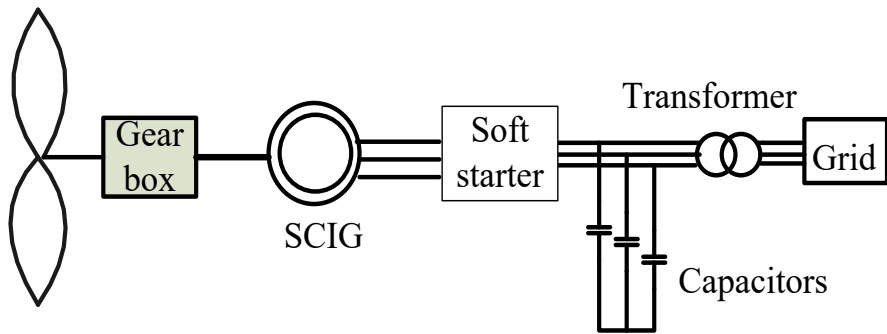


Fig. 2.2. Fixed speed wind turbine power conversion system with SCIG [5].

2.4.2 Variable Speed Wind Turbine with Limited Speed Control

This configuration corresponds to limited variable speed wind turbine with variable generator rotor resistance. It uses a wound rotor induction generator (WRIG) with a variable resistance in the rotor circuit as shown in Fig. 2.3. The change in rotor resistance controls the slip and thus, the power output in the system can be adjusted. The speed adjustment range is typically limited to about 10% above the synchronous speed of the generator.

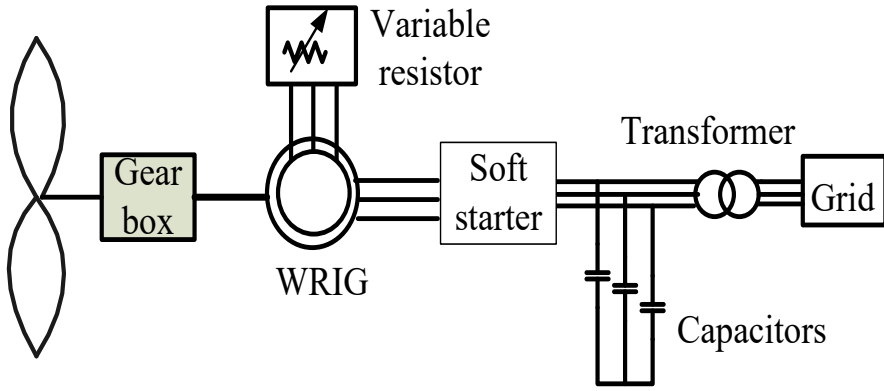


Fig. 2.3. Variable speed wind power conversion system using WRIG with limited speed control [5].

2.4.3 Variable Speed Wind Turbine with Partial Scale Frequency Converter

This arrangement is similar to the WRIG system except that a doubly fed induction generator is used for power generation (Fig. 2.4). The variable resistance in the rotor circuit is replaced by a grid-connected power converter system. The power converter operates as a partial scale frequency converter which is rated at approximately 30% of the nominal generator power. The partial scale frequency converter performs reactive power compensation and smoother grid connection. The use of the converters also allows bidirectional power flow in the rotor circuit and increases the speed range of the generator. This system provides improved power conversion efficiency, extended generator speed range ($\pm 30\%$), and superior dynamic performance as compared to the fixed-speed WECS and the variable resistance configuration. The smaller frequency converter makes this configuration economically productive.

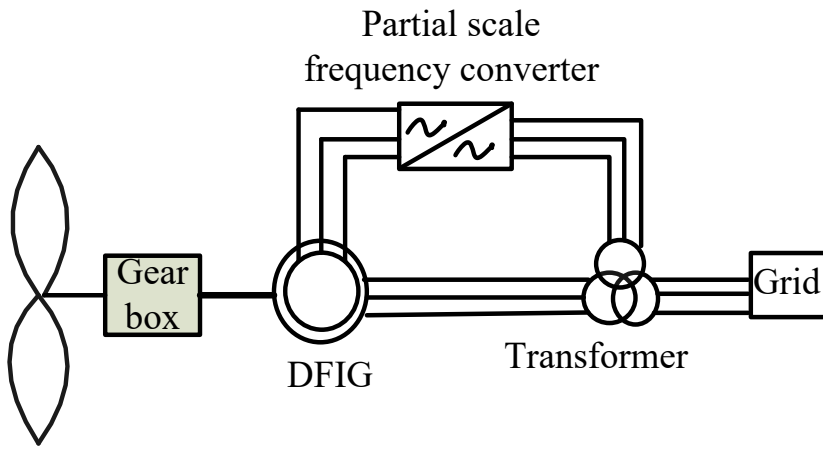


Fig. 2.4. Variable speed wind power conversion system using DFIG with speed control [5].

2.4.4 Full Capacity Converter Operated WECS

This configuration corresponds to the full variable speed wind turbine. Wound rotor induction generator, doubly fed induction generator and permanent magnet synchronous generator have all found applications in this type configuration as shown in Fig. 2.5. The generators are connected to the grid via a full-scale frequency converter with a power rating up to several megawatts and the system can operate without a gearbox arrangement if a low-speed synchronous generator with a large number of poles is used. The frequency converter performs frequency adjustment and reactive power compensation.

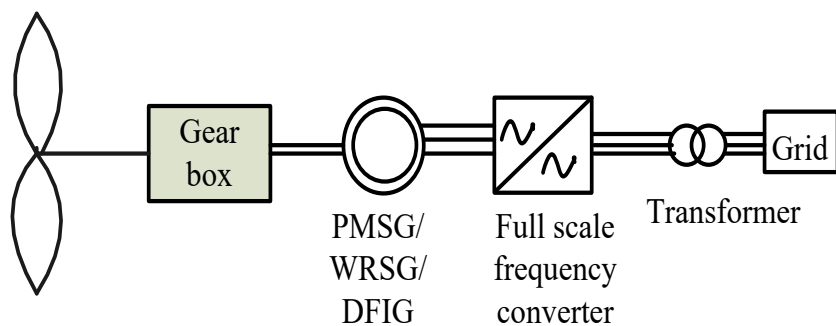


Fig. 2.5. Typical variable speed wind power system with full-scale power conversion [5].

2.5 Electrical Generators in Wind Turbine

Basically a wind turbine can be equipped with any type of three-phase generator. Asynchronous machines such as squirrel cage induction generator, wound rotor induction generator, doubly fed induction generator and synchronous machines such as wound rotor synchronous generator and permanent magnet synchronous generator are the widely used ones in wind power conversion systems.

2.5.1 Synchronous Generators

The synchronous generators are more expensive and structurally complicated than asynchronous machines. However, synchronous generators don't require any reactive magnetizing current for operation as compared to the asynchronous ones. The synchronous generators are more suitable for full-scale power conversion. Two classical types of synchronous generators are commonly used in the wind turbine industry: a) permanent magnet synchronous generator (PMSG) and b) wound rotor synchronous generator.

2.5.2 Permanent Magnet Synchronous Generator

The permanent magnet synchronous generators have the property of self-excitation where the rotor is provided with a permanent magnet pole system and the stator is wound. PMSG with salient pole mechanism is widely used in slow-speed applications and may be the most useful version for wind power applications.

2.5.3 Wound Rotor Synchronous Generator

The stator windings of wound rotor synchronous generators are directly connected to the grid and the rotor windings are excited with dc supply with the help of slip-rings and brushes or with a brushless exciter. As in all synchronous generators, reactive-power output is regulated. In addition, it is possible to set the minimum and maximum frequency for operation on the grid by using WRSG. The voltage and frequency-controlled operation help to regulate the grid voltage and frequency, which can be very important for connections with weak feeders [81].

2.5.4 Asynchronous Generators

The asynchronous machines are low-priced, robust and mechanically simple but their main disadvantage is that the stator needs a reactive magnetization current. The rotor of an asynchronous induction machine can be designed as short-circuited (squirrel cage rotor) or as a wound rotor.

2.5.4.1 Squirrel Cage Induction Generator

The squirrel-cage induction generator (SCIG) has been a prevalent choice in many wind farms because of their unrivaled robustness and low maintenance requirements. Apart from the rotor bearings, they have practically no rotating, wearing parts and, moreover, their price/performance ratio is advantageous. However, the SCIGs need to be equipped with a soft-starter mechanism before grid-connection, because of their steep torque-speed characteristics and high in-rush currents during the transient condition.

2.5.4.2 Wound Rotor Induction Generator

The wound rotor induction generator (WRIG) provides the facility of controllability through the rotor side as a rotor voltage can be impressed in this generator to control the electrical characteristics of the machine. By using power electronic converters, it is possible to extract or impress

power to the rotor circuit and the generator can be excited either from the stator side or the rotor windings.

2.5.5 Doubly Fed Induction Generator

The DFIG is a wound rotor induction generator, where the rotor circuit is connected to the grid through power electronic devices. The ability to supply (or extract) power to (or from) the rotor makes it possible to operate the DFIG at sub-synchronous or super-synchronous speed, while keeping voltage and frequency constant at the stator terminals. The equations for a doubly fed induction machine and squirrel cage machine are identical, except that the rotor voltage is non-zero in the DFIG whereas it is zero in the squirrel cage machine due to the short-circuited rotor. As in the wind turbine context, doubly-fed induction generators and permanent magnet generators seems to be the most attractive solutions to be used to harness the energy from wind. Several advantages of DFIG make it a preferred choice to many researchers. DFIG offers reduced inverter cost, because inverter rating is typically 25% of total system power, while the speed range of the generator is $\pm 33\%$ around the synchronous speed. Also, the cost of the inverter filters and EMI filters is lower than that in WECS with full capacity converters [81], because filters are rated for one-fourth of overall rated per unit value. Improved efficiency and decoupled control of active and reactive power of the generator is also achievable by this generator with a four-quadrant converter connected to the rotor circuit [82]. Conventional squirrel cage asynchronous machines draw very high magnetizing currents from the power grid when recovering from a nearby fault in the power system, which results in a severe voltage dip in the system. An alternative is to use an asynchronous generator with rotor connected to a voltage source converter via slip rings, i.e. a DFIG. Especially, in weak grid system where voltage keeps fluctuating, DFIG is capable of producing or absorbing reactive power to or from the grid in order to maintain grid voltage. Considering the advantages of DFIG in WECS, it has been an interesting option with a growing market

and chosen as the power generation unit in this research. The power flow direction in a DFIG is shown in Fig. 2.6.

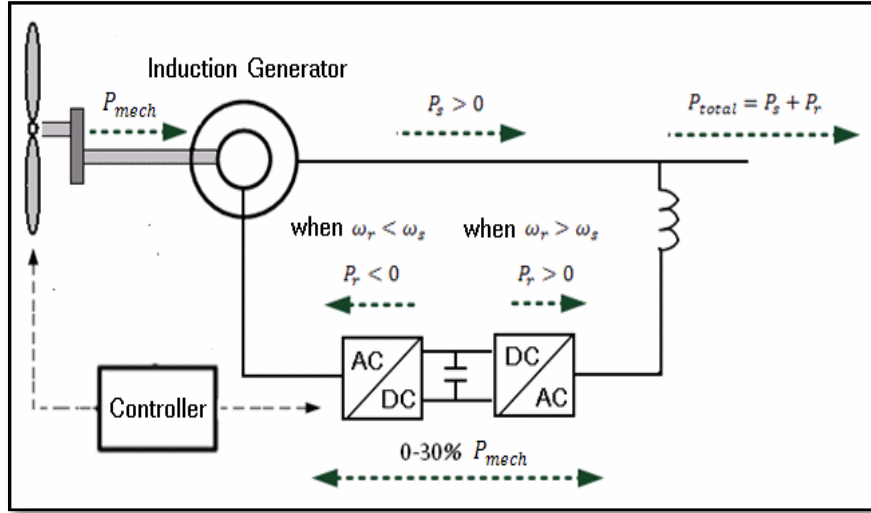


Fig. 2.6. Power flow direction in DFIG based wind power conversion system [83].

To have a good understanding of the DFIG, the following sections describe the steady-state equivalent circuit and the operation principle, as well as the dq-models in the arbitrary and rotor, fixed reference frame.

2.5.5.1 Steady State Equivalent Circuit of DFIG

Fig. 2.7 shows the diagram of the steady-state equivalent circuit of the DFIG, where rotor quantities are referred to the stator side [80].

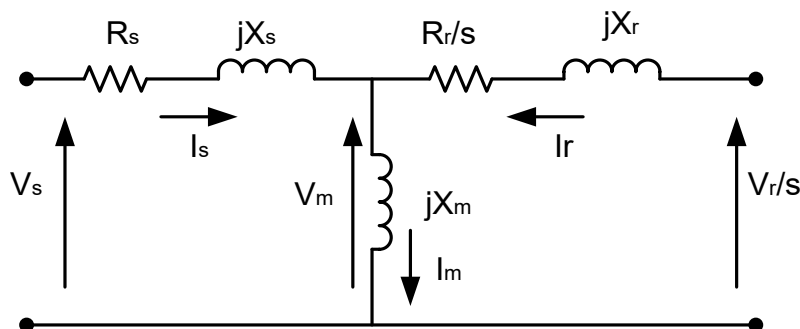


Fig. 2.7. Steady-state equivalent circuit of the DFIG [80].

The equivalent circuit yields the following equations:

$$V_s = I_s R_s + j X_s I_s + V_m \quad (2.14)$$

$$\frac{V_r}{s} = \frac{I_r}{s} R_r + j X_r I_r + V_m \quad (2.15)$$

$$I_m = I_s + I_r \quad (2.16)$$

In the equivalent circuit, V_s and V_r are the stator phase voltage and rotor phase voltage (V), R_s and X_s are the stator resistance and reactance (Ω), R_r and X_r are the rotor resistance and reactance (Ω), X_m is the magnetizing reactance (Ω), s is the generator slip and I_s , I_r and I_m are stator, rotor and magnetizing current (A).

2.5.5.2 Space Vector Model of DFIG

The voltage equations for the stator and rotor of the generator in the arbitrary reference frame are given by [85]

$$\bar{v}_s = R_s \bar{i}_s + p \bar{\psi}_s + j \omega \bar{\psi}_s \quad (2.17)$$

$$\bar{v}_r = R_r \bar{i}_r + p \bar{\psi}_r + j(\omega - \omega_r) \bar{\psi}_r \quad (2.18)$$

The motion equation, which describes the dynamic behavior of the rotor mechanical speed in terms of mechanical and electromagnetic torque

$$J \frac{d\omega_m}{dt} = T_e - T_m \quad (2.19)$$

$$T_e = \frac{3PL_m}{2L_s} Im(\bar{\psi}_s \cdot \bar{i}_r^*) \quad [93] \quad (2.20)$$

\bar{v}_s, \bar{v}_r —Stator and rotor voltage vectors (V).

\bar{i}_s, \bar{i}_r —Stator and rotor current vectors (A).

$\bar{\psi}_s, \bar{\psi}_r$ —Stator and rotor flux-linkage vectors (Wb).

R_s, R_r - Stator and rotor winding resistances (Ω).

ω -Rotating speed of the arbitrary reference frame (rad/s).

ω_r —Rotor electrical angular speed (rad/s).

p -Derivative operator ($p = d/dt$).

P - number of pole pairs.

J -Machine inertia (kgm^2)

The stator and rotor flux linkage vector $\bar{\psi}_s$ and $\bar{\psi}_r$ can be written as

$$\bar{\psi}_s = (L_{\sigma s} + L_m)\bar{l}_s + L_m\bar{l}_r = L_s\bar{l}_s + L_m\bar{l}_r \quad (2.21)$$

$$\bar{\psi}_r = (L_{\sigma r} + L_m)\bar{l}_r + L_m\bar{l}_s = L_m\bar{l}_s + L_r\bar{l}_r \quad (2.22)$$

Where,

$L_s = L_{\sigma s} + L_m$ -Stator self-inductance (H).

$L_r = L_{\sigma r} + L_m$ -Rotor self-inductance (H).

$L_{\sigma s}, L_{\sigma r}$ - Stator and rotor leakage inductances (H).

L_m - Magnetizing inductance (H).

The generator model is in the arbitrary reference frame, rotating in space at the arbitrary speed ω . The model circuit is shown in Fig. 2.8.

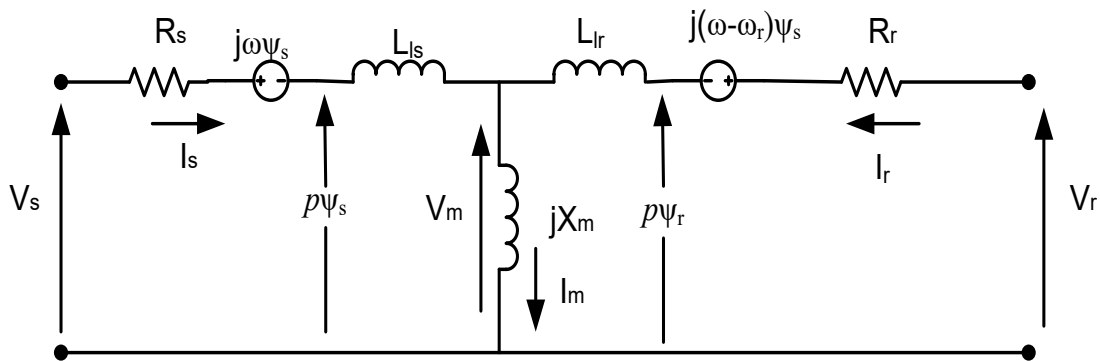


Fig. 2.8. Space vector equivalent circuit of an induction generator in the arbitrary reference frame [85].

To obtain the IG model in the stationary reference frame, we can set the speed of the arbitrary frame ω in the figure to zero since the stationary frame does not rotate in space. In the SCIG, the rotor circuit is shorted and, therefore, the rotor voltage is set to zero, whereas for the DFIG the rotor circuit is connected to a power converter system that controls the speed and torque of the generator.

2.5.5.3 d-q-Model in the Arbitrary Reference Frame

For control of dynamic sequences, the standard equivalent circuit is inadequate, as the model is based on calculations with rms values of voltages and currents. A dynamic model is set up in the form of the two-phase d-q axis representation. The d-q-axis transformation which is often referred to as Park's transformation [123], is a mathematical approach that rotates the reference frame of three-phase systems in order to simplify the analysis of three-phase quantities. The implementation of the d-q transform reduces the three-phase ac quantities to two dc quantities in a balanced three-phase circuit. In the analysis of three-phase induction machines, the transformation converts three-phase stator and rotor quantities into an arbitrary rotating reference frame to eliminate the effect of time-varying inductances. The following assumptions are made to express the continuous-time linear model of the induction machine [84]:

- a) Geometrical and electrical configuration of the machine is symmetrical
- b) Space harmonics of the stator and rotor magnetic flux are negligible
- c) Permeability of iron core is infinite
- d) Stator and rotor windings are sinusoidally distributed in space and substituted by equivalent concentrated winding
- e) Saliency effects are neglected
- f) Skin effect are negligible
- g) End and fringing effects are neglected

All these assumptions do not alter in a serious way the final result for a wide range of induction machines. The d-q-axis model of the induction generator can be obtained by decomposing the space-vectors into their corresponding d-q-axis components (Fig. 2.9).

$$\bar{v}_s = v_{ds} + jv_{qs}; \bar{i}_s = i_{ds} + ji_{qs}; \bar{\psi}_s = \psi_{ds} + j\psi_{qs}; \quad (2.23)$$

$$\bar{v}_r = v_{dr} + jv_{qr}; \bar{i}_r = i_{dr} + ji_{qr}; \bar{\psi}_r = \psi_{dr} + j\psi_{qr}; \quad (2.24)$$

Substituting these equations into equation (2.17) and (2.18) and grouping real and imaginary components on both sides of the equations, the d-q axis voltage equations for the induction generator are obtained [85].

$$v_{ds} = R_s i_{ds} + p\psi_{ds} - \omega\psi_{qs} \quad (2.25)$$

$$v_{dr} = R_r i_{dr} + p\psi_{qs} + \omega\psi_{ds} \quad (2.26)$$

$$v_{dr} = R_r i_{dr} + p\psi_{dr} - (\omega - \omega_r)\psi_{qr} \quad (2.27)$$

$$v_{qr} = R_r i_{qr} + p\psi_{qr} + (\omega - \omega_r)\psi_{ar} \quad (2.28)$$

The d-q-axis flux linkages are obtained as follows.

$$\psi_{ds} = (L_{\sigma s} + L_m)i_{ds} + L_m i_{dr} = L_s i_{ds} + L_m i_{dr} \quad (2.29)$$

$$\psi_{qs} = (L_{\sigma s} + L_m)i_{qs} + L_m i_{qr} = L_s i_{qs} + L_m i_{qr} \quad (2.30)$$

$$\psi_{dr} = (L_{\sigma r} + L_m)i_{dr} + L_m i_{ds} = L_r i_{dr} + L_m i_{ds} \quad (2.31)$$

$$\psi_{qr} = (L_{\sigma r} + L_m)i_{qr} + L_m i_{qs} = L_r i_{qr} + L_m i_{qs} \quad (2.32)$$

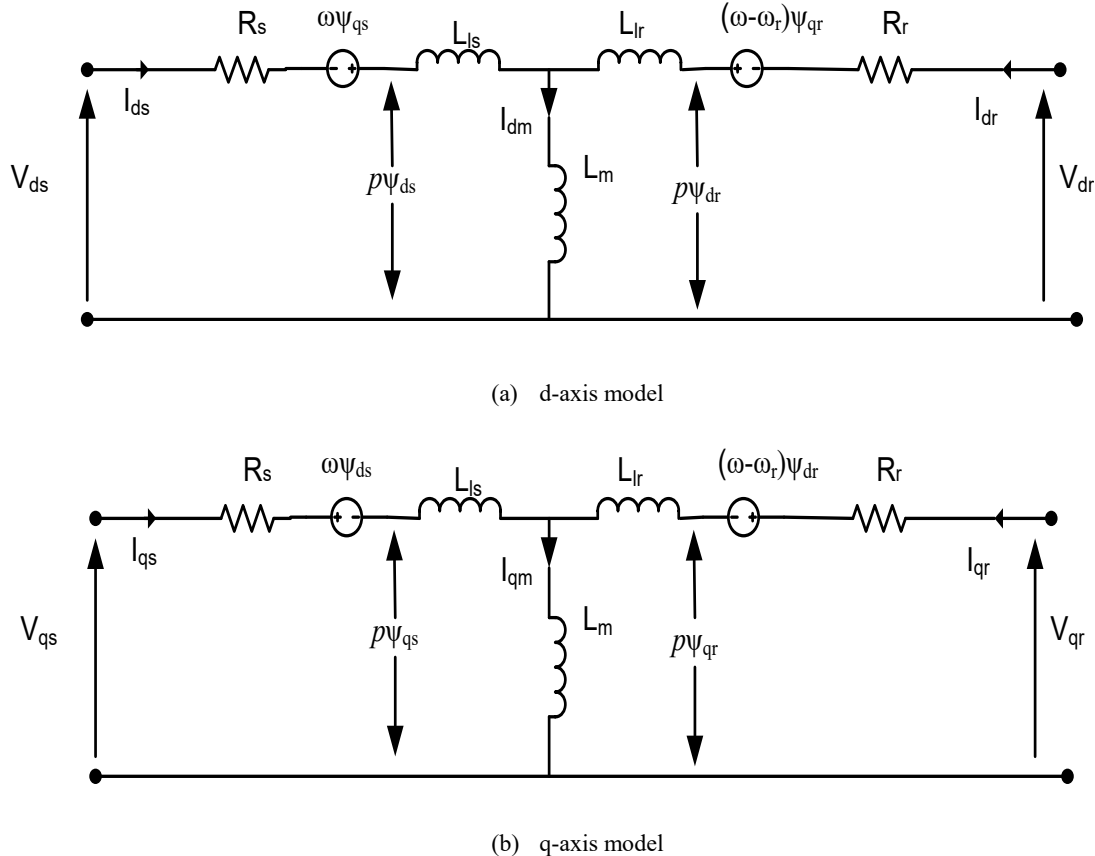


Fig. 2.9. d-q axis equivalent circuits of DFIG in a reference frame with rotational speed ω : (a) d-axis, (b) q-axis [83].

The electromagnetic torque T_e in (2.20) can be expressed by d-q axis flux linkages and currents as well [93].

$$T_e = \frac{3P}{2} (i_{qs}\psi_{ds} - i_{ds}\psi_{qs}) = \frac{3PL_m}{2} (i_{qs}i_{dr} - i_{ds}i_{qr}) = \frac{3PL_m}{2(L_sL_r - L_m^2)} (\psi_{dr}\psi_{qs} - \psi_{ds}\psi_{qr}) \quad (2.33)$$

Thus the motion equation can be expressed as,

$$\begin{aligned} \frac{d\omega_m}{dt} &= \frac{1}{J} (T_e - T_m) \\ &= \frac{1}{J} \left\{ \frac{3PL_m}{2(L_sL_r - L_m^2)} (\psi_{dr}\psi_{qs} - \psi_{ds}\psi_{qr}) - T_m \right\} \end{aligned} \quad (2.34)$$

The d-q axis current-voltage equation along with the torque equation forms the model of the induction generator in the arbitrary reference frame. To obtain the d-q axis model in the synchronous

and stationary reference frames, the speed of the arbitrary reference frame ω can be set to the synchronous (stator) frequency ω_s of the generator and zero, respectively.

2.6 Power Converters

Different types of power converters can be used in wind turbine applications. The power converters basically transform from a fixed voltage and frequency signal to a variable voltage and frequency output. In the following subsections, the configuration of different converter modules will be discussed that are commonly used in wind power generation.

2.6.1 Soft Starter

The soft starter is a power converter connected to fixed speed wind turbines to reduce the transient current during connection or disconnection of the generator to the grid. Using firing angle control of the thyristors, the soft starter ensures a smooth connection of generators to the grid and the system bypasses it at normal operation condition [5].

2.6.2 Diode Rectifier

The diode rectifier is often used in WECS for its cost-effectiveness. It has some applications when modules are connected with a dc-bus system.

2.6.3 The Back-to-Back PWM-VSI

The back-to-back pulse width modulation voltage source inverter (PWM-VSI) is a bi-directional power converter which is the most frequently used three-phase frequency converter in WECS (Fig. 2.10). The major advantage of the PWM-VSI is the capacitor decoupling between the grid inverter and the generator inverter which ensures protection and separate control of two inverters. The drawbacks of this topology are its higher switching losses and relatively shorter lifetime than other

topologies. In this thesis, this converter is utilized as the grid and rotor side power converter for grid-connected application.

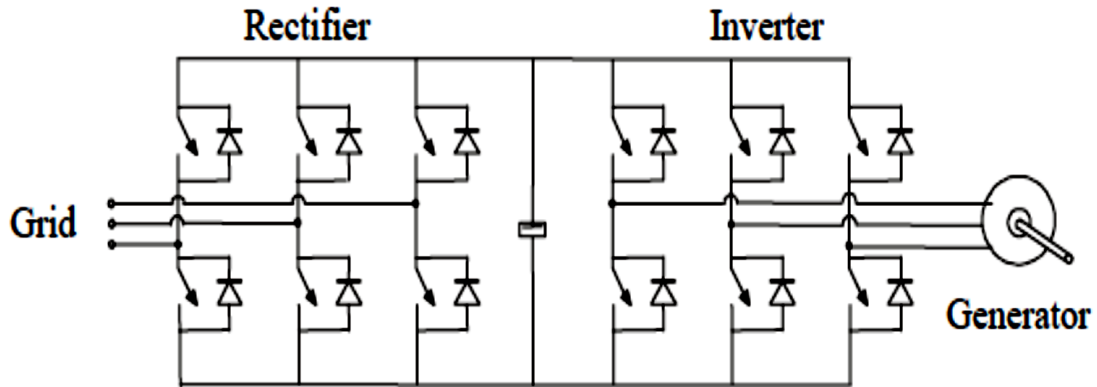


Fig. 2.10. Configuration of back to back PWM-VSI converter topology [80].

2.6.4 Matrix Converter

The key concept of matrix converter is to get desired input current, output voltage by connecting the output terminals of the converter to the input with exact switching frequency. While the absence of the DC-link capacitor provides increased efficiency and prolonged lifetime [85], the output voltage harmonic content of the matrix converter is lower because of its multiple level output voltage. The major disadvantages of the matrix converter are the intrinsic limitation of the output voltage and the lack of protection for fault conditions.

2.6.5 Multilevel Converter

The key purpose of using a multilevel converter (Fig. 2.11) in WECS is to achieve a higher voltage capability. Reduced harmonics in the input and output voltage with lower switching losses have made this topology popular, while voltage imbalance between dc links and unequal current stress on the semiconductors are the drawbacks of this model [10].

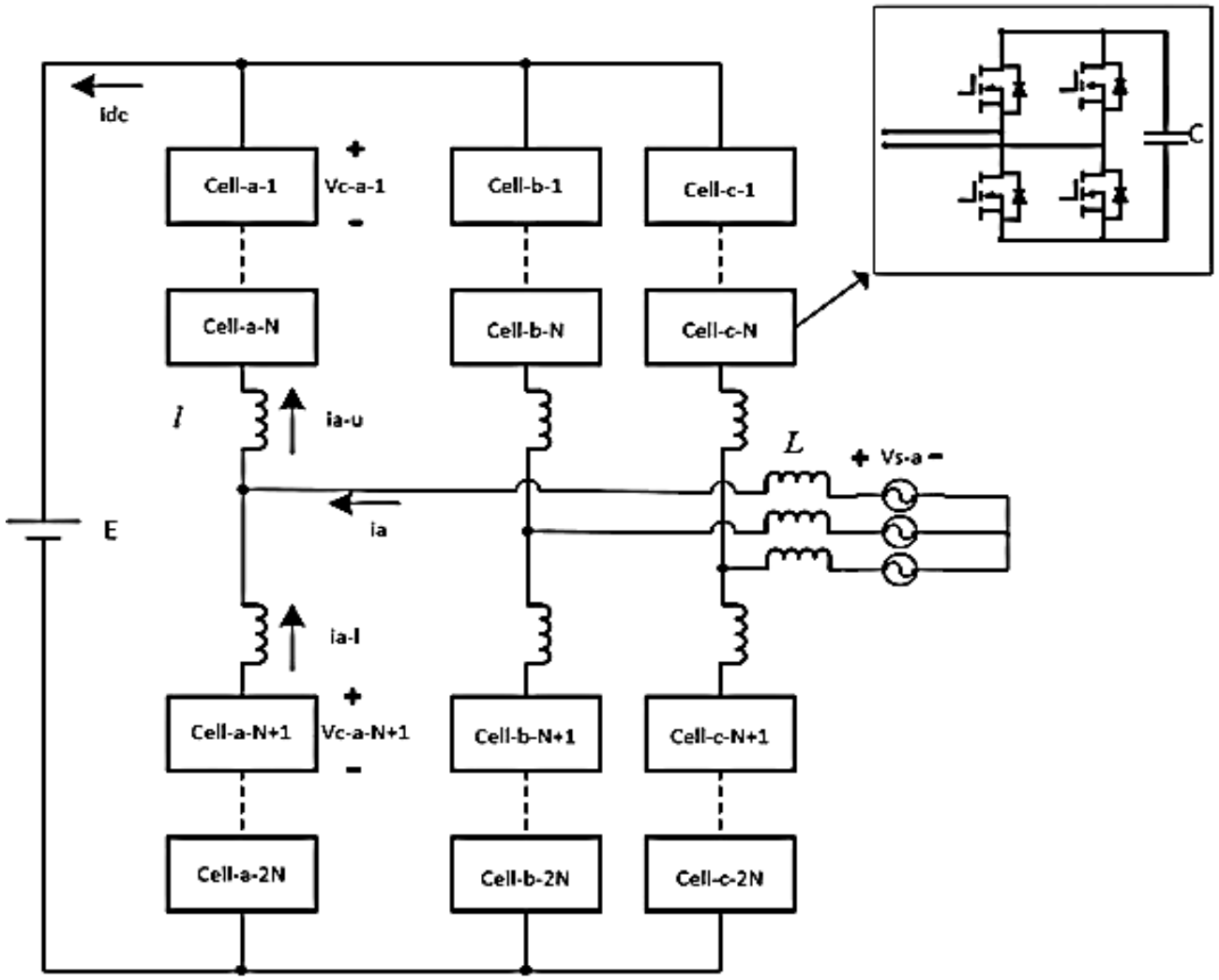


Fig. 2.11. Configuration of multilevel converter topology [10].

2.6.6 Neutral Point Clamped Converter (NPCC)

NPCC is a special type of resonant converter that consists of the conventional back-to-back PWM-VSI and in addition to a resonance circuit backed by inductive energy transfer. This topology reduces switching losses in comparison with the back to back PWM-VSI while the complex control technique and requirement of sensors to detect the zero voltage makes this design implementation commercially inconvenient [86].

2.7 Summary

The typical structure and electrical apparatus of a typical wind energy conversion system are described in this chapter to illustrate a brief idea of wind power generation. Different topologies that are conventionally utilized for wind power conversion, brief description various power converters and basic idea on typical wind turbine generator have been the focus of this chapter. In the next chapter, an adaptive step-size based HCS-MPPT control scheme for DFIG-WECS will be discussed.

Chapter 3

Development and Performance Analysis of an Adaptive Step-Size Based HCS MPPT Controller

Power captured by the blades of a wind turbine is related to several turbine parameters and atmospheric factors. The maximum extracted power from the wind turbine is dependent on the operating point of the wind power conversion system. Maximum power point tracking is tremendously significant in wind power applications as it ensures not only efficient power extraction from the wind turbine but also secures the timely return of the installation cost of the wind plant. In this chapter, the necessary insight will be explained on how the power output of a wind turbine can be regulated by adapting the generator's torque or speed. After that, detailed discussions and results obtained from the proposed adaptive step-size based hill climb search MPPT technique will be illustrated.

3.1 Overview of MPPT Algorithm

The wind turbines are stopped and prevented to supply power in the grid at very low and above the cut-off wind velocity. The typical cut in speed for small scale wind turbine is 3-4 m/s and cut-out speed is 25 m/s. In commercial wind turbines the maximum limit of wind speed is in the range of 40 m/s to 72 m/s. The pitch control mechanisms are activated if the wind speed stays below the cut-off speed and above the rated speed. In such a case, the power control operation is executed to fix the turbine power at rated value. The maximum power point tracking mode is implemented for the moderate range of wind speed which will be the focus of this chapter. Furthermore, MPPT schemes are only applicable for variable speed wind turbines as the turbine speed variation is possible in these turbines while the wind speed changes.

The power captured by the wind turbine is given by the following equation from the previous chapter.

$$P_m = \frac{1}{2} C_p \rho \pi R^2 v_w^3 \quad (2.4)$$

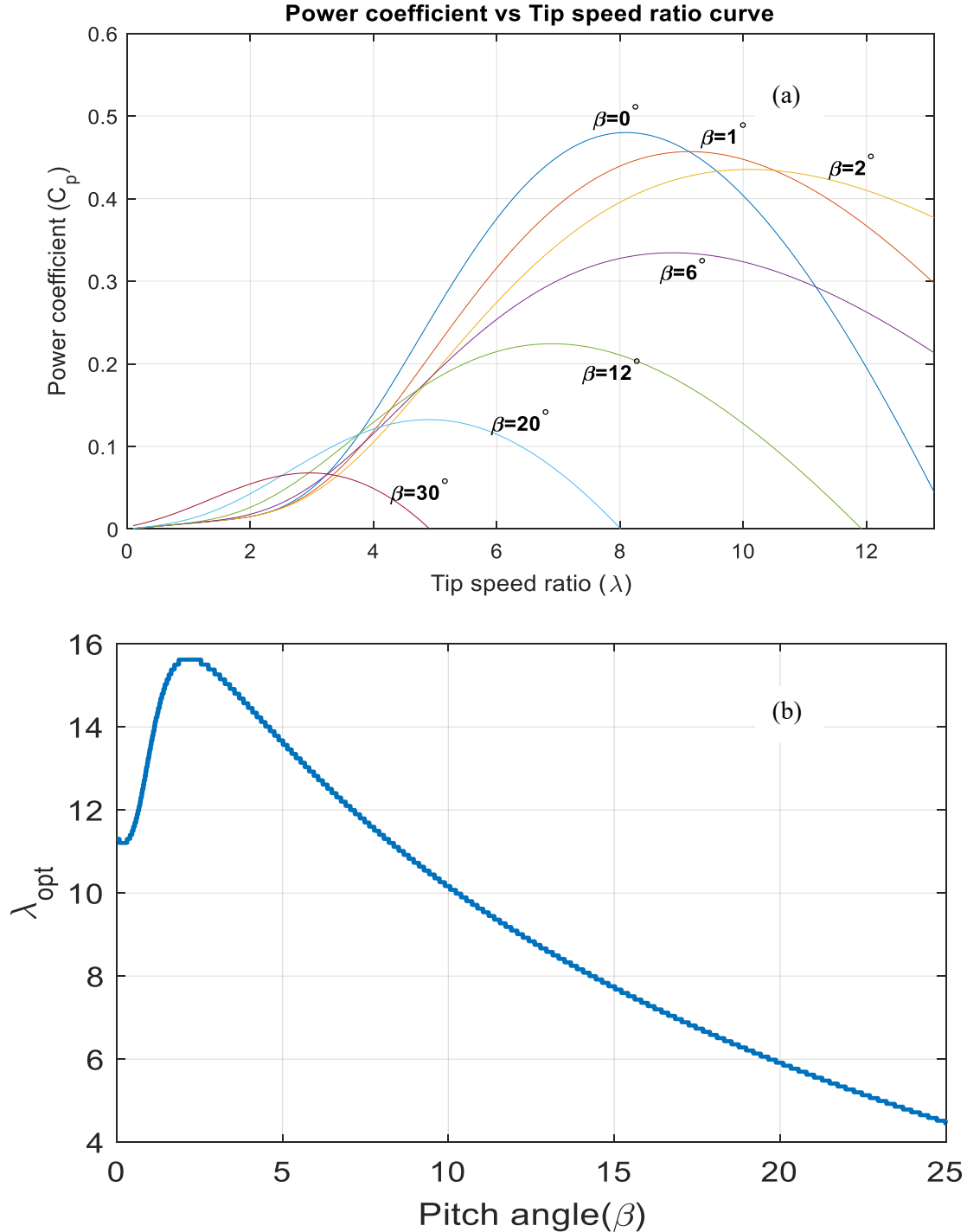


Fig. 3.1. (a) Power coefficient versus tip-speed ratio ($C_p-\lambda$) of wind turbine for various blade pitch angle (β), (b) Optimum tip speed ratio versus pitch angle at corresponding maximum value of power coefficients.

The power coefficient C_p is a non-linear parameter which depends on the turbine design, more specifically it depends on tip speed ratio (λ) and turbine pitch angle (β). In order to obtain the maximum value of the power coefficient, it should adapt to the change of wind speed. The tip speed ratio is an important parameter in wind energy systems. It is defined as the ratio of the blade tip speed to the speed of the incoming wind. The power coefficient is a function of λ and the angle of attack of wind. Fig. 3.1(a) shows the power coefficient versus tip-speed ratio ($C_p-\lambda$) curve of a wind turbine for a constant angle of attack of wind. The optimum tip speed ratio (λ_{opt}) versus pitch angle for each corresponding maximum value of power coefficients ($C_{p,max}$) is shown in Fig. 3.1(b). At the rated (optimal) angle of attack, the maximum power coefficient occurs at the optimal tip speed ratio. When the tip speed angle is fixed, the optimal tip speed ratio (λ_{opt}) is a constant for a specific wind turbine. The speed of the turbine that produces that maximum power is related to λ_{opt} , at wind speed v_w , is defined as

$$\omega_m = \lambda_{opt} \frac{v_w}{R} \quad (3.1)$$

This equation indicates that in order to obtain the maximum power and conversion efficiency, the turbine speed must be made adjustable according to the wind speed. Fig. 3.2 shows the typical characteristics of a wind turbine operating at different wind speeds, where P_m is the mechanical power of the turbine. The P_m versus ω_m curves is obtained with the blade angle of attack set to its optimal value, i.e. $\beta = 0^\circ$.

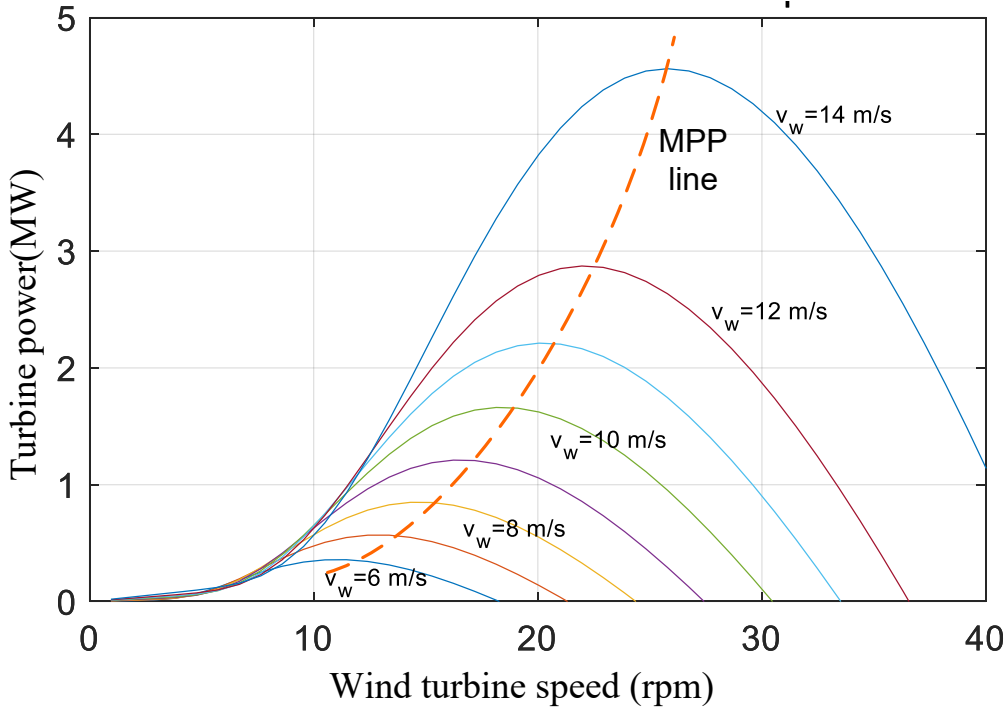


Fig. 3.2. Mechanical power-speed (P_m - ω_m) characteristics and the maximum power point curve (dashed curve) attained at each wind speed, for a blade pitch angle of $\beta = 0^\circ$ and radius = 42 m.

According to the power-speed characteristics curve, mechanical power can be related to the turbine rotor speed as

$$P_m \propto \omega_m^3 \quad (3.2)$$

The mechanical torque produced by the turbine can be expressed as,

$$T_m = \frac{P_m}{\omega_m} \quad (3.3)$$

From equation (3.2) and (3.3), it can be concluded that

$$T_m \propto \omega_m^2 \quad (3.4)$$

In the next sections, different schemes on the MPPT algorithm will be discussed.

Among different power MPPT methods, constant TSR is one of the most popular ones. In this method, the maximum power is achieved by keeping the tip speed ratio to its optimal value. The measured wind speed v_w is used to produce the generator speed reference ω_{ref} according to the optimal

tip speed ratio. The generator speed ω_m is controlled by the power converters and will be equal to its reference in steady state, at which the MPPT is achieved. This approach requires pre-programmed 2-D look-up tables with values of optimal generator speed and corresponding peak power values stored in it. Two other methods that utilize the look-up table method are optimal torque (OT) control and power signal feedback (PSF) control. Both of the methods either utilize a cubic/quadratic optimal mapping function or 2-D look-up tables for fetching the peak power point with an optimal proportionality constant. However, TSR control algorithm requires the predetermined value of the optimal TSR for the turbine which makes this technique intricate for precise control [87] while the PSF method is dependent on the prior knowledge of the turbine maximum power tracking curve [16].

3.1.1 Hill-Climb Search Control

Among different MPPT methods, the hill climb search (HCS) algorithm is the basis for all the parameter-independent MPPT techniques. This method is based on perturbing a control variable in small step-size and observing the resulting changes in the target function until the slope becomes zero. If the change in perturbation results in a boost in power then the same perturbation is applied for the next control instance; otherwise the sign of the perturbation is reversed in order to track in the direction of power at the increasing direction as visualized in Fig. 3.3.

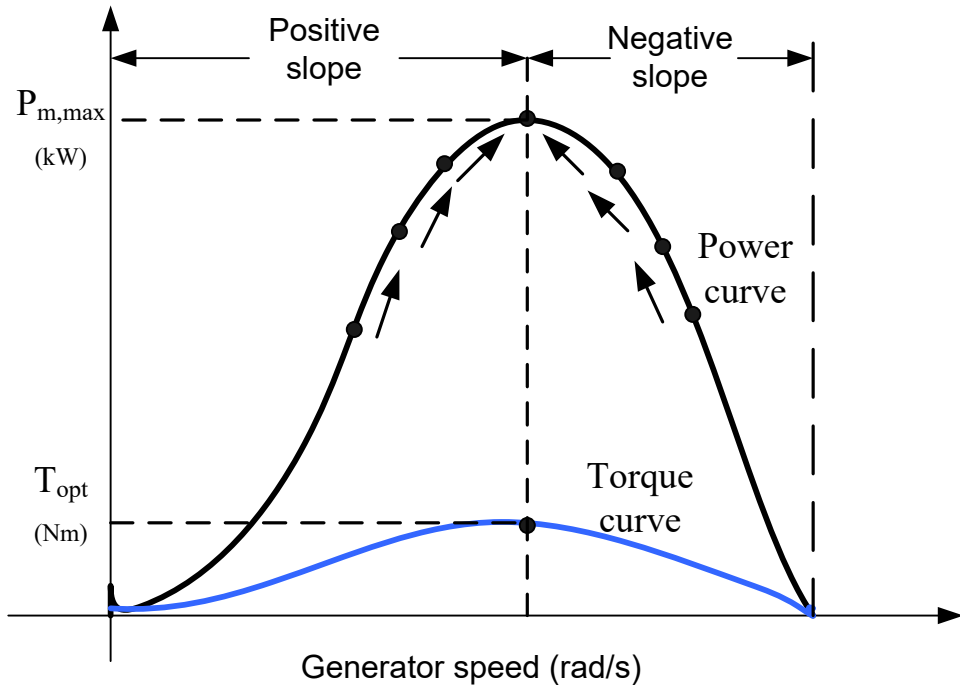


Fig. 3.3. Method of MPP tracking in hill climb search method.

In general, the rotational speed of the rotor is varied in WECS and the mechanical power is observed in P&O algorithm for peak power extraction, while some authors have considered the inverter input voltage [87] or one of the converter variables. For instance, duty cycle of the switches [30] can be considered as the perturbed quantity to search the highest power of the generator. The determination of electrical quantities, such as power and voltage are more reliable and cost-effective compared to mechanical parameters. Hence these techniques are often used to determine system MPP condition.

On the other hand, hill climb search method is very efficient and straightforward and this method does not require any prior knowledge of the wind turbine or generator characteristic curve. Also, the implementation is simple, flexible and this algorithm only requires the measurement of power which is subjected to maximization [88]. Moreover, the HCS controller can operate independently along with variable pitch control while in other algorithms, the optimized operating point needs to be

reprogrammed for every change in pitch angle [26]. All these advantages have made HCS algorithm a popular and vastly implemented technique.

However, the conventional HCS algorithm has few major drawbacks that significantly deteriorate the controller performance under rapidly varying wind conditions. First one is proper identification of perturbation size. A smaller step size boosts the efficiency but reduces the speed of the controller. On the other hand, large perturbation step deteriorates the performance by amplifying the oscillations around MPP. Secondly, the sign of the next perturbation is decided by the change in power of the previous perturbation. Being blind to the wind change, the direction of perturbation might go in the wrong direction. Also, the conventional HCS method suffers from sustained power fluctuation around the maximum power point. These shortcomings can be eliminated by implementing appropriate adaptation strategy.

So far, researchers have attempted to mitigate the deficiencies of classical HCS algorithm through different complicated methods [26-34]. In [28], the maximum power point is obtained by calculating variable step size from the scaled measure of the slope of power with respect to the perturbed generator speed ($\Delta P/\Delta\omega$). This method might fail under rapidly changing wind speed condition because the slope $\Delta P/\Delta\omega$ may not provide an accurate measure of distance from the maximum point as the operating point shifts from one power curve to another for changing wind velocity. Some authors have proposed a search-remember-reuse based HCS controller introducing look-up table based technique by online training of a memory table [29]. However, the control of this system is convoluted due to the computational burden and the requirement of huge memory for the look-up table. Also, the authors have proposed to stop the perturbation while ambiguity appears during the step of decision making about the sign of ΔP_m . Stopping of perturbation can adversely affect the peak power tracking, which is another drawback of the technique. Another approach is discussed in

[30] where MPPT control of the wind generator is accomplished by direct adjustment of dc-dc converter duty cycle. This technique is efficient but only suitable for permanent magnet wind generator and isolated load. Fuzzy logic provides a convenient method of maximum power point tracking as an advanced HCS control technique [31-33]. The adaptation attributes, capability to achieve specified control objective and robustness under turbine parameter uncertainties make the algorithm appealing. However, the developed techniques are practically infeasible because it is not easy to find optimal parameters for the membership functions and. In [34], a disturbance injection based HCS algorithm is proposed where a sinusoidal perturbation is employed instead of constant step. The convergence speed is slow in this method and it is capable of working efficiently only at constant or slowly varying wind speed.

To improve the precision of the conventional P&O method, variable step-size methods have been proposed [26,89-90]. In adaptive step-size methods, the step-size is automatically updated according to the operating point. In variable step-size approach, larger step size is expected when the operating point is away from the peak due to the larger magnitude of $P-\omega$ slope and as the zenith gets nearer, the step size should approach to zero to settle down exactly at the peak point. By following these principles, it is possible to reduce the oscillations, speed up the controller to reach the peak, and successfully track the desired course. In conventional P&O algorithm, the difference between two sampled consecutive points is considered for difference calculation. Further adjustments in the incremental direction are made until the maximum point is found. The following flow chart describes the conventional HCS algorithm.

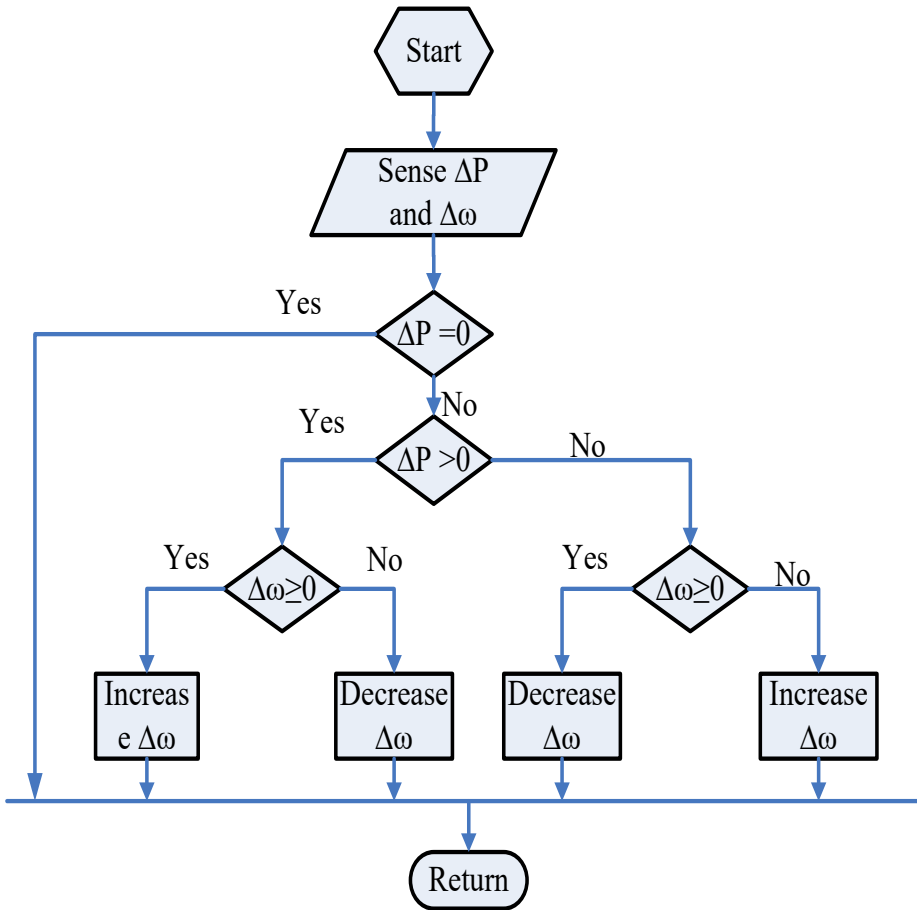


Fig. 3.4. Flow chart of the conventional HCS algorithm for WECS.

In this thesis, an adaptive step size MPPT controller based on HCS algorithm is developed in which the perturbation of rotor speed is decided by the weighted average value of the rotor speed and extracted power samples. The detailed analysis of the proposed algorithm is shown in subsection 3.2.1.

3.2 Description of the Overall Wind Power Control System

The major components of a typical wind energy conversion system include the wind turbine, a generator, turbine and generation control unit along with interconnection apparatus. In the proposed configuration, a DFIG is mechanically coupled with the wind turbine to transform the mechanical energy of wind turbine rotor into electrical energy. A back-to-back converter is implanted in the design

to perform independent control of DC-link voltage and decoupled control of real and reactive power as shown in Fig. 3.5.

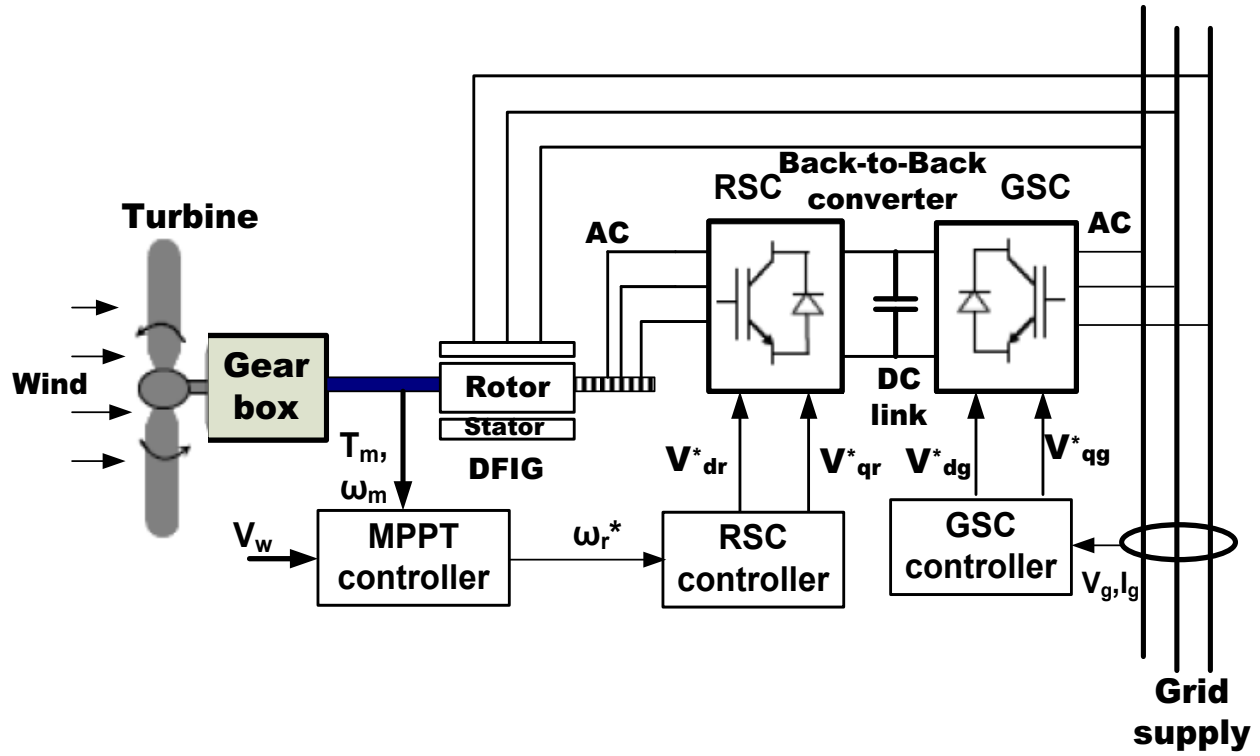


Fig. 3.5. Configuration of the MPPT based converter controlled WECS.

3.2.1 Design of the Proposed Adaptive Step Size HCS-MPPT Controller

An adaptive step size MPPT controller is developed to reduce the power fluctuation. The adjustment in step size for hill climbing continues until the oscillation around maximum power point drops to near zero value. The flow chart is shown in Fig. 3.6 that describes the execution steps of the proposed algorithm.

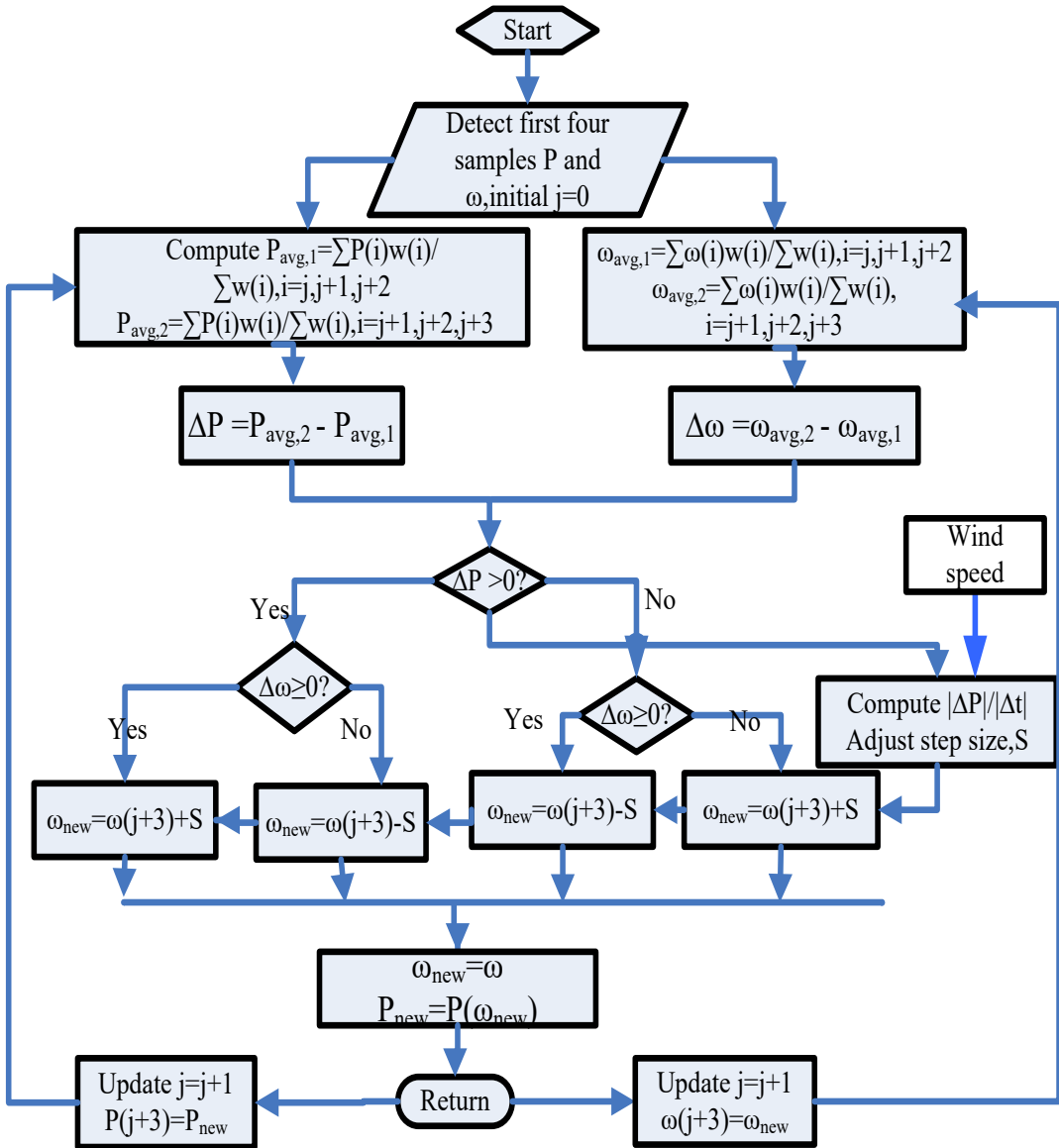


Fig. 3.6. Flow chart of the proposed adaptive step size based MPPT algorithm.

In case of fixed step size based HCS MPPT control, choosing the proper step size is not an easy task. If the step size is smaller, the power tracking behavior of the controller remains appropriate but the controller response gets too slow. As a result, the convergence of the rotor speed to the desired peak point slows down. On the other hand, the larger step size may increase the speed of convergence but at the cost of probable failure to converge at the maximum power point [22] as shown in Figs. 3.7(a) and

3.7(b). The large perturbation step size may either cause added fluctuation near peak point or lead the controller in the wrong direction. The second situation is more likely to occur under sudden change of turbine power due to drastic variation in wind speed. The controller may provide a misleading outcome as it fails to distinguish between the power difference caused by wind variation and the power change prompted by the previous perturbation step. This phenomenon is shown in Fig. 3.7(c) where the step change is drifting towards the right side instead of going to the left direction. The wrong directionality is caused by a larger step size, which eventually leads the power output moving away from the maximum power point and thus reduces the efficiency. On the other hand, in TSR controller, the reference rotor speed is generated instantaneously under sudden fluctuation in wind speed, but the actual tracking performance entirely depends on the PI controller. The machine might experience severe jolt if the parameters of the TSR controller are not calculated precisely.

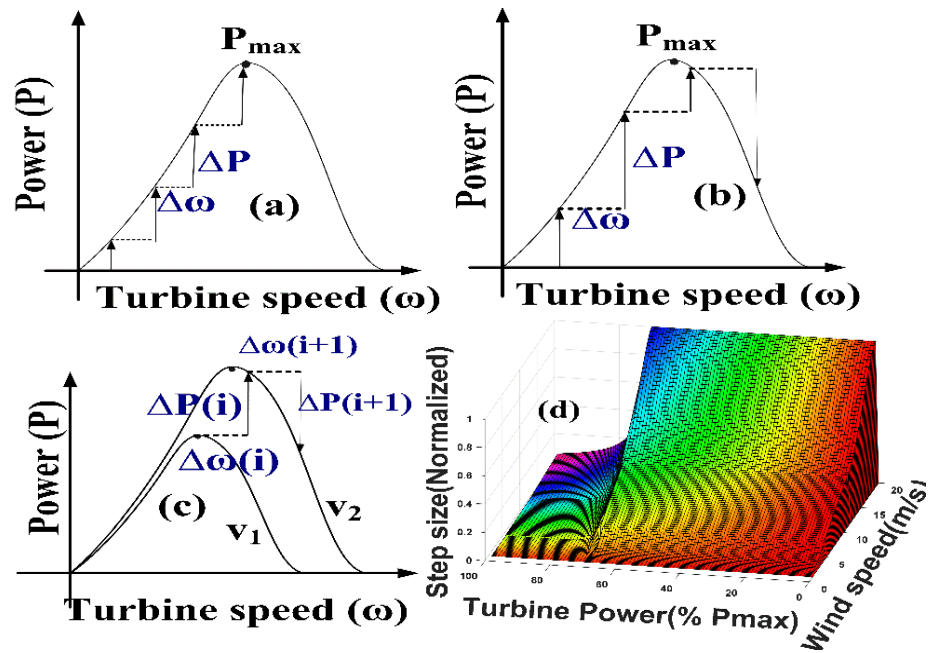


Fig. 3.7. Performance analysis of fixed step size based HCS controller for maximum power tracking: (a) Small step size based tracking with slow convergence, (b) Large step size based tracking led to wrong direction of perturbation, (c) Fixed step size based HCS controller steered to wrong track under drastic change in wind speed, (d) Adaptive step size variation with respect to the change in wind speed and turbine power.

To overcome these disadvantages, the step size is continuously updated according to the rate of change of turbine power output in the proposed MPPT controller. In typical adaptive HCS based MPPT control scheme, only the slope of turbine power versus rotor speed curve is considered for step-size calculation. Adapted step size is determined by the variation of wind power. In most cases, the adaptation rate is derived directly from the steepness of the power-speed curve or by using the look-up table. As a result, though the adaptive step size is varied regularly, the rate of adaption remains unchanged by default. Since the steepness of power output in a wind turbine varies rapidly while the wind speed fluctuates, the adaptation rate needs to be revised proportionally for proper tracking. This feature is often overlooked in designing HCS based controllers due to the exclusion of wind speed data in the design. Besides, when the operating point reaches the peak power for particular wind speed, the step perturbation needs to be reduced gradually. By considering all these facts, the adaptation of step size is varied by selecting six different zones in the domain of wind speed and generated power. The adjustment in step size for rotor speed can be realized by the functions shown in (3.5)-(3.10) and from Table 1. Wind speed domain is divided into three different ranges (slow, medium and strong wind) while output power is separated into two territories, i.e., far and close to maximum output power (P_{max}) for step function generation. The separation between the power zones is determined by general observation of the concavity of the power curve for wind turbines. The adaptive step size for the rotor speed is a combined function of wind speed and power curve steepness as shown in (3.5).

$$S = f(v_w)f(z) \quad (3.5)$$

where, $f(v_w)$ is a function of wind speed, v_w and $f(z)$ is a function of the slope of turbine power, $z=\Delta P/\Delta t$ [91]. In simulation, the power is measured directly from the turbine from the multiplied value of the turbine torque and turbine rotor speed. It is assumed that torque sensor is available in the tower. No delay effect is considered during the power calculation for the data obtained from torque sensor.

However, the average of the three consecutive power samples is taken during the calculation of ΔP . This will compensate for the sensor delay effect on power calculation. In the low power zone, steeply rising functions are chosen for step size when generated power is less than 70% of the maximum power at the measured wind velocity. Above this boundary, the selected functions bring down the step size to a low marginal value to diminish the power fluctuation aptly. The functions for $f(v_w)$ are selected as linear or higher order increasing function of wind speed v_w depending on the zone of operation of the controller as shown in (3.6)-(3.7).

$$f_1(v_w) = a_1 v_w + b_1 \quad (3.6)$$

$$f_2(v_w) = a_2 v_w^3 + b_2 v_w^2 + c_2 v_w + d_2 \quad (3.7)$$

Similarly, three different functions have been chosen for implementing $f(z)$ in (3.8)-(3.10). These functions are sigmoid or inverse sigmoid type.

$$f_1(z) = \alpha \tan^{-1}(\delta z) \quad (3.8)$$

$$f_2(z) = \frac{z}{\sqrt{z^2 + \gamma}} \quad (3.9)$$

$$f_3(z) = \kappa - e^{-\xi \cdot e^{-\frac{z}{\zeta}}} \quad (3.10)$$

where, $\alpha, \delta, \gamma, \kappa, \xi, \zeta$ are constants as shown in Table 3.2.

The constants used in (3.6)-(3.10) are chosen according to the zone of operation and gradient of the power versus rotor speed curve for the specific wind turbine used in simulation.

Table 3.1 Function types used for adaptive step determination

Wind speed range \ Power range	Power $\leq 70\% P_{max}$		Power $> 70\% P_{max}$	
	$f(v_w)$ function type	$f(z)$ function type	$f(v_w)$ function type	$f(z)$ function type
Slow wind $v_w < 5$	1 st order function, $f_1(v_w)$	Inverse tangent function, $f_1(z)$	1 st order function, $f_1(v_w)$	Logistic function, $f_2(z)$
Medium wind $5 \leq v_w \leq 12$	1 st order function, $f_1(v_w)$	Logistic function, $f_2(z)$	1 st order function, $f_1(v_w)$	Gompertz function, $f_3(z)$
Strong wind $v_w > 12$	3 rd order function, $f_2(v_w)$	Logistic function, $f_2(z)$	1 st order function, $f_1(v_w)$	Gompertz function, $f_3(z)$

For any medium power wind turbine, these constants are sorted in between the ranges specified in Table 3.2. For any medium power wind turbine, these constants are sorted for a maximum turbine rotor step size of 0.1 rad/s and wind speed range of 0-20 m/s and verified by simulation. The constants are selected based on trial and error method to maintain continuity of step functions among the zones. The normalized adaptive step size variation is depicted in Fig. 3.7(d) for the designed controller. The variable step function rises progressively along with the wind speed when the turbine power output is far away from the peak power point. Sufficient high values for step size are adopted for perturbation that ensures fast-tracking. In contrast, if the operating point is near the peak power point, the step size is progressively reduced to alleviate power fluctuation. The results obtained from the implementation of this adaptive step size based HCS MPPT control scheme have been demonstrated in section 3.3. In the next section, the arrangements of the grid side and rotor side controller are briefly explained to realize the complete configuration of the DFIG-WECS.

Table 3. 2 Range of coefficients and constants for functional expression of adaptive step size calculation

Constant	Range	Constant	Range	Constant	Range
a_1	0.002-0.05	c_2	-0.02 - 0.005	κ	1-1.2
a_2	-25×10^{-5} - (-4×10^{-6})	d_2	0.001-0.08	ξ	0.05-0.7
b_1	0.001-0.05	α	0.1-0.7	ς	0.0025-0.2
b_2	0.002-0.0008	δ	0.5-2.5	γ	10-800

3.3 Description of the Grid Side and Rotor Side Converter Control of DFIG

DFIG based WECS can operate in sub-synchronous or super-synchronous mode to produce or absorb reactive power to or from the grid. The four-quadrant control of the inverters of the grid side and rotor side provides the desired regulations on both converters.

3.3.1 Grid-Side Power Converter Control

The main purpose of the grid side power converter controller is to keep the dc-link voltage constant irrespective of the value and direction of the rotor power flow. To achieve this goal, the sinusoidal pulse width modulation technique is used. The reference frame is aligned with the stator flux position in the proposed system which allows independent regulation of the dc-link voltage. The block diagram of the grid side converter scheme is depicted in Fig. 3.8. The reference angular position (θ_s) is obtained from the α - β components of grid side flux.

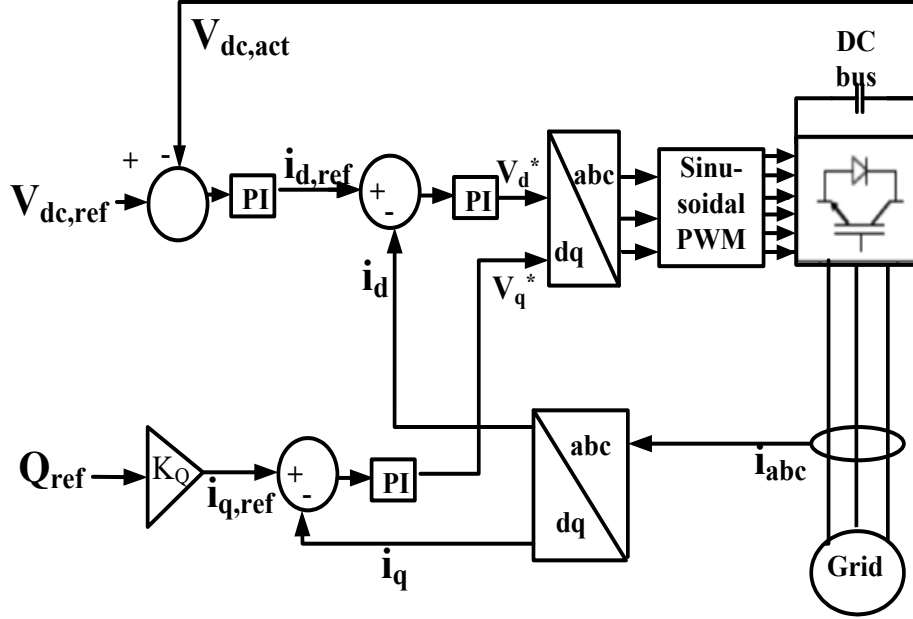


Fig. 3.8. Block diagram of the grid side converter control for the proposed system.

3.3.2 Rotor Side Converter Control

The doubly fed induction generator allows the power injection and extraction at the rotor terminal of the machine. Thus, it provides the feasibility of controlling the generated complex power for both of the super-synchronous and sub-synchronous operation modes. The rotor side converter regulates the slip speed and controls the air-gap power of the induction machine. The precise control of the Sinusoidal PWM converter depends on the accurate measurement of stator voltage and currents, rotor side currents and rotor position [22]. The rotor side converter control block is shown in Fig. 3.9. The controller utilizes the equations shown in (3.11)-(3.15).

$$i_{ms} = \frac{\Psi_{ds}}{L_m} \quad (3.11)$$

$$\sigma = 1 - \frac{L_m^2}{L_s L_r} \quad (3.12)$$

$$\omega_{sl} = \omega_s - \omega_r \quad (3.13)$$

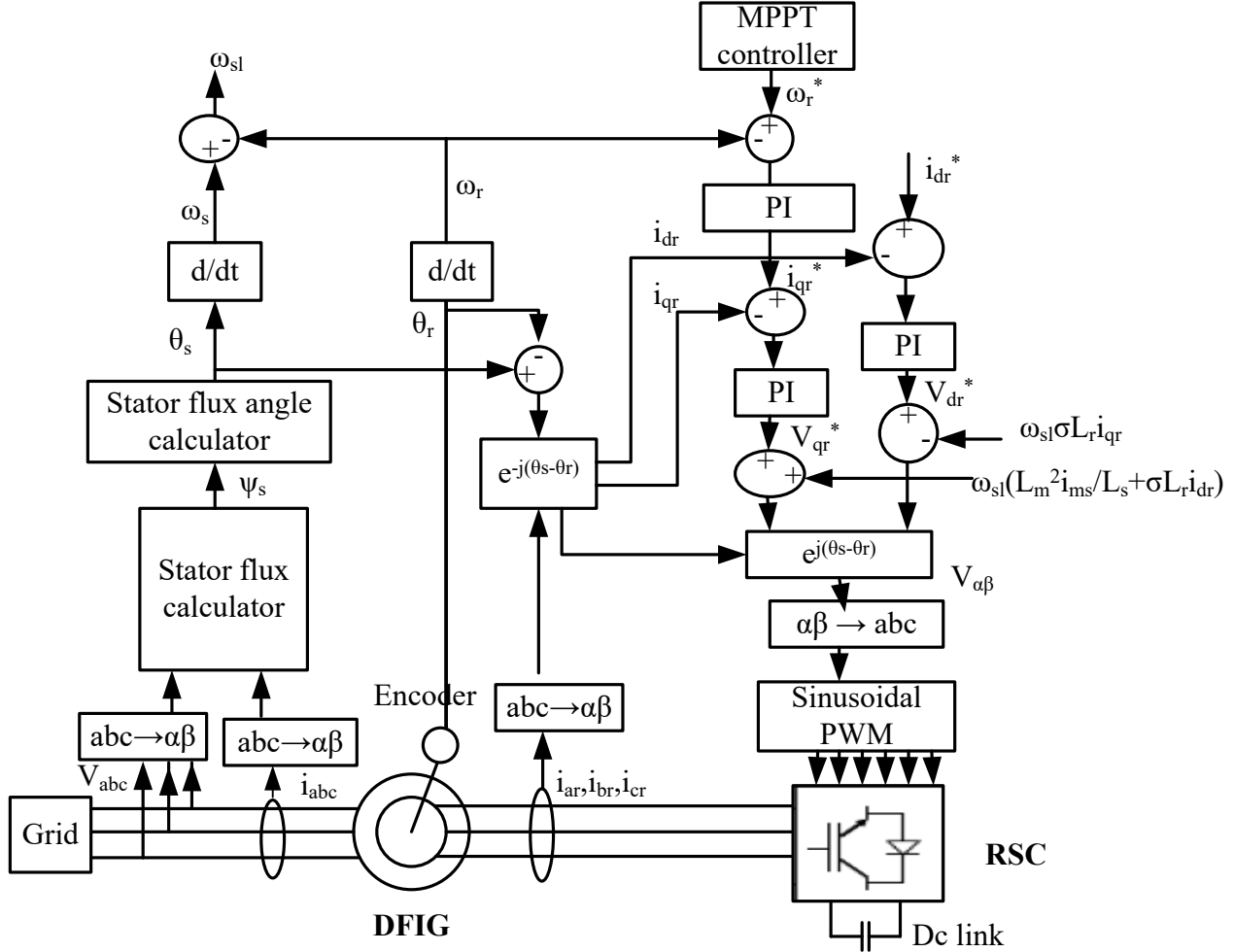


Fig. 3.9. Block diagram of the rotor side converter control.

$$\Psi_{dr} = \frac{L_m^2}{L_s} i_{ms} + \sigma L_r i_{dr} \quad (3.14)$$

$$\Psi_{qr} = \sigma L_r i_{qr} \quad (3.15)$$

Substituting the rotor flux components from (3.14) and (3.15) in (2.27) and (2.28) yields,

$$v_{dr} = R_r i_{dr} + \sigma L_r \frac{di_{dr}}{dt} - \omega_{sl} \sigma L_r i_{qr} \quad (3.16)$$

$$v_{qr} = R_r i_{qr} + \sigma L_r \frac{di_{qr}}{dt} + \omega_{sl} (\frac{L_m^2}{L_s} i_{ms} + \sigma L_r i_{dr}) \quad (3.17)$$

Table 3.3 Wind turbine and DFIG parameters

Parameters	Value	Parameters	Value
Rated turbine power	2 MW	Leakage inductance	0.08 mH
Pitch angle	0°	Magnetizing inductance	2.5 mH
Blade radius	42m	Dc bus capacitance	150 mF
Rated generator power	2 MW	Rated generator torque	5305 Nm
Rated stator current	1673A	Generator inertia	127 kgm ²
Grid voltage	690 V	Grid line resistance	20 uΩ
Grid frequency	60 Hz	Grid line inductance	40 μH
Number of pole pairs	2	Maximum slip	0.33
Leakage resistance	2.9 mΩ	Voltage conversion ratio	1/3

Where, i_{ms} , L_m , L_s , L_r , ω_{sl} and σ are magnetization current, magnetizing inductance, total equivalent stator inductance, total equivalent rotor inductance, slip frequency and leakage factor respectively.

3.4 Simulation Performance of the Proposed Adaptive Step-Size Based MPPT Control of DFIG-WECS

The overall system has been designed for efficient extraction of turbine power. The new adaptive MPPT controller is designed to extract maximum power from the turbine proficiently confirming the availability of the merits of conventional HCS controller whereas the reactive power and torque of the DFIG are controlled by the grid side and rotor side converter. Table 3.3 shows the wind turbine and DFIG parameters that are utilized in simulation. The simulation is performed for a sampling time period of 5 μs. The code for the initialization the DFIG and turbine is outlined in appendix.

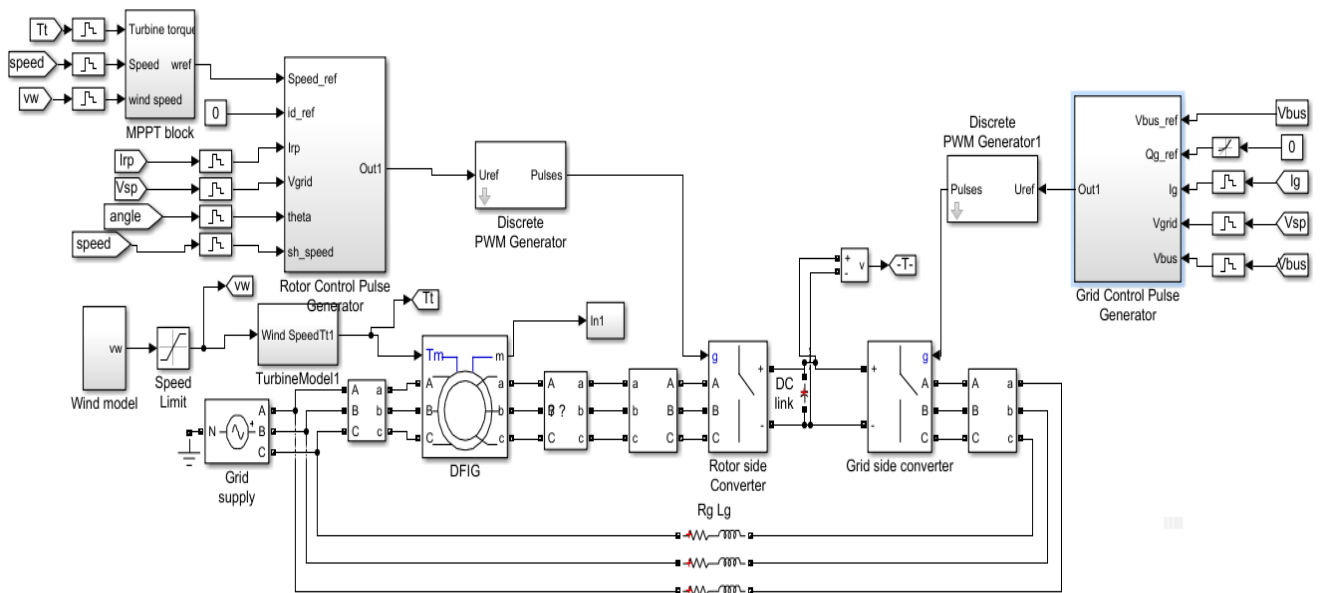


Fig. 3.10. Matlab-Simulink block diagram of overall structure of DFIG-WECS.

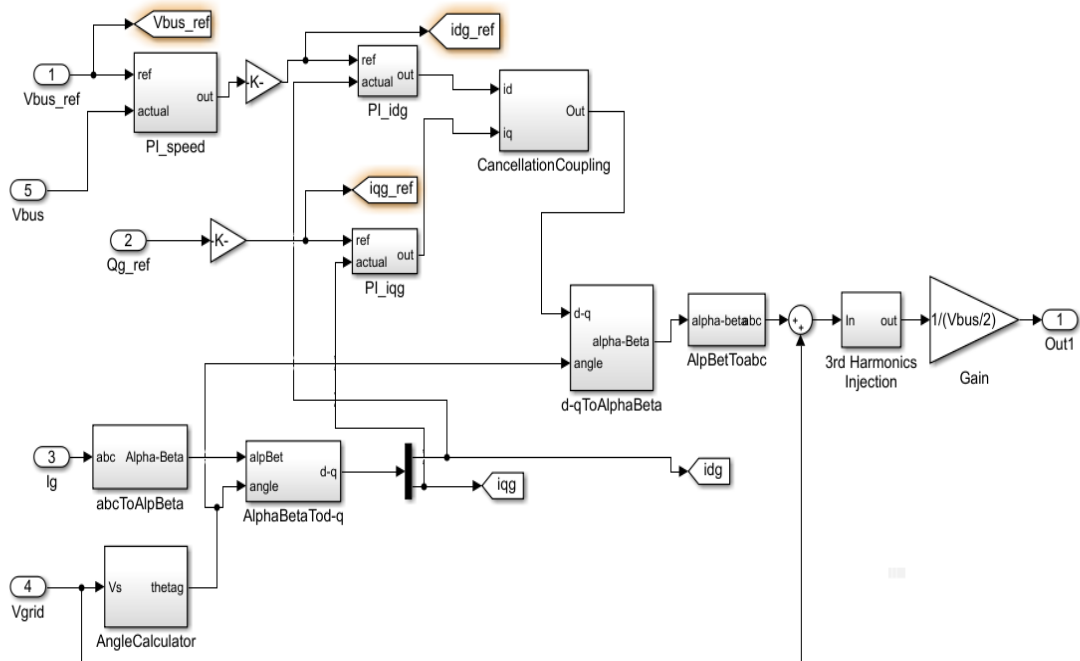


Fig. 3.11. Matlab-Simulink block diagram of GSC control pulse generator.

The simulation configuration for Matlab-Simulink block diagram structure is depicted in Fig. 3.10. In the designed controller, as the peak point gets nearer, the step size approaches zero to settle down the power at the maximum value. The Simulink block diagrams of the grid-side converter (GSC) and rotor side converter (RSC) controls are shown in Figs. 3.11 and 3.12, respectively. The detail block diagram for the subsystems can be found in appendix Figs. B.1-B.9. The GSC converter control targets to regulate the dc-link voltage while RSC controls the machine torque. The proportional and integral constant parameters for the the PI controllers of the GSC and RSC control pulse generation blocks are demonstrated in Table 3.4. The formula for the determination of PI control contants are detailed in Chapter 5. The proportional ($K_{p,vbus}$) and integral contant ($K_{i,vbus}$) for bus voltage control are negtive, however they don't signify positive feedback rather the values are specifically selected for the bus voltage tracking by trial and error. The high gains are selected to quicken the tracking process. The GSC control utilizes a cross-coupling cancellation block which implements the following equations to calculate the appropriate reference voltages.

$$v_{dg,ref} = v'_{dg} - \omega_s i_{qg} L_g \quad (3.18)$$

$$v_{qg,ref} = v'_{qg} + \omega_s i_{dg} L_g \quad (3.19)$$

Similarly, the cross-coupling cancellation block for RSC implements the equations shown in (3.20) and (3.21).

$$v_{dr,ref} = v'_{dr} - \omega_{sl} i_{qr} \sigma L_r \quad (3.20)$$

$$v_{qr,ref} = v'_{qr} + \omega_{sl} (i_{dr} \sigma L_r + \frac{\Psi_s L_m}{L_s}) \quad (3.21)$$

Where, v'_{dg} , v'_{qg} , v'_{dr} , v'_{qr} are the outputs of the current tracking PI blocks for corresponding voltages, i_{dg} , i_{qg} , i_{dr} and i_{qr} are the d-q axis grid converter currents and rotor converter currents, respectively.

The third harmonic injection block is used to increase the amplitude of the output voltage without the loss of quality [93].

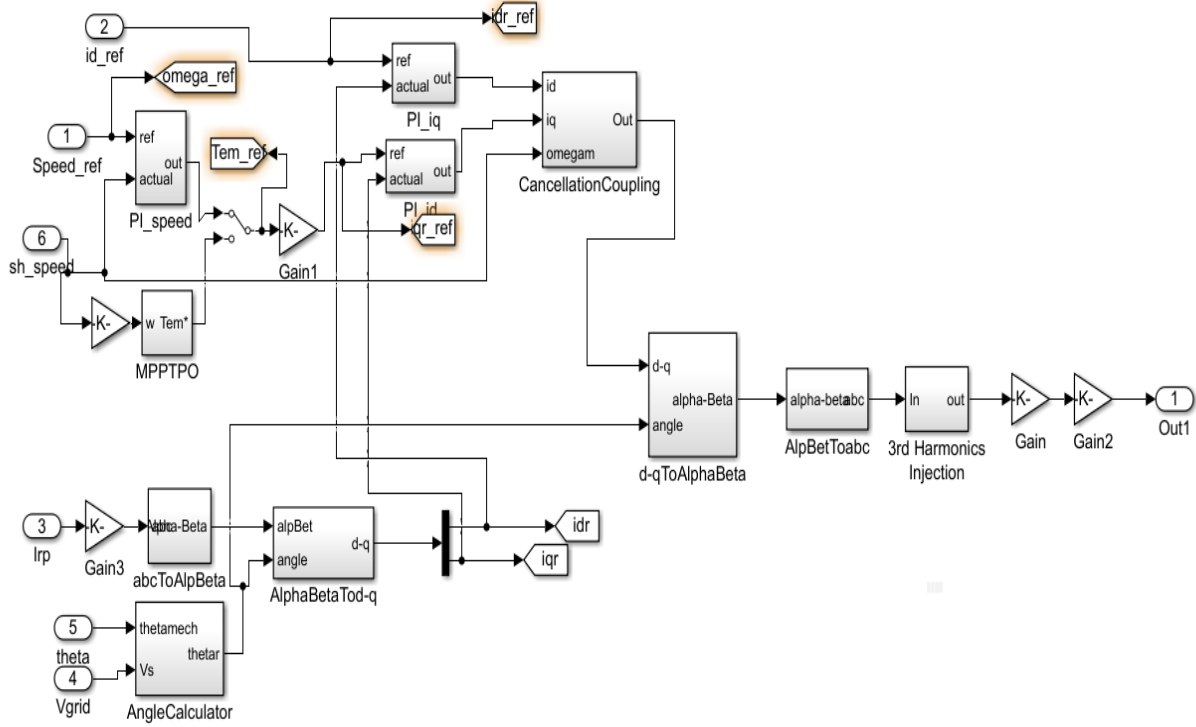


Fig. 3.12. Matlab-Simulink block diagram of RSC control pulse generator.

Table 3. 4 PI controller constants for GSC and RSC control pulse generator

GSC PI controller parameters		RSC PI controller parameters	
$K_{p,vbus}$	-10^4	$K_{p,\omega r}$	6350
$K_{i,vbus}$	-3×10^5	$K_{i,\omega r}$	1.5×10^5
$K_{p,iqg}$	0.0302	$K_{p,iqr}$	8920
$K_{i,iqg}$	0.025	$K_{i,iqr}$	1.2×10^4
$K_{p,idg}$	0.0302	$K_{p,idr}$	8920
$K_{i,idg}$	0.025	$K_{i,idr}$	1.2×10^4

Figs. 3.13(a)-(f) shows the comparative performance analysis of the proposed controller, the conventional HCS controller and constant TSR controller for WECS at a constant wind speed of 10 m/s.

The analysis is done for a scaled version wind turbine with radius of 15 m. Therefore, the maximum power for the turbine is found around 0.2 MW. All other parameters remain same as listed in Table 3.3. The proposed adaptive step controller maintains gradual tracking of speed to reach the peak point as shown in Fig. 3.13(b).

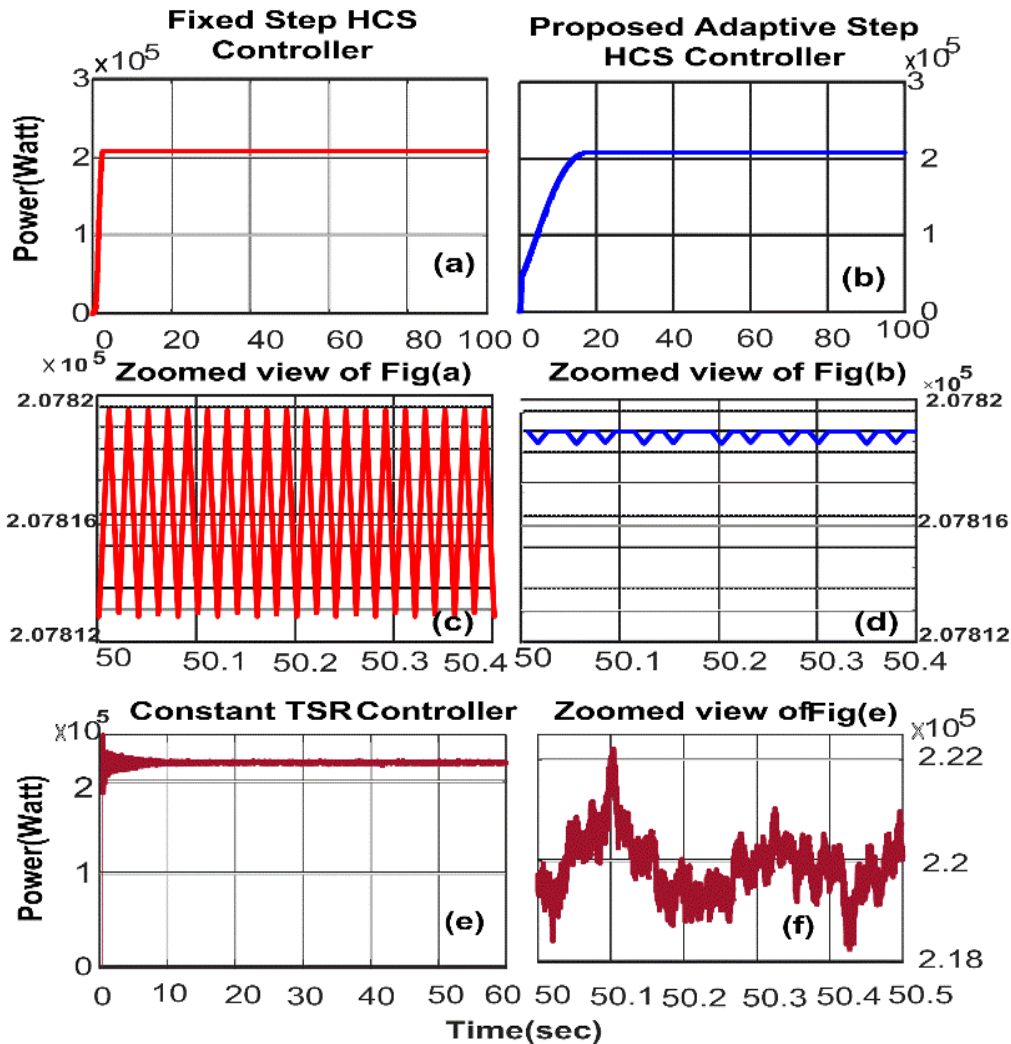


Fig. 3.13. Comparison of turbine output power at constant wind speed 10 m/s: (a) Turbine output power for conventional fixed-step HCS controller; (b) Turbine output power for the proposed controller; (c) Zoom-in view of Fig. (a); (d) Zoom-in view of Fig. (b); (e) Turbine output power for Constant TSR controller; (f) Zoom-in view of Fig. (e).

In Fixed step-size based HCS MPPT control scheme, the power fluctuation sustains even after the maximum power point is achieved (Fig. 3.13(c)) while the power variation in TSR-MPPT controller occurs due to difference of actual rotor speed and reference rotor speed (Fig. 3.13(e-f)). In the figure, the power signal is zoomed-in around the instant of 50 sec. Due to the constant fluctuation of power, efficiency is compromised in fixed-step mode and constant TSR method. In contrast, the proposed adaptive step based MPPT controller can minimize the perturbation of extracted power by the implied convergent attribute of the functions, $f(z)$ as mentioned in (3.8)-(3.10). The superiority of the proposed controller is evident as it diminishes the fluctuation of turbine power to a narrow scale through the adaptation of rotor speed step size as appeared in the zoom-in view of the turbine power (Fig. 3.13(d),(f)).

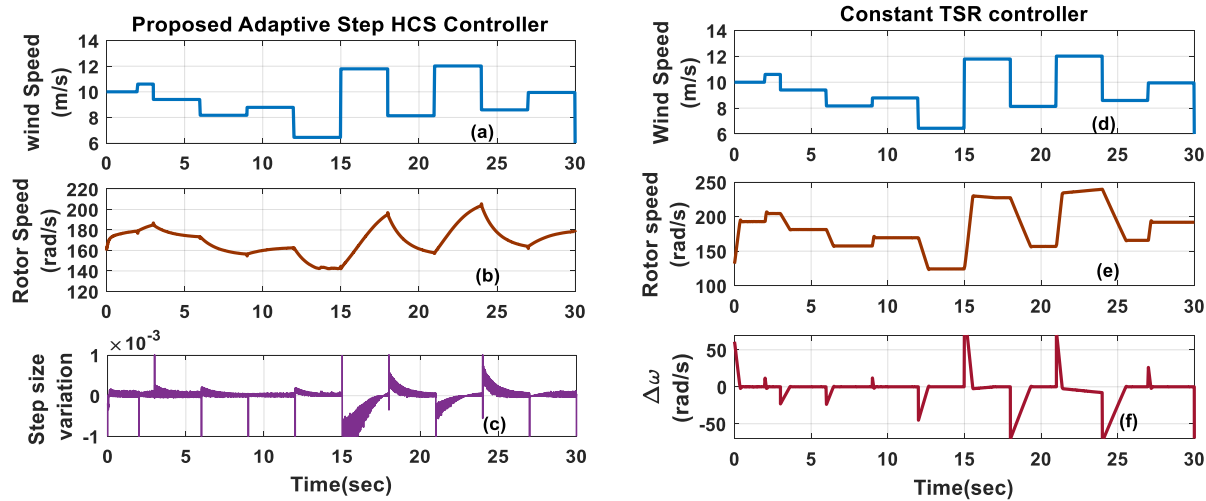


Fig. 3.14. Performance of the proposed and constant TSR controller for random variation in wind speed: (a) Arbitrary wind speed, (b) Generator rotor speed tracking by the proposed controller to maintain MPPT, (c) Adaptation in step size, (d) Random wind profile, (e) Generator rotor speed for constant TSR controller, (f) Deviation of actual rotor speed from reference speed.

Since the HCS control is blind to the atmospheric changes, the perturbation direction at any sample might be dictated by the change in the wind speed rather than the change caused by previous perturbation. To get rid of this shortcoming, the wind speed data is utilized for perturbation calculation

so that any sudden fluctuation in wind speed is detected by the controller. This will allow the controller to pave the rotor perturbation in the proper direction. Fig. 3.14(a)-(f) illustrate the comparative performance between the designed proposed adaptive step based HCS MPPT controller and constant TSR-MPPT controller under randomly changing wind speed condition.

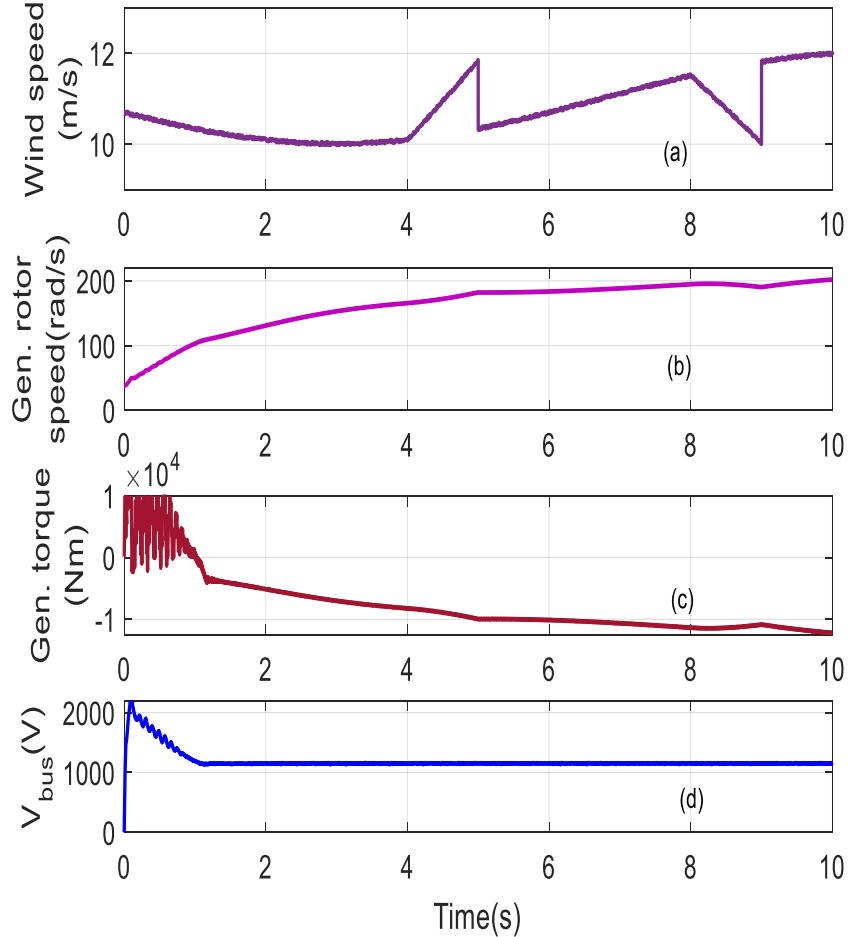


Fig. 3.15. Performance of the DFIG under randomly varied wind speed: (a) Arbitrary variation in wind speed from 10 m/s to 12 m/s, (b) Corresponding variation in generator speed, (c) Change in generator torque, (d) DC-link voltage level.

The performance of the GSC and RSC for DFIG is verified and explained in Figs. 3.15(a)-(d). The figures show that the generator speed and torque are changed accordingly while wind speed varies gradually from 10 ms^{-1} to 12 ms^{-1} (Fig. 3.15(a)). The RSC ensures that the DFIG can track the reference

generator speed and electromechanical torque with the change in wind speed (Fig. 3.15 (b), (c)). By following the optimum rotor speed, the DFIG tracks the peak power point with the help of the control action of RSC. The grid side converter manages to keep the dc-link voltage constant at variable operating condition. The reference dc-link voltage is set to 1150 V. The GSC stabilizes the actual dc voltage at the desired level as shown in Fig. 3.15(d).

3.5 Real-Time Implementation and Results

A prototype for the proposed adaptive step size based MPPT control of DFIG-WECS is tested in laboratory to see the performance of the system in real-time. The experimental setup of the prototype 480VA LabVolt series DFIG based WECS is shown in Fig. 3.16. A 4-pole wound rotor induction machine is commissioned as the DFIG module in the system. The rated voltage at the stator and rotor side is 120/208 V and 360/624 V respectively. The nominal current is 1.33 A/phase. The machine is mechanically coupled with a four-quadrant dynamometer module by a non-slip belt. The dynamometer module can act as a fully configurable prime mover which can be controlled both manually and from host-computer. A programmed mode for wind turbine emulation is installed in dynamometer module which is compatible for wind power generation testing. The wind speed, air density and pulley ratio of the wind turbine emulator can be varied from host computer within the limited range of the dynamometer. The real-time parameter for the DFIG module is shown in Appendix-A. A TTL compatible quadrature encoder output is assembled in the module that has been linked with the incremental encoder interface of the DSP board to measure the actual rotor speed. The quadrature encoder has the resolution of 360 pulses/rev and the rotor position angle can be calculated by the DSP encoder using the equation of $(2\pi/1024)$ rad $\times P$, where P is the number of pulses counted in the counter. Change in wind speed which stiffly influences the turbine power can be detected through the torque sensor incorporated in the same module. The power of the turbine is calculated by multiplying

the torque and speed measurement. For implementation of the MPPT scheme in real time, the step size determination functions are re-evaluated according to the power and wind range of the machine. The voltage and current sensors gather the required voltage and current reading and deliver to DSP board in a form which is compatible for the ADC panel. The ADC channels in DSP board accumulate the voltage, current and torque sensor input and by processing in the designed model in Matlab-Simulink, the PWM signals are generated for the GSC and RSC. A power thyristor module is connected to the stator terminal of the DFIG which operate as GSC block. The purpose of the thyristor unit is to convert the ac output into dc voltage. The dc link contains a $1360\mu\text{F}$ filtering capacitor which is fixed at the inverter input. The maximum voltage capacity of dc bus is 420 V. The power exchange operation from the dc-link stage to the rotor side is executed through an IGBT chopper/inverter module. The pulse signals for both the power thyristor and inverter are produced by the DSP board and interfaced through the slave I/O connector to the miniature banana jack terminals of both converters. To imitate the grid supply, the stator of the doubly fed machine is connected to a 120 V/60 Hz fixed three phase supply voltage. The DSP board DS1104 board is installed in an Intel PC with uninterrupted communication through dual port memory to implement the control scheme in real-time. The DS1104 board is mainly based on a Texas Instrument MPC8240 64-bit floating point digital signal processor. In order to implement the control algorithm, a real-time Simulink model is downloaded to the DSP board using the ControlDesk software. The ControlDesk software is used to download the programs to the DSP board, start and stop the function of the DS1104 as well as create a layout for interfacing with global variables in dSPACE programs. The output signals that are obtained from the machine and the DSP board are observed in the oscilloscope. The power ratings of the DFIG and the converters of the experimental setup are relatively low as compared to the equipment used in wind farms. Although the simulation is performed for large power wind turbine and generator model, some of the parameters have been re-

evaluated for real time implementation of the overall system. One of the goals of the GSC is to maintain unity displacement factor at the stator terminal of the DFIG.

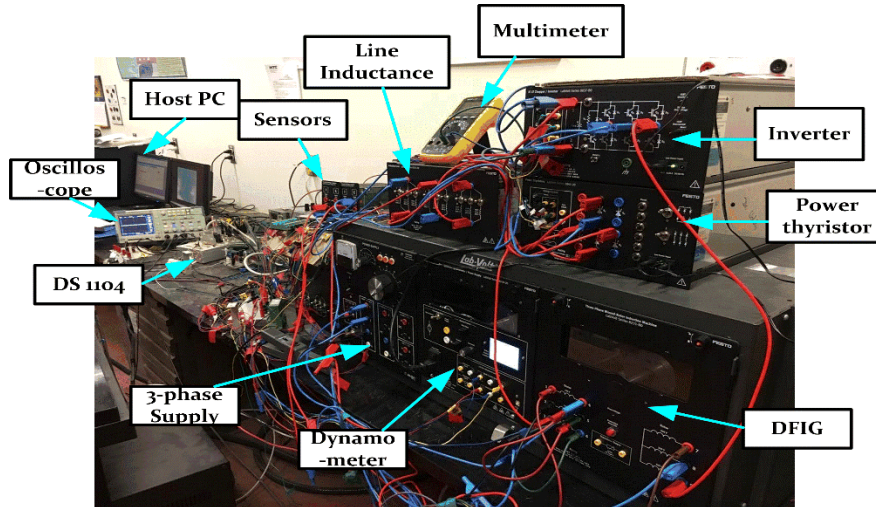


Fig. 3.16. Experimental setup for the proposed DFIG based WECS.

Fig. 3.17 shows the supply voltage and current waveform generated by the DFIG for a phase. The phase angle between the supply voltage and current is found approximately 180° as the machine is supplying power to the grid at super-synchronous mode of operation.

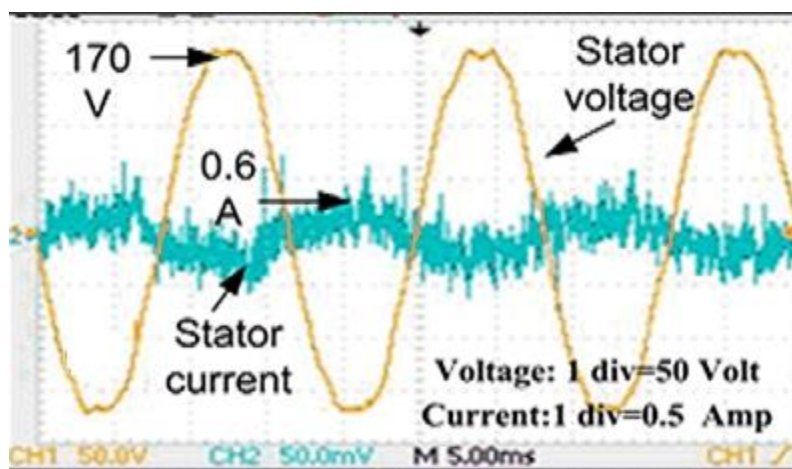


Fig. 3.17. Real-time ‘a’ phase stator voltage and current for the proposed control at super-synchronous mode.

It confirms the unity power factor operation at the supply end. Though the supply side current contains big noises, a larger filter is avoided at the grid side to get rid of relevant losses and loading effect. In this case, the approximate power supplied from the stator is 153 W. The rotor power can be calculated from the stator power and slip speed of the generator. The approximate value for the rotor power is obtained as follows:

$$P_r \cong -sP_s = -\frac{(1800-1908)}{1800} \times 153 = 9.18 \text{ W.}$$

So the total power supplied by the DFIG is $(153+9.18)$ W=162.18 W. The input power form the turbine can be obtained from the turbine torque sensor data and rotor speed and is equal to 214 W for the given stator power. So the efficiency of the generator is found around 75.7%. However, the efficiency varies based on the operating point of the system.

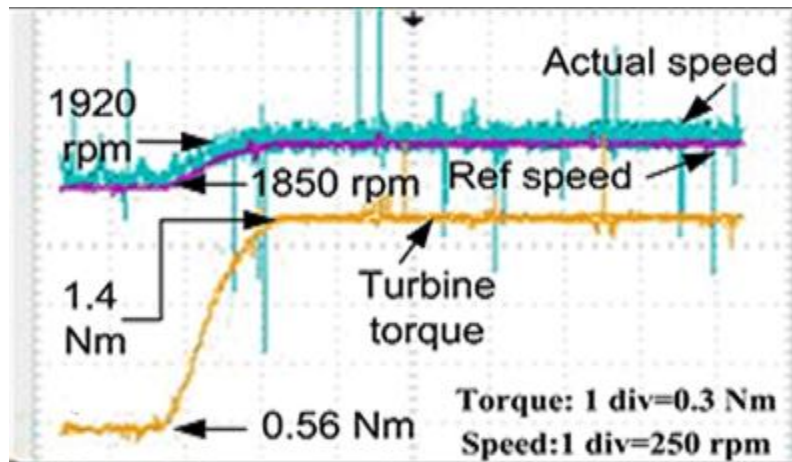


Fig. 3.18. MPPT controller performance for incremental wind speed.

Fig. 3.18 shows the MPPT controller performance for the DFIG while wind speed keeps increasing. For experimentation, the wind speed is elevated from 9.6 ms^{-1} to 10.8 ms^{-1} which corresponds to 12.5% increment from its initial value.

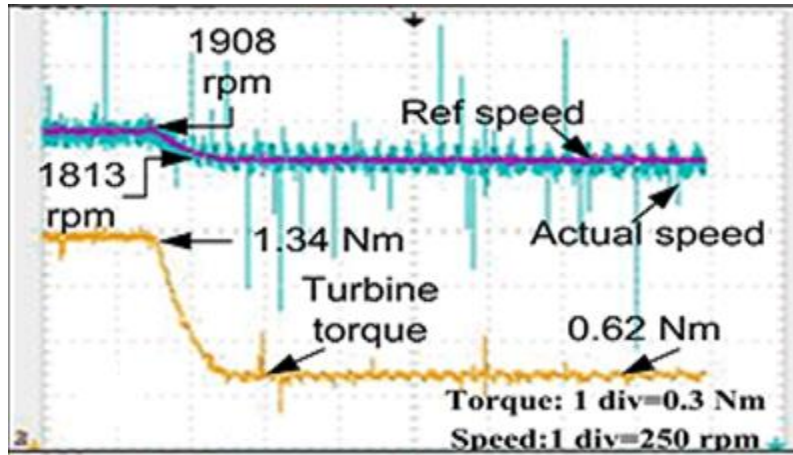


Fig. 3.19. MPPT control action along with GSC and RSC controls of DFIG while wind speed declines.

Eventually, the uprising velocity of wind results in a gradual increase in turbine torque from 0.56 Nm to 1.4 Nm. It is found that the controller attains the peak power point accordingly. A similar observation is monitored for DFIG rotor speed while wind speed decays over time (Fig. 3.19). The actual rotor speed tracks down the reference speed by the action of designed MPPT controller to follow the declined wind speed from 10.65 m/s to 9.8 m/s. The fluctuation in the rotor speed signal is caused by the noise in the sensors, switching pattern and vibration of the machine. The built-in low-pass filter Simulink blocks are used to filter out the current signal noises. In the rotor speed figures, raw data is plotted without filtering so observe the variation of adaptive step changes in rotor speed. Excluding the signal spikes, the observed generator speed reflects the efficacy of the proposed controller in extracting maximum power. The wind turbine emulator acts as a black box that provides us required torque for a particular wind speed without any wind turbine power profile. Only the equivalent turbine radius can be selected in the simulator. Since the turbine power coefficient curve or turbine power curve has not been provided with the emulator, the actual maximum power remains unknown for a specific wind speed. Therefore, the performance of the proposed MPPT controller can't be verified numerically for the hardware setup. Another shortcoming of the setup is its huge vibration. Though the overall setup is placed on a levelled surface and the display panel for the rotor speed measurement shows very little

fluctuation a steady state, the speed sensor data is vastly influenced by the background noise originated from the generator and dynamometer vibration. Therefore, the efficacy of the adaptive step size based HCS-MPPT controller can't be investigated appropriately by measuring the step variations. For voltage source converter control mode of RSC, the dc-link voltage needs to be stabilized at a constant level. In the experimental model, the stabilization of dc-link voltage is achieved by the PI control operation of the GSC. Fig. 3.20 shows the consistency of dc-link voltage while the turbine torque rises from 0.6 Nm to 1.3 Nm. It is observed that the dc-link voltage is maintained at 250 V which is chosen as the reference level. It maintains the voltage level when there is a change of torque at $t=40$ sec. The perturbation and high spikes in the dc-link voltage occurs due to the high-frequency switching of the converters.

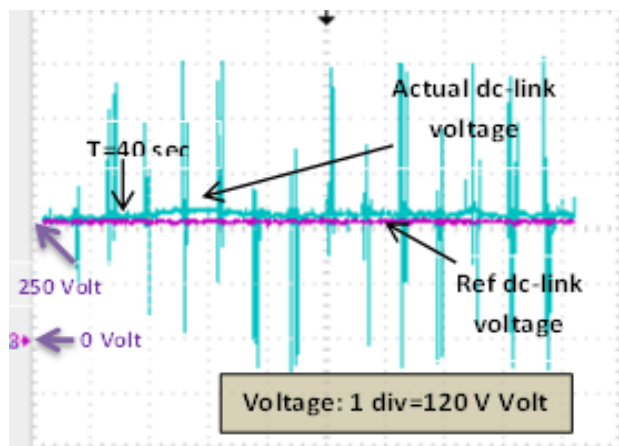


Fig. 3.20. DC-link voltage tracking performance.

3.6 Summary

A new adaptive step-size based MPPT controller has been developed in this thesis for DFIG-WECS. In this work, the step size is calculated based on the rate of change in wind turbine output power and wind speed. The mitigation of power fluctuation near peak power point with faster power tracking has been ensured by the proposed control algorithm under fluctuating wind speed conditions.

The performance of the designed adaptive step size based HCS-MPPT is compared with the conventional fixed-step size based HCS-MPPT and constant TSR MPPT algorithm in simulation. The effectiveness of the proposed MPPT based DFIG-WECS has been verified by efficient power extraction with prompt power tracking capability. Furthermore, PI controller based the grid side and rotor side converter-control of DFIG ensures reactive power control and reference rotor speed tracking, respectively. In the next chapter, a nonlinear control scheme will be designed for more sophisticated control of the DFIG-based WECS and comparative analysis between the PI control and nonlinear control will be demonstrated.

Chapter 4

Design of an Adaptive Backstepping Based Nonlinear Controller for DFIG Based WECS

Many control applications that require high dynamic performance of the DFIG are based on exact linearization method in order to compensate the nonlinear effect of the system. Two-loop control structure is utilized in this method. The nonlinear compensation is implemented in the inner feedback loop whereas the linear compensation is derived on the basis of control objective at the outer control loop. Another nonlinear control method for machine control is energy shaping design which is based on Euler-Lagrange form of dynamic equation. In contrast to the exact linearization design method, which could be characterized as a mathematically motivated approach, the energy shaping design approach has evolved from the physical properties of the system, such as energy conservation and passivity [92]. Another alternative nonlinear control approach is backstepping based control. Backstepping and adaptive backstepping based nonlinear controller can be implemented in the systems that are not exactly linearizable and to systems that are affected by disturbances. Since DFIG inherits nonlinear magnetization characteristics, a well-developed nonlinear control technique is necessary to achieve enhanced dynamic behavior for the control operation of the system. Simple proportional-integral (PI) controllers are executed to regulate the current components of the converters in conventional vector control design of DFIG based wind power system. A major drawback of fixed PI controller is that its gain tuning requires to be accurate for proper tracking. The PI control loop may lead to unstable condition due to excessive integral gain if the machine and grid filter parameters are not precisely known in DFIG based WECS. In this chapter, first, by using the Lyapunov stability theory, a controller

will be designed for grid side converter. Then adaptive backstepping based nonlinear control technique is developed in this thesis for rotor side converter control of DFIG-WECS since the method has the ability to deal with the nonlinear coupling among generator currents and the rotor speed and it can cope with parameter uncertainties. The following sections illustrate the details of the method.

4.1 Overview of Adaptive Backstepping Control

Nonlinear backstepping control is a recursive procedure that interlaces the choice of a Lyapunov function with the design of feedback control. It breaks a design problem for the full system into a sequence of design problems for lower-order systems. P.V. Kokotovic developed this method in 1990 for designing stability controls for nonlinear dynamical systems. It recursively defines a change of coordinates together with a Lyapunov function that simplifies the system and provides a controller to stabilize the system. The approach selects an appropriate function of state variables to obtain a pseudo-control input for a lower dimension subsystem of the overall system. The design process starts at the known-stable sub-system and new controllers are obtained that progressively stabilize the subsystem. An error variable representing the deviation of the pseudo-control from its desired value needs to be introduced in the process. Each backstepping stage results in a new pseudo-control design related to the control input of the previous stage. The final control input stabilizes the system by virtue of a final Lyapunov function, formed by summing up the Lyapunov functions associated with each individual design stage. At this stage, the design objective is achieved.

4.2 Dynamic Model of DFIG for Nonlinear Control

The differential equations representing the model of DFIG can be derived from the ideal three phase, three windings (stator and rotor) configuration of AC induction machine. The equations representing the dynamic model of DFIG are shown in (4.1)-(4.15) obtained from the state space model

in synchronous rotating reference frame. Fig. 4.1 represents the d-q axis equivalent circuit model of DFIG in synchronous coordinate with core loss taken into consideration [93]. It is assumed that all the magnitudes and parameters of the rotor are referred to the stator side. It is worthy to mention here that in most cases, the researchers avoid the resistive core loss branch in the d-q axis model of the DFIG to avoid complicacy. However, this may lead to inaccuracy in the controller design. In this thesis, the voltage and current components in the resistive core loss branch has been taken into consideration and the equations of the DFIG are derived according.

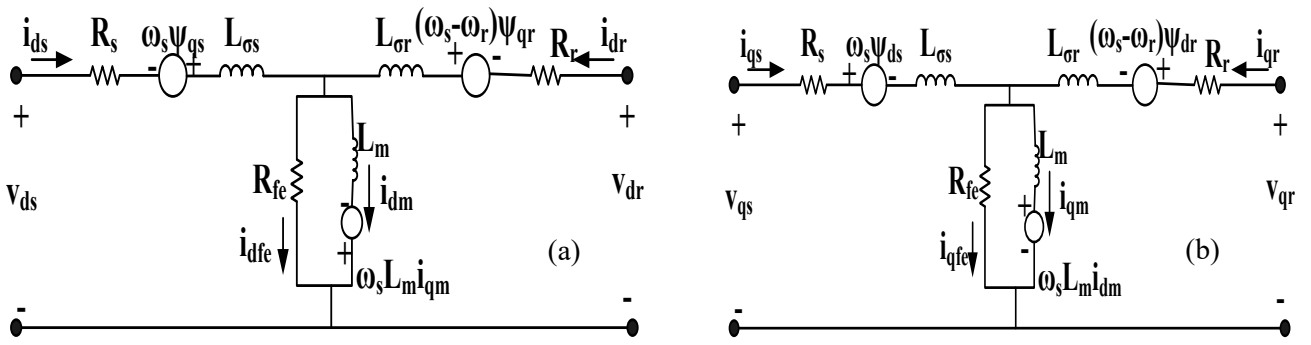


Fig. 4.1. d-q axis equivalent circuits of DFIG in synchronous reference frame referred to stator side with core loss resistance: (a) d-axis and, (b) q-axis.

$$v_{ds} = R_s i_{ds} + p\psi_{ds} - \omega_s \psi_{qs} \quad (4.1)$$

$$v_{qs} = R_r i_{dr} + p\psi_{qs} + \omega_s \psi_{ds} \quad (4.2)$$

$$v_{dr} = R_r i_{dr} + p\psi_{dr} - (\omega_s - \omega_r)\psi_{qr} \quad (4.3)$$

$$\psi_{ds} = L_{\sigma s} i_{ds} + L_m i_{dm} \quad (4.5)$$

$$\psi_{qs} = L_{\sigma s} i_{qs} + L_m i_{qm} \quad (4.6)$$

$$\psi_{dr} = L_{\sigma r} i_{dr} + L_m i_{dm} \quad (4.7)$$

$$\psi_{qr} = L_{\sigma r} i_{qr} + L_m i_{qm} \quad (4.8)$$

$$i_{dm} = i_{ds} + i_{dr} - i_{dfe} \quad (4.9)$$

$$i_{qm} = i_{qs} + i_{qr} - i_{qfe} \quad (4.10)$$

$$L_m \frac{di_{dm}}{dt} = R_{fe} i_{dfe} + \omega_s L_m i_{qm} \quad (4.11)$$

$$L_m \frac{di_{qm}}{dt} = R_{fe} i_{qfe} - \omega_s L_m i_{dm} \quad (4.12)$$

$$J \frac{d\omega_m}{dt} = T_e - T_t \quad (4.13)$$

$$T_e = \frac{3PL_m}{2} (i_{dm} i_{qr} - i_{qm} i_{dr}) \quad (4.14)$$

$$\dot{\omega}_r = \frac{P}{J} (T_e - T_t) = \frac{P}{J} \left\{ \frac{3PL_m}{2} (i_{dm} i_{qr} - i_{qm} i_{dr}) - T_t \right\} \quad (4.15)$$

Some of the above mentioned equations have been already mentioned in Chapter 2. Since, the core-loss resistance of DFIG is considered in this chapter, most of the equations are different from those that have been illustrated in Chapter 2. One of the important features of the backstepping design method is that parameter update laws can be obtained simultaneously with the derivation of control laws. Therefore, the problem associated with parameter uncertainty is expected to be solved easily if the convergence of the parameter is ensured by the applicable theorem. The rotor side converter controller design starts with the machine motion equation to stabilize the rotor actual speed at the reference rotor speed. The subsystem equations are exploited and new controllers are derived by defining appropriate Lyapunov candidate function progressively. The process terminates when the control equations for the reference voltages are derived. The state space model of DFIG can be obtained by modifying (4.1) - (4.15) with d-q axis stator, rotor and core-loss current components are chosen as state variables. The state-space model equations are given by (4.16)-(4.21).

$$\frac{di_{ds}}{dt} = \frac{1}{L_{\sigma s}}(V_{ds} - R_s i_{ds} + \omega_s L_{\sigma s} i_{qs} - R_{fe} i_{dfe}) \quad (4.16)$$

$$\frac{di_{qs}}{dt} = \frac{1}{L_{\sigma s}}(V_{qs} - R_s i_{qs} - \omega_s L_{\sigma s} i_{ds} - R_{fe} i_{qfe}) \quad (4.17)$$

$$\frac{di_{dr}}{dt} = \frac{1}{L_{\sigma r}}(V_{dr} - R_r i_{dr} - \omega_r L_m i_{qs} + (\omega_s L_{\sigma r} - \omega_r L_r) i_{qr} - R_{fe} i_{dfe} + \omega_r L_m i_{qfe}) \quad (4.18)$$

$$\frac{di_{qr}}{dt} = \frac{1}{L_{\sigma r}}(V_{qr} - R_r i_{qr} + \omega_r L_m i_{ds} - (\omega_s L_{\sigma r} - \omega_r L_r) i_{dr} - R_{fe} i_{qfe} - \omega_r L_m i_{dfe}) \quad (4.19)$$

$$\frac{di_{dfe}}{dt} = \frac{V_{ds}}{L_{\sigma s}} + \frac{V_{dr}}{L_{\sigma r}} - \frac{R_s i_{ds}}{L_{\sigma s}} - \frac{\omega_r L_m i_{qs}}{L_{\sigma r}} - \frac{R_r i_{dr}}{L_{\sigma r}} - \frac{\omega_r L_r i_{qr}}{L_{\sigma r}} - \left(\frac{R_{fe}}{L_{\sigma s}} + \frac{R_{fe}}{L_{\sigma r}} + \frac{R_{fe}}{L_m} \right) i_{dfe} + \left(\frac{\omega_r L_m}{L_{\sigma r}} + \omega_s \right) i_{qfe} \quad (4.20)$$

$$\frac{di_{qfe}}{dt} = \frac{V_{qs}}{L_{\sigma s}} + \frac{V_{qr}}{L_{\sigma r}} - \frac{R_s i_{qs}}{L_{\sigma s}} + \frac{\omega_r L_m i_{ds}}{L_{\sigma r}} - \frac{R_r i_{qr}}{L_{\sigma r}} + \frac{\omega_r L_r i_{dr}}{L_{\sigma r}} - \left(\frac{R_{fe}}{L_{\sigma s}} + \frac{R_{fe}}{L_{\sigma r}} + \frac{R_{fe}}{L_m} \right) i_{qfe} - \left(\frac{\omega_r L_m}{L_{\sigma r}} + \omega_s \right) i_{dfe} \quad (4.21)$$

4.3 Description of the System with Control Blocks

In grid-connected DFIG based WECS, back-to-back converters are connected at the rotor side and grid side. The converters are controlled independently by the controller-generated PWM signal. A typical model of grid connected DFIG-WECS is employed in this thesis where the rotor side and grid side converters are driven by the non-linear controller. Fig. 4.2 depicts the configuration of overall WECS with controller blocks [94]. In practical application, the stator of the DFIG is connected to the grid via three phase transformer. The transformer ensures voltage matching between the grid and the generator and provides isolation. An MPPT controller is incorporated in the system to maximize the generated output power. The MPPT algorithm is developed based on constant TSR method. The optimum TSR provides the corresponding rotor speed at different wind speeds. The nonlinear controller is designed to ensure the stability of the system under variable operating condition. The dynamic model of DFIG is utilized to design the controller section to nullify the current error functions.

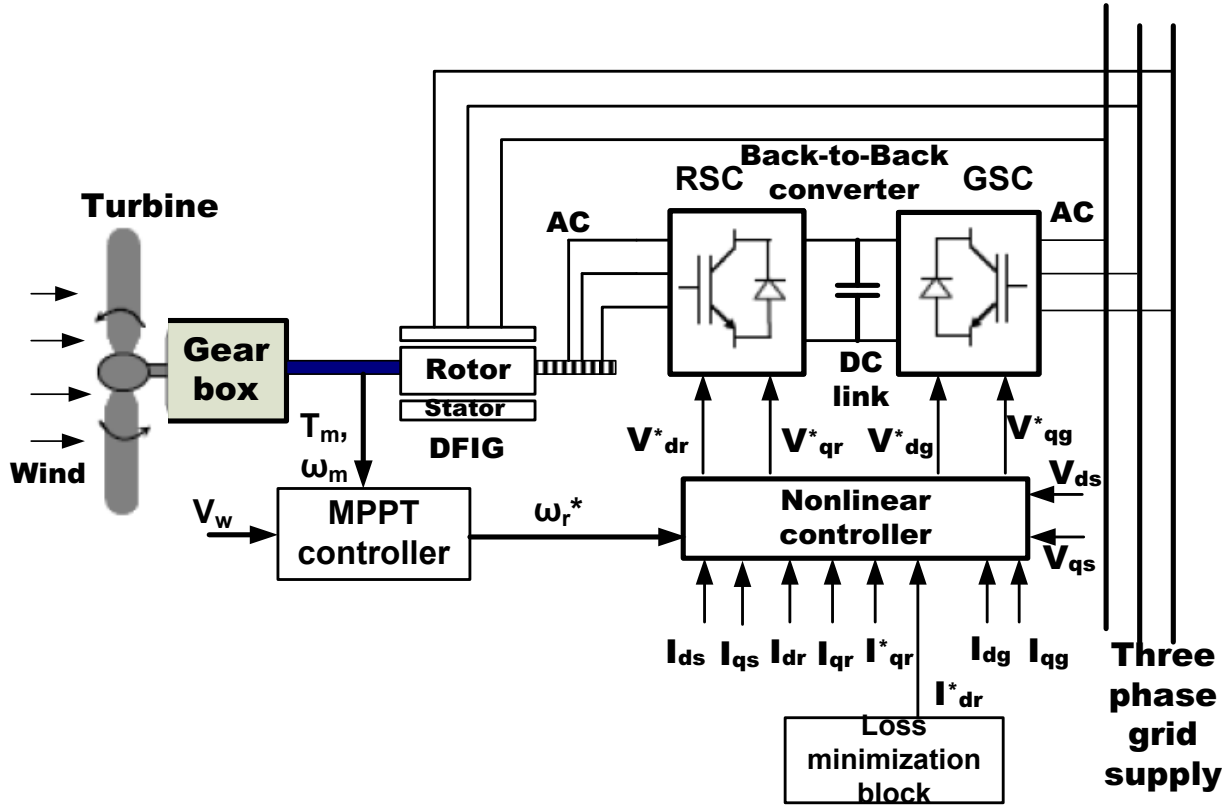


Fig. 4.2. Configuration of the proposed nonlinear controller based DFIG-WECS.

4.3.1 Lyapunov Based Controller for Grid Side Converter Control

The main purpose of the grid side controller is to keep the dc-link voltage constant irrespective of the value and direction of the rotor power flow and to regulate the reactive power on grid side. The GSC is assumed as a controlled voltage source that is connected to the grid with series grid-side resistance (R_g) and inductance (L_g). The Lyapunov method is implemented to obtain the control voltages for the grid side converter control. We assume that the state variables of the GSC controller are defined as,

$$x = [V_{bus} \ i_{cd} \ i_{cq}]$$

Where, V_{bus} is the dc-link voltage, i_{cd} and i_{cq} are d-axis and q-axis grid converter currents, respectively.

The control inputs of the GSC controller are given by,

$$u = [V_{dc} \ V_{qc}]$$

V_{dc} and V_{qc} are the d-axis and q-axis grid converter control voltages, respectively.

The dc-bus voltage (V_{bus}) equation is expressed in (4.22).

$$CV_{bus} \frac{dV_{bus}}{dt} = P_r - P_c \quad (4.22)$$

P_r and P_c are real power exchanged from rotor-side converter and grid side converter.

The error dynamics for bus voltage can be defined as,

$$e_{bus} = V_{bus,ref} - V_{bus} \quad (4.23)$$

$$\dot{e}_{bus} = \dot{V}_{bus,ref} - \dot{V}_{bus} = \dot{V}_{bus,ref} - \frac{1}{CV_{bus}}(P_r - P_c) \quad (4.24)$$

The tracking errors of d-q axis grid side converter current components are given by (4.25) and (4.26).

$$e_1 = i_{cd}^* - i_{cd} \quad (4.25)$$

$$e_2 = i_{cq}^* - i_{cq} \quad (4.26)$$

i_{cd}^* and i_{cq}^* are the reference grid converter currents.

The error dynamics for the GSC control are obtained as follows.

$$e = [e_{bus} \ e_1 \ e_2]$$

The objective of the GSC control is to ensure the convergence of the state variables to their corresponding reference values so that the error functions are stabilized to the equilibrium point, $e = 0$.

At first, the Lyapunov function for bus-voltage error is chosen as,

$$W_{e,bus} = \frac{1}{2} e_{bus}^2 \quad (4.27)$$

The derivative of (4.27) provides

$$\dot{W}_{e,bus} = e_{bus}\dot{e}_{bus} = e_{bus}(\dot{V}_{bus,ref} - \frac{1}{CV_{bus}}(P_r - P_c)) \quad (4.28)$$

To nullify the dc-link voltage error, it can be assumed that

$$-k_{e,bus}e_{bus} = \dot{V}_{bus,ref} - \frac{1}{CV_{bus}}(P_r - P_c) \quad (4.29)$$

$$V_{bus,ref} = \int_0^\tau \left\{ \frac{1}{CV_{bus}}(P_r - P_c) - k_{e,bus}e_{bus} \right\} dt \quad (4.30)$$

Here, τ is the time when dc-link voltage reaches to the value of $V_{bus,ref}$ and $k_{e,bus}$ is a positive constant. Hence, (4.28) is converted into $\dot{W}_{e,bus} = -k_{e,bus}e_{bus}^2$, which is a negative definite function.

The grid converter currents are expressed in (4.31) and (4.32) by investigating the connection between the grid and GSC.

$$\dot{i}_{cd} = \frac{1}{L_g}(V_{dc} - R_g i_{dc} + \omega_s L_{\sigma s} i_{qc} - V_{dg}) \quad (4.31)$$

$$\dot{i}_{cq} = \frac{1}{L_g}(V_{qc} - R_g i_{qc} - \omega_s L_{\sigma s} i_{dc} - V_{qg}) \quad (4.32)$$

The current error dynamics for the converter can be defined by utilizing (4.33) and (4.34).

$$\dot{e}_1 = \dot{i}_{cd}^* - \dot{i}_{cd} = -\frac{1}{L_g}(V_{dc} - R_g i_{dc} + \omega_s L_{\sigma s} i_{qc} - V_{dg}) \quad (4.33)$$

$$\dot{e}_2 = \dot{i}_{cq}^* - \dot{i}_{cq} = -\frac{1}{L_g}(V_{qc} - R_g i_{qc} - \omega_s L_{\sigma s} i_{dc} - V_{qg}) \quad (4.34)$$

Where, $i_{cd}^* = i_{cq}^* = 0$, with assumptions that the reference grid converter currents remain constant. The final Lyapunov candidate function for GSC is chosen as

$$V_1(e_{bus}, e_1, e_2) = \frac{1}{2}e_{bus}^2 + \frac{1}{2}e_1^2 + \frac{1}{2}e_2^2, \quad (4.35)$$

such that V_1 is a positive definite function, i.e. $V_1(0,0,0) = 0, V_1(e_{bus}, e_1, e_2) > 0$, for all $e_{bus}, e_1, e_2 \in D - \{0\}$, where D is an open and connected subset of \mathbb{R}^3 .

The derivative of V_1 in terms of error dynamics can be expressed as,

$$\dot{V}_1 = e_{bus}\dot{e}_{bus} + e_1\dot{e}_1 + e_2\dot{e}_2$$

$$= -k_{e,bus} e_{bus}^2 + e_1 \left(-\frac{1}{L_g} (V_{dc} - R_g i_{dc} + \omega_s L_{\sigma s} i_{qc} - V_{dg}) \right) + e_2 \left(-\frac{1}{L_g} (V_{qc} - R_g i_{qc} - \omega_s L_{\sigma s} i_{dc} - V_{qg}) \right) \quad (4.36)$$

The control voltages are chosen as,

$$V_{dc}^* = k_1 e_1 L_g + R_g i_{dc} - \omega_s L_{\sigma s} i_{qc} + V_{dg} \quad (4.37)$$

$$V_{qc}^* = k_2 e_2 L_g + R_g i_{qc} + \omega_s L_{\sigma s} i_{dc} + V_{qg} \quad (4.38)$$

After replacing the terms V_{dc} and V_{qc} in (4.36) by utilizing the corresponding voltage control from (4.37) and (4.38), the derivative of the Lyapunov candidate function becomes,

$$\dot{V}_1 = -k_{e,bus} e_{bus}^2 - k_1 e_1^2 - k_2 e_2^2 \quad (4.39)$$

With choice of $k_{e,bus}, k_1, k_2 > 0$, the function, $\dot{V}_1(e_{bus}, e_1, e_2) < 0$ on the domain $D = \mathbb{R}^3 - \{0\}$, i.e. is a negative definite function. Therefore, the equilibrium point, $e_{bus} = 0, e_1 = 0, e_2 = 0$ is globally asymptotically stable which ensures the dc bus voltage and reference current tracking requirements are met.

4.3.2 Rotor Side Converter Control for Backstepping Based Nonlinear Control Approach

The doubly fed induction generator provides the feasibility of controlling the generated power for both of the super-synchronous and sub-synchronous operation modes. The rotor side converter regulates the slip speed and controls the air-gap power of the induction machine. During the derivation of the RSC controller for backstepping and adaptive backstepping based nonlinear control, it is assumed that the grid voltage remains constant. As a result, the stator current remains unchanged in balanced condition for stator voltage oriented control scheme. Therefore, the d-q axis stator current components (i_{ds}, i_{qs}) are considered as constants and this assumption will not affect the grid converter

control because the rotor and grid converter works independently. It is also assumed that the voltage across the magnetization branch of the DFIG and the core-loss resistance are fixed at rated grid-voltage supply. Hence, the core-loss current components (i_{dfe}, i_{qfe}) are also considered as constants in the RSC controller design. Backstepping based nonlinear control approach is adopted to obtain the control laws for the rotor side converter control.

The state variables of the controller are defined as,

$$x = [\omega_r \ i_{dr} \ i_{qr}]$$

The control inputs for RSC control are defined as,

$$u = [V_{dr} \ V_{qr}]$$

The state equations are defined in (4.15), (4.18) and (4.19).

$$\dot{\omega}_r = \frac{P}{J}(T_e - T_t) = \frac{P}{J}\left\{ \frac{3PL_m}{2}(i_{dm}i_{qr} - i_{qm}i_{dr}) - T_t \right\} \quad (4.15)$$

$$\dot{i}_{dr} = \frac{1}{L_{\sigma r}}(V_{dr} - R_r i_{dr} - \omega_r L_m i_{qs} + (\omega_s L_{\sigma r} - \omega_r L_r) i_{qr} - R_{fe} i_{dfe} + \omega_r L_m i_{qfe}) \quad (4.18)$$

$$\dot{i}_{qr} = \frac{1}{L_{\sigma r}}(V_{qr} - R_r i_{qr} + \omega_r L_m i_{ds} - (\omega_s L_{\sigma r} - \omega_r L_r) i_{dr} - R_{fe} i_{qfe} - \omega_r L_m i_{dfe}) \quad (4.19)$$

The error functions are given by,

$$e_\omega = \omega_r^* - \omega_r \quad (4.40)$$

$$e_3 = i_{dr}^* - i_{dr} \quad (4.41)$$

$$e_4 = i_{qr}^* - i_{qr} \quad (4.42)$$

where, ω_r^* is the reference rotor speed provided by the MPPT controller block, i_{dr}^* and i_{qr}^* are the reference d-axis and q-axis rotor current components, respectively. The aim of backstepping based controller is to minimize the control errors so that the rotor speed, d-axis q-axis rotor current merges to the corresponding reference values. Thus the error variables for the rotor converter control system are

defined as, $e = [e_\omega \ e_3 \ e_4]$, such that the equilibrium point is $e = 0$. The backstepping controller is designed in two steps.

Step-I: To stabilize the mechanical dynamics of the DFIG system, the Lyapunov function candidate is chosen as,

$$V_\omega = \frac{1}{2} e_\omega^2 \quad (4.43)$$

$$\begin{aligned} \dot{V}_\omega &= e_\omega \dot{e}_\omega = e_\omega (-\dot{\omega}_r) \\ &= e_\omega \left[\frac{P}{J} \left\{ \frac{3PL_m}{2} (-i_{dm} i_{qr} + i_{qm} i_{dr}) + T_t \right\} \right] \end{aligned} \quad (4.44)$$

We assume,

$$-k_\omega e_\omega = \frac{P}{J} \left\{ \frac{3PL_m}{2} (-i_{dm} i_{qr} + i_{qm} i_{dr}) + T_t \right\} \quad (4.45)$$

Where, k_ω is a positive constant.

From the d-q axis model of DFIG derived in synchronous reference frame, we get

$$i_{dm} = i_{ds} + i_{dr} - i_{dfe} \quad (4.9)$$

$$i_{qm} = i_{qs} + i_{qr} - i_{qfe} \quad (4.10)$$

$i_{ds}, i_{qs}, i_{dr}, i_{qr}, i_{dm}, i_{qm}, i_{dfe}, i_{qfe}$ are the d-q axis stator, rotor, magnetization and core-loss current components, respectively.

By utilizing (4.9) and (4.10), (4.45) is converted as follows:

$$\begin{aligned} k_\omega e_\omega &= \left[\frac{3P^2 L_m}{2J} \{ (i_{ds} + i_{dr} - i_{dfe}) i_{qr} - (i_{qs} + i_{qr} - i_{qfe}) i_{dr} \} - \frac{PT_t}{J} \right] \\ &\Rightarrow (i_{qs} - i_{qfe}) i_{dr} + i_{qr} i_{dr} - (i_{ds} - i_{dfe}) i_{qr} - i_{dr} i_{qr} = -\frac{2k_\omega e_\omega J}{3P^2 L_m} - \frac{2T_t}{3PL_m} \end{aligned}$$

$$\Rightarrow (i_{qs} - i_{qfe})(i_{dr}^* - e_3) - (i_{ds} - i_{dfe})(i_{qr}^* - e_4) = -\frac{2k_\omega e_\omega J}{3P^2 L_m} - \frac{2T_t}{3PL_m} \quad (4.46)$$

The q axis reference current component for the rotor side converter is found from (4.46).

$$i_{qr}^* = \frac{1}{(i_{ds} - i_{dfe})} \left\{ (i_{qs} - i_{qfe})i_{dr}^* + \frac{2T_t}{3PL_m} + \frac{2k_\omega e_\omega J}{3P^2 L_m} \right\} \quad (4.47)$$

Since, the core resistance R_{fe} is large, the d-axis core current component (i_{dfe}) is much smaller compared to the d-axis stator current component (i_{ds}). Hence, the denominator term of (4.47) is nonzero, i.e.

$$i_{ds} - i_{dfe} \neq 0$$

The derivative of the Lyapunov function becomes,

$$\dot{V}_\omega = -k_\omega e_\omega^2 - \frac{3P^2 L_m}{2J} \{(i_{qs} - i_{qfe})e_3 e_\omega - (i_{ds} - i_{dfe})e_4 e_\omega\} \quad (4.48)$$

Hence, \dot{V}_ω becomes negative semi-definite function if $i_{qr}^* = i_{qr}$.

Step-II:

It is assumed that i_{dr}^* is a constant. The error dynamics of the proposed RSC control is expressed in (4.49),(4.50) and (4.51) by shifting the origin of the state variables to their corresponding reference point.

$$\dot{e}_\omega = \left[\frac{P}{J} \left\{ \frac{3PL_m}{2} (-i_{dm} i_{qr} + i_{qm} i_{dr}) + T_t \right\} \right] \quad (4.49)$$

$$\dot{e}_3 = \dot{i}_{dr}^* - \dot{i}_{dr}$$

$$= \dot{i}_{dr}^* - \frac{1}{L_{\sigma r}} \{ V_{dr} - R_r i_{dr} - \omega_r L_m i_{qs} + (\omega_s L_{\sigma r} - \omega_r L_r) i_{qr} - R_{fe} i_{dfe} + \omega_r L_m i_{qfe} \} \quad (4.50)$$

$$\dot{e}_4 = \dot{i}_{qr}^* - \dot{i}_{qr}$$

$$= \dot{i}_{qr}^* - \frac{1}{L_{\sigma r}} \{ V_{qr} - R_r i_{qr} + \omega_r L_m i_{ds} - (\omega_s L_{\sigma r} - \omega_r L_r) i_{dr} - R_{fe} i_{qfe} - \omega_r L_m i_{dfe} \} \quad (4.51)$$

Also,

$$\begin{aligned} i_{qr}^* &= \frac{1}{(i_{ds} - i_{dfe})} \left\{ (i_{qs} - i_{qfe}) i_{dr}^* + \frac{2k_\omega e_\omega J}{3P^2 L_m} \right\} \\ &= -\frac{2k_\omega^2 e_\omega J}{3P^2 L_m (i_{ds} - i_{dfe})} \end{aligned} \quad (4.52)$$

Now the final Lyapunov function is chosen as,

$$V_F = V_\omega + \frac{1}{2} e_3^2 + \frac{1}{2} e_4^2 \quad (4.53)$$

such that V_F is a positive definite function, i.e. $V_F(0) = 0, V_F(e_\omega, e_3, e_4) > 0$, for all $e_\omega, e_3, e_4 \in D - \{0\}$.

$$\begin{aligned} \dot{V}_F &= \dot{V}_\omega + e_3 \dot{e}_3 + e_4 \dot{e}_4 \\ &= -k_\omega e_\omega^2 - \frac{3P^2 L_m}{2J} \left\{ (i_{qs} - i_{qfe}) e_3 e_\omega - (i_{ds} - i_{dfe}) e_4 e_\omega \right\} + e_3 \left\{ -\frac{1}{L_{\sigma r}} \{V_{dr} - R_r i_{dr} - \omega_r L_m i_{qs} + (\omega_s L_{\sigma r} - \omega_r L_r) i_{qr} - R_{fe} i_{dfe} + \omega_r L_m i_{qfe}\} \right\} + e_4 \left\{ i_{qr}^* - \frac{1}{L_{\sigma r}} \{V_{qr} - R_r i_{qr} + \omega_r L_m i_{ds} - (\omega_s L_{\sigma r} - \omega_r L_r) i_{dr} - R_{fe} i_{qfe} - \omega_r L_m i_{dfe}\} \right\} \\ &= -k_\omega e_\omega^2 - \frac{3P^2 L_m}{2J} \left\{ (i_{qs} - i_{qfe}) e_3 e_\omega - (i_{ds} - i_{dfe}) e_4 e_\omega \right\} + e_3 \left\{ -\frac{1}{L_{\sigma r}} \{V_{dr} - R_r i_{dr} - \omega_r L_m i_{qs} + (\omega_s L_{\sigma r} - \omega_r L_r) i_{qr} - R_{fe} i_{dfe} + \omega_r L_m i_{qfe}\} \right\} + e_4 \left\{ -\frac{2k_\omega^2 e_\omega J}{3P^2 L_m (i_{ds} - i_{dfe})} - \frac{1}{L_{\sigma r}} \{V_{qr} - R_r i_{qr} + \omega_r L_m i_{ds} - (\omega_s L_{\sigma r} - \omega_r L_r) i_{dr} - R_{fe} i_{qfe} - \omega_r L_m i_{dfe}\} \right\} \\ &= -k_\omega e_\omega^2 + e_3 \left\{ -\frac{1}{L_{\sigma r}} \{V_{dr} - R_r i_{dr} - \omega_r L_m i_{qs} + (\omega_s L_{\sigma r} - \omega_r L_r) i_{qr} - R_{fe} i_{dfe} + \omega_r L_m i_{qfe}\} - \frac{3P^2 L_m}{2J} (i_{qs} - i_{qfe}) e_\omega \right\} + e_4 \left\{ -\frac{2k_\omega^2 e_\omega J}{3P^2 L_m (i_{ds} - i_{dfe})} - \frac{1}{L_{\sigma r}} \{V_{qr} - R_r i_{qr} + \omega_r L_m i_{ds} - (\omega_s L_{\sigma r} - \omega_r L_r) i_{dr} - R_{fe} i_{qfe} - \omega_r L_m i_{dfe}\} + \frac{3P^2 L_m}{2J} (i_{ds} - i_{dfe}) e_\omega \right\} \end{aligned} \quad (4.54)$$

With the assumptions,

$$-k_3 e_3 = -\frac{1}{L_{\sigma r}} \{ V_{dr} - R_r i_{dr} - \omega_r L_m i_{qs} + (\omega_s L_{\sigma r} - \omega_r L_r) i_{qr} - R_{fe} i_{dfe} + \omega_r L_m i_{qfe} \} - \frac{3P^2 L_m}{2J} (i_{qs} - i_{qfe}) e_\omega \quad (4.55)$$

And,

$$-k_4 e_4 = -\frac{2k_\omega^2 e_\omega J}{3P^2 L_m (i_{ds} - i_{dfe})} - \frac{1}{L_{\sigma r}} \{ V_{qr} - R_r i_{qr} + \omega_r L_m i_{ds} - (\omega_s L_{\sigma r} - \omega_r L_r) i_{dr} - R_{fe} i_{qfe} - \omega_r L_m i_{dfe} \} + \frac{3P^2 L_m}{2J} (i_{ds} - i_{dfe}) e_\omega \quad (4.56)$$

Where, k_3 and k_4 are closed loop positive feedback constants.

We obtain the control laws by utilizing (4.55) and (4.56).

$$V_{dr}^* = k_3 e_3 L_{\sigma r} + R_r i_{dr} + \omega_r L_m i_{qs} - (\omega_s L_{\sigma r} - \omega_r L_r) i_{qr} + R_{fe} i_{dfe} - \omega_r L_m i_{qfe} - \frac{3P^2 L_m L_{\sigma r}}{2J} (i_{qs} - i_{qfe}) e_\omega \quad (4.57)$$

$$V_{qr}^* = k_4 e_4 L_{\sigma r} + \frac{3P^2 L_m L_{\sigma r}}{2J} (i_{ds} - i_{dfe}) e_\omega - \frac{2k_\omega^2 e_\omega J L_{\sigma r}}{3P^2 L_m (i_{ds} - i_{dfe})} + R_r i_{qr} - \omega_r L_m i_{ds} + (\omega_s L_{\sigma r} - \omega_r L_r) i_{dr} + R_{fe} i_{qfe} + \omega_r L_m i_{dfe} \quad (4.58)$$

Now, the derivative of final Lyapunov function takes the form of (4.59) after replacing the terms V_{dr} and V_{qr} in (4.54) with the corresponding control laws expressed in (4.57) and (4.58).

$$\dot{V}_F = -k_\omega e_\omega^2 - k_3 e_3^2 - k_4 e_4^2 \quad (4.59)$$

Thus, \dot{V}_F becomes a negative definite function. Therefore, the equilibrium point ($e_\omega = 0, e_3 = 0, e_4 = 0$) is globally asymptotically stable. Therefore, the stability of the rotor voltage control loop is ensured.

In the controller design, the nonlinearity effect of the machine appears for the presence of the term, $i_{dm}i_{qr}$ in the machine torque equation. The linear controllers often overlook the nonlinear terms. They also avoid system disturbances to eradicate design complicity. As a result, the design accuracy might be compromised. The nonlinear controller in the proposed design helps to achieve fast dynamic behavior which improves the transient response of the grid-connected DFIG, particularly under wind speed fluctuation and voltage disturbance. The outcome of the proposed controller will be discussed in the result section.

4.4 Adaptive Backstepping Based Rotor Side Converter Control with Adaptation of Magnetizing Inductance

For control purpose, usually the nominal values of the machine parameters are utilized. For a grid connected DFIG, the stator and rotor winding resistance and leakage reactance are considered to remain unchanged as the supply frequency is constant and the temperature variation is insignificant. However, the magnetizing inductance value may alter at different level of magnetization. At variable wind speed, the rotor side converter regulates the speed and flux of the machine and the level of magnetization. Thus, it necessitates the adaptation of magnetizing inductance during operation [93]. The magnetizing inductance is updated online to cope with the variations. The adaptive backstepping based control is the extended version of the backstepping control which is derived in the previous section. The state variables, state equations and control inputs remain same in this design. The effect of magnetizing inductance estimation is taken into consideration during the calculation of the stator and rotor equivalent inductance. It isn't shown in the calculation steps to avoid complexity.

The adaptive backstepping controller design starts with the state equation for speed error function as found in (4.49).

$$\begin{aligned}\dot{e}_\omega &= \frac{P}{J} \left\{ \frac{3PL_m}{2} (-i_{dm}i_{qr} + i_{qm}i_{dr}) + T_t \right\} \\ &= \frac{3P^2L_m}{2J} \{ (i_{qs} - i_{qfe})i_{dr} - (i_{ds} - i_{dfe})i_{qr} \} + \frac{PT_t}{J} \quad (4.60)\end{aligned}$$

In the first stage, the error function for the adapted value of the magnetization inductance is expressed in (4.61).

$$e_{L1} = L_m - \hat{L}_{m1} \quad (4.61)$$

The actual and first estimation for the magnetizing inductance are given as L_m and \hat{L}_{m1} , respectively.

The Lyapunov candidate function for stabilization of rotor speed is chosen as,

$$V_\omega = \frac{1}{2} e_\omega^2 + \frac{1}{2} e_{L1}^2 \quad (4.62)$$

$$\begin{aligned}\dot{V}_\omega &= e_\omega \dot{e}_\omega + e_{L1} \dot{e}_{L1} \\ &= e_\omega \left\{ \frac{3P^2L_m}{2J} \{ (i_{qs} - i_{qfe})i_{dr} - (i_{ds} - i_{dfe})i_{qr} \} + \frac{PT_t}{J} \right\} + e_{L1}(-\dot{\hat{L}}_{m1}) \\ &= e_\omega \left\{ \frac{3P^2(e_{L1} + \hat{L}_{m1})}{2J} \{ (i_{qs} - i_{qfe})i_{dr} - (i_{ds} - i_{dfe})i_{qr} \} + \frac{PT_t}{J} \right\} + e_{L1}(-\dot{\hat{L}}_{m1}) \\ &= e_\omega \left\{ \frac{3P^2\hat{L}_{m1}}{2J} \{ (i_{qs} - i_{qfe})i_{dr} - (i_{ds} - i_{dfe})i_{qr} \} + \frac{PT_t}{J} \right\} \\ &\quad + e_{L1} \left[\frac{3P^2e_\omega}{2J} \{ (i_{qs} - i_{qfe})i_{dr} - (i_{ds} - i_{dfe})i_{qr} \} - \dot{\hat{L}}_{m1} \right] \\ &= e_\omega \left\{ \frac{3P^2\hat{L}_{m1}}{2J} \{ (i_{qs} - i_{qfe})(i_{dr}^* - e_3) - (i_{ds} - i_{dfe})(i_{qr}^* - e_4) \} + \frac{PT_t}{J} \right\} + e_{L1} \left[\frac{3P^2e_\omega}{2J} \{ (i_{qs} - i_{qfe})i_{dr} - (i_{ds} - i_{dfe})i_{qr} \} - \dot{\hat{L}}_{m1} \right] \quad (4.63)\end{aligned}$$

We assume,

$$-k_\omega e_\omega = \frac{3P^2\hat{L}_{m1}}{2J} \{ (i_{qs} - i_{qfe})i_{dr}^* - (i_{ds} - i_{dfe})i_{qr}^* \} + \frac{PT_t}{J};$$

$$\dot{L}_{m1} = \frac{3P^2 e_\omega}{2J} \{ (i_{qs} - i_{qfe}) i_{dr} - (i_{ds} - i_{dfe}) i_{qr} \};$$

$$e_3 = i_{dr}^* - i_{dr}$$

$$e_4 = i_{qr}^* - i_{qr}$$

With these assumptions (4.63) becomes

$$\begin{aligned} \dot{V}_\omega &= e_\omega \dot{e}_\omega + e_{L1} \dot{e}_{L1} \\ &= -k_\omega e_\omega^2 + \frac{3P^2 \hat{L}_{m1} (i_{ds} - i_{dfe}) e_\omega e_4}{2J} - \frac{3P^2 \hat{L}_{m1} (i_{qs} - i_{qfe}) e_\omega e_3}{2J} \end{aligned} \quad (4.64)$$

With the assumed equations, the derivative of the Lyapunov function in (4.64) becomes a negative semi-definite function.

The reference current i_{qr}^* is obtained from the assumption as follows.

$$\Rightarrow i_{qr}^* = \frac{1}{(i_{ds} - i_{dfe})} \{ (i_{qs} - i_{qfe}) i_{dr}^* + \frac{2T_t}{3P\hat{L}_{m1}J} + \frac{2k_\omega e_\omega}{3P^2 \hat{L}_{m1}} \} \quad (4.65)$$

Taking the derivative of i_{qr}^* , we get,

$$\begin{aligned} i_{qr}^* &= \frac{1}{(i_{ds} - i_{dfe})} \left\{ (i_{qs} - i_{qfe}) i_{dr}^* - \frac{2T_t \dot{\hat{L}}_{m1}}{3P^2 \hat{L}_{m1}^2 J} + \frac{2k_\omega \dot{e}_\omega}{3P^2 \hat{L}_{m1}} - \frac{2k_\omega e_\omega \dot{\hat{L}}_{m1}}{3P^2 \hat{L}_{m1}^2} \right\} \\ &= \frac{1}{(i_{ds} - i_{dfe})} \left\{ -\frac{PT_t e_\omega}{\hat{L}_{m1}^2 J^2} \{ (i_{qs} - i_{qfe}) i_{dr} - (i_{ds} - i_{dfe}) i_{qr} \} - \frac{2k_\omega^2 e_\omega}{3P^2 \hat{L}_{m1}} \right. \\ &\quad \left. - \frac{k_\omega e_\omega^2}{J \hat{L}_{m1}^2} \{ (i_{qs} - i_{qfe}) i_{dr} - (i_{ds} - i_{dfe}) i_{qr} \} \right\} \end{aligned}$$

In the second stage, the error for magnetization inductance is defined as

$$e_{L2} = L_m - \hat{L}_{m2}$$

\hat{L}_{m2} is the second estimated value for the magnetizing inductance.

Next, the final Lyapunov function V_{Fp} is defined as follows,

$$V_{Fp} = V_\omega + \frac{1}{2} e_3^2 + \frac{1}{2} e_4^2 + \frac{1}{2\beta} e_{L2}^2 \quad (4.66)$$

It is assumed that i_{dr}^* remains unchanged during operation and β is a positive constant.

$$\begin{aligned} & \therefore \dot{V}_{Fp} = \dot{V}_\omega + e_3 \dot{e}_3 + e_4 \dot{e}_4 + \frac{1}{\beta} e_{L2} \dot{e}_{L2} \\ &= \dot{V}_\omega + e_3 \left\{ i_{dr}^{*\cdot} - \frac{1}{L_{\sigma r}} \{ V_{dr} - R_r i_{dr} - \omega_r L_m i_{qs} + (\omega_s L_{\sigma r} - \omega_r L_r) i_{qr} - R_{fe} i_{dfe} + \omega_r L_m i_{qfe} \} \right\} \\ &+ e_4 \left\{ i_{qr}^{*\cdot} - \frac{1}{L_{\sigma r}} \{ V_{qr} - R_r i_{qr} + \omega_r L_m i_{ds} - (\omega_s L_{\sigma r} - \omega_r L_r) i_{dr} - R_{fe} i_{qfe} - \omega_r L_m i_{dfe} \} \right\} \\ &+ \frac{1}{\beta} e_{L2} (-\dot{\hat{L}}_{m2}) \\ &= -k_\omega e_\omega^2 + \frac{3P^2 \hat{L}_{m1} (i_{ds} - i_{dfe}) e_\omega e_4}{2J} - \frac{3P^2 \hat{L}_{m1} (i_{qs} - i_{qfe}) e_\omega e_3}{2J} + e_3 \left\{ -\frac{1}{L_{\sigma r}} \{ V_{dr} - R_r i_{dr} - \omega_r L_m i_{qs} + \right. \\ &\quad \left. (\omega_s L_{\sigma r} - \omega_r L_r) i_{qr} - R_{fe} i_{dfe} + \omega_r L_m i_{qfe} \} \right\} + e_4 \left[\frac{1}{(i_{ds} - i_{dfe})} \left\{ -\frac{PT_t e_\omega}{\hat{L}_{m1}^2 J^2} \{ (i_{qs} - i_{qfe}) i_{dr} - \right. \right. \\ &\quad \left. \left. (i_{ds} - i_{dfe}) i_{qr} \} \right\} - \frac{2k_\omega^2 e_\omega}{3P^2 \hat{L}_{m1}} - \frac{k_\omega e_\omega^2}{J \hat{L}_{m1}^2} \{ (i_{qs} - i_{qfe}) i_{dr} - (i_{ds} - i_{dfe}) i_{qr} \} \right\} - \frac{1}{L_{\sigma r}} \{ V_{qr} - R_r i_{qr} + \right. \\ &\quad \left. \omega_r L_m i_{ds} - (\omega_s L_{\sigma r} - \omega_r L_r) i_{dr} - R_{fe} i_{qfe} - \omega_r L_m i_{dfe} \} \right] + \frac{1}{\beta} e_{L2} (-\dot{\hat{L}}_{m2}) \end{aligned}$$

$$\begin{aligned}
&= -k_\omega e_\omega^2 + \frac{3P^2 \hat{L}_{m1} (i_{ds} - i_{dfe}) e_\omega e_4}{2J} - \frac{3P^2 \hat{L}_{m1} (i_{qs} - i_{qfe}) e_\omega e_3}{2J} \\
&\quad + e_3 \left\{ -\frac{1}{L_{\sigma r}} \{V_{dr} - R_r i_{dr} - \omega_r \hat{L}_{m2} i_{qs} + (\omega_s L_{\sigma r} - \omega_r L_r) i_{qr} - R_{fe} i_{dfe} + \omega_r \hat{L}_{m2} i_{qfe}\} \right\} \\
&\quad + e_4 \left[\frac{1}{(i_{ds} - i_{dfe})} \left\{ -\frac{PT_t e_\omega}{\hat{L}_{m1}^2 J^2} \{(i_{qs} - i_{qfe}) i_{dr} - (i_{ds} - i_{dfe}) i_{qr}\} - \frac{2k_\omega^2 e_\omega}{3P^2 \hat{L}_{m1}} \right. \right. \\
&\quad \left. \left. - \frac{k_\omega e_\omega^2}{J \hat{L}_{m1}^2} \{(i_{qs} - i_{qfe}) i_{dr} - (i_{ds} - i_{dfe}) i_{qr}\} \right\} \right. \\
&\quad \left. - \frac{1}{L_{\sigma r}} \{V_{qr} - R_r i_{qr} + \omega_r \hat{L}_{m2} i_{ds} - (\omega_s L_{\sigma r} - \omega_r L_r) i_{dr} - R_{fe} i_{qfe} - \omega_r \hat{L}_{m2} i_{dfe}\} \right] \\
&\quad + \frac{1}{\beta} e_{L2} (-\dot{\hat{L}}_{m2}) + \frac{1}{L_{\sigma r}} e_3 e_{L2} \omega_r i_{qs} - \frac{1}{L_{\sigma r}} e_3 e_{L2} \omega_r i_{qfe} - \frac{1}{L_{\sigma r}} e_4 e_{L2} \omega_r i_{ds} \\
&\quad + \frac{1}{L_{\sigma r}} e_4 e_{L2} \omega_r i_{dfe} \\
&= -k_\omega e_\omega^2 + e_3 \left[-\frac{1}{L_{\sigma r}} \{V_{dr} - R_r i_{dr} - \omega_r \hat{L}_{m2} i_{qs} + (\omega_s L_{\sigma r} - \omega_r L_r) i_{qr} - R_{fe} i_{dfe} + \omega_r \hat{L}_{m2} i_{qfe}\} \right. \\
&\quad \left. - \frac{3P^2 \hat{L}_{m1} (i_{qs} - i_{qfe}) e_\omega}{2J} \right] \\
&\quad + e_4 \left[\frac{1}{(i_{ds} - i_{dfe})} \left\{ -\frac{PT_t e_\omega}{\hat{L}_{m1}^2 J^2} \{(i_{qs} - i_{qfe}) i_{dr} - (i_{ds} - i_{dfe}) i_{qr}\} - \frac{2k_\omega^2 e_\omega}{3P^2 \hat{L}_{m1}} - \frac{k_\omega e_\omega^2}{J \hat{L}_{m1}^2} \{(i_{qs} - i_{qfe}) i_{dr} - (i_{ds} - i_{dfe}) i_{qr}\} \right\} \right. \\
&\quad \left. - \frac{1}{L_{\sigma r}} \{V_{qr} - R_r i_{qr} + \omega_r \hat{L}_{m2} i_{ds} - (\omega_s L_{\sigma r} - \omega_r L_r) i_{dr} - R_{fe} i_{qfe} - \omega_r \hat{L}_{m2} i_{dfe}\} + \right. \\
&\quad \left. \frac{3P^2 \hat{L}_{m1} (i_{ds} - i_{dfe}) e_\omega}{2J} \right] + e_{L2} \left\{ \frac{1}{L_{\sigma r}} e_3 \omega_r i_{qs} - \frac{1}{L_{\sigma r}} e_3 \omega_r i_{qfe} - \frac{1}{L_{\sigma r}} e_4 \omega_r i_{ds} + \frac{1}{L_{\sigma r}} e_4 \omega_r i_{dfe} - \frac{\dot{\hat{L}}_{m2}}{\beta} \right\}
\end{aligned} \tag{4.67}$$

With the assumptions,

$$-k_3 e_3 = -\frac{1}{L_{\sigma r}} \left\{ V_{dr} - R_r i_{dr} - \omega_r \hat{L}_{m2} i_{qs} + (\omega_s L_{\sigma r} - \omega_r L_r) i_{qr} - R_{fe} i_{dfe} + \omega_r \hat{L}_{m2} i_{qfe} \right\} - \frac{3P^2 \hat{L}_{m1} (i_{qs} - i_{qfe}) e_\omega}{2J}; \quad (4.68)$$

$$\begin{aligned} -k_4 e_4 = & \frac{1}{(i_{ds} - i_{dfe})} \left\{ -\frac{PT_t e_\omega}{\hat{L}_{m1}^2 J^2} \{ (i_{qs} - i_{qfe}) i_{dr} - (i_{ds} - i_{dfe}) i_{qr} \} - \frac{2k_\omega^2 e_\omega}{3P^2 \hat{L}_{m1}} - \frac{k_\omega e_\omega^2}{J \hat{L}_{m1}^2} \{ (i_{qs} - i_{qfe}) i_{dr} - \right. \\ & \left. (i_{ds} - i_{dfe}) i_{qr} \} \right\} - \frac{1}{L_{\sigma r}} \left\{ V_{qr} - R_r i_{qr} + \omega_r \hat{L}_{m2} i_{ds} - (\omega_s L_{\sigma r} - \omega_r L_r) i_{dr} - R_{fe} i_{qfe} - \omega_r \hat{L}_{m2} i_{dfe} \right\} + \\ & \frac{3P^2 \hat{L}_{m1} (i_{ds} - i_{dfe}) e_\omega}{2J}; \end{aligned} \quad (4.69)$$

$$\frac{1}{L_{\sigma r}} e_3 \omega_r i_{qs} - \frac{1}{L_{\sigma r}} e_3 \omega_r i_{qfe} - \frac{1}{L_{\sigma r}} e_4 \omega_r i_{ds} + \frac{1}{L_{\sigma r}} e_4 \omega_r i_{dfe} - \frac{\dot{\hat{L}}_{m2}}{\beta} = 0;$$

Here, k_3 and k_4 are positive constants.

We obtain the control laws by utilizing (4.68) and (4.69).

$$V_{dr}^* = k_3 e_3 L_{\sigma r} + R_r i_{dr} + \omega_r \hat{L}_{m2} i_{qs} - (\omega_s L_{\sigma r} - \omega_r L_r) i_{qr} + R_{fe} i_{dfe} - \omega_r \hat{L}_{m2} i_{qfe} - \frac{3P^2 \hat{L}_{m1} L_{\sigma r} (i_{qs} - i_{qfe}) e_\omega}{2J} \quad (4.70)$$

$$\begin{aligned} V_{qr}^* = & k_4 e_4 L_{\sigma r} + \frac{L_{\sigma r}}{(i_{ds} - i_{dfe})} \left\{ -\frac{PT_t e_\omega}{\hat{L}_{m1}^2 J^2} \{ (i_{qs} - i_{qfe}) i_{dr} - (i_{ds} - i_{dfe}) i_{qr} \} - \frac{2k_\omega^2 e_\omega}{3P^2 \hat{L}_{m1}} - \frac{k_\omega e_\omega^2}{J \hat{L}_{m1}^2} \{ (i_{qs} - \right. \right. \\ & \left. \left. i_{qfe}) i_{dr} - (i_{ds} - i_{dfe}) i_{qr} \} \right\} + R_r i_{qr} - \omega_r \hat{L}_{m2} i_{ds} + (\omega_s L_{\sigma r} - \omega_r L_r) i_{dr} + R_{fe} i_{qfe} + \omega_r \hat{L}_{m2} i_{dfe} + \right. \\ & \left. \frac{3P^2 L_{\sigma r} \hat{L}_{m1} (i_{ds} - i_{dfe}) e_\omega}{2J} \right\} \end{aligned} \quad (4.71)$$

Hence, the derivative of final Lyapunov function can be expressed as (4.72) after replacing the terms V_{dr} and V_{qr} in (4.67) by utilizing (4.70) and (4.71).

$$\dot{V}_{Fp} = -k_\omega e_\omega^2 - k_3 e_3^2 - k_4 e_4^2 \quad (4.72)$$

When, $\dot{L}_{m2} = \beta \left(\frac{1}{L_{\sigma r}} e_3 \omega_r i_{qs} - \frac{1}{L_{\sigma r}} e_3 \omega_r i_{qfe} - \frac{1}{L_{\sigma r}} e_4 \omega_r i_{ds} + \frac{1}{L_{\sigma r}} e_4 \omega_r i_{dfe} \right) \quad (4.73)$

\dot{V}_{Fp} becomes a negative semi-definite function with positive feedback constants $k_\omega, k_3, k_4, \beta$. The magnetization inductance can be estimated from (4.73). Since the error variable e_{L2} is absent in (4.72), only the boundedness of the state variables is proven from the above derivation. The system is assumed to be autonomous. So, we can use LaSalle's theorem to check whether the equilibrium point is asymptotically stable.

Let us assume, $\dot{V}_{Fp} = 0$

Utilizing (4.72), we get, $e_\omega = 0, e_3 = 0, e_4 = 0$.

$$\therefore \dot{e}_3 = 0, \dot{e}_4 = 0.$$

Applying the control voltages from (4.70) and (4.71) into the state error equations of (4.50) and (4.51), we obtain

$$\begin{aligned} \dot{e}_3 &= -k_3 e_3 + e_{L2} (i_{qs} \omega_r^* - i_{qs} e_\omega - \omega_r^* i_{qfe} + e_\omega i_{qfe}) = -k_3 e_3 + e_{L2} (i_{qs} \omega_r^* - i_{qs} e_\omega - \omega_r^* i_{qfe} + \\ &\quad e_\omega i_{qfe}) \end{aligned} \quad (4.74)$$

$$\begin{aligned} \dot{e}_4 &= -k_4 e_4 + e_{L2} (i_{ds} \omega_r^* - i_{ds} e_\omega - \omega_r^* i_{dfe} + e_\omega i_{dfe}) = -k_4 e_4 + e_{L2} (i_{ds} \omega_r^* - i_{ds} e_\omega - \omega_r^* i_{dfe} + \\ &\quad e_\omega i_{dfe}) \end{aligned} \quad (4.75)$$

Applying $e_\omega = 0, e_3 = 0, e_4 = 0$ in (4.74) and (4.75), it is found that $e_{L2} = 0$, under the conditions of $i_{ds} \neq i_{dfe}$ and $i_{qs} \neq i_{qfe}$. On the contrary, by plugging the error variable values in (4.64), no decision can be made about the convergence of the error variable e_{L1} .

Therefore, it can be concluded that the equilibrium point $(e_\omega, e_3, e_4, e_{L2}) = 0$ is globally asymptotically stable. Also, the estimated magnetization inductance \hat{L}_{m2} will converge to the rated value. Hence, by utilizing the adaptive backstepping based nonlinear control, the stability of the rotor converter control loop is achieved. The equation for the estimation of the magnetization inductance is also obtained from it.

4.5 Development of Loss Minimization Algorithm

The loss minimization algorithm for the proposed DFIG is evaluated based on stator voltage oriented control scheme, i.e. $v_{qs}=0$. At steady-state, d-q axis iron loss current components can be derived from Figs. 4.1(a) and 4.1(b) as,

$$i_{dfe} = \frac{\omega_s L_m}{R_{fe}} (i_{dm} - i_{qm}) \quad (4.76)$$

$$i_{qfe} = \frac{\omega_s L_m}{R_{fe}} (i_{dm} + i_{qm}) \quad (4.77)$$

Again, the d-q axis stator voltage components can be written as,

$$i_{ds} = \frac{V_s - \omega_s L_m i_{dm}}{R_s} \quad (4.78)$$

$$i_{qs} = -\frac{\omega_s L_m i_{qm}}{R_s} \quad (4.79)$$

$$i_{qr} = (1 + \frac{2s\omega_s L_m}{R_{fe}}) i_{qm} + \frac{s\omega_s L_m i_{dm}}{R_s} \quad (4.80)$$

$$i_{dm} = i_{qm} - \frac{R_{fe} i_{qfe}}{\omega_s L_m} \quad (4.81)$$

By utilizing (4.9)-(4.12) and (4.78)-(4.81) and performing the differentiation, it can be shown

$$\frac{di_{ds}}{di_{dr}} = -\frac{\omega_s L_m}{R_s} \frac{di_{dm}}{di_{dr}} \quad (4.82)$$

$$\frac{di_{qs}}{di_{dr}} = -\frac{\omega_s L_m}{R_s} \frac{di_{qm}}{di_{dr}} \quad (4.83)$$

$$\frac{di_{qr}}{di_{dr}} = \left(1 + \frac{2s\omega_s L_m}{R_{fe}}\right) \frac{di_{qm}}{di_{dr}} + \frac{s\omega_s L_m}{R_{fe}} \frac{di_{dm}}{di_{dr}} \quad (4.84)$$

$$\frac{di_{dfe}}{di_{dr}} = 1 + \left(\frac{\omega_s L_m}{R_s} - 1\right) \frac{di_{dm}}{di_{dr}} \quad (4.85)$$

$$\frac{di_{qfe}}{di_{dr}} = 1 + \left(\frac{\omega_s L_m}{R_s} - 1\right) \frac{di_{dm}}{di_{dr}} \quad (4.86)$$

$$\frac{di_{qfe}}{di_{dr}} = \frac{\omega_s L_m}{R_{fe}} \frac{di_{dm}}{di_{dr}} + \left(\frac{2\omega_s L_m}{R_{fe}} - \frac{\omega_s L_m}{R_s}\right) \frac{di_{qm}}{di_{dr}} \quad (4.87)$$

$$\frac{di_{qm}}{di_{dr}} = \left(\frac{2R_s}{R_{fe}-R_s}\right) \frac{di_{dm}}{di_{dr}} \quad (4.88)$$

From the estimated value of medium power DFIGs, we can assume, $R_{fe} \gg \omega_s L_m$ [93]. Thus the following equation can be derived:

$$\frac{di_{dm}}{di_{dr}} = \frac{R_s}{R_s + \omega_s L_m} \quad (4.89)$$

The overall resistive power loss in DFIG is defined as,

$$P_{loss} = R_s(i_{ds}^2 + i_{qs}^2) + R_r(i_{dr}^2 + i_{qr}^2) + R_{fe}(i_{dfe}^2 + i_{qfe}^2) \quad (4.90)$$

Loss will be minimized when, $\frac{dP_{loss}}{di_{dr}} = 0$

$$R_s \left(i_{ds} \frac{di_{ds}}{di_{dr}} + i_{qs} \frac{di_{qs}}{di_{dr}} \right) + R_r \left(i_{dr} + i_{qr} \frac{di_{qr}}{di_{dr}} \right) + R_{fe} \left(i_{dfe} \frac{di_{dfe}}{di_{dr}} + i_{qfe} \frac{di_{qfe}}{di_{dr}} \right) = 0 \quad (4.91)$$

By replacing the machine parameter terms with constants

$$\frac{di_{dm}}{di_{dr}} = \frac{R_s}{R_s + \omega_s L_m} = A, \frac{s\omega_s L_m}{R_{fe}} = B, \frac{\omega_s L_m}{R_s} = C, \frac{2R_s}{R_{fe}-R_s} = D$$

Equation (4.91) can be simplified as,

$$\begin{aligned}
& R_s(-CAi_{ds} - CDAi_{qs}) + R_r \left(i_{dr} + i_{qr}((1+2B)DA + BA) \right) + R_{fe} \left(\left(i_{ds} + i_{dr} - \frac{R_s i_{dr} - V_s}{R_s + \omega_s L_m} \right) \{(C-1)A + 1\} + \right. \\
& \quad \left. \left\{ \left(\frac{C}{1+C} \right) i_{qs} + i_{qr} \right\} \{BA + 2B - C\} DA \right) = 0 \\
\Rightarrow & R_r i_{dr} + R_{fe} \left(i_{dr} - \frac{R_s i_{dr}}{R_s + \omega_s L_m} \right) \{(C-1)A + 1\} = CAR_s(i_{ds} + Di_{qs}) - R_r i_{qr} \{(1+2B)DA + BA\} - \\
& R_{fe} \left(i_{ds} + \frac{V_s}{R_s + \omega_s L_m} \right) \{(C-1)A + 1\} - R_{fe} \left[\left\{ \left(\frac{C}{1+C} \right) i_{qs} + i_{qr} \right\} \{BA + 2B - C\} DA \right] \quad (4.92)
\end{aligned}$$

Finally, (4.80) provides the reference d-axis rotor current for loss reduction model in the following form:

$$\begin{aligned}
i_{dr}^* = & \\
& \frac{CAR_s(i_{ds} + Di_{qs}) - R_r i_{qr} \{(1+2B)DA + BA\} - R_{fe} \left(i_{ds} + \frac{V_s}{R_s + \omega_s L_m} \right) \{(C-1)A + 1\} - R_{fe} \left[\left\{ \left(\frac{C}{1+C} \right) i_{qs} + i_{qr} \right\} \{BA + 2B - C\} DA \right]}{R_r + R_{fe} \{(C-1)A + 1\} \left(1 - \frac{R_s}{R_s + \omega_s L_m} \right)} \quad (4.93)
\end{aligned}$$

The control signal i_{dr}^* is dependent on d-q axis stator current, q axis rotor current component, supply voltage and frequency which can be obtained from current, voltage and speed sensors. Here,

$$\begin{aligned}
(C-1)A + 1 &= \frac{\omega_s L_m - R_s}{\omega_s L_m + R_s} + 1 > 1; \\
1 - \frac{R_s}{R_s + \omega_s L_m} &> 0; \\
R_{fe}, R_r &> 0
\end{aligned}$$

Hence, the denominator of (4.93) is always greater than zero and the reference d-axis rotor current will never become undefined. The machine ratings and adaptation rules provide the required resistance, inductance and constant parameters. The inclusion of iron loss component in the proposed controller ensures precision in the loss reduction model.

4.6 Simulation Results

The performance of the proposed nonlinear controller integrated with machine loss reduction for DFIG based WECS is investigated in simulation at different operating conditions with MATLAB/Simulink model. The nonlinear controllers are designed to force the error function of the state variables to null point and thus, stabilize the machine about the desired equilibrium state. The simulation results of the proposed controller are compared with the conventional PI controlled converter operation in DFIG-WECS. The simulation parameters of the designed controllers are presented in Table 4.1. The simulation block diagram of the proposed scheme is shown in appendix.

Table 4. 1 Simulation parameters for PI and nonlinear controller

PI Controller Parameters	Simulation data	Nonlinear Controller Parameters	Simulation data
$K_{p,vbus}, K_{i,vbus}$	$-10^4, -3 \times 10^4$	k_1, k_2	200, 200
$K_{p,idr}, K_{i,idr}$	$8920, 1.3 \times 10^4$	k_3, k_4	20, 30
$K_{p,iqr}, K_{i,iqr}$	$8920, 1.3 \times 10^4$	k_ω	500
$K_{p,idc}, K_{i,idc}$	0.03, 0.3	β	3.2×10^{-12}
$K_{p,iqc}, K_{i,iqc}$	0.0289, 0.33	k_{vdc}	200

4.6.1 Rotor Side Converter (RSC) Control Performance

The rotor side converter control is used to track the reference rotor speed generated by the MPPT controller, and to follow the reference d-axis rotor current. The RSC control block produces control voltages (V_{dr}^* and V_{qr}^*) according to (4.70) and (4.71). Pulse width modulation block generates the pulses for the RSC by utilizing the reference control voltages. The performance of the proposed nonlinear controller for RSC control is compared with the traditional PI controller and displayed in Fig. 4.3(b-d). It is evident from these figures that the rotor speed error exhibit less fluctuation for the proposed nonlinear controller as compared to the PI controller. For d-q axis rotor current errors, it is

found that both controllers perform equally. However, the current errors from the PI controller are less than its counterpart at certain patches. By following the reference speed produced by the MPPT controller, the proposed controller ensures maximum power extraction from the wind turbine.

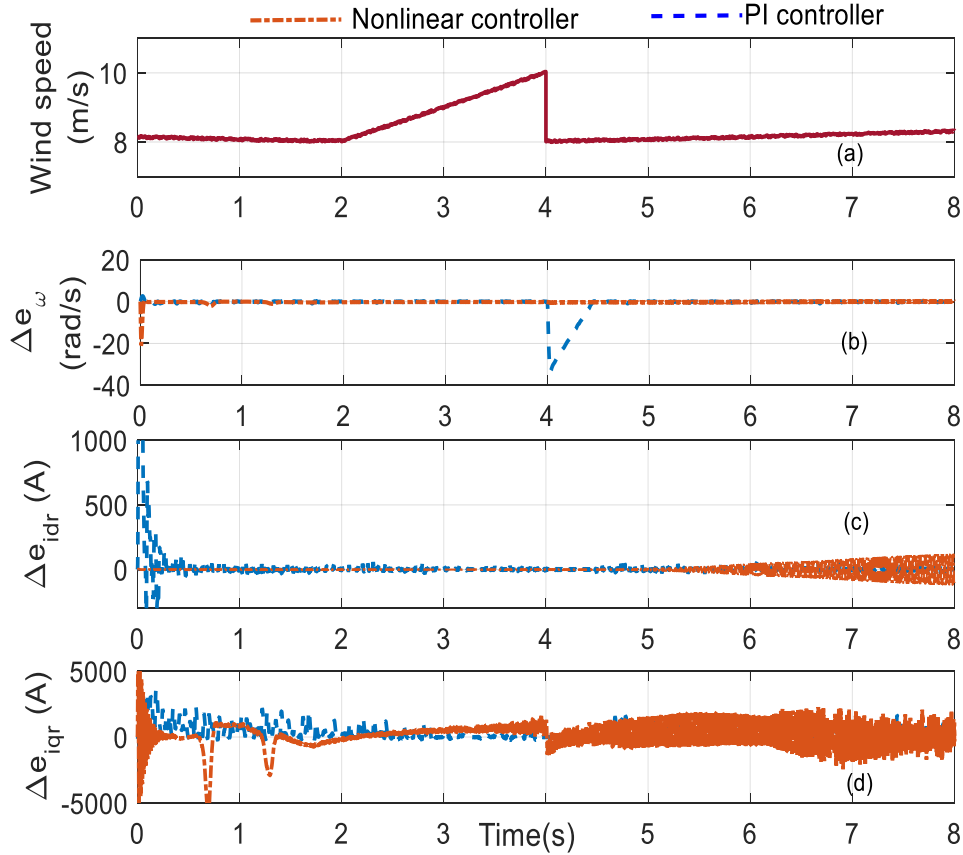


Fig. 4.3. Comparative simulation results between PI controller and the proposed nonlinear controller for RSC control of DFIG under variable wind speed: (a) Variation in wind speed, (b) Rotor speed error, (c) d-axis rotor current error, (d) q-axis rotor current error.

4.6.2 Grid Side Converter (GSC) Control Performance

The target of the grid side converter control is to regulate the DC-link voltage. The controller forces the error function (e_1 and e_2) to converge to zero. Fig. 4.4 displays the comparative analysis between the nonlinear controller and PI controller based GSC control operation. The figure shows that the dc-link voltage error is asymptotically diminished when the actual dc-link voltage approaches the

reference value. The converter current error functions depict better asymptotic convergence for the proposed controller compared to the PI counterpart. The average power associated with grid side converter is approximately 0.9 MW. The proposed controller stabilizes the grid side converter output by nullifying the grid converter current errors.

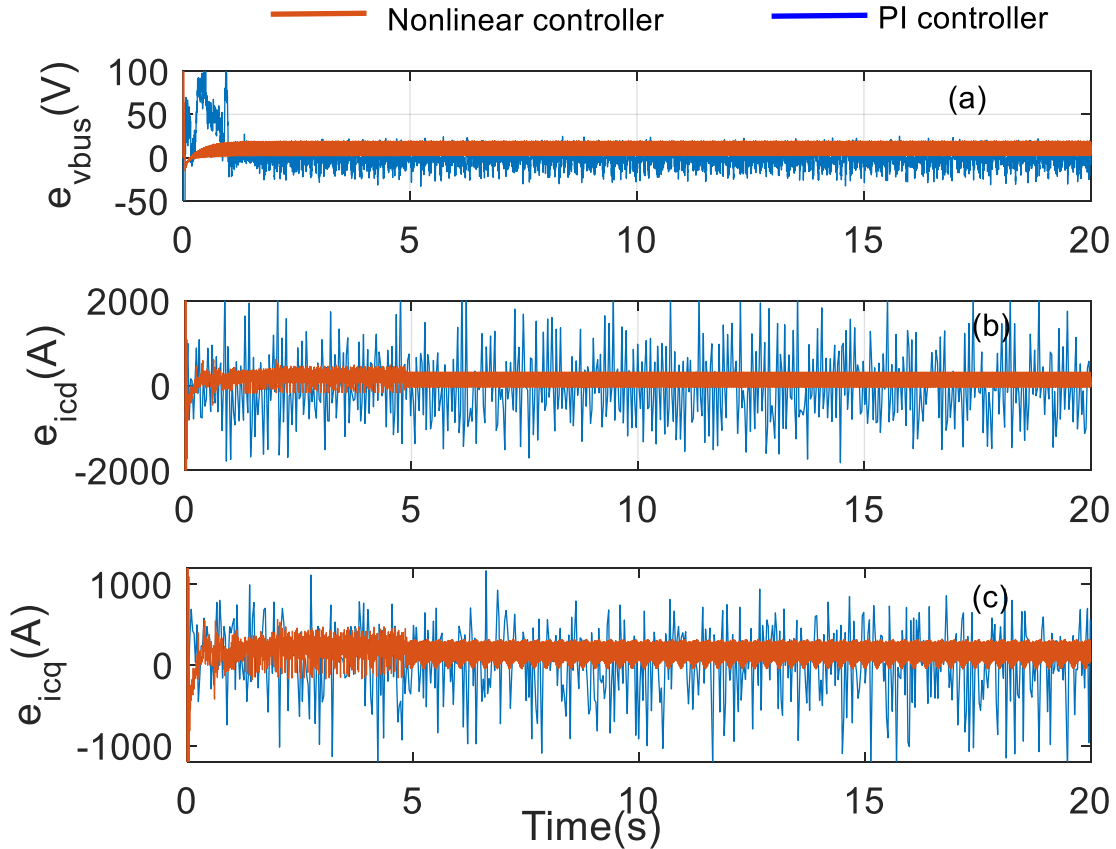


Fig. 4.4. Comparative simulation results between PI controller and proposed nonlinear controller for GSC control of DFIG under variable wind speed: (a) dc-link voltage error , (b) d-axis grid converter current error , (c) q-axis grid converter current error .

To design the RSC and GSC control, the constants $k_1, k_2, k_3, k_4, k_{\omega}, \beta$ and γ are deliberately chosen as shown in Table 4.2 to ensure that the desired error function remains under control. Fig. 4.5 exhibits the comparative analysis between the virtual control inputs for the proposed nonlinear control and conventional PI control of the RSC and GSC. Figs. 4.5(a) and 4.5(b) show the d-q axis rotor control voltages for nonlinear and PI controlled rotor side converter, respectively. The variation of q-axis rotor

control voltage (V_{qr}^*) is affected by the change of wind speed and corresponding generator torque whereas, the reference d-axis rotor current enforce the alteration of d-axis rotor control voltage (V_{dr}^*). Figs. 4.5(c) and 4.5(d) depict the d-q axis virtual control voltages for GSC for the proposed nonlinear and PI controller, respectively. The nonlinear controlled system differs from the PI controlled counterpart in terms of three reference parameters, e.g. $V_{bus,ref}$, i_{qr}^* and i_{dc}^* . In PI controlled system, the dc-link reference voltage is stabilized at 1200 volt whereas it is determined by (4.30) in nonlinear control. Similarly, the q-axis rotor reference current can be obtained according to $i_{qr}^* = \frac{T_{em}}{-1.5P\frac{L_m}{L_s}|\psi_s|}$ for PI control while (4.65) provides i_{qr}^* for nonlinear control. The adaptive backstepping based nonlinear controller has high gain values. Due to the effect of all these factors, the control input voltages of PI controlled DFIG-WECS differ from the adaptive backstepping based nonlinear controlled module for both the grid-side and rotor-side converters as shown in Fig. 4.5.

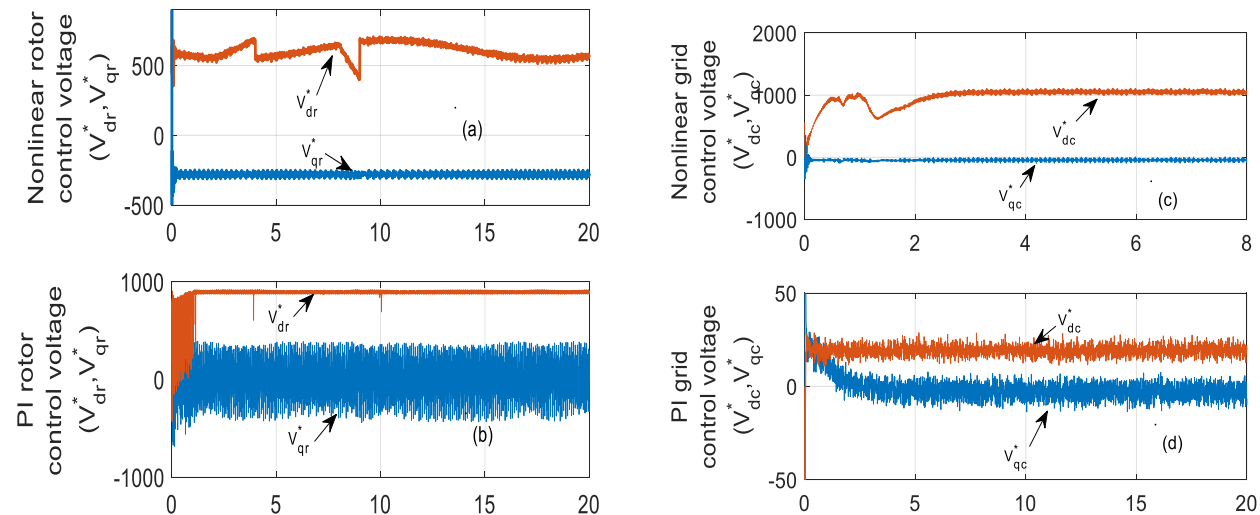


Fig. 4.5. Control input performance comparison between the proposed nonlinear controller and PI controller for GSC and RSC control under variable wind speed: (a) Nonlinear rotor control voltages (Volt), (b) PI controlled rotor control voltages for RSC, (c) Nonlinear grid converter control voltages, (d) Control voltages for grid side converter under PI control .

In nonlinear controller, the control voltages are converted to reference v_a^*, v_b^*, v_c^* voltages by using dq-

abc transformation and then normalized by $\frac{V_{bus}}{2}$. The three phase reference voltages will then be utilized to generate the PWM signal for the converter.

One of the typical sources of instability which might unsettle a grid-connected system is grid voltage fluctuation. Distortion at grid side can be originated from the addition of reactive power compensation equipment, nonlinear load condition or by sudden phase voltage failure. A nonlinear controller at the machine side is the appropriate option to handle the grid voltage fluctuation which prevents the machine from running into the failure zone. Fig. 4.6 illustrates the ability of the proposed nonlinear system to settle down if the DFIG undergoes any abnormality at grid voltage. The system is simulated for a 10% rise and dip in grid voltage in between of t=2 to 2.5 sec (Fig. 4.6(a),(d)). It is observed that the DFIG rotor speed varies very little (Fig. 4.6(b)) and stator power (Fig. 4.6(c)) follows the change of grid voltage after transitory fluctuation.

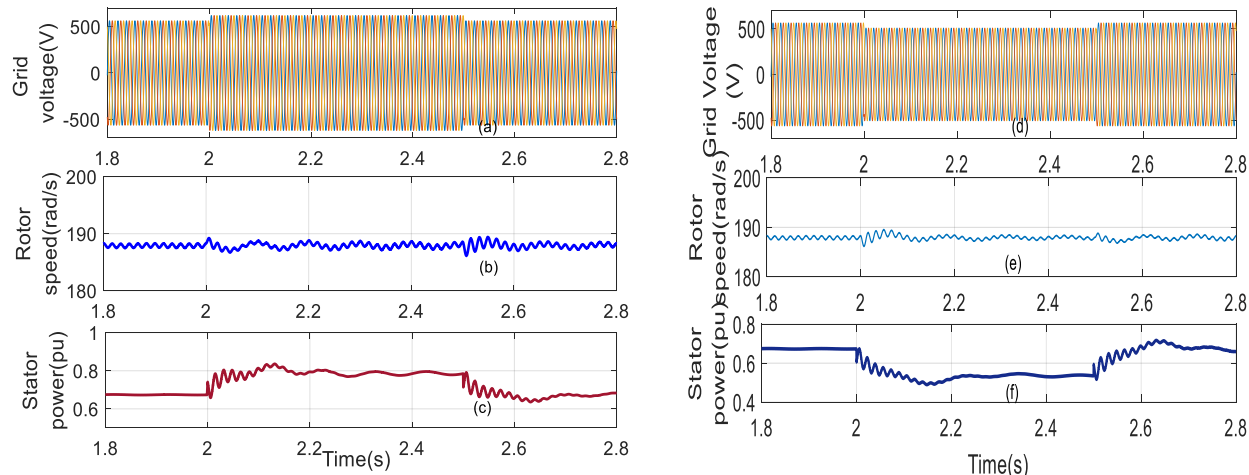


Fig. 4.6. Generator output performance for a momentary change in grid voltage for wind speed of 10 m/s: (a) 10% increase in grid voltage between t=2 to 2.5 sec, (b) Corresponding change in rotor speed , (c) Stator power output in p.u., (d) 10% dip in grid voltage between t=2 to 2.5 sec, (e) Corresponding change in rotor speed , (f) Stator power output in p.u.

The variation in rotor speed is negligible (Fig. 4.6(e)) and stator power (Fig. 4.6(f)) decreases due to the symmetric voltage dip at the grid end. This simulation is performed by adjusting the

reference rotor speed to the synchronous speed. However, the performance of the nonlinear controller, during symmetric and asymmetric grid voltage dip, needs to be investigated thoroughly by analyzing its effect on dc-link voltage, rotor side current and voltages which hasn't been done in this chapter.

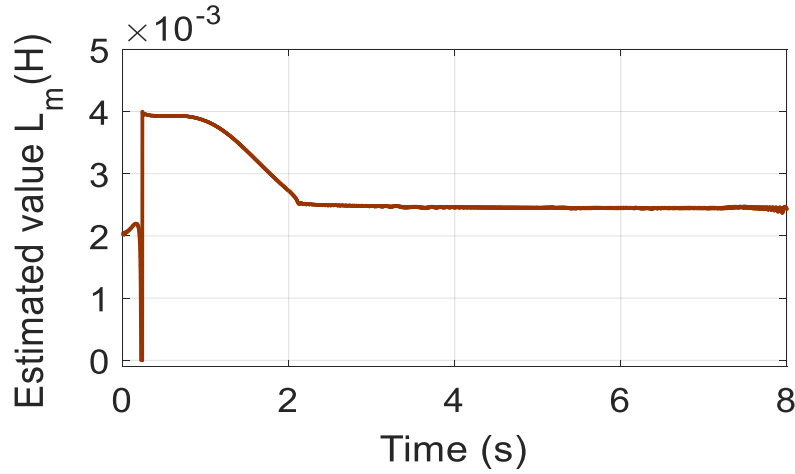


Fig. 4.7. Performance of the online parameter estimation Estimated value of magnetizing inductance under rated condition

The parameter update law provides the estimated value of magnetizing inductance. Fig. 4.7 demonstrates the estimated value of the parameter under rated condition. The figure is obtained by using (4.73). The magnetizing inductance stabilizes very close to the nominal value, $L_m=2.5$ mH. Finally, the loss minimization block is activated to reduce the total power loss of the machine. Fig. 4.8 illustrates the performance of the loss reduction scheme. The d-axis rotor reference current is executed to abate the loss amount. It is perceived that average machine loss is reduced by 1.7% in reference to its initial value after the loss minimization algorithm is activated. Considering the power rating of the DFIG, the loss reduction by the proposed model will be 0.01% which is comparatively small for commercial wind power system. The changes in reference rotor currents are shown in Figs. 4.8(b) and 4.8(c) to illustrate the effect of the activation of the loss reduction block. The wind speed is varied to observe the performance of the loss reduction block at a variable rotor speed. Fig. 4.8(d) illustrates the

efficacy of the loss minimization scheme while the performance is compared without activating the loss minimization block for different rotor speeds of DFIG.

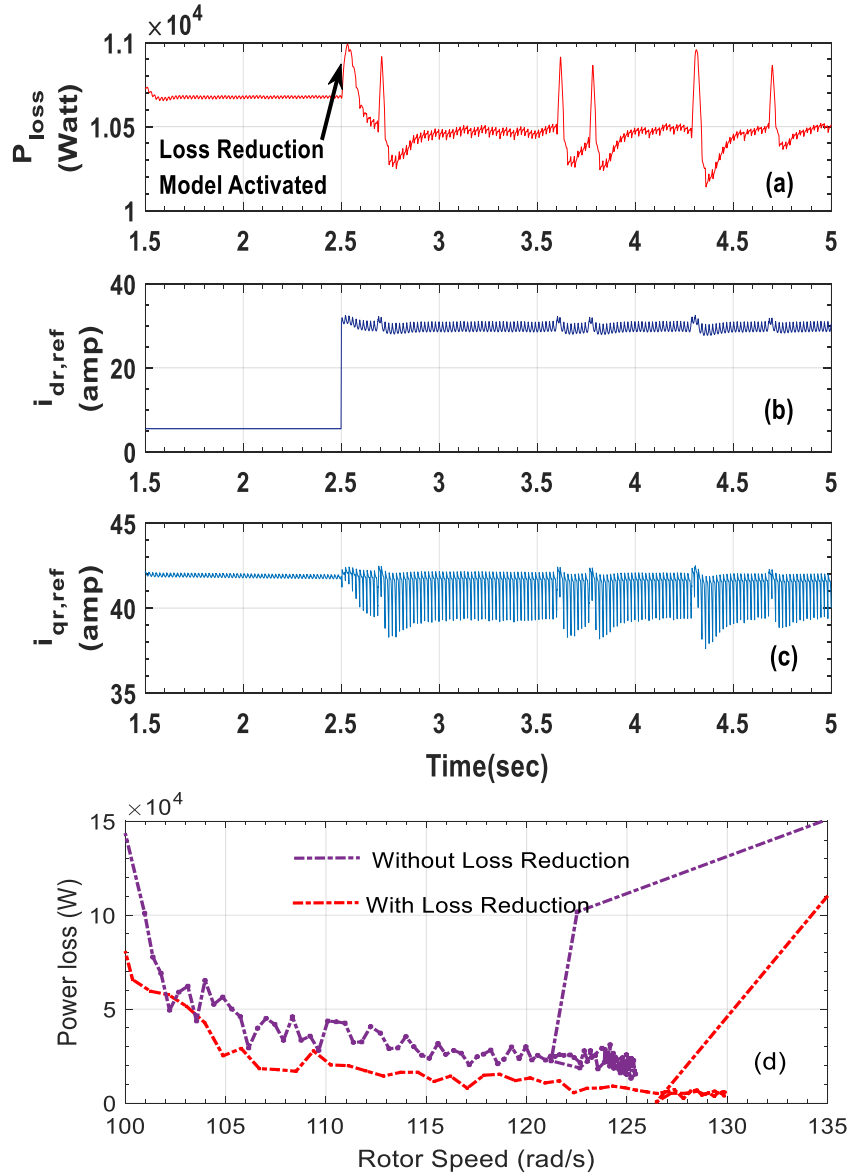


Fig. 4.8. Effect of machine loss minimization scheme: (a) Overall machine loss when loss reduction model is activated at $t=2.5$ sec, (b) Corresponding change in reference d-axis rotor current, (c) Reference q-axis rotor current, (d) Power loss comparison with and without activation of the loss reduction model for variable rotor speed.

It is observed that the power loss reduction model works effectively for the entire range of speed variation and thus it yields power savings and economic operation of the DFIG-driven WECS.

The core loss in a generator is almost constant with fixed stator flux whereas the copper losses may vary under variable load or grid demand condition. The variation in rotor speed and temperature can affect the rotor resistance and any change in rotor resistance will reflect proportionally to machine power loss. Hence, machine loss minimization models are sensitive to the variation in rotor resistance. In this thesis, the rotor resistance is assumed to be constant. However, to verify the rotor winding resistance sensitivity on the loss reduction model, simulation is performed with the loss reduction block for step change of rotor resistance. Fig. 4.9 demonstrates the effectiveness of loss reduction model for the variation of rotor winding resistance.

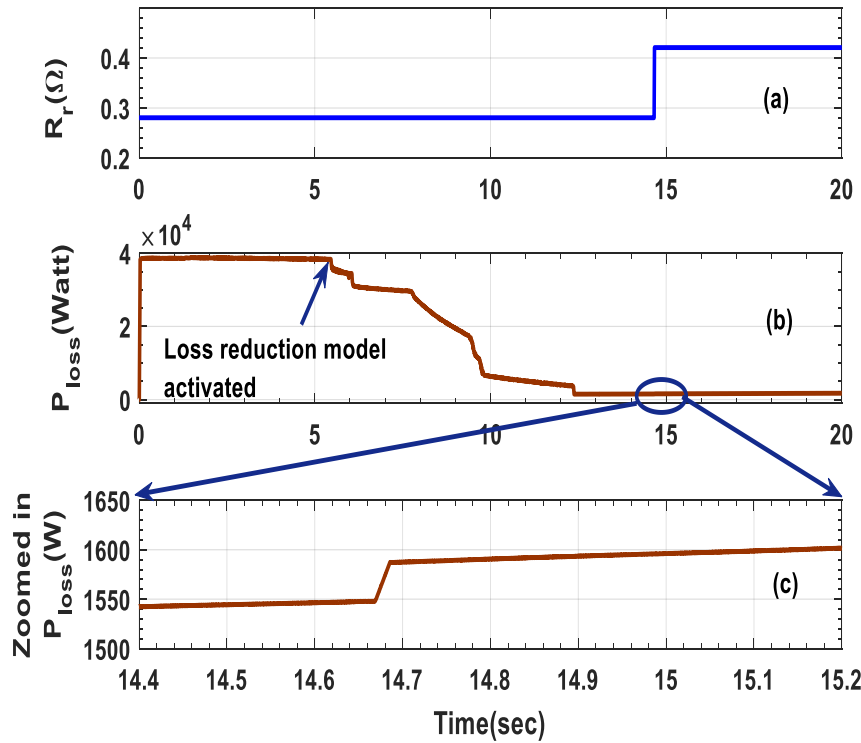


Fig. 4.9. Parameter sensitivity analysis for proposed loss minimization scheme: (a) Increment of rotor resistance by 50% during simulation at $t=14.65$ sec, (b) Overall machine loss when loss reduction model is activated at $t=5.5$ sec, (c) Zoomed-in view for power loss at the instant of the change in rotor resistance.

It is observed from Fig. 4.9(b) that when the loss reduction model is activated at $t=5$ sec, the power loss reduces significantly and settles after 12.5 sec. The rotor resistance is increased by 50% of

its rated value at $t=14.65$ sec (Fig. 4.9(a)), but the increase in corresponding power loss is very insignificant. To clarify the result, the zoom-in view of Fig. 4.9(b) is plotted in Fig. 4.9(c)).

4.7 Real-Time Implementation and Results

A prototype for the proposed nonlinear controller based DFIG-WECS is built to observe the performance of the proposed WECS in real-time. Fig. 4.10 illustrates the variation of wind speed and the power generated by the machine (Fig. 4.10(a)-(b)). The wind speed is emulated to vary in between 3.2 m/s to 9.4 m/s. The constant TSR based MPPT controller provides the rotor reference speed for the controller and the DFIG reacts accordingly to follow the speed. Backstepping based nonlinear control algorithm is applied to obtain the control voltages.

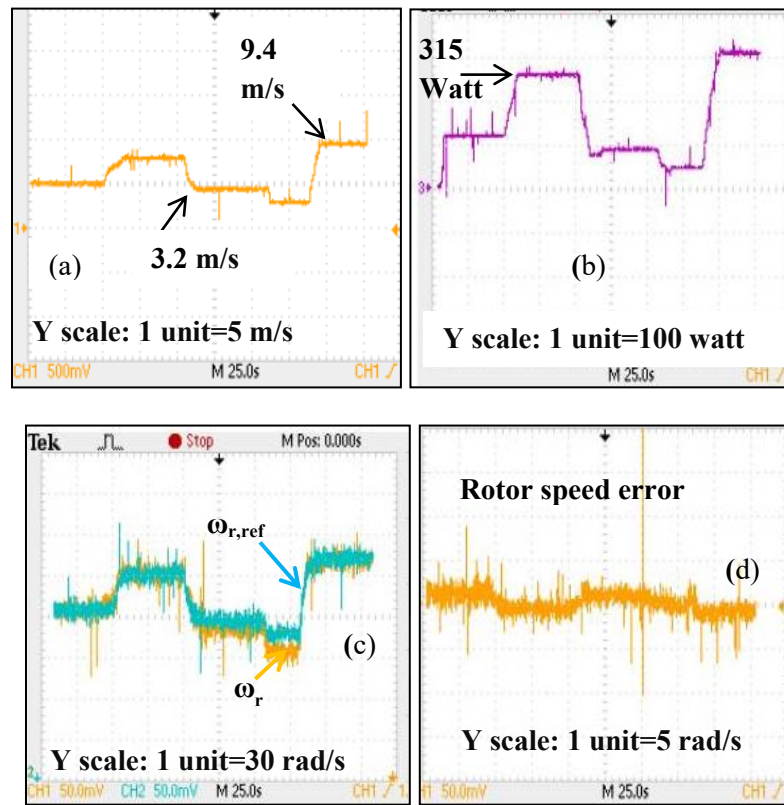


Fig. 4.10. Experimental performance of the proposed nonlinear controller based DFIG-WECS: (a) variation in wind speed generated by the turbine emulator (b) Corresponding power produced by the DFIG, (c) reference speed generation, and (d) rotor speed error.

The value of the magnetization inductance of the machine is collected from the machine specification. The parameter update rule is avoided in the implementation to avoid design complexity. The core resistance is determined from the no-load test. At low power, the rotor speed can't track the reference speed properly due to saturation of d-axis rotor current component. Overall the controller ensures the maximum power extraction by minimizing the rotor speed error under variable wind speed as demonstrated in Fig. 4.10 (c) & (d). The graphs suggest that the proposed nonlinear controller is capable of minimizing the speed error under variable wind speed. The performance of the nonlinear controller depends on the elimination of d-q axis current error functions. Fig. 4.11 demonstrates the performance of the nonlinear controller designed for the rotor side converter.

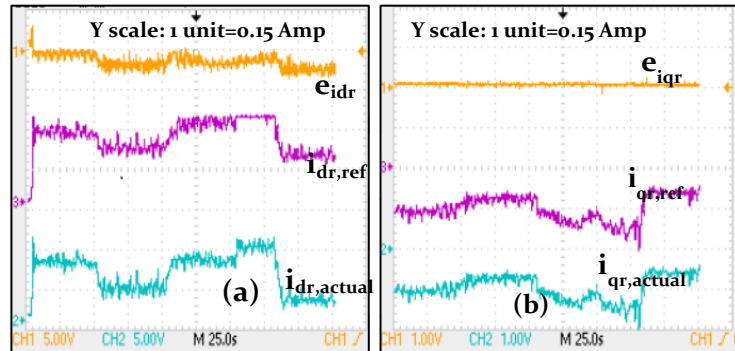


Fig. 4.11. Experimental performance of the proposed nonlinear controller based RSC of DFIG: (a) d-axis rotor currents and errors,(b) q-axis rotor currents and error dynamics under varying wind speed.

The d and q –axis machine rotor currents follow the reference values competently while the wind speed is varied according to the wind profile displayed in Fig. 4.10(a). The d-axis rotor current error fluctuates around zero axis (Fig. 4.11(a)) whereas the q-axis rotor current is precisely nullified by the controller action (Fig. 4.11(b)). There are few instants where the tracking isn't exact. This occurs due to the saturation of the current controllers.

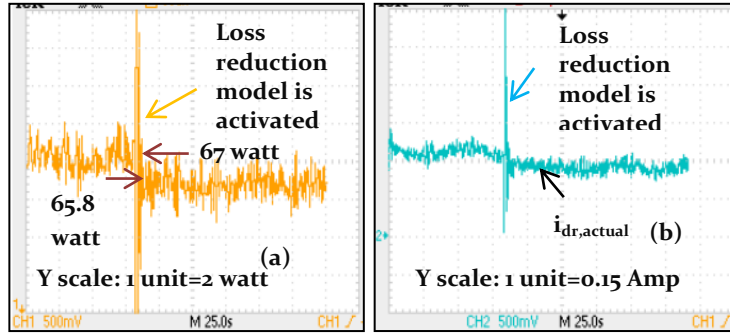


Fig. 4.12. Experimental performance of the machine loss reduction model (a)Total power loss before and after the activation of loss reduction algorithm, (b) Corresponding change in d-axis rotor current of DFIG.

Fig. 4.12 demonstrates the performance of the proposed machine loss reduction algorithm developed for the doubly-fed machine. After the activation of the loss reduction algorithm, the average estimated total core and copper power loss of the machine is reduced by 1.8% with respect to its initial value for input torque of 0.9 Nm as shown in Fig. 4.12(a). The efficiency improvement of the loss reduction block is 0.34% at the rated condition with respect to the power rating of DFIG. The variation in d-axis rotor current is caused by the change of the corresponding reference current to reduce the machine losses (Fig. 4.12(b)). The successful implementation of loss reduction block ensures enhanced efficiency of the overall DFIG-WECS up to a certain extent.

4.8 Summary

The state space model of a DFIG has been developed incorporating iron loss component in the design. The nonlinear control scheme utilizes Lyapunov theorem based control for the grid side controller and adaptive backstepping based nonlinear control algorithm to generate the control voltages for rotor side converter. The proposed controller guarantees the convergence of error functions to the null point and affirms maximum power extraction through reference rotor speed tracking. Considering the uncertainty of magnetizing inductance under dynamic operating condition, the estimation model of the parameter is also formulated. Furthermore, a loss minimization algorithm incorporating iron loss

has been devised to achieve improved efficiency. The performance of the proposed DFIG based WECS has been tested and compared with the benchmark tuned PI controller under different operating conditions such as variable wind speed, grid voltage disturbance, and parameter uncertainties. The simulation and experiment results demonstrate that the proposed control scheme exhibits better grip over the state variables compared to the conventional PI controller by diminishing the error function while the turbine experiences intermittent wind speed fluctuations. However, the speed and current tracking aren't accurate when generator current goes into saturation. The proficiency of the proposed loss reduction model is also verified by the experimental model. In the next chapter, in order to take the advantages of intelligent algorithms and to overcome the disadvantages of conventional PI and nonlinear controllers, an ANFIS based NFC is developed to control the DFIG-WECS.

Chapter 5

ANFIS based Control of DFIG-WECS in Grid Connected Mode

In grid connected mode, a DFIG is expected to operate at optimum speed to deliver maximum output power in the grid while the voltage, frequency and harmonic regulations need to be fulfilled. Intelligent control techniques, such as adaptive fuzzy control [56], dynamic Q-learning based fuzzy control [124], brain emotional learning based intelligent control [125], energy function based optimal control [51] have been studied in literature. Neural network (NN), neuro-fuzzy (NF) or adaptive network-based fuzzy inference system based control have not been thoroughly investigated for online control of grid-connected DFIG. Adaptive neuro-fuzzy inference system (ANFIS) provides adaptability on choosing the membership functions and fast convergence due to its hybrid learning. Moreover, ANFIS architecture has the distinguishing feature of modeling a highly nonlinear system, as it combines the competence of fuzzy reasoning in handling uncertainties and learning aptitude of neural network from complex system. Therefore, an ANFIS based NFC controller is designed for converter control for real and reactive power control of DFIG-WECS.

5.1 Description of the ANFIS Based Control Operation

For the control operation of DFIG based WECS, few researches have been conducted on designing controller to control the converters by utilizing fuzzy logic and artificial neural network algorithms. ANFIS can be considered as an intelligent and powerful processing tool for pattern recognition and controller design because it combines the advantages of both the fuzzy logic and neural network algorithms. The following subsections illustrate the structure of ANFIS network and demonstrate the ANFIS based controller configuration of the DFIG-WECS primarily linked with grid.

5.1.1 ANFIS Network

Adaptive neuro-fuzzy inference system consists of a fuzzy inference system whose membership functions can be reconstructed by using an authentic input-output data set. The parameters associated with the membership functions are obtained by gradient descent algorithm. When the gradient vector is determined, it utilizes one of its optimization techniques to adjust the parameters to reduce the error function. This error function is usually defined by the sum of the squared difference between measured and reference outputs. ANFIS networks usually utilize a combination of least squares estimation and back propagation for membership function parameter estimation. The details of ANFIS structure can be found in [95, 96]. Fig. 5.1 illustrates a generalized configuration of ANFIS network.

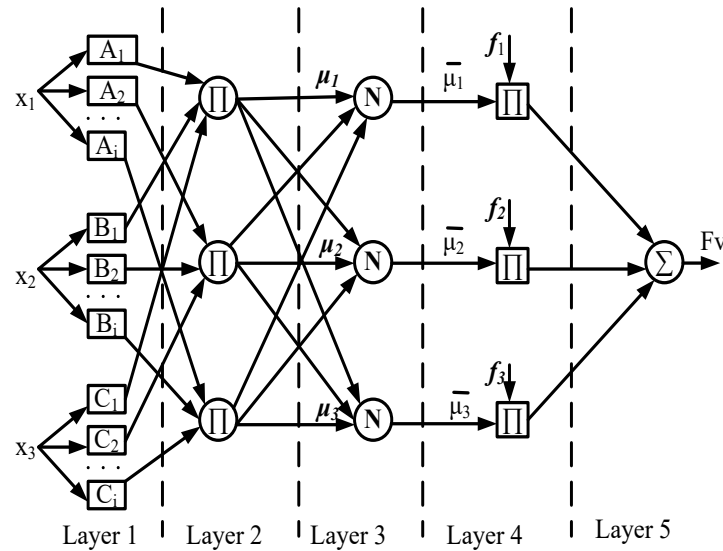


Fig. 5.1. Schematic of typical ANFIS architecture.

In the proposed controller, an online self-tuning algorithm is developed to adjust the precondition and consequent parameter of the ANFIS structure. The Takagi-Sugeno-Kang (TSK) fuzzy rule-based control system is utilized for accuracy and it has linear defuzzification rule. The node functions of each layer are described as follows.

Layer 1: The first layer is also known as the fuzzification layer, a number of membership functions are assigned to each input. Only one input is used in this layer for the proposed DFIG based WECS which is the normalized error function of bus voltage (V_{bus}), rotor speed (ω_r) or reactive power (Q_s) based on the converter control. The membership functions are defined in this stage. For simplicity of the control action, only triangular and trapezoidal membership functions are used (Fig. 5.2).

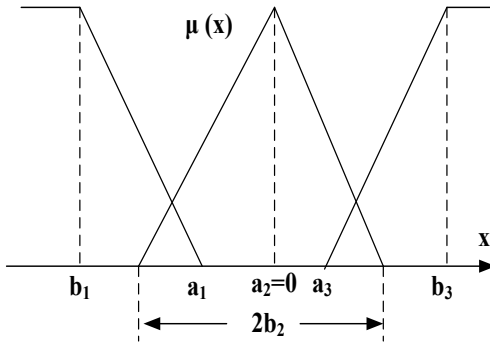


Fig. 5.2. Membership function for input data x .

The corresponding node equations are given as:

$$\mu_{A1}^1(x) = \begin{cases} 1, & x \leq b_1 \\ \frac{x-a_1}{b_1-a_1}, & b_1 < x < a_1 \\ 0, & x \geq a_1 \end{cases} \quad (5.1)$$

$$\mu_{A2}^2(x) = \begin{cases} 0, & |x| \geq b_2 \\ 1 + \frac{x-a_2}{a_2+b_2}, & x > -b_2 \\ 1 + \frac{x-a_2}{a_2-b_2}, & x < b_2 \end{cases} \quad (5.2)$$

$$\mu_{A3}^3(x) = \begin{cases} 0, & x \leq a_3 \\ \frac{x-a_3}{b_3-a_3}, & a_3 < x < b_3 \\ 1, & x \geq b_3 \end{cases} \quad (5.3)$$

where, x is the input for the layer, a_1, b_1, a_2, b_2, a_3 and b_3 are the parameters defined in the corresponding membership function which needs to be tuned during control action. For control purposes, the value of a_2 is chosen as zero.

Layer 2: In this layer, each node multiplies the entering signals and directs the output to the next level that represents the individual firing strength μ_i of a rule.

$$\mu_i = \mu_{A1}^i(x)\mu_{A2}^i(x)\mu_{A3}^i(x) \quad (5.4)$$

For the proposed controller only one input is chosen. So, the second layer can be ignored and the output of first layer goes to the third layer.

$$\mu_1 = \mu_{A1}^1(x), \mu_2 = \mu_{A2}^2(x), \mu_3 = \mu_{A3}^3(x) \quad (5.5)$$

Layer 3: Each block in the third layer which is also known as normalization stage, estimates the proportion of the i -th rule firing strength ($\bar{\mu}_i$) to the sum of the firing strength of all rules.

$$\bar{\mu}_i = \frac{\mu_i}{\mu_1 + \mu_2 + \mu_3} \quad (5.6)$$

Layer 4: In this layer, the function, f_i is calculated as the linear activation function. A single input first order Sugeno fuzzy model is utilized in this model.

$$f_i = \beta_0^i + \beta_1^i x, i=1,2,3 \quad (5.7)$$

In this stage, the parameters β_0, β_1 are tuned based on the operating condition of DFIG. These parameters are known as consequent parameters.

Layer 5: The final layer is the output layer which computes the overall output by combining the incoming data.

$$F_v = \bar{\mu}_1 f_1 + \bar{\mu}_2 f_2 + \bar{\mu}_3 f_3 \quad (5.8)$$

The outputs of the ANFIS controller are i_{dr}^* and i_{qr}^* for RSC control and i_{dg}^* for GSC control.

5.1.2 Online Self-tuning Algorithm

It is impossible to calculate the desired outputs of the ANFIS controller, which are d-q axis currents for rotor and grid sides (i_{dr} , i_{qr} , i_{dg} , i_{qg}). Hence training data sequence can't be obtained especially for variable wind speed. Therefore, an unsupervised self-tuning algorithm is developed in the work. The controller targets to minimize the objective function which is a squared normalized error function of the ANFIS controller input. The objective function is defined as,

$$W = \frac{1}{2} e^2 = \frac{1}{2} \left(\frac{x^* - x}{x_{rated}} \right)^2 \quad (5.9)$$

where x^* , x and x_{rated} are the reference, actual and rated value of the variable and x is scalar.

5.1.3 Tuning of Pre-Condition and Consequent Parameters

The learning rule of the proposed controller can be given as [117]:

$$a_i(n+1) = a_i(n) - \gamma_{ai} \frac{\partial W}{\partial a_i}, \quad b_i(n+1) = b_i(n) - \gamma_{bi} \frac{\partial W}{\partial b_i} \quad (5.10)$$

Where, γ_{ai} and γ_{bi} are the learning rates of the corresponding parameters. The derivatives can be defined as:

$$\frac{\partial W}{\partial a_i} = \frac{\partial W}{\partial e} \frac{\partial e}{\partial x} \frac{\partial x}{\partial f} \frac{\partial f}{\partial \mu_{Ai}^l} \frac{\partial \mu_{Ai}^l}{\partial a_i}, \quad \frac{\partial W}{\partial b_i} = \frac{\partial W}{\partial e} \frac{\partial e}{\partial x} \frac{\partial x}{\partial f} \frac{\partial f}{\partial \mu_{Ai}^l} \frac{\partial \mu_{Ai}^l}{\partial b_i} \quad (5.11)$$

Now we get, $\frac{\partial W}{\partial e} = e = \frac{x^* - x}{x_{rated}}$, $\frac{\partial e}{\partial x} = -\frac{1}{x_{rated}}$ and $\frac{\partial x}{\partial f} = J$, assuming J is the Jacobian matrix of the system. It is very difficult to determine system's Jacobian matrix. For decoupled control of DFIG, the system is assumed as a single input single output system and then the Jacobian matrix is considered as a positive constant. Considering that the effect of J is included in tuning rate parameter, the update rule for the consequent parameter is given as:

$$a_1(n+1) = a_1(n) - \gamma_{a1} e(n) \frac{f_1(n)}{\sum \mu_{A1}^1} \frac{1-\mu_{A1}^1(n)}{b_1(n)-a_1(n)} \quad (5.12)$$

$$b_1(n+1) = b_1(n) - \gamma_{b1} e(n) \frac{f_1(n)}{\sum \mu_{A1}^1} \frac{\mu_{A1}^1(n)}{b_1(n)-a_1(n)} \quad (5.13)$$

$$b_2(n+1) = b_2(n) + \gamma_{b2} e(n) \frac{f_2(n)}{\sum \mu_{A2}^2} \frac{1-\mu_{A2}^2(n)}{b_2(n)} \quad (5.14)$$

$$a_3(n+1) = a_3(n) - \gamma_{a3} e(n) \frac{f_3(n)}{\sum \mu_{A3}^3} \frac{1-\mu_{A3}^3(n)}{b_3(n)-a_3(n)} \quad (5.15)$$

$$b_3(n+1) = b_3(n) - \gamma_{b3} e(n) \frac{f_3(n)}{\sum \mu_{A3}^3} \frac{\mu_{A3}^3(n)}{b_3(n)-a_3(n)} \quad (5.16)$$

Similarly, the update laws for tuning the consequent parameters can be obtained as:

$$\beta_0^i(n+1) = \beta_0^i(n) - \gamma_{\beta_0^i} e(n) \frac{f_i(n)}{\sum \mu_{Ai}^i} \frac{\mu_i}{\mu_1+\mu_2+\mu_3} \quad (5.17)$$

$$\beta_1^i(n+1) = \beta_1^i(n) - \gamma_{\beta_1^i} e(n) \frac{f_i(n)}{\sum \mu_{Ai}^i} \frac{\mu_i x}{\mu_1+\mu_2+\mu_3} \quad (5.18)$$

5.2 Control of Grid-Connected DFIG in Normal Condition

When DFIG is operated in grid-connected mode, the stator voltage remains constant. Usually the grid side converter is designed to operate in unity power factor. Thus the grid side converter control is not as complicated as the rotor side converter control.

5.2.1 RSC Control by ANFIS Method for Grid-Connected Mode

The rotor side converter magnetizes the machine through the rotor side converter. Fig. 5.3 shows the RSC control scheme using the proposed ANFIS architecture for grid connected DFIG. As DFIG provides decoupled control of real and reactive power, two different ANFIS structures have been employed to generate the reference d-axis and q-axis rotor currents (i_{dr}^* and i_{qr}^*).

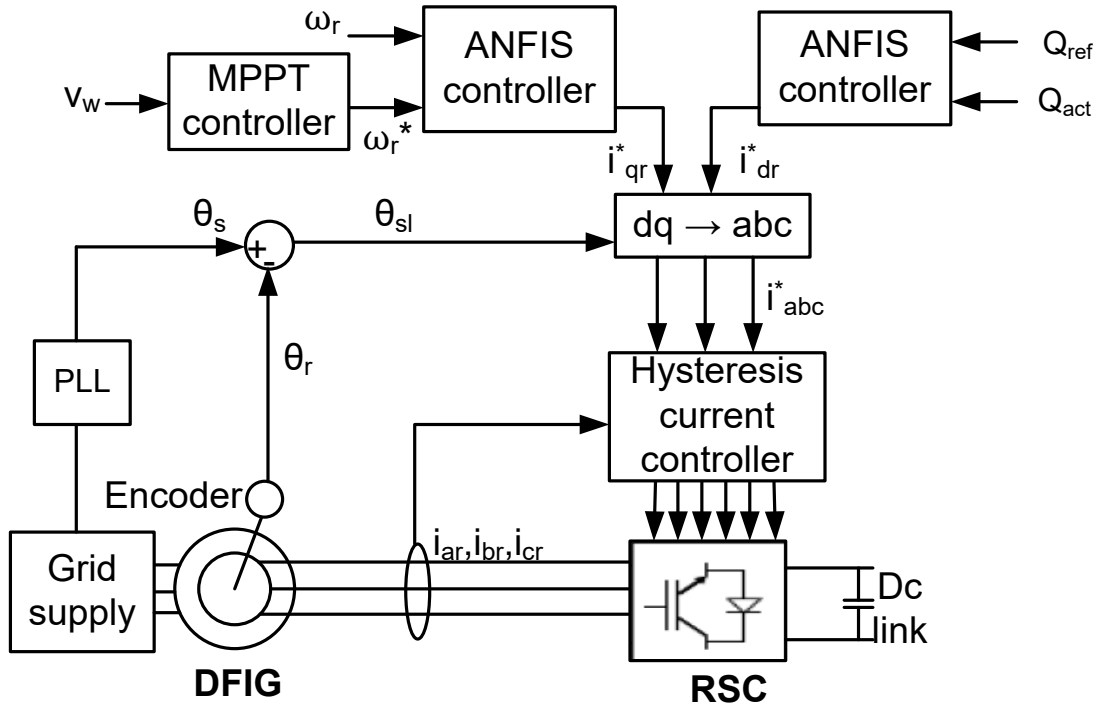


Fig. 5.3. ANFIS architecture based RSC control for grid-connected mode of DFIG.

5.2.2 GSC control in Grid-Connected Mode

While the RSC converter executes the challenging part of the DFIG, the grid side converter maintains the dc-link voltage constant irrespective of the value and direction of the rotor power flow. It is also possible to control the flow of reactive power by GSC. The ANFIS controller based configuration is implemented in GSC control to regulate the dc-link voltage as depicted in Fig. 5.4. The reference q-axis grid current component can be obtained from the reactive power demanded by the grid operator. The objective function of the ANFIS controller will ensure that the bus voltage error is converged to zero.

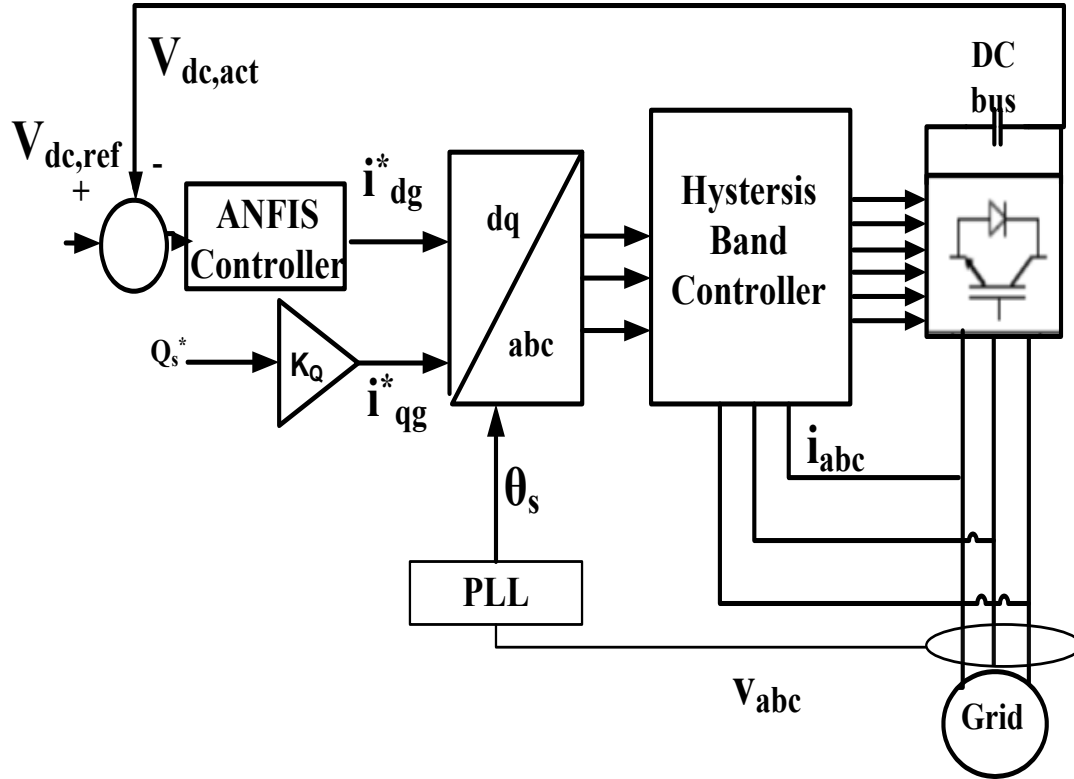


Fig. 5.4. ANFIS architecture based GSC control of DFIG.

The performance of the proposed ANFIS architecture based controller for DFIG-WECS is investigated in simulation at different operating conditions individually for grid-connected case. The simulation block diagram of the proposed ANFIS structure is shown in appendix. The outcomes of the simulation study are outlined in the following subsections.

5.2.3 Control Performance in Grid-Connected Mode for Normal Grid Condition

Speed and direction of wind at a location vary randomly with time. Therefore, the adaptability of controller is critical for wind power generators to operate effectively. ANFIS based controllers have the unique property of handling uncertainty and fast convergence in varying condition. In this thesis, the efficacy of the ANFIS controlled RSC for grid connected DFIG is observed under variable wind speed as shown in Fig. 5.5. The wind speed variation is depicted in Fig. 5.5(a). It is found that the

ANFIS controlled RSC maintains the rotor speed of the generator according to the MPPT control algorithm (Fig. 5.5(b)). It also regulates the d-q axis rotor current according to the demanded value to control the real and reactive power as shown in Fig. 5.5(c,d)).

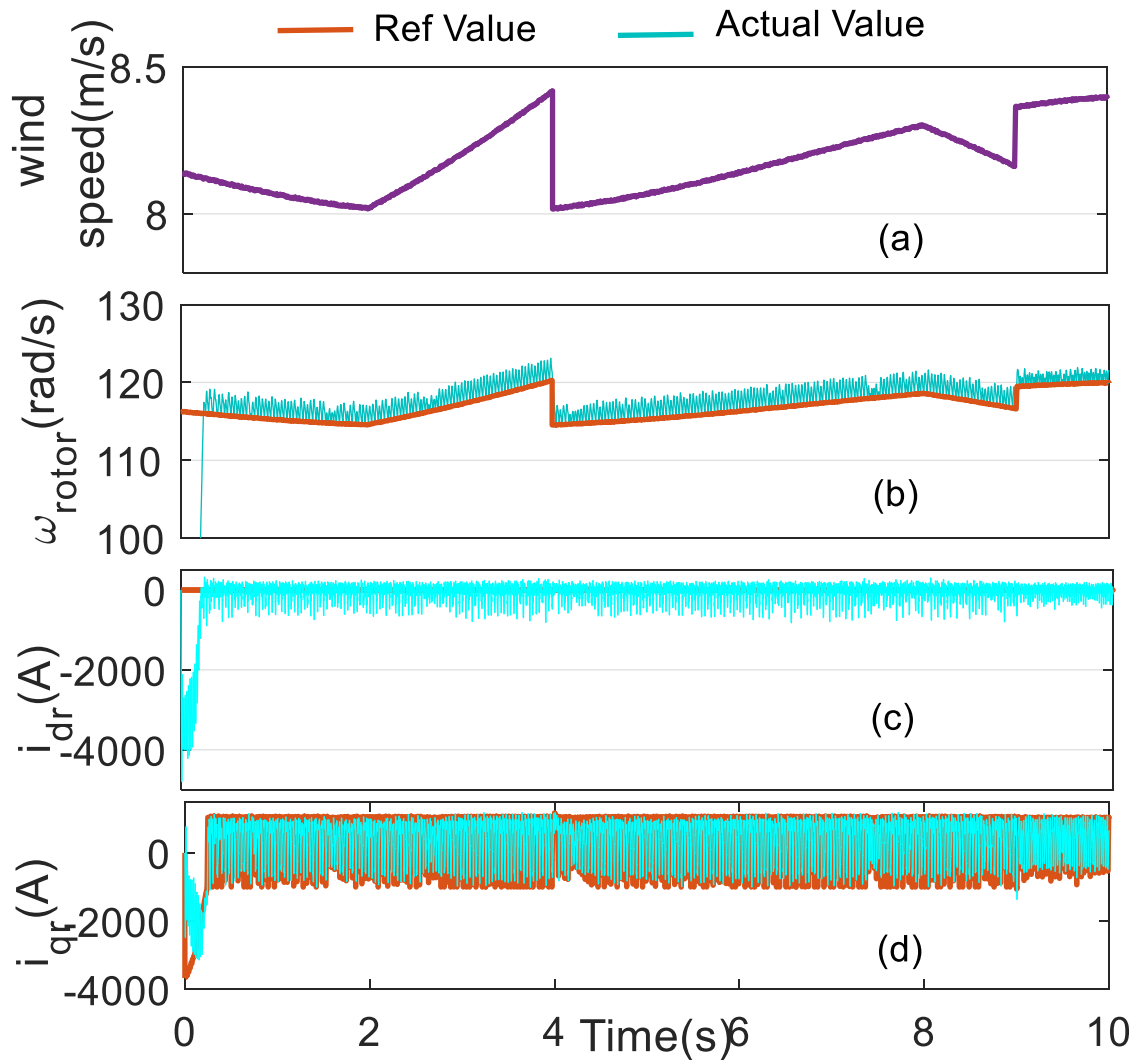


Fig. 5.5. Performance of the ANFIS based RSC control: (a) Variation in wind speed, (b) Corresponding change in generator speed, (c) Reference and actual d-axis rotor current, (d) Reference and actual q-axis rotor current.

The GSC is also controlled by the ANFIS based controller to regulate the d-q axis grid current components so that they follow the corresponding reference currents. The ANFIS controller generates

the reference control current i_{dg}^* for the grid converter. The other reference current component i_{qg}^* is obtained from the demanded reactive power. The controller performance is shown in Fig. 5.6.

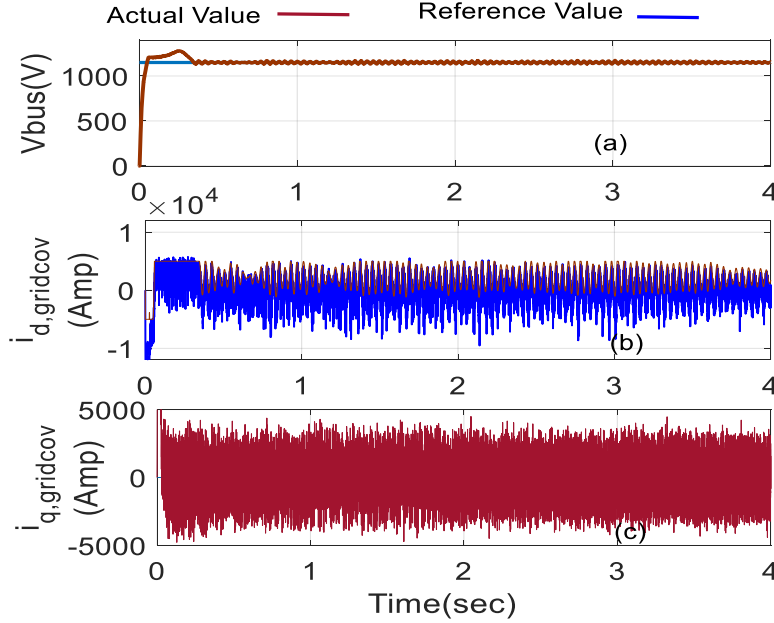


Fig. 5.6. Performance of the ANFIS based GSC control: (a) DC-link voltage, (b) d-axis grid current component, (c) q-axis grid current component.

In DFIG, it is possible to control the reactive power requirement from RSC. Fig. 5.7 shows the feature for the proposed controller. The reference reactive power is varied from 0 to 0.5 MVAR by employing step function (Fig. 5.7(a)). The desired value of d-axis rotor current follows the variation of the reactive power and the actual current component successfully can follow the trajectory of the reference current as observed in Fig. 5.7(b) and the three phase rotor current also changes accordingly (Fig. 5.7(c)). The analysis proves the accuracy and effectiveness of the ANFIS structure based controller in grid-connected DFIG based WECS.

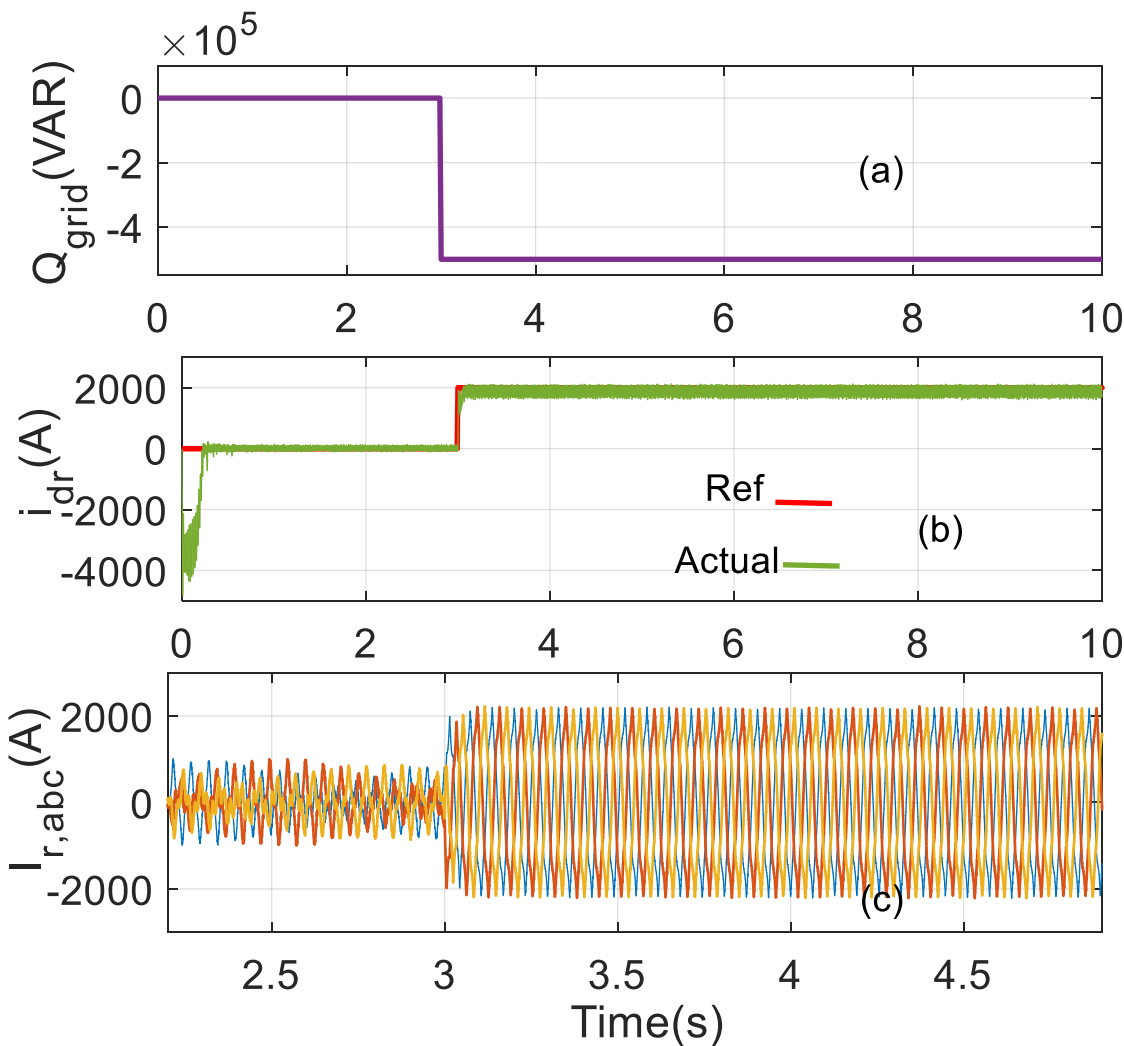


Fig. 5.7. ANFIS based controller performance for step change in reactive power: (a) Variation in reference value of reactive power, (b) Corresponding change in reference and actual d-axis rotor currents, (c) Three phase rotor currents.

5.3 Performance Comparison among Controllers for Grid-Connected DFIG-WECS

The performance of the grid connected DFIG-WESC has been investigated for conventional PI, nonlinear and ANFIS based controllers under various operating conditions. First, the simulation is performed for a step change in wind speed from 6 m/s to 8 m/s for each controller. The results are shown in Fig. 5.8. In the PI controllers, the proportional and integral constants are selected according to

the following table [93]. It is observed that the PI controller has relatively high overshoot, ANFIS controller shows slightly high steady state error at low wind speed and the nonlinear controller exhibits good tracking performance.

Table 5.1 PI controller constants for comparative analysis

Rotor side PI controller parameters	Stator side PI controller parameters
$k_{p,idr} = k_{p,iqr} = 2\omega_{idr}\sigma L_r - R_r$	$k_{p,vbus} = -10^4$
$k_{i,idr} = k_{i,iqr} = \omega_{idr}^2 \sigma L_r$	$k_{i,vbus} = -3 \times 10^5$
$k_{p,\omega r} = 2\omega_b J/P$	$k_{p,icd} = k_{p,icq} = 2\omega_{ic} L_g - R_g$
$k_{i,\omega r} = \omega_b^2 J/P$	$k_{i,icd} = k_{i,icq} = \omega_{ic}^2 L_g$
$\omega_{idr} = 100 \times \frac{1}{t_{ca}}, t_{ca} = \frac{\sigma L_r}{R_r}$	$\omega_{ic} = 2\pi f_s$
$\omega_b = \frac{1}{t_{cb}}, t_{cb} = 0.005$	

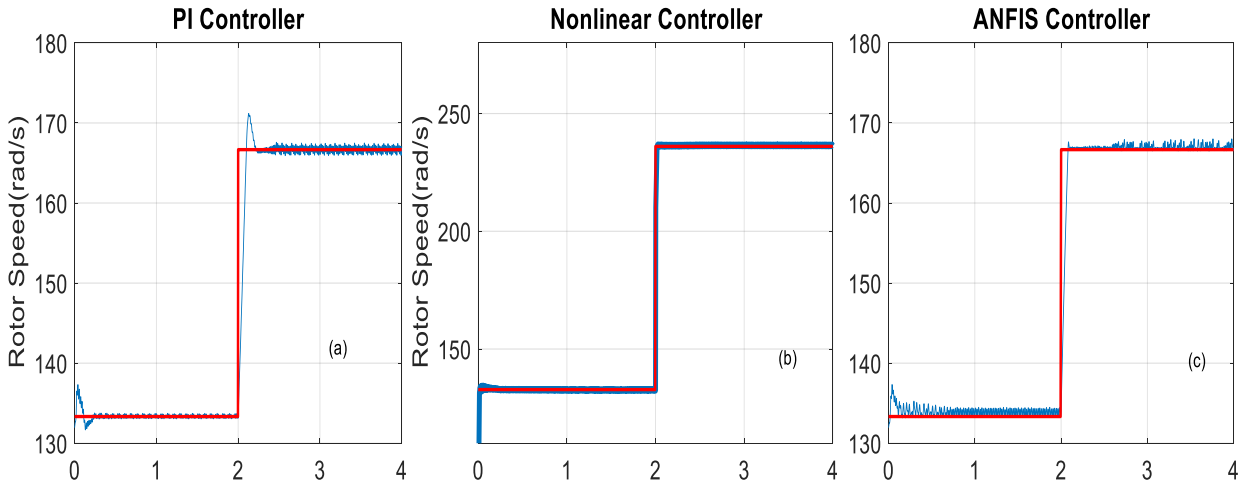


Fig. 5.8. Comparative rotor speed response for a step increase in wind speed: (a) PI, (b) Nonlinear, (c) ANFIS.

The dc-link voltage tracking performance of the controllers is also compared and shown in Figs. 5.9(a)-(c). The adaptive backstepping based nonlinear controller has very high ripples in dc-link voltage while the ANFIS based NFC controller shows the most satisfactory performance in voltage tracking.

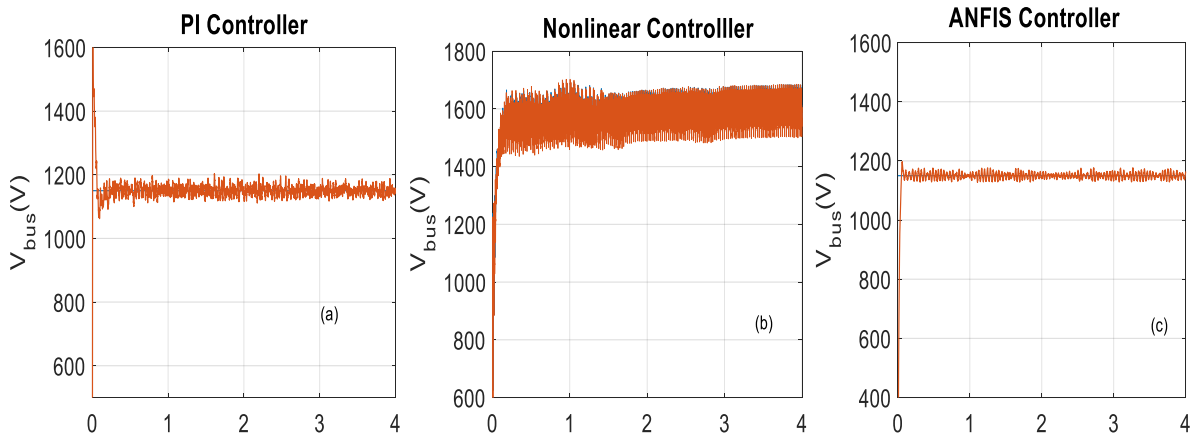


Fig. 5.9. Comparative dc-link voltage tracking performance at variable wind speed: (a) PI, (b) Nonlinear, (c) ANFIS.

Similarly, d-axis rotor current responses are investigated in Fig. 5.10 for a step change in reactive power demand. The PI controller shows fast current tracking while the nonlinear controller displays high overshoot and ANFIS controller experiences steady state error when the demanded reactive power is high.

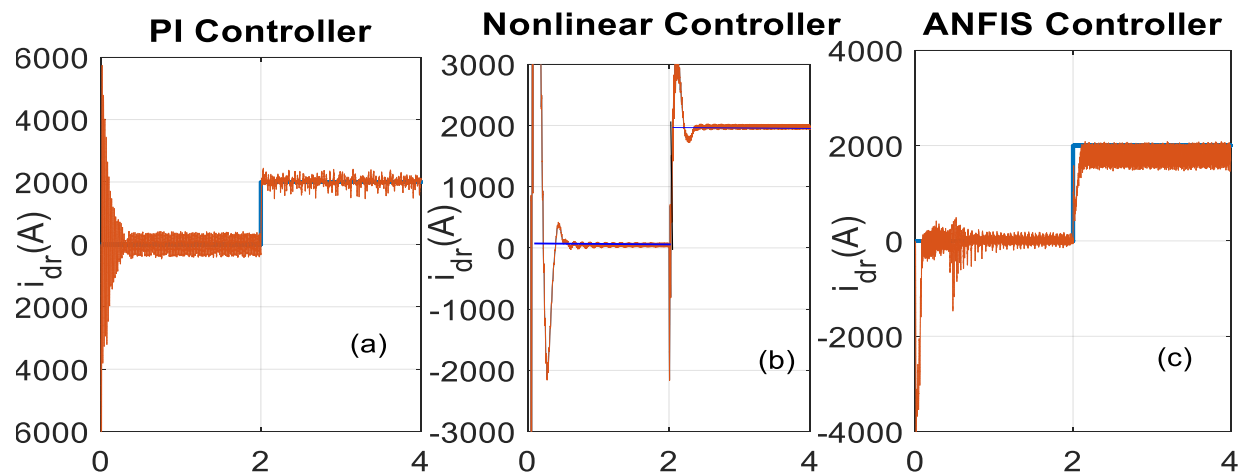


Fig. 5.10. Comparative d-axis rotor current tracking response for a step change in reactive power demand at $t=2$ sec: (a) PI, (b) Nonlinear, (c) ANFIS.

The summary of the performance comparison among the three controllers is presented in Table 5.2.

Table 5.2 Performance comparison among the proposed controllers

Operating condition	Property	PI controller	Adaptive-backstepping nonlinear controller	ANFIS based controller
Speed convergence characteristics	Speed settling time	Less than 0.2s	Less than 0.05s	Less than 0.15s
	Speed overshoot	3.5%	0.4%	0.6%
DC bus voltage convergence at variable wind flow	Voltage settling time	Less than 0.1s	Less than 0.05s	Less than 0.05s
	Voltage fluctuation	Low	High	Very low
d-axis rotor current at step rise in reactive power demand	Current settling time	Less than 0.1s	More than 0.5 s	Less than 0.2s
	Steady state error	Negligible	Negligible but very high overshoot	Relatively higher error with fluctuation
Computational burden	Block computation speed	Low	Medium	High
Ripple in grid currents at fixed wind speed		Moderate	Moderate	Moderate
Performance under grid voltage disturbance		Average	Good	Better than others

5.4 Control of Grid-Connected DFIG Under Voltage Dip Conditions

ANFIS has been found a suitable candidate to cope with the system uncertainties, such as wind speed variation, instance of voltage-dip occurrence. It has the ability to bypass the dependency on system mathematical model in the design of controller. Therefore, the ANFIS based current control technique is proposed in this thesis for converter control with grid voltage disturbances. The GSC and

RSC control is developed for grid-connected DFIG driven WECS where the voltage-dip condition is compensated by generating a reference demagnetization current fed to the hysteresis current controller. The proposed controller aims to regulate the rotor speed to follow the MPPT controller generated reference speed and reactive power control during normal operation. Under voltage dip condition, the controllers adjust the positive sequence d-q axis current components both at the grid and rotor sides by supplying required reactive power to the grid to minimize the effect of grid voltage fluctuations. The precondition and consequent parameters of the ANFIS controller are continuously updated based on the back-propagation algorithm. The performance of the controller is verified in simulation under symmetrical and asymmetrical voltage dip conditions. The ANFIS structure and parameter update rules remain the same as illustrated in section 5.1. The effect of grid voltage dip on DFIG control is discussed below.

In partial voltage dips, the stator voltage drops below its rated voltage but remains above zero. The stator flux can be evaluated by using the following expression.

$$\frac{d}{dt} \psi_s = v_s - \frac{R_s}{L_s} \psi_s \quad (5.19)$$

The solution of this ordinary differential equation has two parts-a) the homogeneous solution, b) the particular solution. The homogeneous solution is the transient or natural response of the equation and the particular solution is the steady state response.

$$\psi_s = \psi_{sn} + \psi_{sf} \quad (5.20)$$

In (5.20), the homogenous solution is referred to as natural flux (ψ_{sn}) and the particular solution is referred to as forced flux (ψ_{sf}). [93]

$$\psi_{sf} = \frac{V_{fault}}{j\omega_s} e^{j\omega_s t} \quad (5.21)$$

$$\psi_{sn} = \psi_{no} e^{-\frac{t}{\tau_s}} \quad (5.22)$$

Where,

V_{fault} is the grid voltage right after the fault has occurred and stator time constant, $\tau_s = \frac{L_s}{R_s}$.

The natural flux is a transient flux caused by the grid voltage fault and its initial value is ψ_{no} . The natural flux decays over time. During normal operation, only forced flux is present in the stator. On the contrary, both natural flux and forced flux are present in the machine in partial voltage dip condition. The trajectory of the stator flux is shown in Fig. 5.12 during the partial voltage dip in alpha-beta plane. The forced flux makes the space vector trace a circle and the natural flux causes the shift of its center.

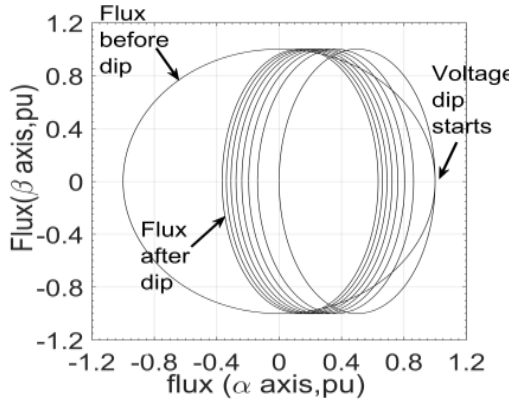


Fig. 5.11. Change of stator flux when three phase dip starts at the end of the first quarter of a voltage cycle.

Under symmetrical voltage dip condition, high voltages are induced in the rotor mainly due to the presence of natural flux [93]. Therefore, the effect of the natural flux needs to be reduced by appropriate control mechanism to avoid saturation at the rotor end. In a balanced three phase system, only positive sequence stator flux is present. Negative sequence stator flux builds up in asymmetrical voltage dip condition, such as phase to phase voltage dip. The zero sequence can only create a leakage flux if the neutral terminal of the machine is grounded [93]. If the neutral is isolated, the zero sequence voltage has no effect on the behavior of the machine. In the simulation study, the neutral of the DFIG has no ground connection. Hence, the effect of the zero sequence flux is ignored in the equations. In asymmetric voltage dip condition, the total stator flux can be given as

$$\psi_s = \psi_s^+ + \psi_s^- + \psi_{sn} \quad (5.23)$$

Where, ψ_s^+ and ψ_s^- are the positive and negative sequence stator flux respectively. The addition of these two fluxes provides the steady state stator flux. They are functions of grid voltage. On the contrary, ψ_{sn} is not dependent on the grid voltage. The initial value of this transitory flux is ψ_{no} which guarantees that there is no discontinuity in the total flux [93].

Fig. 5.12 illustrates the presence of natural flux and negative sequence stator flux that appear during asymmetrical voltage dip condition.

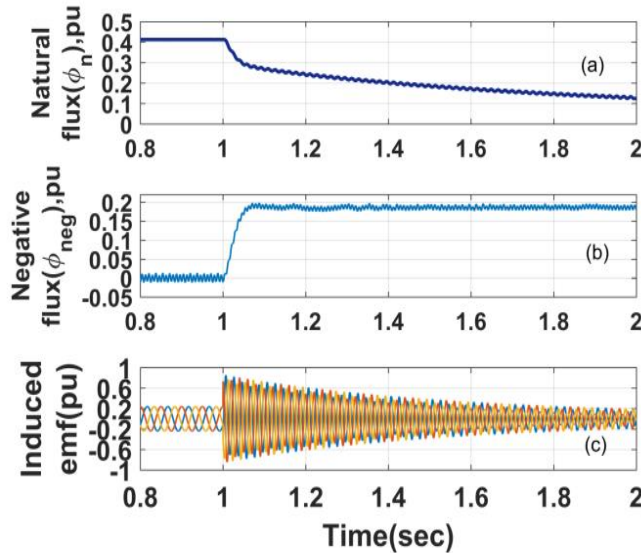


Fig. 5.12. Effect of voltage dip (a) Natural flux due to symmetrical dip, (b) Negative sequence stator flux due to asymmetrical dip, (c) Sudden rise in induced emf at rotor windings.

In Fig. 5.13, the ANFIS controlled operation for DFIG based WECS is demonstrated for voltage-dip condition. The amplitude of the stator flux is dependent on the moment of occurrence of voltage dips as shown in Fig. 5.11. Since the moment of occurrence of voltage dip is unpredictable, ANFIS controller is suitable for such situations. Therefore, to cope up with uncertainties associated with voltage-dip occurrence and machine nonlinearities, the ANFIS based current control scheme is developed to regulate the converters for grid-connected DFIG.

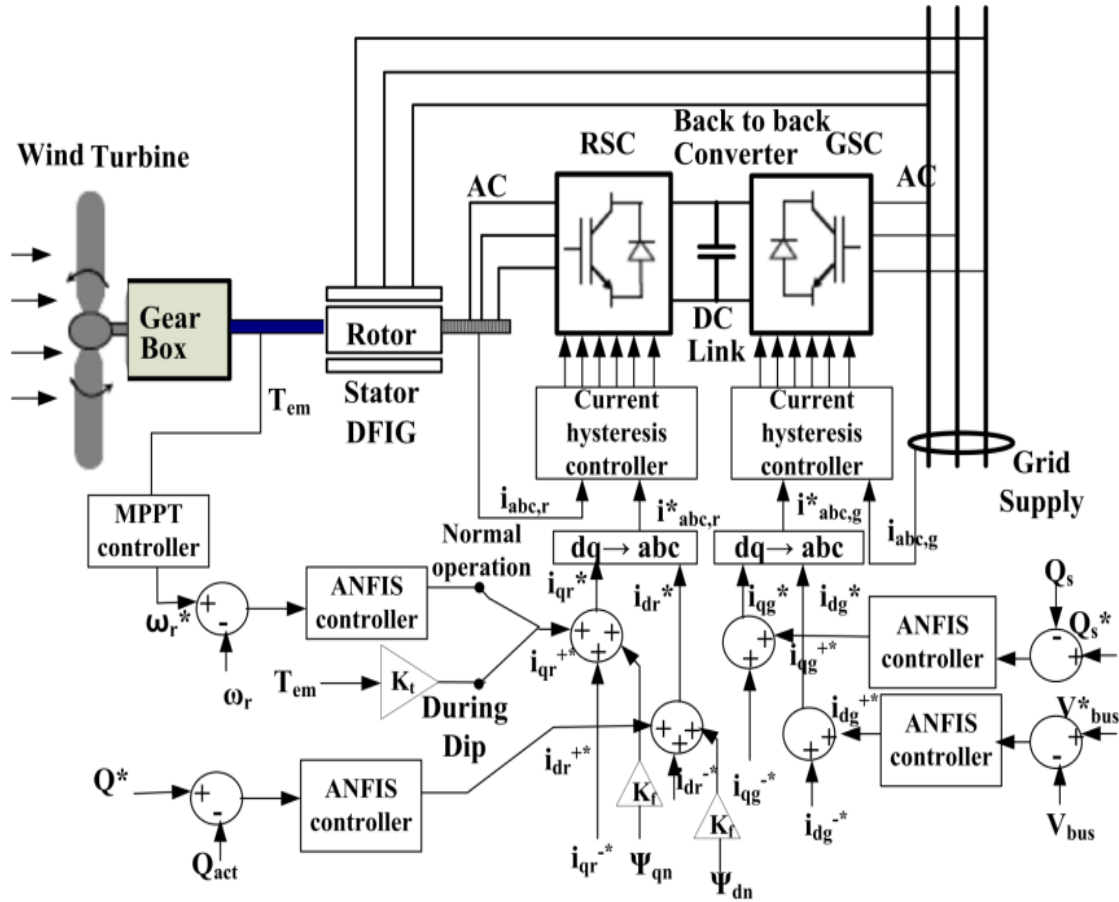


Fig. 5.13. Overall configuration of the DFIG-WECS with ANFIS controller for voltage dip condition.

5.5 Converter Control in Voltage Dip Conditions

Any disturbance at grid voltage causes significant perturbation in the induced emf at rotor. The rotor induced electromagnetic force increases notably and creates overvoltage during severe voltage dip condition. Therefore, the effect of voltage dip has to be minimized through current loop control at the rotor converter control circuit to avoid converter saturation. In this subsection, ANFIS based converter control scheme is illustrated for grid-connected DFIG under voltage fluctuation. The Matlab-Simulink configuration for the ANFIS based DFIG-WECS control is depicted in Fig. 5.14. In the figure, the wind speed is 10 m/s for studying the performance of the system at a constant wind speed. For variable speed

analysis, the wind model shown in section 2.1 can be utilized. Also a step rise in the reference reactive power is provided for the time span when voltage dip occurs. The sampling time period is 50 μ s.

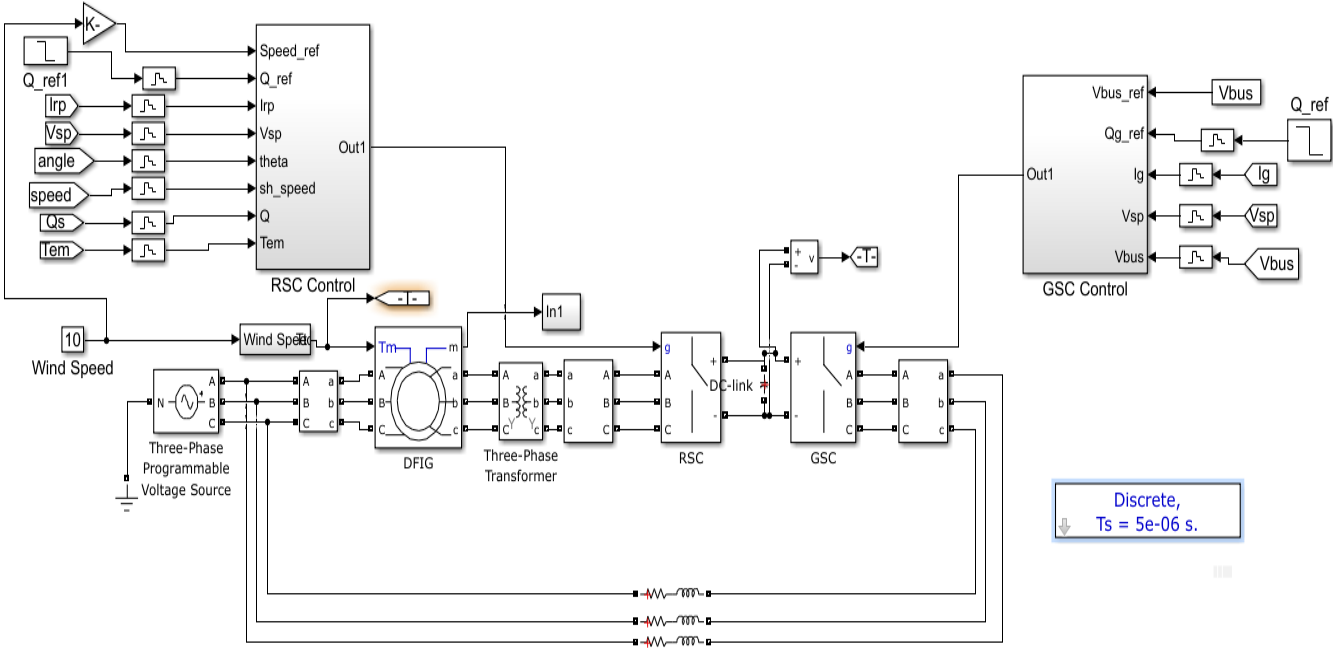


Fig. 5.14. Overall Configuration for the ANFIS based DFIG-WECS control in voltage dip.

a) GSC Control

The grid side converter control for the proposed system is shown in Fig. 5.11. GSC control aims to generate the reference d-q axis grid current (i_{dg}^* and i_{qg}^*). Each reference current is combination of two reference current components-positive and negative sequence current, i.e.,

$$i_{dg}^* = i_{dg}^{+*} + i_{dg}^{-*} \quad (5.24)$$

$$i_{qg}^* = i_{qg}^{+*} + i_{qg}^{-*} \quad (5.25)$$

Since the neutral terminal of the DFIG stator is not grounded, the zero sequence current is ignored throughout the analysis. Two ANFIS controllers are designed to generate the positive sequence reference currents. One controller provides the current i_{dg}^{+*} by minimizing the bus voltage error, the

other one yields the component i_{qg}^{+*} by maintaining the reactive power to the grid demand. To reduce the effect of negative sequence fluxes, the reference grid current components with negative sequence are considered as zero, i.e. $i_{dg}^{-*} = 0, i_{qg}^{-*} = 0$. The Matlab-Simulink block diagram for GSC control is shown in Fig. 5.15(a) for better understanding. A PLL is used inside the angle calculator block to determine the angle of rotation of the grid voltage. Fig. 5.15(b) shows the positive and negative sequence decomposition model for the GSC.

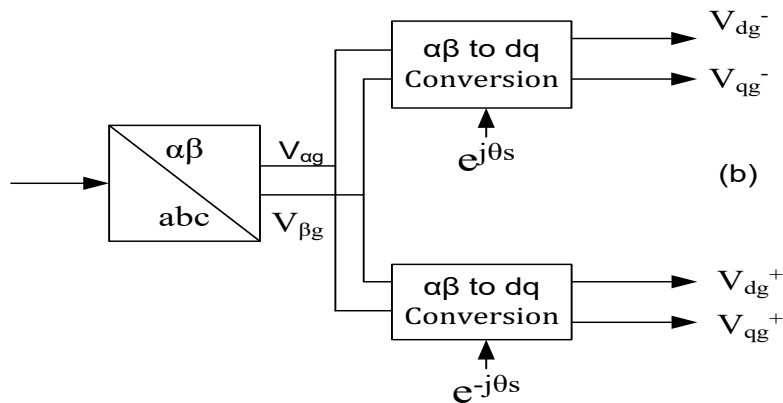
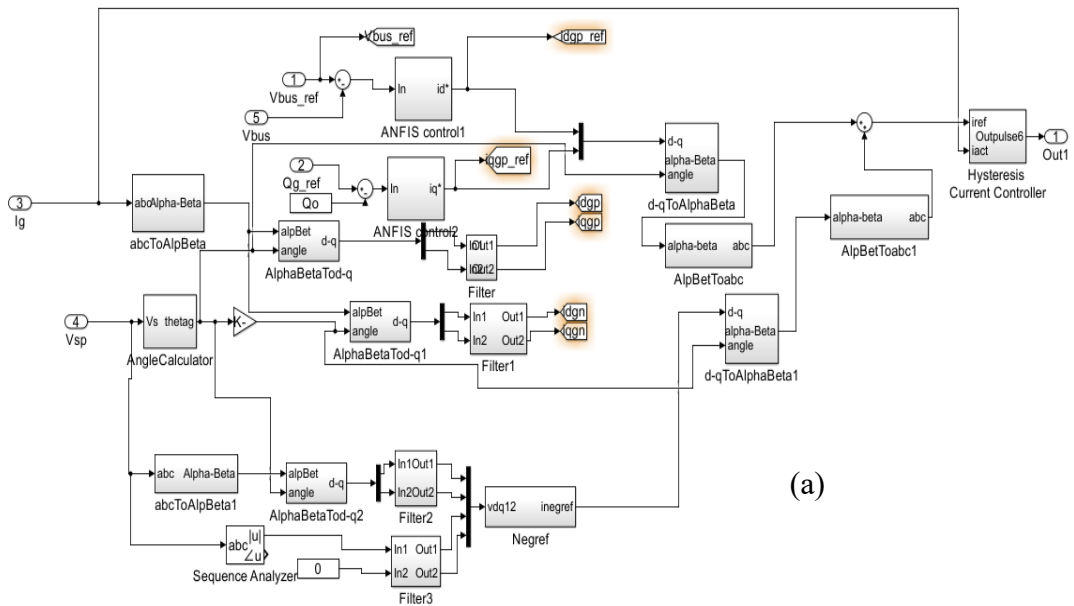


Fig. 5.15. (a) MATLAB-Simulink block diagram for ANFIS based GSC control during voltage dip, (b) Block diagram for sequence decomposition.

b) RSC Control

The rotor side converter control of the proposed configuration consists of two ANFIS based NFC controller. The rotor controller utilizes hysteresis current control that compares between $i_{abc,ref}$ and $i_{abc,act}$ to generate the control pulses. The three-phase reference rotor currents are obtained from dq to abc transformation block. The reference currents are found from (5.26) and (5.27).

$$i_{dr}^* = i_{dr}^{+*} + i_{dr}^{-*} + i_{dr}^{n*} \quad (5.26)$$

$$i_{qr}^* = i_{qr}^{+*} + i_{qr}^{-*} + i_{qr}^{n*} \quad (5.27)$$

The positive sequence reference current components, i_{dr}^{+*} and i_{qr}^{+*} are gained from the ANFIS blocks. i_{dr}^{-*} and i_{qr}^{-*} are the negative sequence reference current components that target to minimize the voltage imbalance of the grid phases. i_{dr}^{n*} and i_{qr}^{n*} are the reference demagnetization current components. These current components are introduced to reduce the effect of natural flux of the machine. While voltage sag occurs, the positive sequence stator flux drops down from its normal value but the negative sequence and natural flux components increase suddenly. The high emf induced in the rotor by the latter two fluxes may cause overvoltage and saturation at the rotor converter end. The solution for this problem is to introduce demagnetization current that will reduce the unexpected fluxes and hence will decrease the induced emf at the rotor. From the rotor flux equation, we get

$$\vec{\psi}_r = \frac{L_m}{L_s} \vec{\psi}_s + \sigma L_r \vec{i}_r \quad (5.28)$$

From this equation, it is evident that the rotor flux can be reduced by inducing a rotor current opposite the corresponding stator flux component such as,

$$i_{dr}^{-*} = -k_{d1} \psi_{ds}^- \quad (5.29)$$

$$i_{dr}^{n*} = -k_{d2} \psi_{ds}^n \quad (5.30)$$

Where, k_{d1} and k_{d2} are constants.

Thus, (5.28) can be rewritten with individual current components as shown in (5.31) and (5.32).

$$\psi_{dr}^- = \left(\frac{L_m}{L_s} - \sigma L_r k_{d1} \right) \psi_{ds}^- \quad (5.31)$$

$$\psi_{dr}^n = \left(\frac{L_m}{L_s} - \sigma L_r k_{d2} \right) \psi_{ds}^n \quad (5.32)$$

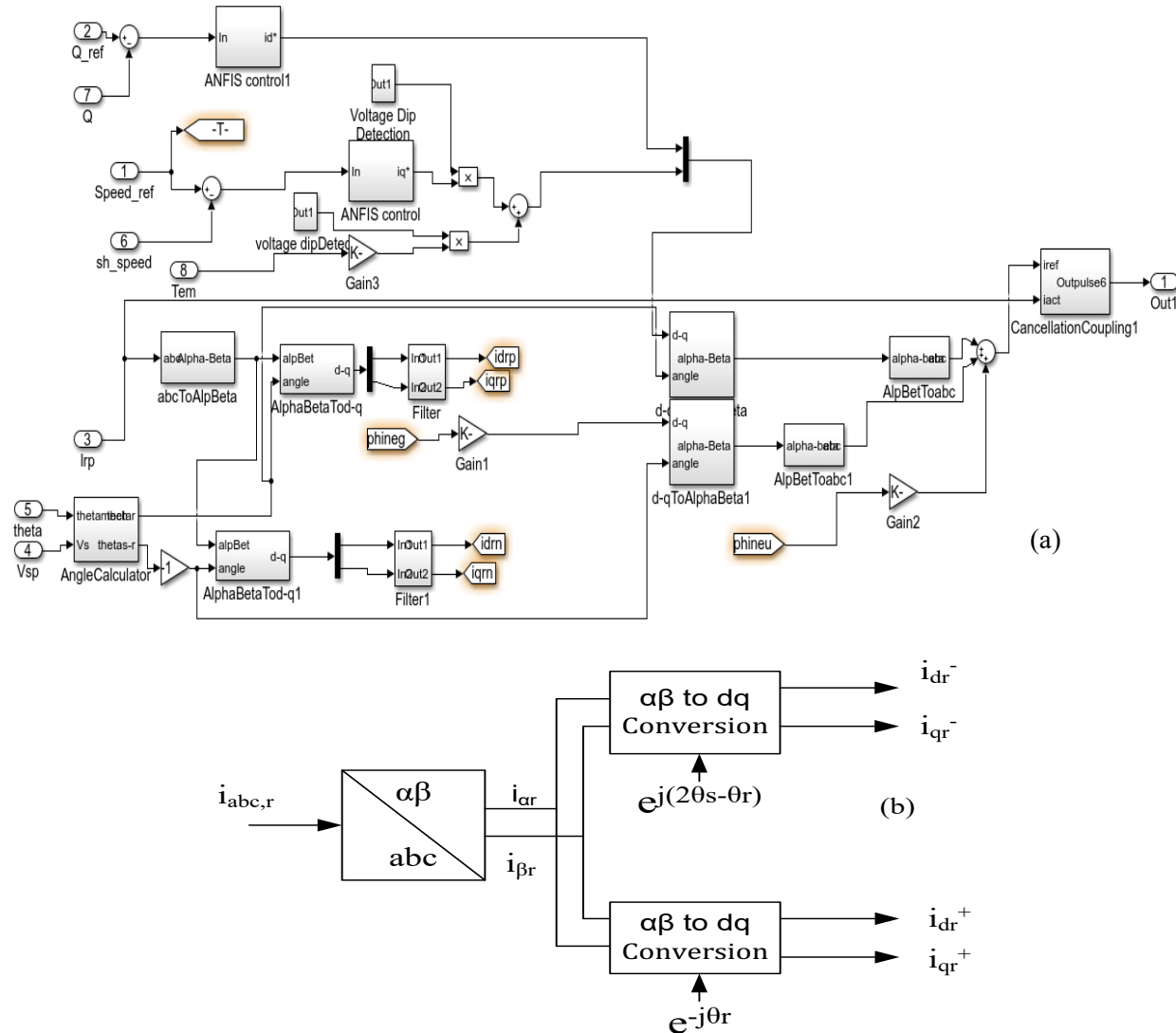


Fig. 5.16. (a) Simulink configuration for ANFIS based RSC control during voltage dip. (b) Block diagram for rotor current sequence decomposition.

Thus, the negative sequence and natural reference d-axis current components for rotor control are chosen according to (5.29) and (5.30). To reduce the effect of q-axis fluxes, the q-axis rotor current components are considered as zero, i.e. $i_{qr}^{-*} = 0, i_{qr}^{n*} = 0$. The Simulink block diagram for rotor current control is shown in Fig. 5.16(a) and the sequence decomposition block diagram for rotor currents are shown in 5.16(b).

5.6 Simulation Results for Voltage Dip Conditions

The ANFIS controller is designed to minimize the adverse effect of the voltage dip conditions. The performance of the proposed controller is investigated in simulation at asymmetrical and symmetrical voltage dips. Fig. 5.17 illustrates the proficiency of the proposed ANFIS based control scheme for a three-phase symmetric severe voltage dip (Fig. 5.17(a)). The positive sequence d-q axis rotor currents are maintained to their reference level during voltage droop to supply the demanded reactive and active power by the machine (Fig. 5.17(b) and (e)). The ANFIS controller executes maximum power tracking scheme by regulating the rotor speed at the reference point before and after the dip occurrence (Fig. 5.17(c)). The demand q –axis positive rotor current ($i_{qr,ref}^+$) is determined by the electromechanical torque (T_{em}) of the machine during voltage dip (Fig. 5.17(d)). To minimize the power fluctuation, the reference negative sequence rotor currents are calculated from negative flux components of stator (i_{dr}^{-*} and i_{qr}^{-*}) to generate the required demagnetization effect. The positive sequence stator flux (Fig. 5.17(f)) follows the changes in grid voltage.

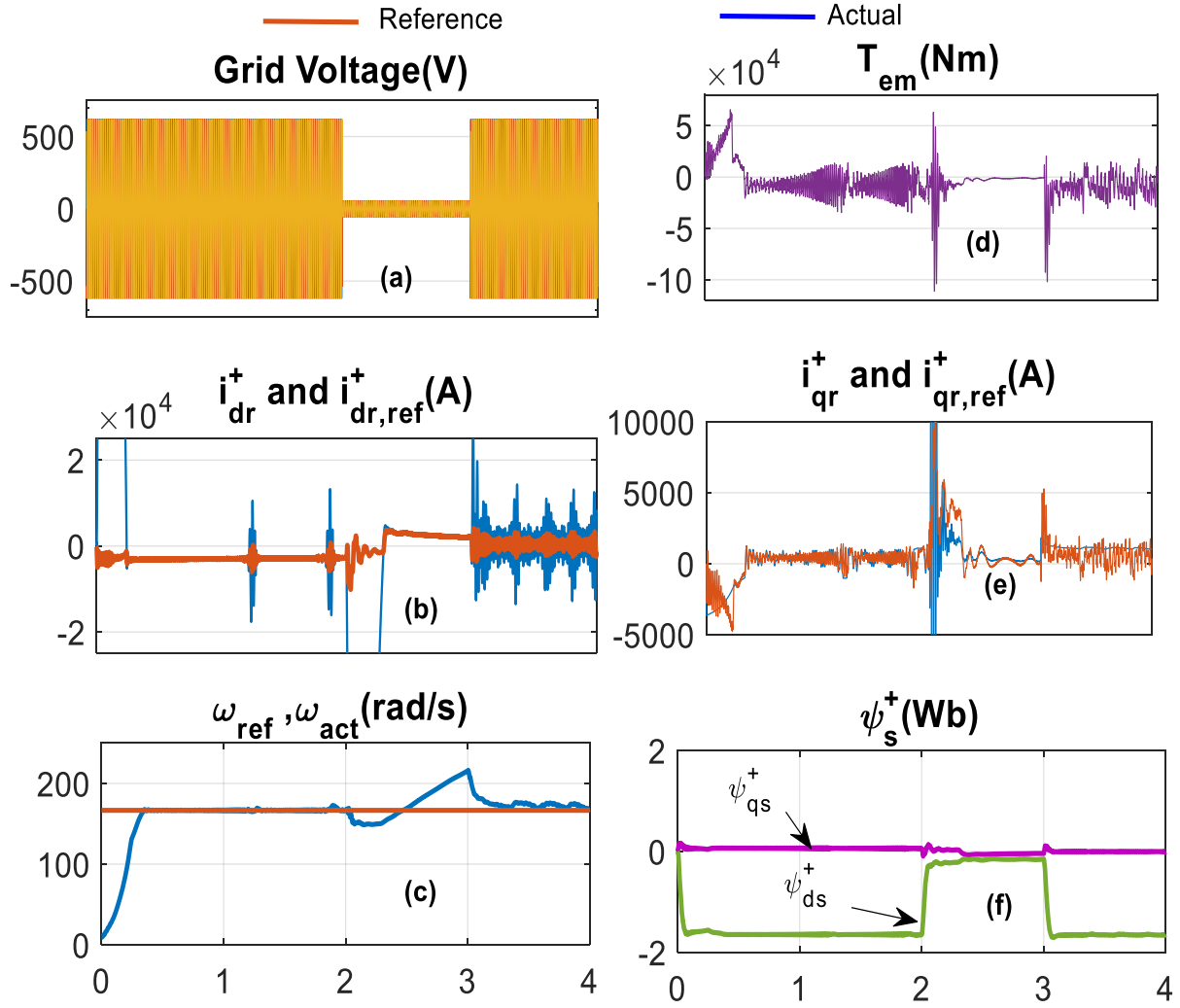


Fig. 5.17. Performance of the proposed ANFIS based DFIG-WECS for 90% three-phase symmetrical voltage dip: (a) Grid voltage, (b) Positive sequence d-axis rotor currents, (c) Reference and actual rotor speed, (d) Electromechanical Torque, (e) Positive sequence q-axis rotor current, (f) d-q axis stator flux.

Fig. 5.18 illustrates the proficiency of the proposed ANFIS based GSC control scheme for a three-phase symmetric severe voltage dip. The dc-link voltage (Fig. 5.18(a)) is maintained at the reference level by the control action of the GSC. The d-axis grid current component (Fig. 5.18(b)) and three phase grid currents (Fig. 5.18(c)) suggest that the ANFIS based GSC controller is capable of controlling the current as per the demand.

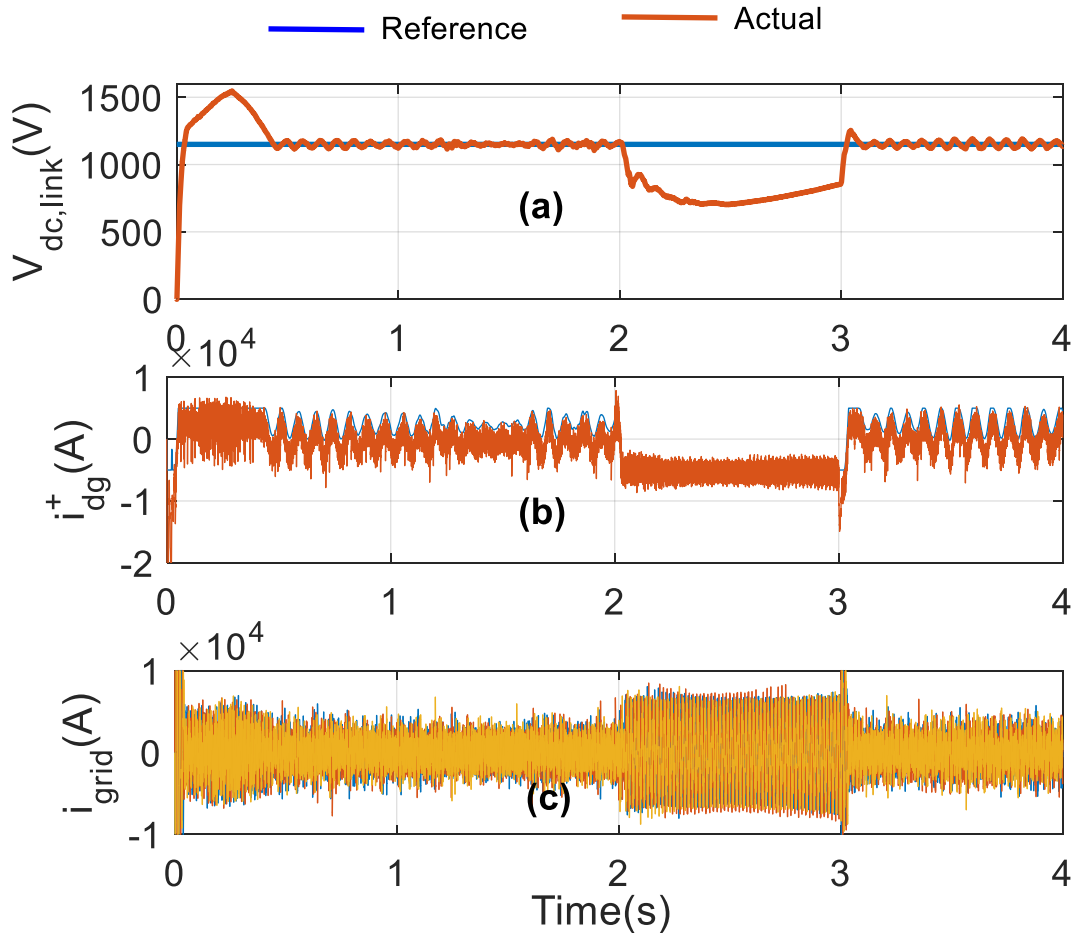


Fig. 5.18. Performance of the proposed ANFIS for 90% three phase symmetrical voltage dip: (a) dc-link voltage, (b) Positive sequence d-axis grid current, (c) Three phase grid currents.

A phase-to-phase 40% dip is created with phase \underline{a} and \underline{b} at the grid end for duration of 0.5 s in simulation (Fig. 5.19(a)). The rotor speed maintains MPPT before and after the dip as shown in Fig. 5.19(b). The machine torque shows large fluctuation during voltage dip while the ANFIS controller ensures the proper tracking of d-q axis positive sequence reference rotor currents and keep the three phase rotor currents under control (Fig. 5.19(b),(e) and (f)). The q –axis positive sequence rotor current ($i_{qr,ref}^+$) aims to stabilize the stator power while the d –axis rotor current ($i_{dr,ref}^+$) regulates the reactive power from RSC end. The torque variation is also shown in Fig. 5.19(d). The rotor current remains

within limit due to the control action of the adaptive NFC controller. Thus the current saturation during voltage dip is avoided.

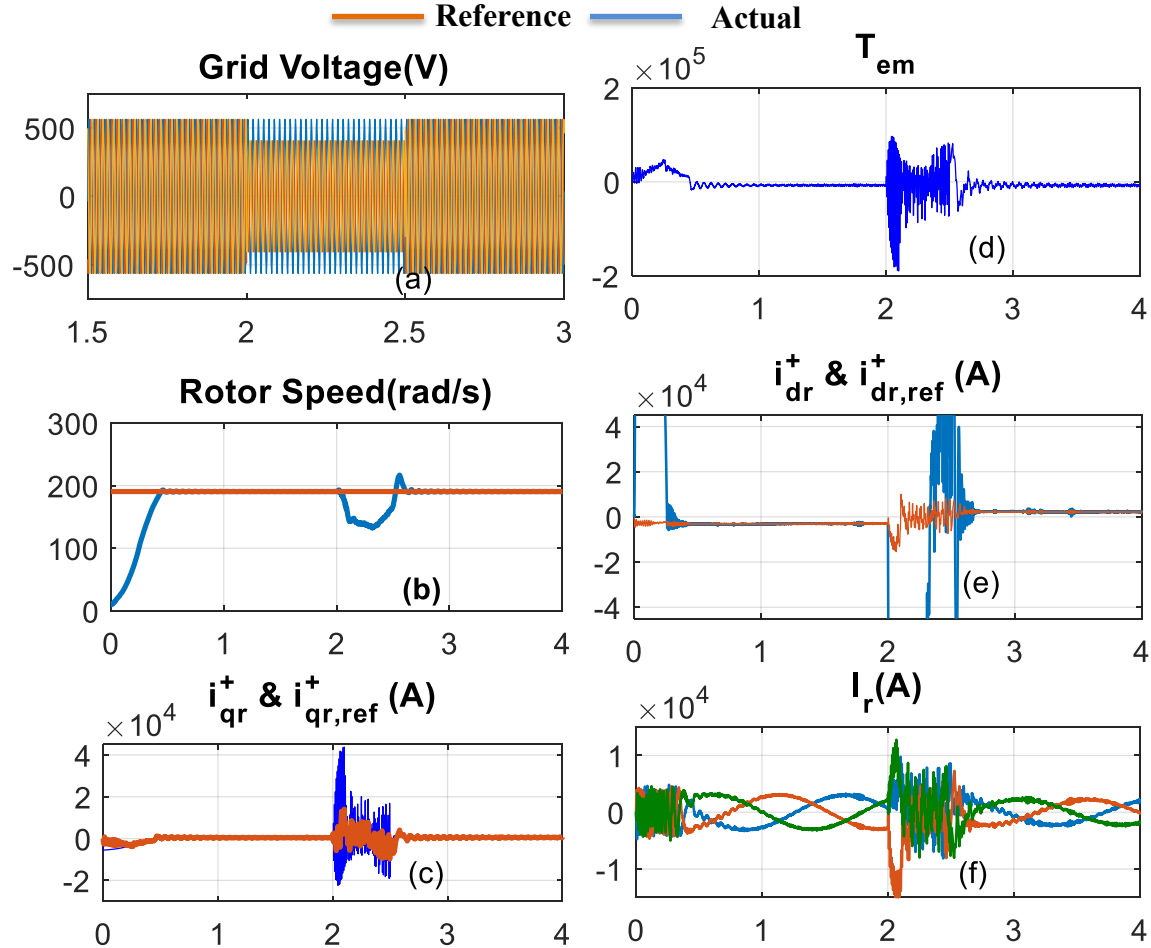


Fig. 5.19. Performance of the proposed ANFIS based DFIG-WECS for phase-to-phase 40% voltage dip: (a) Grid voltage, (b) Reference and actual rotor speed, (c) Positive sequence q-axis rotor current, (d) Electromechanical torque, (e) Positive sequence d-axis rotor currents, (f)Three phase rotor current.

Fig. 5.20 illustrates the efficacy of the controller for the aforementioned dip condition. The GSC maintains the dc-link voltage to the desired level (Fig. 5.20(a)). The voltage dip creates an overvoltage on rotor side (Fig. 5.20(d)). However, the voltage-overlimit situation is evaded through the ANFIS control action. The imbalance among the phase voltages creates the negative sequence current and flux components. The positive sequence d-axis grid current component drops (Fig. 5.20(b)) while negative

sequence d-axis grid current component rises during the voltage dip (Fig 5.20(d)). During imbalance period, the negative stator flux rises suddenly (Fig 5.20(f)) and therefore, the fluctuation of the real and reactive power is unavoidable. Severe overvoltage condition might occur if the dip condition sustains for a longer period. Hardware solutions, such as crowbar protection need to be activated in such condition to prevent the damage in the machine.

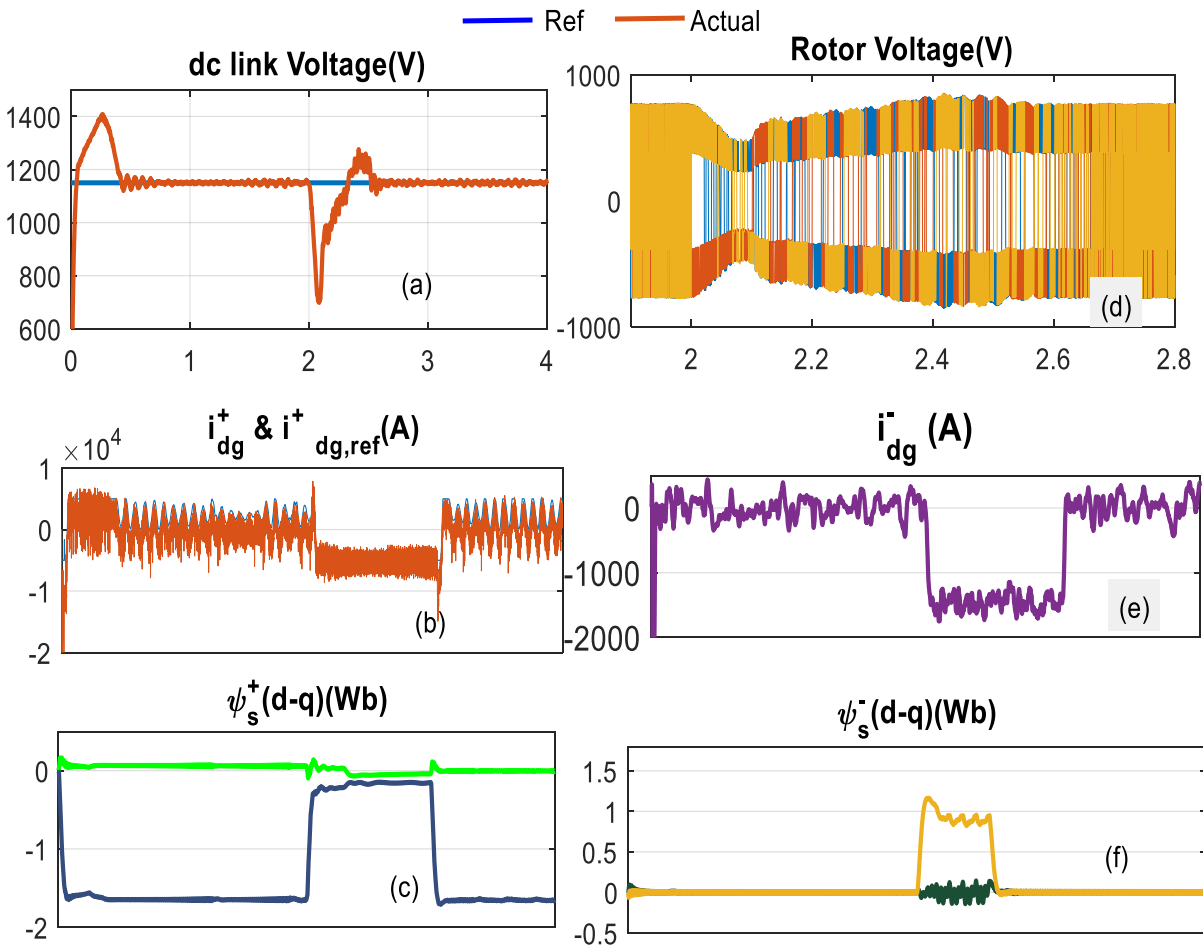


Fig. 5.20. Performance of the proposed ANFIS based GSC control for phase-to-phase 40% voltage dip: (a) dc-link voltage, (d)Positive sequence d-q axis grid current, (c) Positive sequence stator flux, (d) Three phase rotor voltage, (e) Negative sequence d-q axis rotor current, (f) Negative sequence d-q axis stator flux.

Finally, the updated values of the membership function parameters and the linear parameters are shown in Fig 5.20. Figs. 5.20(a-d) shows the parameter variations for variable wind speed at normal grid voltage. In this figures, a_3 , b_2 , b_3 are the membership function parameters as illustrated in Fig. 5.2

and β_0^2 is one of the consequent parameters. Similarly, Figs. 5.20(e-h) corresponds to the variation of same parameters for grid voltage dip condition.

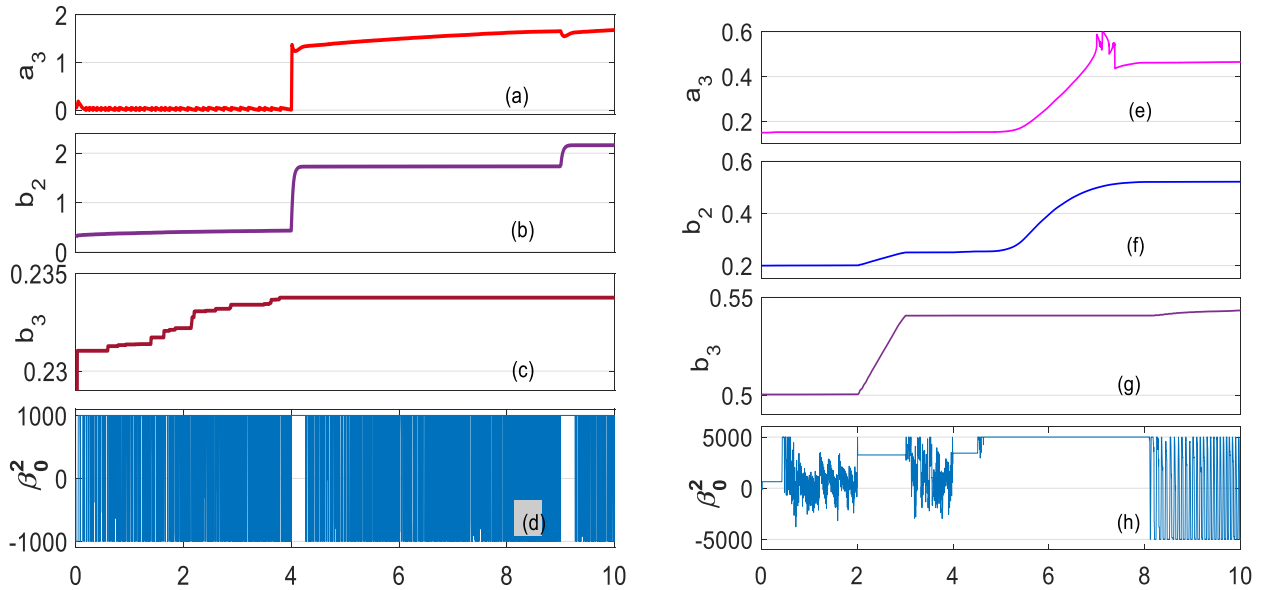


Fig. 5.21. Updated value of the membership function parameters and consequent parameters: (a-d) For variable wind speed at normal grid voltage, (e-h) For grid voltage dip condition:(a) a_3 , (b) b_2 , (c) b_3 , (d) β_0 , (e) a_3 , (f) b_2 , (g) b_3 , (h) β_0 .

5.7 Summary

A novel ANFIS based NFC scheme for grid-connected DFIG driven WECS has been developed and presented in this chapter. The performance of the proposed controller has been investigated under normal and voltage dip conditions. The simulation results suggest that the NFC is capable of regulating the grid side and rotor side converter currents according to the demanded value in normal operating condition. During voltage dip conditions, the proposed scheme prevents the saturation of the rotor side converter by adjusting the positive sequence rotor currents and injecting demagnetizing current to compensate the negative sequence current components. The grid side converter contributes by balancing the dc-link voltage. Thus it is capable of avoiding saturation of RSC and overvoltage at dc-

link terminal. The robustness of the designed ANFIS architecture based controller is justified by its independency on the system's mathematical model and rigorous control over the generator currents during small and severe symmetric voltage dips.

Chapter 6

Intelligent Control of DFIG Driven WECS in Standalone Mode

In micro-grid application, DFIG based wind energy system can operate in either standalone or grid-connected mode. If the users stay far away from the supply grid, an isolated generation system is required. The stand-alone mode is required where the grid voltage is not available such as remote area or in case of grid-power failure when the generators have to fulfill emergency power demand of local loads. In the islanded mode of operation, the machine is equipped with power electronics interfaces to regulate voltage and frequency at the load end. One of the main challenges of islanding operation of DFIG based WECS is to regulate the autonomous frequency of the generation system. Unlike grid-connected system where the frequency is determined by the grid voltage, the DFIG confronts the loss of frequency reference in an isolated system. Furthermore, voltage regulation and speed limit of wind turbine are the two other concerns related with the standalone operation of DFIG-WECS. Due to the intermittent nature of wind flow, the wind generator can't sustain its operation without the support of additional power sources. Auxiliary energy sources such as internal combustion engine, photovoltaic panels are often integrated into the system to provide appropriate performance [93]. Especially, in wind driven power system operating at standalone mode, supporting energy storage system increases the power quality of the generation unit [97-98]. In this thesis, battery units are utilized as the storage unit because of its high energy density. In order to ensure effective functioning of the battery storage system, power flow management is a critical aspect to be investigated. Optimization of the battery power supply is vital for the longevity of storage supply lifespan and to achieve better efficiency. So far, the researchers have mainly investigated the modeling and control features of energy storage units for grid connected wind power generation systems. Although intelligent control techniques may

provide efficient control features with rigorous convergence characteristics under promptly varying conditions [99-105], until now, only a handful of attempts have been made for energy optimization in WECS by adopting intelligent algorithm such as genetic algorithm, particle swarm optimization (PSO) [111] , artificial bee colony algorithm, grey wolf optimization [109] etc. Among these techniques, grey wolf optimization is a meta-heuristic robust optimization technique which is inspired by the hunting method of grey wolves [106]. Compared to the other stochastic optimization techniques, GWO method provides the ability to avoid local optima, easier implementation with few parameters to adjust [107, 108]. In wind power application, the maximum power tracking with the utilization of grouped grey wolf optimizer [109] and optimal blade pitch control via GWO-PID controller [110] are few of the significant works done by researchers that utilize the grey wolf optimization technique. However, the controllers are applied for grid-connected DFIG system. Standalone operation has not been considered in those works. Simulated annealing PSO [111] and improved PSO algorithm [112] are presented for capacity optimization of wind/solar hybrid energy system to minimize one-time investment and operation cost. Yet, power optimization and energy management haven't been considered in the work. Therefore, two different intelligent control schemes have been developed in this chapter to control DFIG based WECS for standalone operation mode. First, an ANFIS based control scheme is developed for standalone operation mode of DFIG-WECS where the load side converter is driven by neuro-fuzzy network based control scheme. The proposed controller aims to regulate the frequency and the terminal voltage to a specified value. The sample input-output data for the training of ANFIS structure are taken from the transient and steady state response of the DFIG-WECS operated with tuned PI controller under variable demand power and fluctuating wind speed conditions. The Gaussian type of function is selected as membership function, and the combined back-propagation and least square function algorithm are utilized for training the proposed ANFIS structure.

Secondly, a novel energy management scheme is introduced to regulate the battery power supply of DFIG driven wind energy system. The proposed algorithm is based on grey wolf optimization technique that calculates the optimum reference current for the bidirectional buck-boost converter placed between the battery unit and the dc-link. A boost converter preceded by the rectifier unit is placed between the stator and the dc-link. The boost converter current control ensures maximum power extraction from the turbine. In addition, a PI controller based rotor side converter control is designed for standalone operation mode of DFIG-WECS to regulate the output frequency and the terminal voltage at the load end. The proposed algorithm is tested in simulation. Also, real-time experiment has been done in the laboratory for a standalone DFIG driven wind power system prototype to verify the outcome of the overall configuration.

6.1 Description of the ANFIS Based Control of DFIG-WECS in Standalone Mode

For a standalone application of WECS, the system needs to have sufficient storage capacity to handle power variations from the available wind energy source. In order to cope with machine nonlinearities and uncertainties at variable wind speed and load conditions, ANFIS based NFC scheme is chosen in this thesis to control the converters for isolated operation of DFIG. The overall structure of the proposed standalone operation for DFIG based WECS is demonstrated in Fig. 6.1.

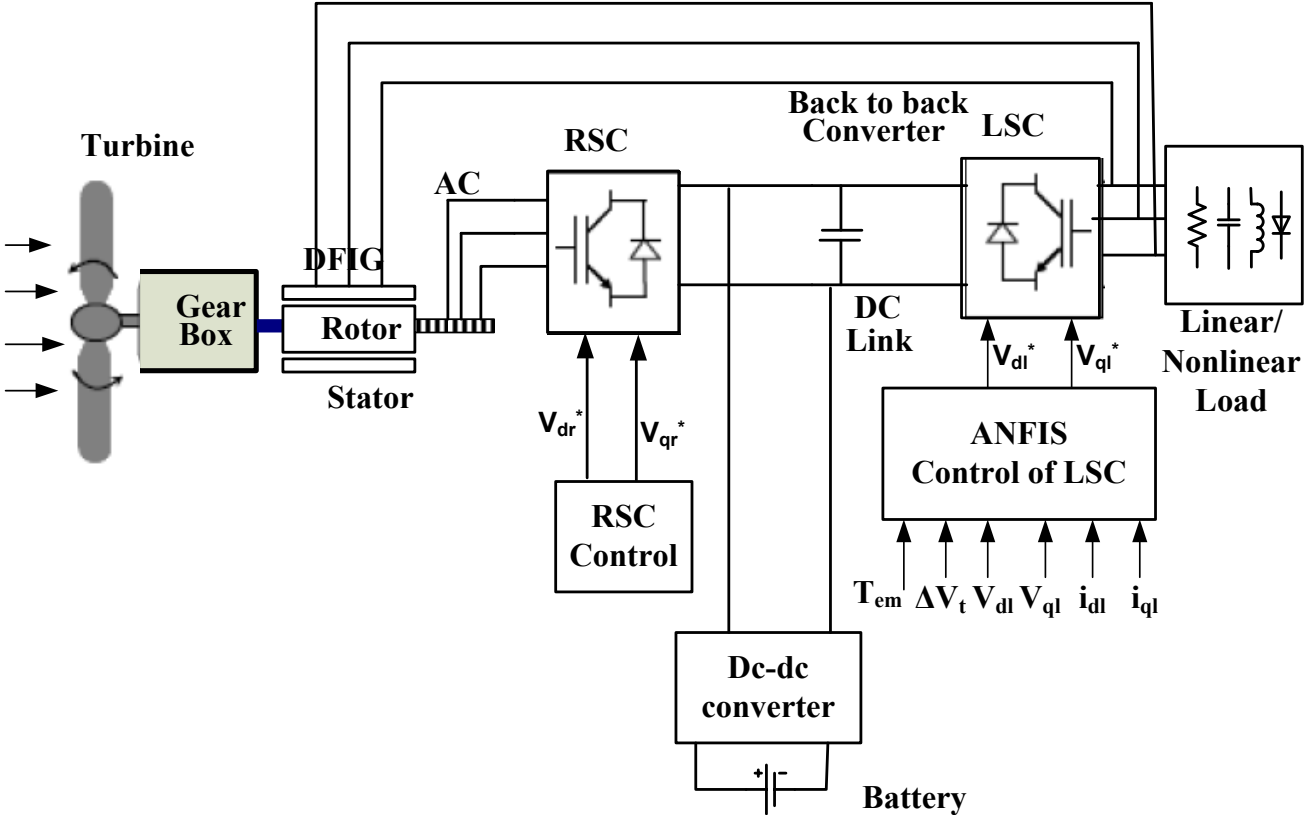


Fig. 6.1. Overall configuration of the SA-WECS with ANFIS based NFC control.

The proposed controller utilizes gradient descend algorithm to adjust the parameters in order to reduce the error function defined in (6.1).

$$V_{\text{err}} = V_x^{\text{ref}} - V_x^{\text{mes}} \quad (6.1)$$

where, V_x^{ref} is the reference d-q axis load side voltage used for training and V_x^{mes} is the measured reference voltages at the previous iteration step. The layers of the ANFIS structure are the same as described in section 5.1. The description is skipped in this chapter to avoid redundancy. However, in standalone mode, the proposed structure utilizes Gaussian membership functions as shown in Fig. 6.2.

The equation for the Gaussian membership function can be expressed as

$$f(x) = e^{-\frac{(x-m_i)^2}{2\delta_i^2}} \quad (6.2)$$

where, x is the input for the layer, m_i and δ_i are the mean value and standard deviation of data respectively for the corresponding membership function.

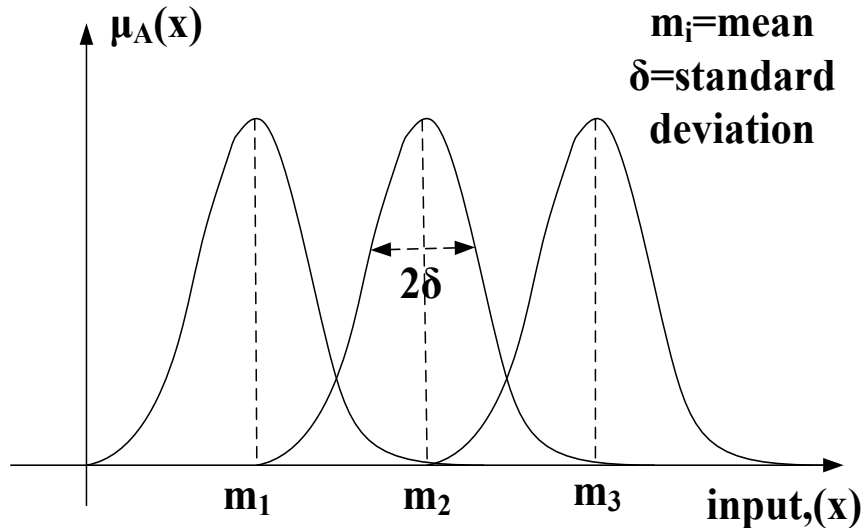


Fig. 6.2. Gaussian membership functions for input data.

6.1.1 ANFIS Based Converter Control Operation in SA Mode

In standalone environment, intermittent wind speed and variable load power demand make the operation of wind-based power systems challenging to maintain constant output voltage and frequency of the DFIG. The battery storage system is integrated in the system and connected to dc link terminal via dc-dc converter to supply the demand in case of energy shortage and as energy storage in the case of excessive wind power generation. The control strategies for the load side converter (LSC) and rotor side converter are described in the following subsections for standalone mode of operation of DFIG.

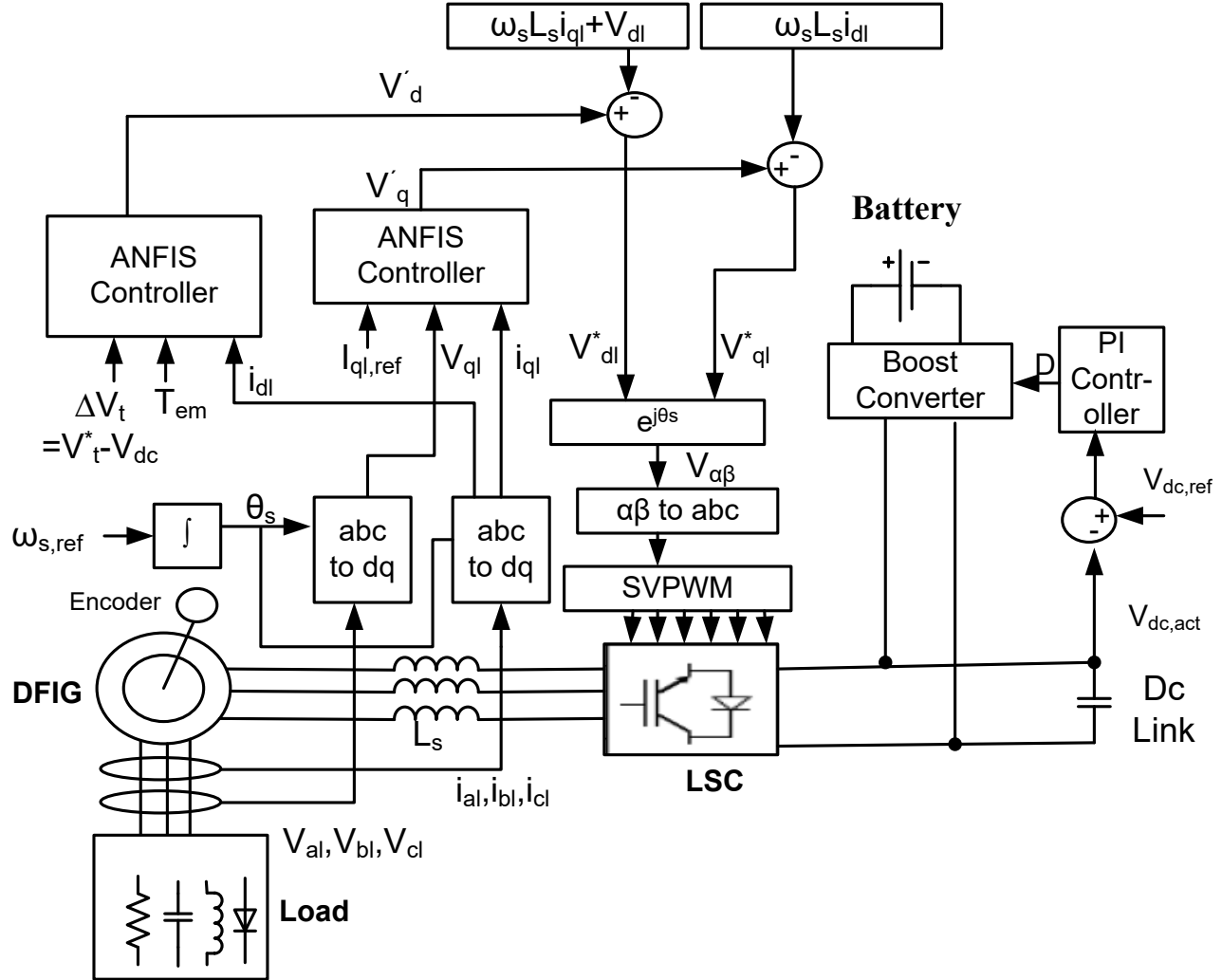


Fig. 6.3. Proposed ANFIS based LSC control for SA mode of DFIG.

6.1.1.1 Proposed ANFIS Based LSC Control for SA Mode

In SA mode, the control complexity lies in the fact that stable grid voltages are not available. The output voltage and frequency have been controlled by the LSC. Fig. 6.3 illustrates the LSC control arrangement for DFIG supplying power to linear and/or nonlinear loads. An ANFIS based on Takagi–Sugeno method having 3:3:3:1:1 architecture is modeled to generate the control d-axis voltage. The number of nodes present in each layer of ANFIS structure is indicated by the numerical ratio. The

model has three inputs, e.g. electromechanical torque (T_{em}), d-axis load current (i_{dl}) and difference between desired terminal voltage and bus voltage ($V_{t,ref} - V_{dc}$). The block yields reference d-axis load voltage (V_{dl}^*) as output. The other ANFIS structure generates the q-axis reference load voltage (V_{ql}^*) by using actual q-axis load voltage (V_{ql}), actual and reference q-axis load current (i_{ql} and $i_{ql,ref}$) as inputs having similar structure with different number of nodes and training data pairs. The trial input-output data for the training of ANFIS structure are generated from the PI controlled converter based DFIG in standalone environment. The reference phase voltage for the load is selected as 590 V whereas, the stator flux position (θ_s) is derived from a free running integral of the stator frequency demand, ω_s^* (60 Hz).

$$\theta_s = \int \omega_s^* dt \quad (6.3)$$

The battery is connected to the dc-link via a boost converter. The converter regulates constant voltage at the dc-link end. When generation exceeds the demand of the load, a dumping load needs to be activated which is not shown in the figure.

6.1.1.2 PI Control of RSC in SA Mode

While the LSC controls the load voltage and frequency, the RSC acts upon reference currents to maintain the stator flux orientation. With this indirect orientation scheme, the q-axis rotor current (i_{qr}) can no longer be used to control the generator torque; this is entirely appropriate for the stand-alone application in which the demand load power and power-share of battery effectively determine the torque for a given shaft speed. It is also possible to control the magnetization of the machine by the variation of d-axis reference rotor current ($i_{dr,ref}$) component as shown in Fig. 6.4. The RSC control configuration utilizes PI controllers to implement the proposed design. Typically, in autonomous operation of DFIG, the rotor side fully contributes to the magnetizing current component. Therefore,

the stator flux is controlled using the q-axis load current i_{ql} . The reference q-axis rotor current, i_{qr}^* is controlled by i_{ql} which forces the orientation of the reference frame along the stator flux vector position.

$$i_{qr}^* = -\frac{L_s}{L_m} i_{ql} \quad (6.4)$$

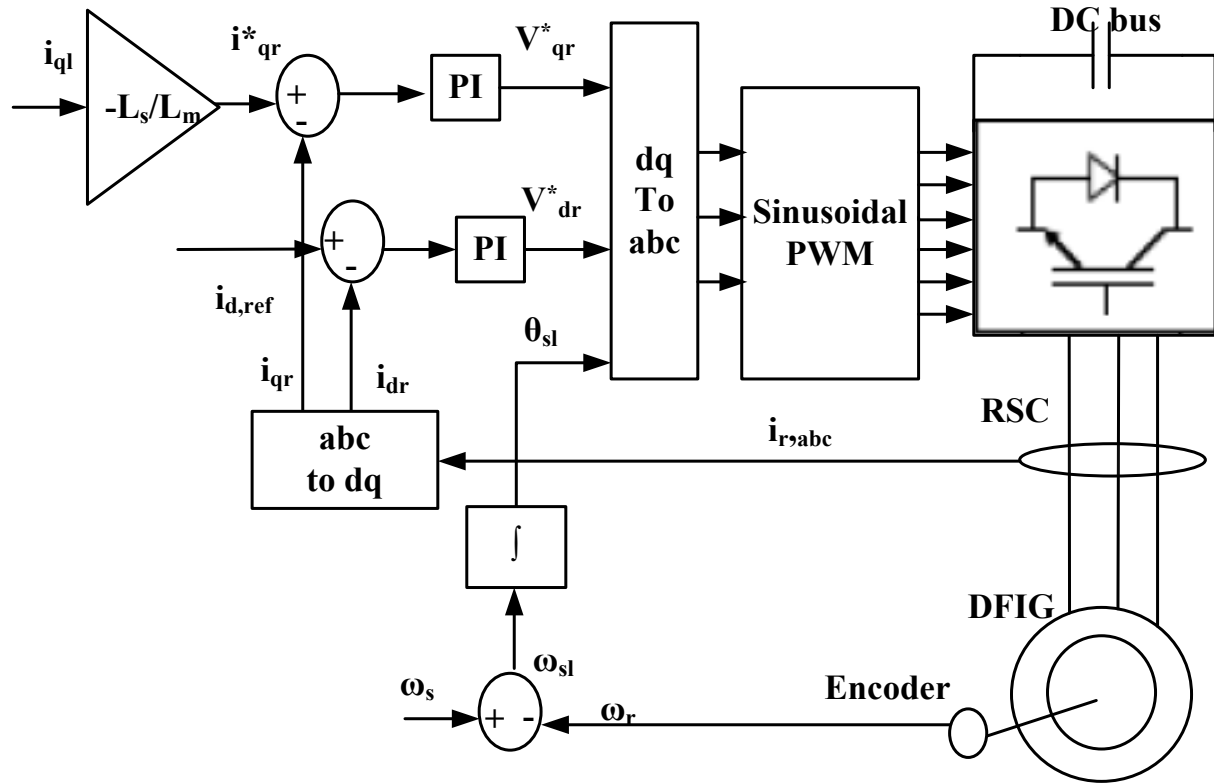


Fig. 6.4. RSC control scheme for SA mode of DFIG.

6.1.2 Simulation Results of the ANFIS Controller in SA Mode

The performance of the proposed ANFIS controller based DFIG-WECS is investigated in simulation at different operating conditions such as variable wind speed, load variation for standalone mode. The target of the LSC control is to keep the output voltage and frequency of the DFIG to a

steady level. For simplification of the control algorithm, it is assumed the load power demand is always less than the generated power of the wind turbine. Fig. 6.5 illustrates the proficiency of the proposed ANFIS based LSC control scheme while there is a step increase of demand power from 0.2 MW to 0.3 MW at load end at $t=0.5$ sec (Fig. 6.5(a)). The aim of the proposed controller is to keep the supply voltage fixed at 590 V(rms) which is accomplished effectively even after sudden change of power demand by users (Fig. 6.5(b)). The voltage signal contains several harmonic components. It is possible to eliminate the harmonic components by adding active harmonic filters. The demand power is fulfilled by the current escalation from 370 A to 540 A as seen in phase \underline{a} load current graph (Fig. 6.5(c)). The selected reference frequency is 30 Hz in this figure.

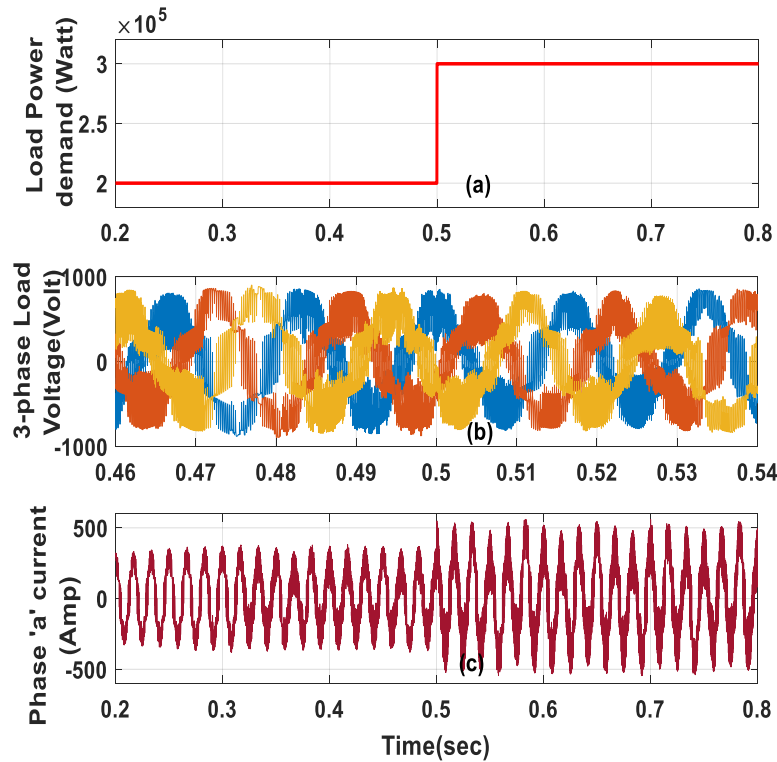


Fig. 6.5. Performance of the proposed ANFIS on SA mode for step increase in load demand: (a) Demand load power, (b) 3-phase voltage across load end, (c) 'a' phase load current.

Whenever the load power demand increases, the speed droop will occur. In the proposed controller, the q-axis load current will also increase when the demanded load power rises. As a result, in the RSC controller, the reference q-axis rotor current will also increase. The q-axis rotor voltage will eventually rise and thus the RSC will force the rotor speed to be restored in its required point. However, a droop control loop needs to be induced in the design to ensure tight frequency control at the load end.

In addition, the output characteristics of the DFIG are tested for varying wind speed as shown in Fig. 6.6. The rotor speed and the dc-link voltage (Figs. 6.6(b) & 6.6(c)) follow the wind speed fluctuation smoothly to maintain the torque and stator power output at the desired level. The LSC controller also ensures the stable output at the load end by maintaining the voltage roughly around 590 V and frequency at 60 Hz. Figs. 6.6(d) and 6.6(e) delineate the results which confirm the efficacy of the ANFIS based control algorithm of LSC for DFIG operated WECS with isolated load. Thus the ANFIS based NFC controller is capable of controlling the generator outputs by offline tuning of control parameters with the variation of wind velocity.

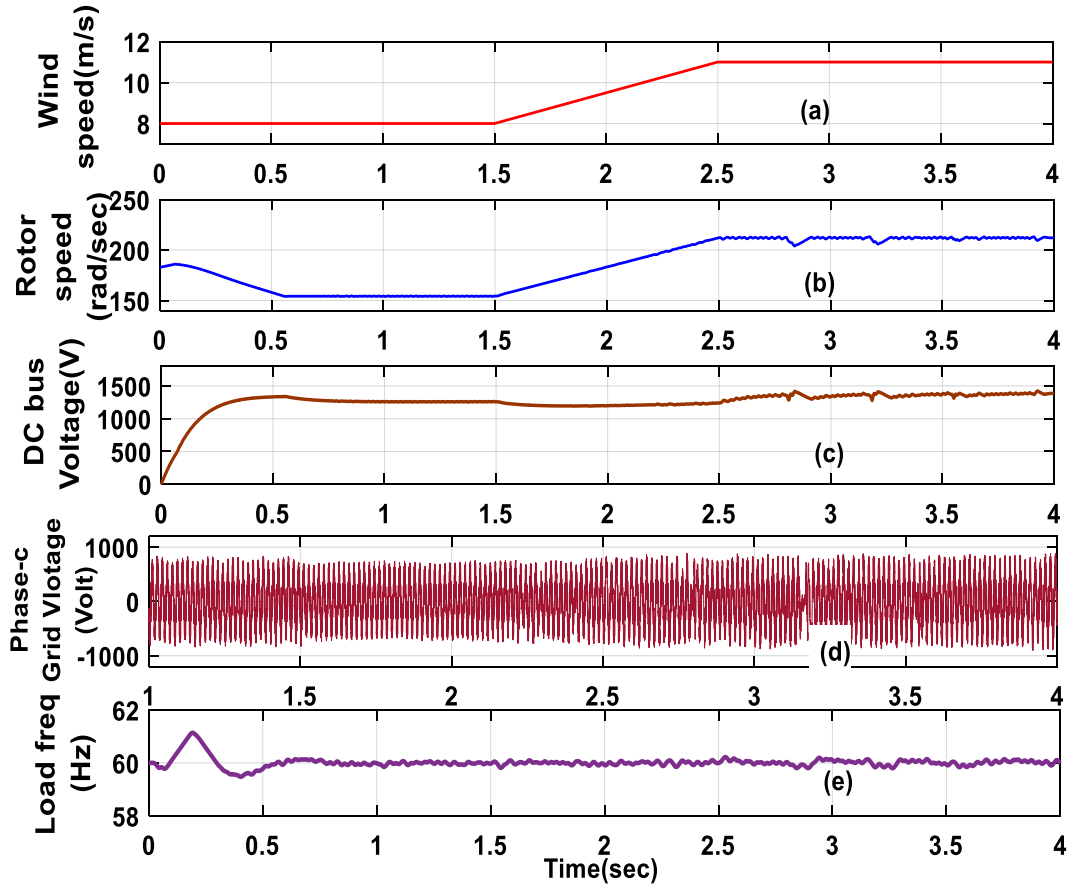


Fig. 6.6. Performance of the control system in SA mode under variable wind speed: (a) Wind speed, (b) Generator speed in rad/sec, (c) DC bus voltage, (d) Grid voltage of phase-c, (e) Frequency of load voltage.

6.2 GWO Based Battery Power Management in Standalone Mode

Although the typical implementation of DFIG are found in grid-connected system for wind power applications, in case of power outage of the main grid, the local power source needs to take over the control of islanded loads. In such cases, the generator should have enough capacity to supply power to local base load. For a standalone application of WECS, the power capacity of auxiliary storage unit is crucial to handle power variations from the involved wind energy source. DFIG can successfully function in isolated mode if supporting energy sources such as battery, fuel cells, internal combustion engine or long term energy storages are connected to the DC or AC side. In Fig. 6.7, the standalone

mode of operation is shown for DFIG based WECS with a battery storage connected at the dc-link end. From the consumer's perspective, having a battery storage system is meaningful only if the energy from the battery can be used in an advantageous manner which allows for better self-consumption and reduction in the cost of purchasing electricity from the grid. In term of storage capacity, it does not need to have such a big capacity which is able to provide backup electricity for several days, but just enough to function as a buffer. Hence, an effective power optimization algorithm is necessary to manage the proficient power exchange from the battery unit to the generator. In this thesis, grey wolf optimization based power management algorithm is chosen for battery power control. The reasons behind the choice of GWO method are its fast convergence and ability to avoid local optima during the search process.

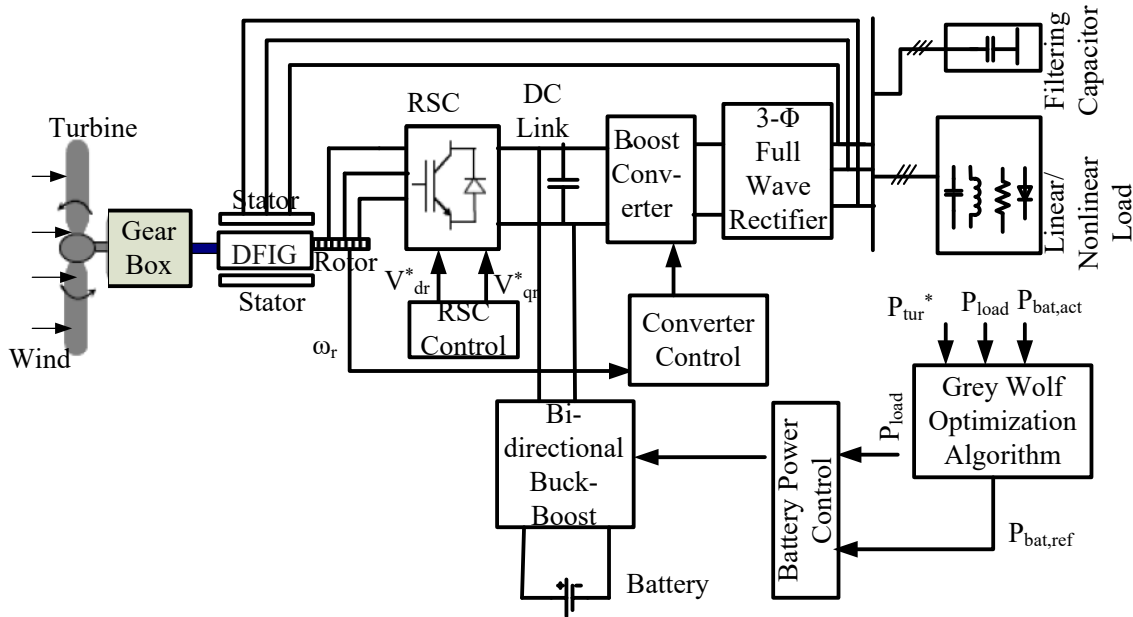


Fig. 6.7. Overall configuration of the DFIG-WECS at standalone mode with battery storage power management.

In standalone mode of operation for DFIG based WECS, the rotor side converter (RSC) ensures the power supply to the consumers at constant amplitude and frequency by controlling the rotor current. In

Fig. 6.7, the standalone mode of operation is shown for DFIG based WECS with a battery storage connected at the DC-link [113].

Table 6.1 Wind turbine, DFIG, battery and load parameters

Parameters	Value
Rated turbine power	350 W
Pitch angle	0°
Equivalent blade radius	1.8 m
Rated generator power	480 VA
dc bus capacitance	1 mF
Load frequency	60 Hz
Rated load voltage (rms)	30 V
Nominal battery voltage	12 V
Rated capacity	8 Ah
Maximum battery power	75 W
Rated load	500 W

The stator of the DFIG is connected to a full wave three phase rectifier block followed by a boost converter circuit. The output of the boost converter provides the required power for the DC-link end. A battery is also connected to the dc-link via a bidirectional Buck-Boost converter. The GWO algorithm implementation block provides the reference battery power ($P_{ref,bat}$) to optimize the power generation and absorption by the battery supply. The dumping load absorbs excessive power when the turbine power exceeds the combined limit of the load demand and maximum battery power which is not shown in the figure. Besides, filtering capacitors are connected to the stator of the DFIG to suppress the high-frequency harmonics from the supply. Table 6.1 shows the specification of the wind turbine, DFIG, battery and load parameters for simulation and real-time implementation.

6.2.1 Description of the Control Operation

The implementation of GWO algorithm based power management for islanded operation of DFIG is suggested in this work for improved control and efficient energy management. The following subsections illustrate the converter schemes and detail analysis of GWO method.

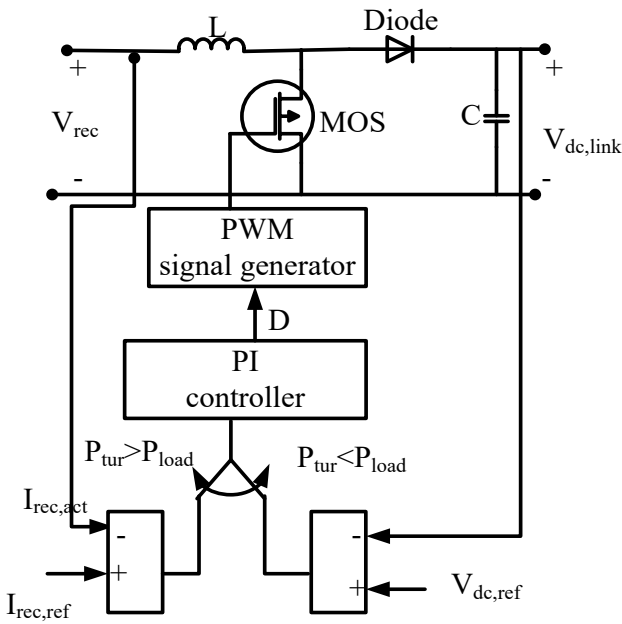


Fig. 6.8. Boost converter control for different operational mode of DFIG.

6.2.1.1 Boost Converter Control Operation

The boost converter input is connected to the rectified dc output. The boost converter control is dependent on the power generation of the wind turbine. There are two possible cases for converter control.

Case-I: If $P_{tur} > P_{load}$, the generated power is greater than the demanded load power. In such case, boost converter operates in current control mode. The target optimum power from a wind turbine can be written as follows [119].

$$P_{opt} = 0.5\rho AC_{opt} \left(\frac{\omega_m R}{\lambda_{opt}}\right)^3 = k_{opt} \omega_m^3 \quad (6.5)$$

where,

$$k_{opt} = 0.5\rho A C_{opt} \left(\frac{R}{\lambda_{opt}}\right)^3.$$

The maximum power point extraction from the wind turbine is ensured by the generation of optimum rectifier output current according to (6.5).

$$I_{rec,ref} = \frac{k_{opt}\omega_m^3 - P_{load}}{\frac{3\sqrt{3}}{\pi}V_{load,peak}} \quad (6.6)$$

The battery keeps charging and the dc-link voltage is determined by the boost converter operation. If the dc-link voltage exceeds the maximum limit, the dumping load is activated for excess power dissipation.

Case-II: When $P_{tur} < P_{load}$, the boost converter switches to voltage control mode. The reference dc-link voltage is calculated from the generated load voltage. The battery discharges in this mode and supplies the demanded current to the rotor converter circuit. The GWO operation block determines the optimum point battery power supply while peak power is extracted from the wind turbine.

6.2.1.2 RSC Control Operation in Standalone Mode

In SA mode, the control complexity lies in the fact that stable grid voltages are not available. The output voltage and frequency need to be controlled by the converters. The RSC is designed to stabilize the load voltage and frequency as shown in Fig. 6.9. The reference rms terminal voltage for the load is chosen as 15 volt for simulation whereas the stator flux position (θ_s) is derived from a free running integral of the stator frequency demand ω_s^* (60 Hz). Typically, in autonomous operation of DFIG, the rotor side fully contributes to the magnetizing current component. With indirect orientation scheme, i_{qr} can no longer be used to control the generator torque. The turbine power, demanded load

power and battery supply effectively determines the torque for a given shaft speed. The stator flux is controlled using the q-axis load current, i_{ql} . The reference q-axis rotor current, i_{qr}^* is controlled according to (6.4).

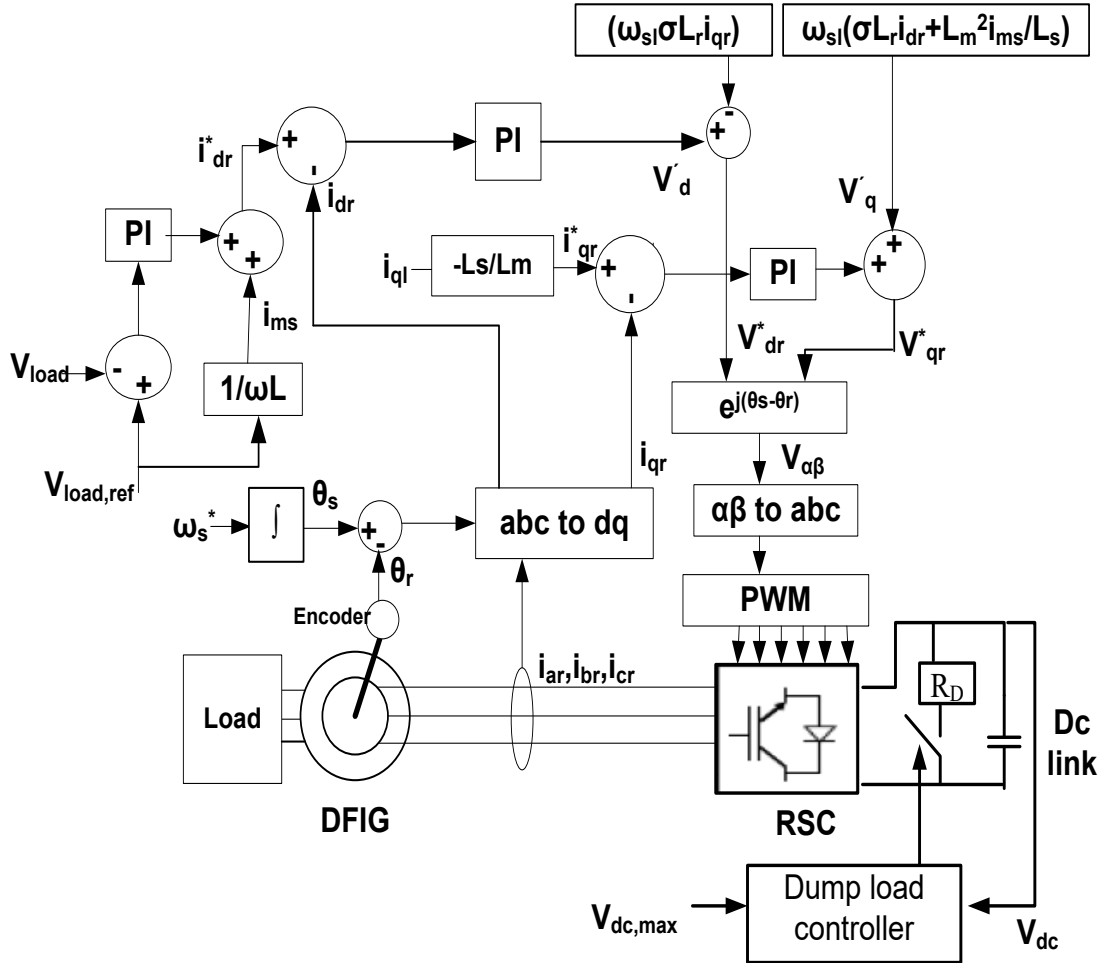


Fig. 6.9. RSC control for SA mode of DFIG.

This current equation forces the orientation of the reference frame along the stator flux vector position. The rotor d-axis current i_{dr} has two components: the magnetizing current $i_{dr,m}$ and load demand current $i_{dr,l}$. The current component $i_{dr,m}$ fulfills the no-load reactive power demand of DFIG and $i_{dr,l}$ contributes to the load reactive power requirements [102]. The reference d-axis rotor current components are shown in (6.7)-(6.9).

$$i_{dr,l}^* = (k_p + k_i s)(V_{load,ref} - V_{load,act}) \quad (6.7)$$

$$i_{dr,m} = \frac{V_{load,act}}{\omega L_m} \quad (6.8)$$

$$i_{dr}^* = i_{dr,l}^* + i_{dr,m} \quad (6.9)$$

The proportional and integral constants for the PI control blocks utilized in boost converter, bidirectional converter RSC control are determined by trial and error method so that the controllers can track the required voltages and currents properly. The component values and control parameters are mentioned in Table 6.2. The simulation block diagram of the proposed scheme is shown in appendix.

6.2.2 Grey Wolf Optimization

In this section, the inspiration of the proposed GWO method is discussed with the mathematical model.

6.2.2.1 Inspiration

Grey wolves (*Canis lupus*) are predators that mostly prefer to live and hunt in groups. The interesting fact of these animals is that they maintain strict social dominant hierarchy. The top member in the hierarchy is the alpha (α) wolf and the subsequent ranks are assigned for beta (β), delta(δ) and omega (ω) wolves. The ω wolves keep exploring in arbitrary domain to improve the global optimization while the α , β , δ guide them towards the fittest position. For mathematical model, it is considered that the alpha provides the fittest solution while beta and delta are in second and third best position, respectively.

6.2.2.1 Encircling Pattern

The prey encircling of grey wolves can be modeled as follows [106]

$$\vec{N} = |\vec{M} \cdot \vec{X}_p(j) - \vec{X}(j)| \quad (6.10)$$

$$\vec{X}(j+1) = \vec{X}_p(j) - \vec{R} \cdot \vec{N} \quad (6.11)$$

Table 6. 2 Boost and bidirectional buck-boost converter parameters

Parameters	Value
<u>Boost converter</u>	
Inductance, L	1 mH
Switching frequency, f	25kHz
Capacitance	1.36 mF
K _p ,k _i	-0.04,-0.08
<u>Bidirectional buck-boost</u>	
<u>converter</u>	
Inductance, L	2.5 mH
Switching frequency, f	25kHz
Capacitance	1000 uF
K _p ,k _i	0.02,0.005

Where j indicates the current iteration, $\vec{R} = 2\vec{k} \cdot \vec{u}_1 - \vec{k}$, $\vec{M} = 2\vec{u}_2$, \vec{X}_p is the current position of the prey, \vec{X} is the current position vector of the wolf, the components of \vec{k} linearly decreases from 2 to 0 and \vec{u}_1, \vec{u}_2 are random vectors in [0,1]. To illustrate (6.10) and (6.11) the position update of wolves is shown in Fig. 6.10 in a two-dimensional space. It is evident that a grey wolf in the position of (x, y) can update its position according to the position of the prey (x_p,y_p). The fittest position can be searched in random space by adjusting the vectors \vec{M} and \vec{R} . For instance, a wolf can reach in position (x_p-x,y) can be reached by setting $\vec{M} = (1,1)$ and $\vec{R}=(0,1)$.

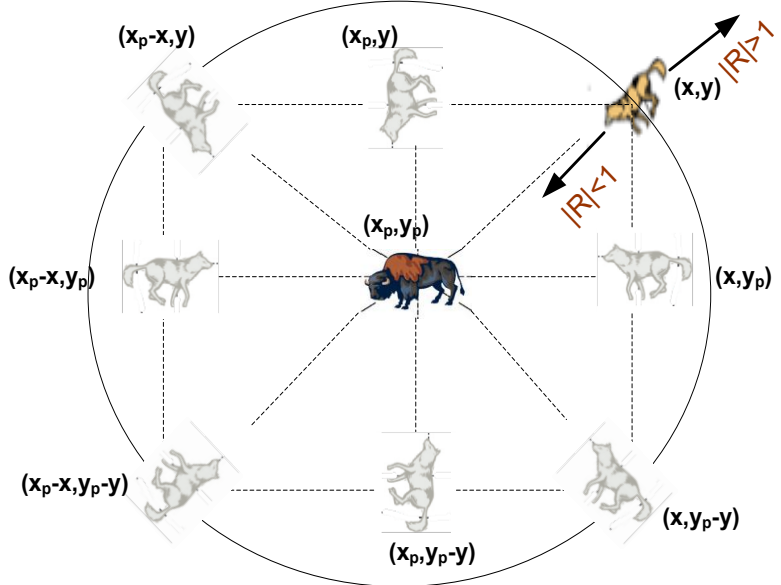


Fig. 6.10. Position update pattern of wolves using random vectors.

6.2.2.2 Position Update Mechanism

Grey wolves have the ability to recognize the location of prey and encircle them. Alpha leads the hunting and beta and delta are likely to follow the alpha. During optimization, the first three fittest solutions are obtained by these three entities. Other wolves are considered as GO and reposition themselves with respect to the position of α , β and δ . The following equations are utilized to the positions of the wolves in updating their positions.

$$\vec{N}_\alpha = |\vec{M}_1 \cdot \vec{X}_\alpha - \vec{X}| \quad (6.12)$$

$$\vec{N}_\beta = |\vec{M}_2 \cdot \vec{X}_\beta - \vec{X}| \quad (6.13)$$

$$\vec{N}_\delta = |\vec{M}_3 \cdot \vec{X}_\delta - \vec{X}| \quad (6.14)$$

Where, \vec{X}_α is the position of alpha, \vec{X}_β is the position of beta, \vec{X}_δ is the position of delta and \vec{X} indicates the current position of the solution. $\vec{M}_1, \vec{M}_2, \vec{M}_3$ are random vectors. Equations (6.15)-(6.18) calculate

the distance between current solution and alpha, beta and delta respectively. The final position can be calculated by utilizing the following equations.

$$\vec{X}_1 = \vec{X}_\alpha - \vec{R}_1 \cdot \vec{N}_\alpha \quad (6.15)$$

$$\vec{X}_2 = \vec{X}_\beta - \vec{R}_2 \cdot \vec{N}_\beta \quad (6.16)$$

$$\vec{X}_3 = \vec{X}_\delta - \vec{R}_3 \cdot \vec{N}_\delta \quad (6.17)$$

$$\vec{X}(j+1) = \frac{\vec{X}_1 + \vec{X}_2 + \vec{X}_3}{3} \quad (6.18)$$

Here, $\vec{R}_1, \vec{R}_2, \vec{R}_3$ are random vectors and j is the number of iterations.

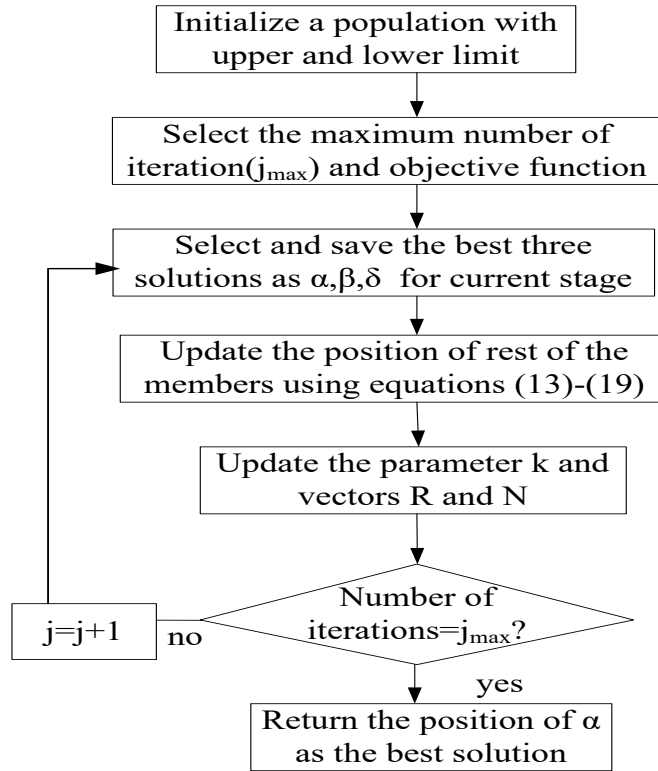


Fig. 6.11. Flow chart of GWO algorithm.

The vectors \vec{R} and \vec{N} are random and adaptive and these two vectors provides the exploration and exploitation for the GWO algorithm. The exploration mechanism is activated when \vec{R} is greater

than 1 or less than -1. The vector \vec{N} also defines exploration if it has a value greater than 1. Oppositely, the exploitation is executed when $|R| < I$ and $N < I$ as shown in Fig. 6.10. In coding scheme, R is decreased linearly during optimization in order to emphasize exploitation as the iteration counter increases. However, N is generated arbitrarily throughout optimization to ensure exploration or exploitation at any stage. The flow chart in Fig. 6.11 illustrates the general steps of the GWO algorithm. The coding scheme for GWO algorithm is given in appendix.

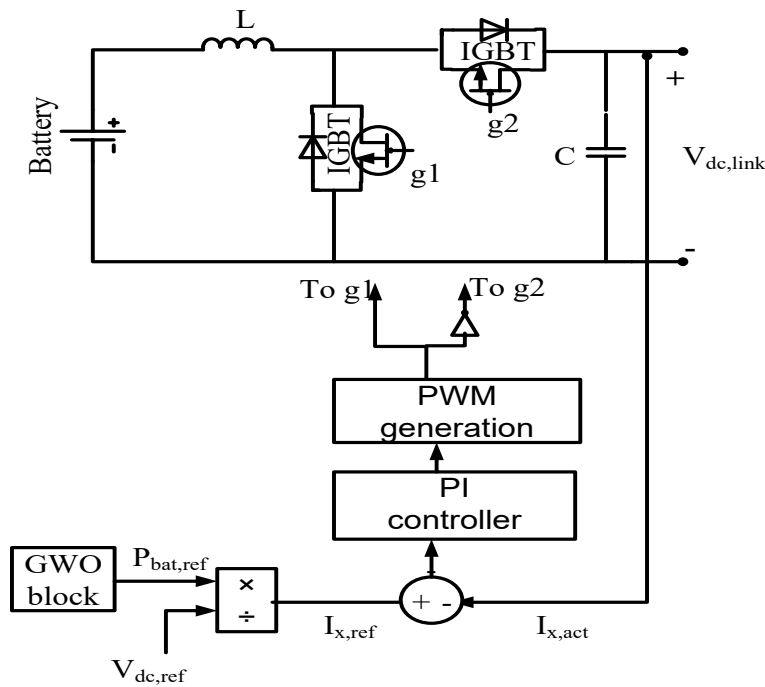


Fig. 6.12. Battery power control with bidirectional buck-boost converter.

6.2.3 Power Management Strategy for Battery Storage

The battery storage system is connected with the proposed DFIG via a bi-directional buck-boost converter to accommodate the power flow in both directions. When the battery is discharged, the switch g_2 is consistently turned off and the converter operates in boost mode [114]. When switch g_1 is turned off, the current flows through the body diode of switch g_1 . The bidirectional converter switches

to buck mode when the battery is charged. When the battery is completely charged, the GWO power generation block saturates at its maximum limit. At this point, the dc-link voltage keeps increasing until the power dumping load gets activated. The bidirectional power converter continuously regulates the power flow from and towards the battery which is controlled by the battery control block as shown in Fig. 6.12.

The GWO technique is utilized to obtain the reference battery power for the inverter control unit. The GWO block collects the actual battery power ($P_{bat,act}$), demand load power (P_{load}) and generator power as the input and generates the optimum power reference signal for the storage power control block by utilizing the following objective function.

$$f_{ob} = (P_{load} - k_{opt}\omega_m^3 - P_{bat,act})^2 \quad (6.19)$$

The actual battery power is measured by multiplying the battery voltage and current obtained from the battery model. For the GWO coding scheme, the maximum and minimum power limit of the search space is set as $P_{bat,max}$ and $-P_{bat,max}$, respectively. The maximum number of iteration is set as 500. After each iteration the error calculated by the objective function is stored while the best three solutions of battery reference power are saved as α, β and δ . The other members in the search space are updated concurrently by modifying random vectors R and N. After attaining maximum iteration, the final value of α is returned as the optimized reference value for battery power.

6.2.4 Dumping Power Control

When the dc link voltage exceeds its maximum limit, the dump load control is activated to absorb the excessive energy. The exact nature of the dump load depends on the application of standalone system. Space heating via resistive load or water pumping for irrigation can be two possible options [115]. The required condition for activation of the dumping power load is shown in (6.20).

$$P_{dump} = \begin{cases} P_{tur} + P_{bat,max} - P_{load}, & \text{when } v_{dc} > v_{dc,max} \\ 0, & \text{when } v_{dc} < v_{dc,max} \end{cases} \quad (6.20)$$

6.3 Simulation Results

The efficacy of the proposed GWO algorithm based battery power control strategy has been tested in simulation for standalone DFIG under variable wind speed and load changing conditions. Sample results are presented below.

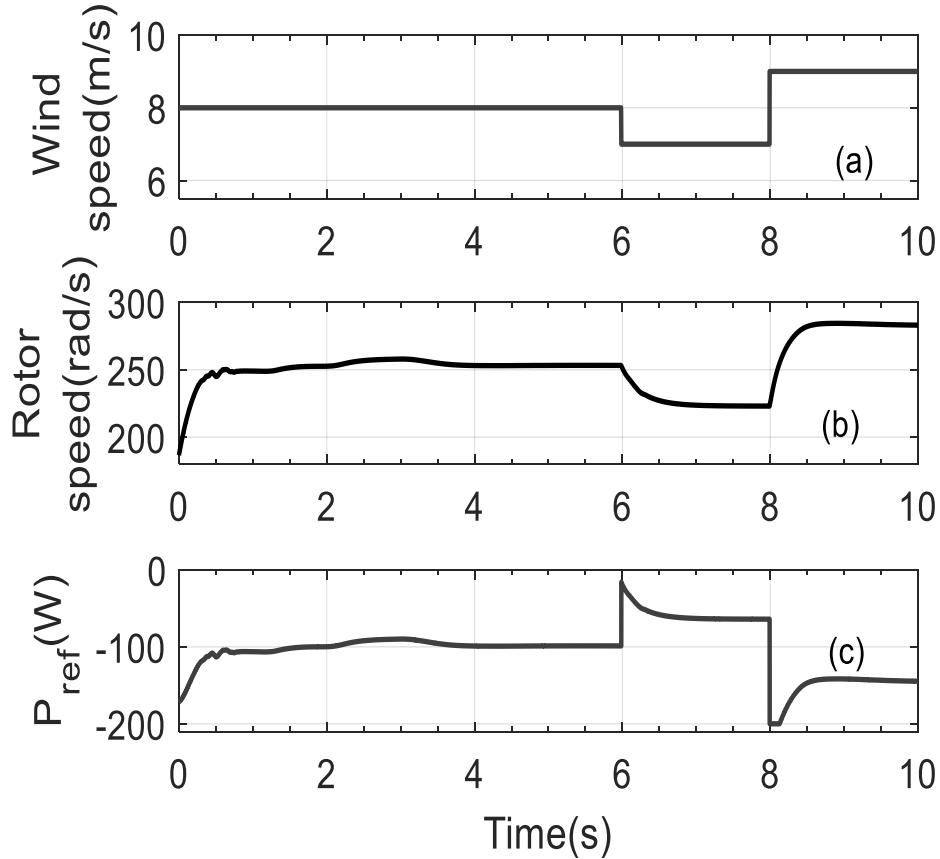


Fig. 6.13. Performance in the proposed standalone DFIG for wind speed variation: (a) Step changes in wind speed, (b) Variation in rotor speed, (c) Corresponding change in reference power generation from GWO block.

In Fig. 6.13, the rotor speed variation and change in reference power generation from the GWO block is illustrated while wind speed undergoes though step changes within the range of 6 ms^{-1} to 10 ms^{-1} (Fig. 6.13(a)). The rotor speed varies accordingly to ensure the MPPT operation while the GWO

block generates the power to calculate the reference charging current for the battery unit load (Fig. 6.13(b,c)). Fig. 6.14 shows the performance of the converters while the wind turbine power varies (Fig. 6.14(a)). The reference and actual current at the input of the boost converter is depicted in Fig. 6.14(b). The generated current successfully follows the tracking current which ensures maximum power extraction by the rectifier. Furthermore, the optimization battery power is executed by the GWO algorithm as the output current of the bidirectional buck-boost converter tracks the reference current (Fig. 6.14(c)).

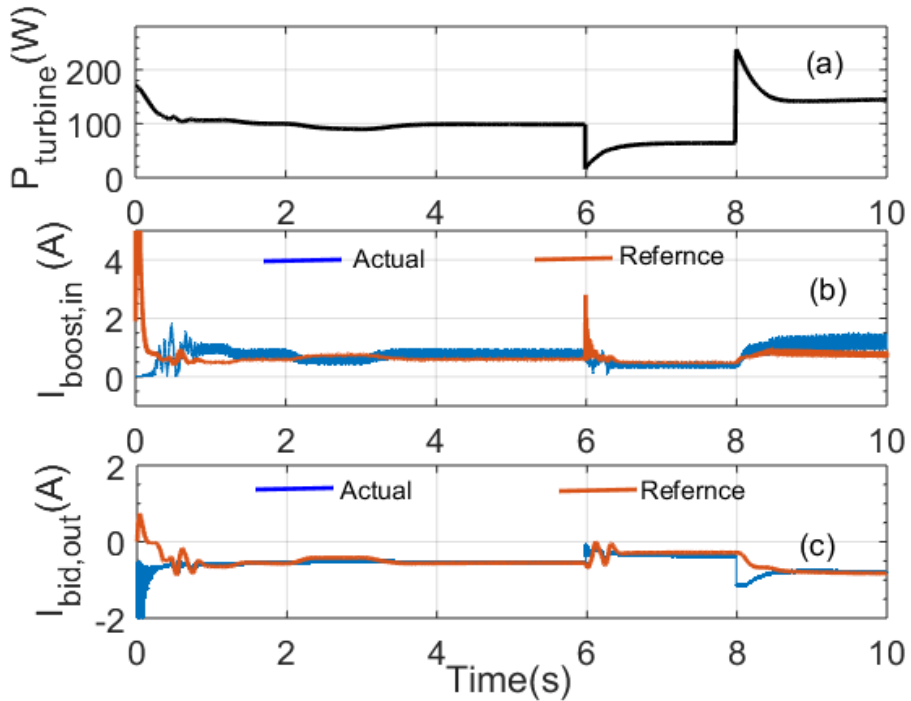


Fig. 6.14. Boost converter and bidirectional controller control performance for the proposed standalone DFIG under variation of wind power: (a) Variation in turbine power, (b) Reference and actual input current of the boost converter, (c) Reference and actual current at the output of the bidirectional buck-boost converter.

In Fig 6.15, the RSC control performance is shown. The terminal voltage and frequency is stabilized at approximately 15 V(rms) and 60 Hz respectively (Fig. 6.15(a,b)). Also, the corresponding dc-link voltage, rectifier output voltage, battery voltage and current are depicted in Fig. 6.15(c-f)). The output

frequency shows slight deviation with the variation of wind speed. To manage tight frequency control, a droop control loop has to be introduced in the design.

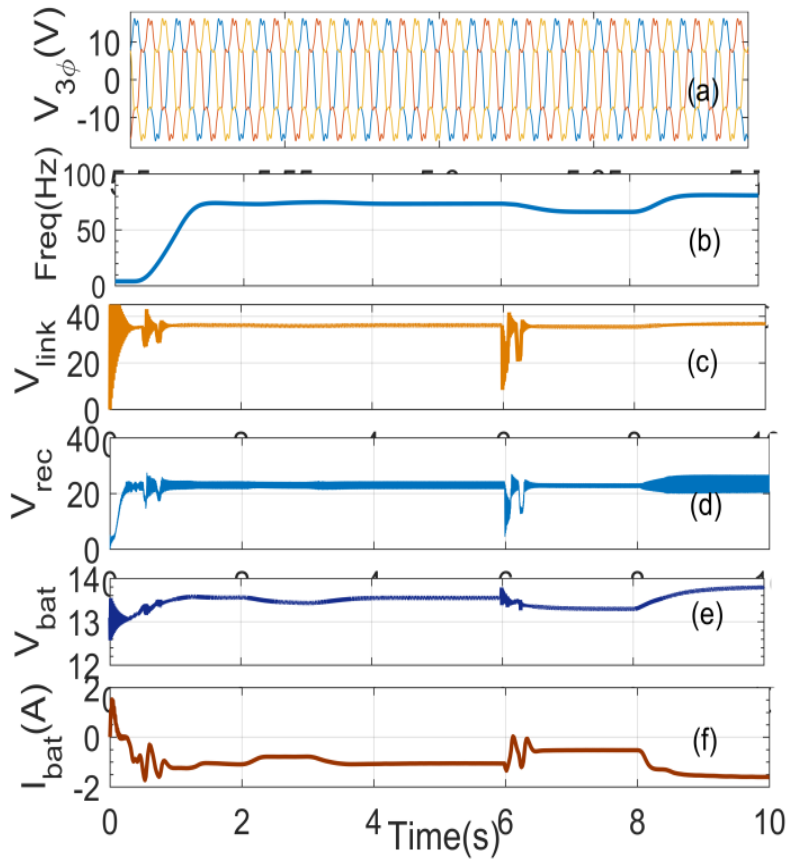


Fig. 6.15. Performance of RSC and battery control unit for step variation in wind speed: (a) Zoomed in Load voltage (b) load frequency (Hz), (c) DC link voltage, (d) Corresponding output voltage of 3-phase rectifier, (e) Battery voltage , (f) Battery current variation.

Fig. 6.16 illustrates the converter performances for three different loads (500 , 1000 and 1500Ω). The terminal voltage and frequency vary very slightly for change in loads (Fig. 6.16(a,b)) which proves the effectiveness of the RSC control. The error between the actual load frequency and the reference frequency is shown Fig. 6.16(c). The GWO reference power variation and actual output current of bidirectional buck-boost converter are also demonstrated in Fig. 6.16(d,e) for different loads. The zoom-in views of the Figs. 6.16(a-e) are depicted in Figs. 6.16(f-j), respectively for better illustration.

The proposed power management scheme ensures instant power control of the battery unit through its energy management algorithm.

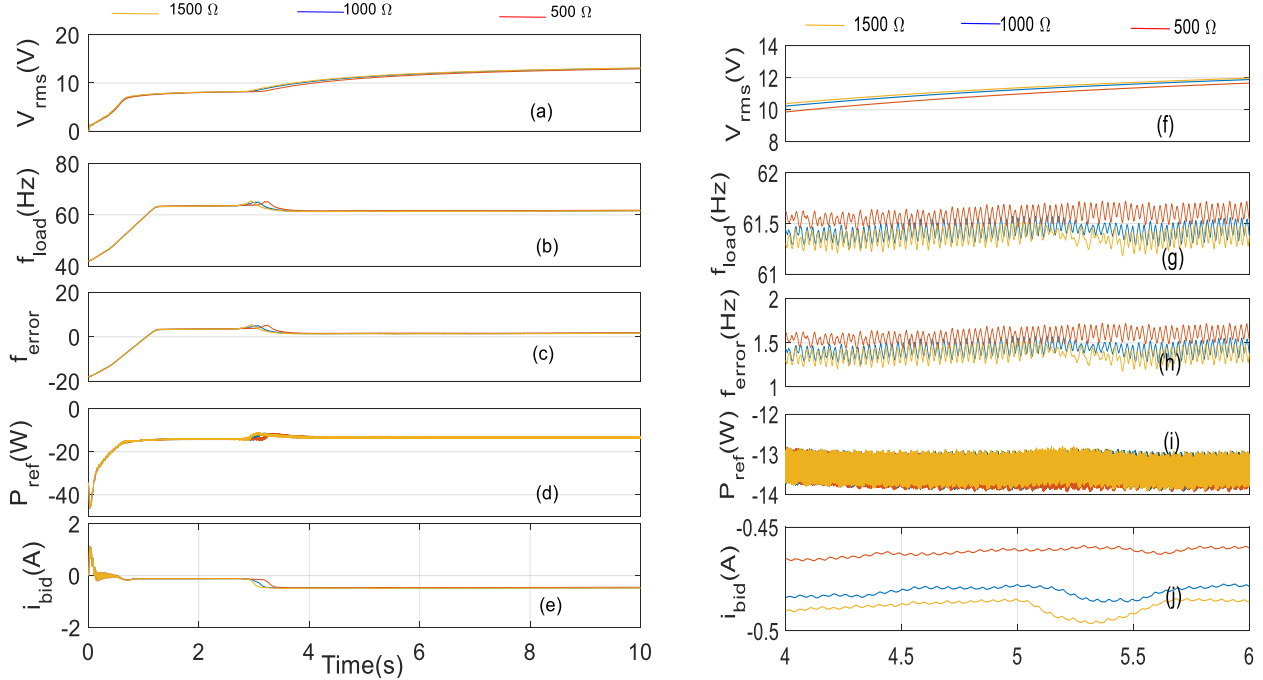


Fig. 6.16. Performance of RSC and converter controllers for variation in load: (a) rms terminal voltage, (b) Load frequency, (c) Difference between reference and actual frequency, (d) Reference power generated by GWO block,(e) Corresponding output current of bidirectional buck-boost converter (f) Zoom-in view of (a), (g) Zoom-in view of (b), (h) Zoom-in view of (c), (i) Zoom-in view of (d), (j) Zoom-in view of (e).

Fig. 6.17(d) shows the convergence curve of the error function for 300 iterations for the corresponding wind variation. The convergence of the actual and reference current output from the bidirectional converter proves that the converter is capable to control the current for battery power optimization (Fig. 6.17(c)). The reference power generated from the GWO block is shown in Fig. 6.17(b).

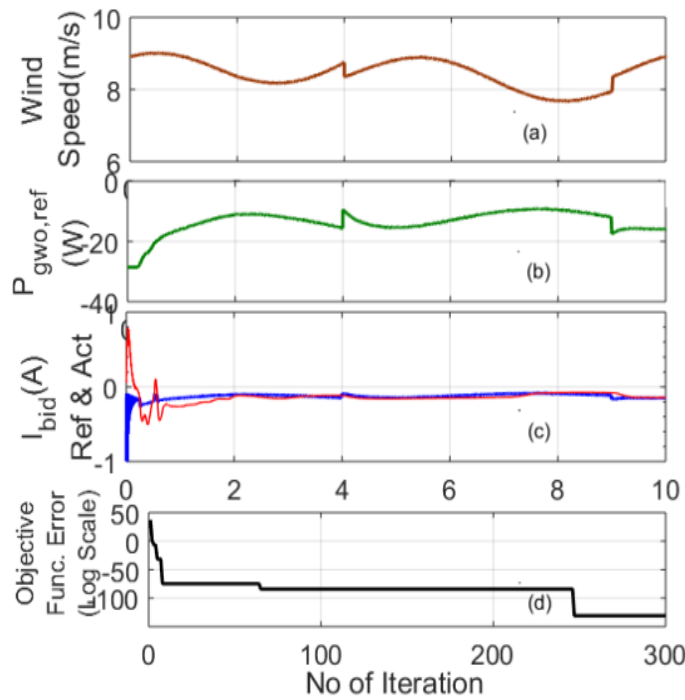


Fig. 6.17. Performance of the GWO algorithm: (a) Variation in turbine power, (b) Reference power generated by GWO block, (c) Reference and actual current of bidirectional converter, (d) Convergence curve for the objective function (in \log_{10} scale).

6.4 Real-Time Implementation and Results

A prototype for the proposed GWO method based battery power control for DFIG-WECS has been built to test the performance in real-time as shown in Fig. 6.18. The experimentation is done with a 480 VA DFIG prototype in the laboratory using MATLAB-Simulink and dSPACE DS1104 board. The parameters for the DFIG and wind turbine are mentioned in Table 6.1. Fig. 6.19 illustrates the RSC control performance for the proposed standalone system. The three phase load voltage is shown for a reference rms terminal voltage is selected as 25 volt at 25 Hz. In this case, the wind speed is chosen as 6 m/s through the command input terminal of the wind turbine emulator.

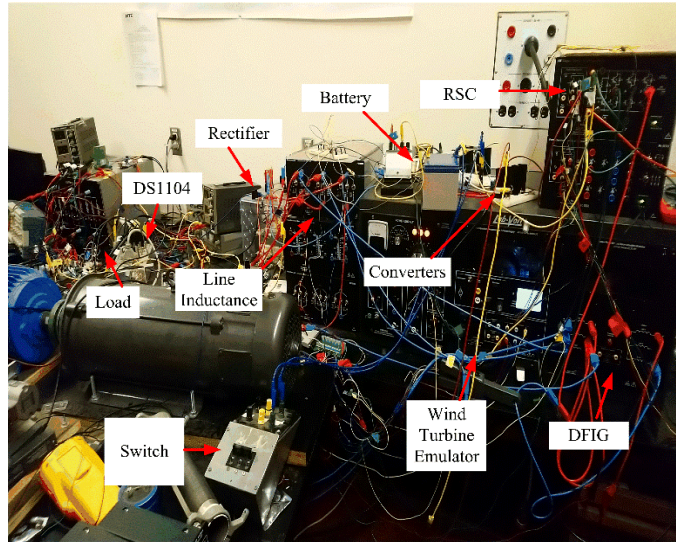


Fig. 6.18. Experimental setup for the proposed standalone DFIG-WECS.

Attempts have been made to operate the system with a reference load frequency of 60 Hz. The machine experiences huge vibration and loud noise on that condition and the RSC fails to follow the command signal above 30 Hz. Further investigation is required to fix the issue.

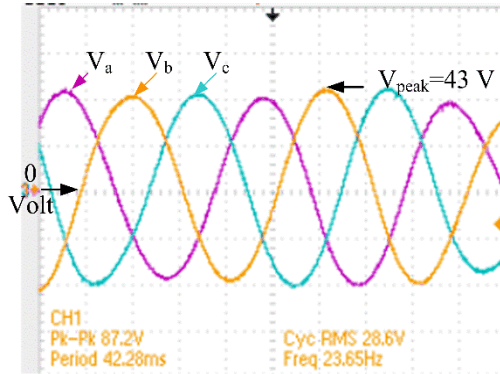


Fig. 6.19. Voltage output for the standalone system at wind speed 6 m/s and 600Ω load.

Fig. 6.20 shows the boost converter control performance while maintaining the maximum power point tracking at variable wind speed. The turbine power varies while the wind speed is changed in between 4.5 m/s to 11 m/s. The rectifier output current follows the variation to ensure the maximum power extraction according to (6.6).

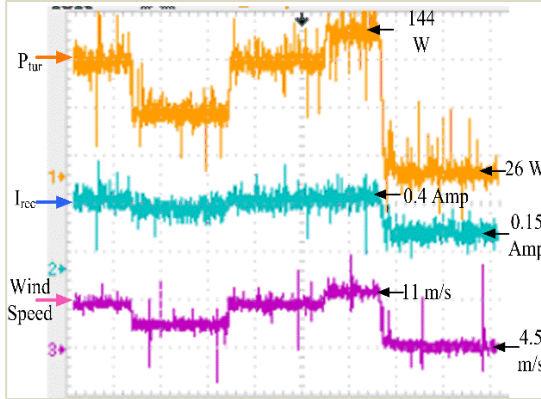


Fig. 6.20. Performance of the boost converter controller with MPPT scheme.

The battery power is controlled through the bidirectional buck-boost converter while GWO block generates the reference output current from the converter. The reference battery power (P_{gwo}) changes when turbine speed and turbine power alters. The corresponding variation of the output current from the bidirectional converter suggests that the controller is capable of maintaining the optimum power flow from and towards the battery as shown in Fig. 6.21.

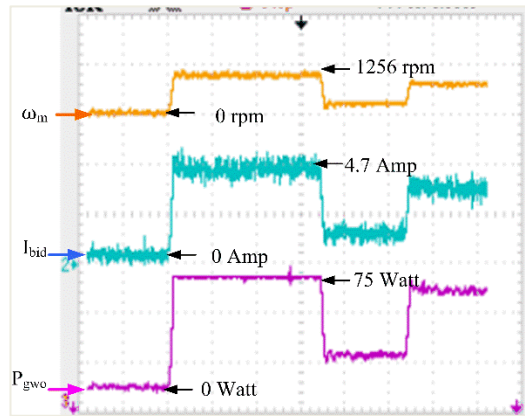


Fig. 6.21. Performance of the proposed GWO based power flow control using bidirectional buck-boost converter.

6.5 Discussion

A novel ANFIS based NFC scheme for DFIG operated WECS has been developed in this chapter. The performance of the proposed controller has been investigated for isolated load under

different operating conditions. The simulation results suggest that the LSC and GSC controller altogether contribute to MPPT control by adjusting the rotor speed and machine torque with the variation of wind speed. Also, the proposed controller is capable of maintaining constant voltage and frequency at the load end even after the abrupt variation of the required power demand and wind speed. The analysis of the proposed scheme suggests the efficacy of the designed ANFIS architecture based controller in standalone operating mode of DFIG-WECS. Furthermore, a novel grey wolf optimization based power management algorithm for isolated-DFIG based WECS is presented. The performance of the proposed control system is investigated for variable conditions. The GWO algorithm effectively generates the power reference for the converter control of the battery source. The convergence speed and ability to avoid local optima in random search space by the GWO scheme suggests the superiority and improved robustness over other optimization techniques. The RSC control helps to maintain constant voltage and frequency at the load end while the rectifier and boost converter ensures constant dc-link voltage and current control during abrupt variation of the load power demand and wind speed. Simulation results show satisfactory performance of the designed control system by coordinating the power flow of the battery unit along with proper regulation of voltage and frequency at the load terminal. The model is successfully implemented in real-time laboratory prototype with limited frequency control and the effectiveness of the proposed scheme is verified under changing conditions.

Chapter 7

Conclusion

7.1 Summary

A comprehensive study on various converter control techniques for wind energy conversion system has been outlined in this thesis. The summary of the thesis is outlined as follows.

- A general overview and historical background on wind energy conversion system are highlighted at the beginning of the thesis. In literature review, various WECS control techniques and recent trends on wind power control system development have been focused. The literature review on the existing and state-of-the-art technology helps to build up a solid conceptual background on the research topic and to identify the specific objectives to work on.
- The major components of wind turbine are discussed briefly with their functionality. The mathematical model of wind flow generation, wind power generation equation with turbine parameters, application-oriented variation in power converter topologies and illustration of generator model, particularly the analytical representation of the steady state, state space and d-q axis model of DFIG have been discussed in detail.
- A new adaptive step size based MPPT controller has been proposed with PI controlled GSC and RSC power control mechanism. Detail model of the proposed MPPT controller with converter control diagram is illustrated. Also, the performance of the proposed controller is compared with the conventional HCS and TSR control techniques.
- The analytical model of a nonlinear controller based on adaptive backstepping algorithm for stabilization of the WECS is illustrated incorporating loss minimization algorithm of the DFIG. A parameter adaptation technique has been devised to adapt with parameter uncertainties.

- An ANFIS based neuro-fuzzy controller is illustrated for GSC and RSC control for grid-connected DFIG driven WECS for DFIG-WECS. The performance of the controller is tested in simulated in normal grid voltage for reactive power and wind speed variation.
- The comparative analysis among the control techniques, e.g. PI control, adaptive backstepping based nonlinear control and ANFIS based NFC control has been presented for grid-connected DFIG. The benefits and drawbacks of each controller are investigated on different operating conditions.
- A low computational NFC controller is designed for converter control of grid-connected DFIG based WECS during voltage dip condition. The control operation is investigated for symmetric and asymmetric voltage dips. The robustness of the designed controller is tested by analyzing the voltage, power and current associated with dc-link, rotor and stator of DFIG.
- A novel grey wolf optimization based battery power management algorithm for isolated DFIG based WECS has been presented which targets enhanced power optimization and longevity of battery storage with rigorous voltage and frequency control and dumping load management.
- The proposed model for MPPT and nonlinear control of DFIG-WECS in grid connected mode and GWO technique based battery power control in DFIG in standalone mode have been successfully implemented in the real-time environment using DSP controller board DS1104 for a laboratory 480 VA DFIG. The proposed schemes are tested under variable operating conditions to verify the performance of the controllers.

7.2 Major Contributions of the Thesis

The major contributions of this thesis are listed below:

- An adaptive step size based HCS controller is developed to mitigate the deficiencies of other techniques by incorporating wind speed measurement in the controller design of DFIG driven WECS. The function-based adaptive control scheme evaluates the step size by measuring the wind speed and turbine power slope. The proposed controller reduces the steady-state power fluctuation and provides better speed tracking performance compared to the conventional HCS-MPPT controller and constant TSR based MPPT control technique.
- An adaptive backstepping based nonlinear controller has been introduced that incorporates parameter uncertainties and machine nonlinearities in the design stage while ensuring stability of the closed-loop control system through Lyapunov stability theorem. The aim of the controller is to regulate the converter control voltages incorporating the machine parameter adaptation along with a loss reduction model. The simulation and experiment results demonstrate that the proposed control scheme exhibits better grip over the rotor side and grid side converter control of DFIG-WECS compared to the conventional PI controller.
- A low computational adaptive network fuzzy interference system based NFC scheme is developed to add robustness in control of DFIG based WECS under normal grid voltage. The precondition and consequent parameters of the ANFIS controller are continuously updated based on back-propagation and hybrid learning scheme, which generates voltage control outputs by utilizing TSK fuzzy rule.
- For voltage dip situation in grid-connected DFIG, a detail ANFIS based NFC scheme is provided for wind-powered generator. The proposed controller adjusts the positive sequence d-q axis current components both at the grid and rotor sides by supplying required reactive power to the grid to minimize the effect of grid voltage fluctuations. The superiority of the proposed model is proven by its ability to cope with symmetric and asymmetric voltage dip conditions.

- An offline tuned adaptive neuro-fuzzy controller for standalone DFIG-WECS has been developed. The proposed scheme demonstrates improved dynamic performance under variable wind speed and load conditions by maintaining stable output voltage and frequency.
- A meta-heuristic robust optimization technique called grey wolf optimization is proposed to provide efficient energy flow to and from the battery in standalone operation of DFIG-WECS. The proposed system consists of bidirectional buck-boost converter, PI controlled rotor side converter and GWO based battery storage control to provide improved energy management strategy for islanded operation of DFIG in wind power system. The efficacy of the proposed configuration is verified through simulation and laboratory experiments for standalone operation mode of DFIG. However, the RSC control shows limitation on load frequency control above 30 Hz.

7.3 Future Scopes of Work

This thesis develops and investigates different types of converter control techniques to achieve either high dynamic performance and/or loss minimization of DFIG-WECS for both grid-connected and standalone mode operations. However, there are scopes to improve the developed techniques further which are outlined below.

- In the development of the adaptive step size based MPPT controller, a number of parameters have been used in the proposed model. In variable speed operation, the determination of these parameters could be cumbersome. In future work, a smart algorithm will be developed to determine the adaptive step size with respect to wind speed and turbine power variation.
- In the design of the adaptive backstepping based nonlinear control scheme, any external disturbance hasn't been considered. The performance of the proposed controller is not compared with any other nonlinear controller. So, future work can be done by designing other popular robust control schemes, such as H_∞ controller, sliding mode controller, passivity based controller for DFIG-WECS.

- The ANFIS based NFC has been designed for the compensation of voltage dip of grid-connected DFIG. However, the design has limited application due to the lack of hardware solutions in case of severe voltage dip or extreme imbalance condition. In future, a complete model can be developed to have low voltage ride-through capability combining software and hardware for extreme grid voltage dip condition.
- GWO based battery power optimization is developed for energy management of standalone operation of DFIG-WECS. In future, other intelligent control such as particle swarm optimization, artificial bee colony optimization will be developed to compare the performance of the proposed scheme with the advanced techniques.
- Another major challenge for DFIG driven WECS is the execution of an efficient, cost effective energy management algorithm in remote area power system equipped with hybrid renewable power supply or systems that are connected to microgrid. Also, there are challenges in smooth transition of power supply while switching occurs between islanded and grid-connected power system. These challenges need to be investigated in future works.

7.4 Concluding Remarks

An elaborated synopsis on different control techniques for DFIG driven WECS has been presented in this thesis. Starting from the concept of conventional PI control, the thesis presents advanced intelligent control techniques such as ANFIS based NFC control for grid-connected mode and GWO algorithm based control for standalone mode of operation for DFIG-WECS. The developed techniques are verified in a laboratory prototype. By conducting this research, various control-related challenges of wind energy conversion system have been solved. The proposed concepts will benefit the operation of wind farms both economically and technically if the models are implemented in the real-world environment.

References

- [1] World Energy overview, US Department of Energy, International Energy Annual, 1999 (IEA:1999).
- [2] S. Mathew, Wind Energy-Fundamentals- Resource Analysis and Economics, Berlin Heidelberg: Springer-Verlag, 2006.
- [3] International Energy Agency (IEA), Energy and Climate Change -World Energy Outlook Special Report, pp.36, WEO 2015.
- [4] Global wind report-2018, pp.26, Global Wind Energy Council (GWEC), December 2018.
- [5] T. Ackermann, Wind Power in Power Systems, West Sussex, England : John Wiley & sons Ltd, 2005.
- [6] J.R. Ramler, R.M. Donovan, —Wind turbines for electric utilities: Development status and economics”. DOE/NASA/1028-79/23, NASA TM-79170, AIAA-79-0965,1979.
- [7] S.J. Savonius , —The S-rotor and its applications”, Journal of Mechanical Engineering , vol. 53, no. 5, pp.333-338,1931.
- [8] H. Snel, —Review of the Present Status of Rotor Aerodynamics”, Wind Energy, vol. 1, no. 1, pp. 46-69, 1998.
- [9] R.W. Thresher, D.M. Dodge, —Trends in the Evolution of Wind Turbine Generator Configurations and Systems”, Wind Energy, vol. 1, no. 1, pp. 70-85, 1998.
- [10] E. Hau, Wind Turbines: Fundamentals, Technologies, Application, Economics, Berlin Heidelberg: Springer-Verlag, 2006.
- [11] A. Miller, E. Muljadi, and D. S. Zinger, —Avariable speed wind turbine power control”, IEEE Transaction on Energy Conversion, vol. 12, pp. 181 -187, June 1997.
- [12] L. J. Fingersh and P.W. Carlin, —Results from the NREL variable-speed test bed,” ASME 17th Wind Energy Symposium ,USA, January 1998, pp. 233–237.
- [13] D. Kumar, K. Chatterjee, —Areview of conventional and advanced MPPT algorithms for wind energy systems”, Renewable and Sustainable Energy Reviews, vol. 55, pp. 957–970, March 2016.
- [14] I.K. Buehring, L.L. Freris, —Control policies for wind-energy conversion systems” IEE Proceedings C - Generation, Transmission and Distribution ,vol. 128 , no. 5, pp. 253,Sep. 1981.
- [15] G. Hua, Y. Geng, —Anovel control strategy of MPPT taking dynamics of wind turbine into account”, 37th IEEE Power Electronics Specialist Conference, Jeju, South Korea, 2006, pp. 1–6.
- [16] M.A. Abdullah, A.H.M. Yatim, C.W. Tan, R. Saidur, —Areview of maximum power point tracking algorithms for wind energy systems”, Renewable and Sustainable Energy Reviews, vol. 16, pp. 3220–3227, 2012.

- [17] Y. Zhao, C. Wei, Z. Zhang, W. Qiao, —A review on position/speed sensorless control for permanent-magnet synchronous machine-based wind energy conversion systems”, IEEE Journal of Emerging and Selected Topics in Power Electronics, vol. 1, pp. 203–216, 2013.
- [18] S. Morimoto, H. Nakayama, M. Sanada, Y. Takeda, —Sensorless output maximization control for variable-speed wind generation system using IPMSG”, IEEE Transactions on Industry Applications, vol. 41, pp. 60–67, 2005.
- [19] M. G. Simoes, B. K. Bose, and R. J. Spiegel, —Design and performance evaluation of a fuzzy-logic-based variable-speed wind generation system”, IEEE Transactions on Industry Applications., vol. 33, pp. 956–965, July/Aug. 1997.
- [20] M. N. Uddin and N. Patel —Maximum Power Point Tracking Control of IPMSG Incorporating Loss Minimization and Speed Sensorless Schemes for Wind Energy System”, IEEE Transactions on Industry Applications , vol. 52, no. 2, pp. 1902-1912, April 2016.
- [21] J. Hui , A. Bakhshai, P. Jain —A sensor-less adaptive maximum power point extraction method with voltage feedback control for small wind turbines in off-grid applications” IEEE Journal Emerging on Selected Topic of Power Electronics, vol. 3, pp.817-828, Sep. 2015.
- [22] H. Li, K.L. Shi, P.G. McLaren, —Neural-network-based sensorless maximum wind energy capture with compensated power coefficient”, IEEE Transactions on Industry Applications, vol. 41, no. 6, Dec. 2005.
- [23] C. Wei, Z. Zhang, W. Qiao, L. Qu, —Reinforcement-learning-based intelligent maximum power point tracking control for wind energy conversion systems”, IEEE Transactions on Industrial Electronics, vol. 62, pp. 6360-6370, Oct. 2015.
- [24] R. Yan . N. Masood, T.K. Saha, —Anew tool to estimate maximum wind power penetration level: In perspective of frequency response adequacy”, Applied Energy, vol. 154, pp. 209–220, Sep 2015.
- [25] G.D. Moor, H.J. Beukes, —Maximum power point trackers for wind turbines”, IEEE 35th Annual Power Electronic Specialist Conference, Germany, 2004, pp. 2044–2049.
- [26] M.R. Kazmi, H. Goto, H.-J.Guo, O. Ichinokura, —Anovel algorithm for fast and efficient speed-sensorless maximum power point tracking in wind energy conversion systems”, IEEE Transactions on Industrial Electronics, vol. 58, pp. 29–36, 2011.
- [27] J. Yaoqin, Y. Zhongqing, C. Binggang, —Anew maximum power point tracking control scheme for wind generation”, International Conference on Power System Technology, China, 2002, pp. 144–148.
- [28] V. Agarwal, R.K. Aggarwal, P. Patidar, and C. Patki, —Anovel scheme for rapid tracking of maximum power point in wind energy generation systems,” IEEE Transactions on Energy Conversion, vol. 25, pp. 228-236, March 2010.

- [29] Q. Wang and L. Chang, —Aintelligent maximum power extraction algorithm for inverter-based variable speed wind turbine systems,” IEEE Transactions on Power Electronics, vol. 19, pp. 1242-1249, Sept. 2004.
- [30] E. Koutroulis and K. Kalaitzakis,—Design of a maximum power tracking system for wind-energy-conversion applications” IEEE Transactions on Industrial Electronics , vol. 53, pp. 486-494, April 2006.
- [31] M. Azzouz,A.I. Elshafei and H. Emara—Evaluation of fuzzy-based maximum power-tracking in wind energy conversion systems”, IET Renewable Power Generation, vol. 5, pp.422-430, Nov. 2011 .
- [32] V. Calderaro, V. Galdi,A. Piccolo and P. Siano, —Afuzzy controller for maximum energy extraction from variable speed wind power generation systems”, Electric Power System Research, vol. 78, pp. 1109–1118, June 2008.
- [33] R. Chedid, F. Mrad, M. Basma –Intelligent control of a class of wind energy conversion systems”, IEEE Transactions on Energy Conversion, vol. 14, pp. 1597-1604, December 1999.
- [34] Y. Higuchi, N. Yamamura, and M Ishida, —An improvement of performance for small-scaled wind power generating system with permanent magnet type synchronous generator”, 26th Annual Conference of the IEEE Industrial Electronics Society (IECON), Japan, Oct. 2000.
- [35] M.A. Abdullah, A.H.M. Yatim , C.W. Tan, —Anonline optimum-relation-based maximum power point tracking algorithm for wind energy conversion system”, Australasian Universities Power Engineering Conference (AUPEC), Australia, Sep-Oct. 2014, pp. 1-6.
- [36] A. Urtasun, P. Sanchis and L. Marroyo, —Small wind turbine sensorless MPPT robustness analysis and lossless approach”, IEEE Transactions on Industry Applications, vol. 50, pp. 4113-4121,Nov. 2014.
- [37] M. Azzouz , A.I. Elshafei and H. Emara, —Evaluation of fuzzy-based maximum power-tracking in wind energy conversion systems”, IET Renewable Power Generation, Vol. 5, pp. 422-430, 2011.
- [38] H. Nian, P. Cheng and Z. Q. Zhu, —Coordinated direct power control of DFIG system without phase-locked loop under unbalanced grid voltage conditions”, IEEE Trans. on Power Electronics, vol. 31, pp. 2905-2917, April 2016.
- [39] S. Z. Chen, N. C. Cheung, K. C. Wong and J. Wu, —Integral sliding-mode direct torque control of doubly-fed induction generators under unbalanced grid voltage”, IEEE Transactions on Energy Conversion, vol. 25, pp. 356-368, June 2010.
- [40] M. K. Bourdoulis and A. T. Alexandridis, —Direct power control of DFIG Wind systems based on nonlinear modeling and analysis”, IEEE Journal of Emerging and Selected Topics in Power Electronics, vol. 2, pp. 764-775, Dec 2014.

- [41] J. Hu, J. Zhu and D.G. Dorrel, —Acomparative study of direct power control of AC/DC converters for renewable energy generation”, 37th Annual Conference on IEEE Industrial Electronics Society (IECON), Melbourne, VIC, Australia, 2011,pp. 3578-3583.
- [42] M. A. Rahman, D. M. Vilathgamuwa, M. N. Uddin, and K. Tseng, —Nonlinear control of interior permanent-magnet synchronous motor”, IEEE Transaction on Industry Applications, vol. 39, pp. 408-416, March/April 2003.
- [43] W. Qiao, L Qu and R. G. Harley, —Control of IPM synchronous generator for maximum wind power generation considering magnetic saturation”, IEEE Transaction on Industry Applications, vol. 45, no. 3,pp. 1095-1105, May 2009.
- [44] P. Xiong and D. Sun, —Backstepping-based DPC strategy of a wind turbine-driven DFIG under normal and harmonic grid voltage”, IEEE Transaction on Power Electronics, vol. 31, pp. 4216-4225, June 2016.
- [45] N. Khemiri, A. Khedher, M. F. Mimouni, —Abackstepping control strategy applied to the connected hybrid renewable energy system operated in MPPT”, 8th International Conference and Exhibition on Ecological Vehicles and Renewable Energies (EVER), Monte Carlo, Monaco,2013.
- [46] M. E. Azzaoui, H. Mahmoudi and C. Ed-dahmani, —Backstepping control of a doubly fed induction generator integrated to wind power system”, 2nd International Conference on Electrical and Information Technologies (ICEIT), Tangiers, Morocco, 2016.
- [47] J. Koupeny, M. Siebrecht; S. Luecke; A. Mertens, —Observer-based online parameter estimation of doubly fed induction generators based on the gradient descent method”, International ETG Congress, Bonn, 2015, pp. 1-8.
- [48] B. Bossoufi ,M. Karim, A. Lagrioui, M. Taoussi, A. Derouich, —Observer backstepping control of DFIG-generators for wind turbines variable-speed: FPGA-based implementation”, Renewable Energy, vol. 81,pp. 903-917, 2015.
- [49] X. Wang, D. Sun and Z. Q. Zhu, —Resonant-based backstepping direct power control strategy for DFIG under both balanced and unbalanced grid conditions”, IEEE Transactions on Industry Applications, vol. 53, pp. 4821-30, Sep. 2017.
- [50] A. Tohidi, H. Hajieghrary, and M. A. Hsieh, —Adaptive disturbance rejection control scheme for DFIG-based wind turbine: theory and experiments” IEEE Transactions on Industry Applications, vol. 52, no. 3, pp. 2006-2015, May/June 2016.
- [51] S. Ebrahimkhani, —Rbust fractional order sliding mode control of doubly-fed induction generator (DFIG)-based wind turbines”, ISA Transactions (Elsevier), vol. 63, pp. 343-354,2016.
- [52] E. Kamal, M. Oueidat, A. Aitouche, and R. Ghorbani, —Rbust scheduler fuzzy controller of DFIG wind energy systems”, IEEE Transactions on Sustainable Energy, vol. 4, no. 3, pp. 706-715, July 2013.

- [53] M.Bezza, B.EL.Moussaoui and A.Fakkar, —Sensorless MPPT fuzzy controller for DFIG wind turbine”, Energy Procedia(Elsevier), Vol. 18, pp. 339 – 348,2012.
- [54] X. Yin, Y.G. Lin, W. Li, H.W. Liu, and Y.J. Gu , —Fuzzy-logic sliding-mode control strategy for extracting maximum wind power”, IEEE Transactions on Energy Conversion, vol. 30, no. 4, pp. 1267–1278, December 2015.
- [55] B.Hamane , M. Benghanem , A.M. Bouzid , A. Belabbes ,M. Bouhamida ,A. Draouf , —Control for variable speed wind turbine driving a doubly fed induction generator using fuzzy-PI control”, Energy Procedia (Elsevier), vol. 18, pp. 476 – 485,2012.
- [56] X. ZHANG, D. XU, Y. LIU, —Intelligent control for large-scale variable speed variable pitch wind turbines”, Journal of Control Theory and Applications, vol. 3, pp. 305- 311, 2004.
- [57] H. M. Jabr, D. Lu and N. C. Kar, —Design and implementation of neuro-fuzzy vector control for wind-driven doubly-fed induction generator”, IEEE Transactions on Sustainable Energy, vol. 2, no. 4,pp. 404-413, October 2011.
- [58] X. Kong, X. Liu, K. Y. Lee, —Data-driven modelling of a doubly fed induction generator wind turbine system based on neural networks” , IET Renewable Power Generation, vol. 8, no. 8,pp. 849-857, Nov. 2014.
- [59] E.B. Muhando,T. Senju, K. Uchida, H. Kinjo, T. Funabashi, —Stochastic inequality constrained closed-loop model-based predictive control of MW-class wind generating system in the electric power supply”, IET Renewable Power Generation, vol. 4, no. 1,pp. 23-35, 2010.
- [60] B. Beltran, M. El Hachemi-Benbouzid, T. Ahmed-Ali, —Second-order sliding mode control of a doubly-fed induction generator driven wind turbine” , IEEE Transaction of Energy Conversion, vol. 27, no. 2, pp. 261–269,2012.
- [61] Grid Code—High and Extra High Voltage, E.ON Netz GmbH, Bayreuth, Germany, April 2006.
- [62] M. Tsili and S. Papathanassiou, —A review of grid code technical requirements for wind farms,” IET Renewable Power Generation, vol. 3, no. 3, pp. 308–332,Sep. 2009.
- [63] Y. Wang, Q. Wu, W. Gong, and M. P. S. Gryning, — $H\infty$ robust current control for DFIG-based wind turbine subject to grid voltage distortions”, IEEE Transactions on Sustainable Energy, vol. 8, no. 2, pp. 816-825, April 2017.
- [64] C. Wessels, F. Gebhardt, and F. W. Fuchs, —Fault ride-through of a DFIG wind turbine using a dynamic voltage restorer during symmetrical and asymmetrical grid faults”, IEEE Transactions on Power Electronics, vol. 26, no. 3,pp. 807-815, March 2011.
- [65] Z. Xie, X. Zhang, S. Yang and L. Wang, —Improved ride-through control of DFIG during grid voltage swell”, IEEE Transactions on Industrial Electronics, vol. 62, no. 6,pp. 3584-3594, June 2015.

- [66] M. Rahimi M. Parniani, –Efficient control scheme of wind turbines with doubly fed induction generators for low voltage ride-through capability enhancement”, IET Renewable Power Generation, vol. 4 , no. 3 , pp. 242-252, May 2010.
- [67] M. Lawan, M. Camara, J. Raharijaona, –Wind turbine and batteries with variable speed Diesel generator for micro-grid applications” 7th International Conference on Renewable Energy Research and Applications (ICRERA), Peris,France,2018.
- [68] N. Mendis, K. M. Muttaqi, S. Sayeef and S. Perera, –Standalone operation of wind turbine-based variable speed generators with maximum power extraction capability” , IEEE Transactions on Energy Conversion, vol. 27, no. 4, December 2012.
- [69] B. Housseini ; A. F. Okou ; R. Beguenane, –Energy management strategy of on-grid/off-grid wind energy battery-storage system”, IEEE Canadian Conference on Electrical and Computer Engineering (CCECE), Vancouver, BC, Canada,May 2016.
- [70] R. Peña, R. Cardenas , E. Escobar , J. Clare , P. Wheeler ,—Control strategy for a doubly-fed induction generator feeding an unbalanced grid or stand-alone load”, Electric Power Systems Research, vol. 79, no. 2, pp. 355-364, Feb. 2009.
- [71] S. Mahmodicherati, M. Elbuluk, Y. Sozer, –Direct power control of a doubly fed induction generator wind power system with seamless transition between stand-alone and grid-connected modes”, IEEE Energy Conversion Congress and Exposition (ECCE), 18-22 Sept., 2016.
- [72] A. Gundavarapu, H. Misra, A. K. Jain, –Direct torque control scheme for DC voltage regulation of the standalone DFIG-DC system”, IEEE Transactions on Industrial Electronics, vol. 16, no. 5, pp-3502-3512, 2016.
- [73] A. B. Ataji , Y. Miura , T. Ise and H. Tanaka, –Direct voltage control with slip angle estimation to extend the range of supported asymmetric loads for stand-alone DFIG”, IEEE Transactions on Power Electronics, vol. 31, no. 2, pp. 1015-1025, March 2015.
- [74] Y. Zhang and B. T. Ooi, –Stand-alone doubly-fed induction generators (DFIGs) with autonomous frequency control”, IEEE Transactions on Power Delivery, vol. 28, no. 2, pp. 752-759, April 2013.
- [75] G. Iwanski, –DFIG based standalone power system operating at low load conditions”, 13th European Conference on Power Electronics and Applications, 2009,Barcelona,Spain,.

- [76] R. Cardenas , R. Peña, J. Proboste, G. Asher,, J. Clare, –MRAS observer for sensorless control of standalone doubly fed induction generators”, IEEE Transactions on Energy Conversion, vol. 20, pp. 710 – 718, December 2005.
- [77] S. Agrawal, S. R. Mohanty, V. Agarwal, –Harmonics and interharmonics estimation of DFIG based standalone wind power system by parametric techniques” International Journal of Electrical Power & Energy Systems (Elsevier), vol. 67, pp. 52-65, May 2015.
- [78] S. R. Paital, S. Patra A. K. Singh, A. Mohanty, P. K. Ray, –Reactive power compensation using PSO controlled UPFC in a microgrid with a DFIG based WECS”, Annual IEEE India Conference (INDICON), Dec.2015, New Delhi, India.,
- [79] P. M. Anderson, A. Bose, –Stability simulation of wind turbine systems”, IEEE Transactions on Power Apparatus and Systems, vol. 102, no. 12, pp.3791-3795, December 1983.
- [80] B. Wu,Y. Lang, N. Zargari,S. Kouro, *Power Conversion and Control of Wind Energy Systems* , IEEE Press , John Wiley & Sons ,2011.
- [81] S. Müller, M. Deicke & W. D. Doncker, –Doubly fed induction generator systems for wind turbines”, IEEE Industry Applications Magazine ,vol. 8,no. 3, May-June, 2002.
- [82] <http://www.ni.com/example/31272/en/>
- [83] P.C. Krause,O. Wasynczuk, S.D. Sudhoff , Analysis of Electric Machinery and Drive Systems, IEEE Press, Wiley, New York, 1995.
- [84] L. H. Hansen, L. Helle, F. Blaabjerg, E. Ritchie, S. Munk-Nielsen, H. Bindner, P. Sørensen and B. Bak-Jensen, –Conceptual survey of generators and power electronics for wind turbines”, Risø-R-1205(EN), Risø National Laboratory, Roskilde, Denmark, December 2001.
- [85] P.C. Krause, C.H. Thomas, –Simulation of symmetrical induction machinery”, IEEE Transactions on Power Apparatus and Systems, vol. 84 , no. 11 , pp. 1038-1053, Nov. 1965.
- [86] R. Cardenas ; R. Pena ; G. Tobar ; J. Clare ; P. Wheeler ; G. Asher, –Stability analysis of a wind energy conversion system based on a doubly fed induction generator fed by a matrix converter”, IEEE Transactions on Industrial Electronics, vol. 56, pp. 4194 – 4206, Oct. 2009.
- [87] M. Kesraoui, N. Korichi, A. Belkadi , –Maximum power point tracker of wind energy conversion system” Journal of Renewable Energy, vol. 36, pp. 2655–2662, 2011.
- [88] T. Tanaka, T. Toumiya and T. Suzuki, –Output control by hill-climbing method for a small scale wind power generating system”,Renewable Energy, vol. 12, pp.387-400, December 1997.

- [89] C. Patsios, A. Chaniotis, A. Kladas, —Ahybrid maximum power point tracking system for grid-connected variable speed wind-generators” , IEEE Power Electronics Specialists Conference(PESC) , pp. 1749–1754, 2008.
- [90] C.Y. Lee, Y.X. Shen, J.C. Cheng, Y.Y. Li, C.W. Chang, —Neural networks and particle swarm optimization based MPPT for small wind power generator”, Vol. 60, World Academy of Science, Engineering and Technolog , pp. 17–23, 2009.
- [91] M. N. Uddin, I. K. Amin, —Adaptive step size based hill-climb search algorithm for MPPT control of DFIG-WECS with reduced power fluctuation and improved tracking performance”, Electric Power Components and Systems, vol. 46, no. 19-20, pp. 2203-2214, 2018.
- [92] D. G. Taylor, —Nonlinear control of electric machines: an overview”, IEEE Control Systems Magazine, vol. 14 , no. 6 , Dec. 1994.
- [93] G. Abad, J. López, M. Rodríguez, L. Marroyo, G. Iwanski, Doubly Fed Induction Machine, Modeling and Control for Wind Energy Generation, IEEE Press Series on Power Engineering, Wiley Publications, 2011.
- [94] I. K. Amin and M. N. Uddin, —Nonlinear control operation of DFIG based WECS with stability analysis”, IEEE Industry Applications Society Annual Meeting, Cincinnati, OH, USA, Oct. 2017.
- [95] J.-S. R. Jang, C.-T. Sun, and E. Mizutani, Neuro-fuzzy and soft computing: a computational approach to learning and machine intelligence, Upper Saddle River, NJ: Prentice Hall, 1997.
- [96] F. Karay and C. deSilver, Soft computing and intelligent systems design: theory, tools, and applications, Pearson Publishing Inc., 2004.
- [97] L. Wei, G. Joos, J. Belanger, "Real-time simulation of a wind turbine generator coupled with a battery-supercapacitor energy storage system", IEEE Transaction on Industrial Electronics, vo1.57, no.4, pp.1137-1145, Dec. 2010.
- [98] S. Vazquez, S. M. Lukic, E. Galvan, L. G. Franquelo and J. M. Carrasco, "Energy storage systems for transport and grid applications," IEEE Transaction on Industrial Electronics, vol. 57, no. 12, pp. 3881-3895, Dec. 2010.
- [99] L. Qu and W. Qiao, —Constant power control of DFIG wind turbines with supercapacitor energy storage”, IEEE Transactions on Industry Applications, vol. 47, pp. 359 -367, Jan. 2011.
- [100] A. Abedini and H. Nikkhajoei, —Dynamic model and control of a wind-turbine generator with energy storage”, IET Renewable Power Generation, vol. 5, pp. 67-78, Jan. 2011.
- [101] S. A. Saleh, —Testing a unit commitment based controller for grid-connected PMG-based WECSs with generator-charged battery units”, IEEE Transactions on Industry Applications, vol. 55, no. 3,pp. 2185-2187, May/June 2019.

- [102] N. Mendis, K. M. Muttaqi and S. Perera, –Active power management of a super capacitor-battery hybrid energy storage system for standalone operation of DFIG based wind turbines”, IEEE Industry Applications Society Annual Meeting , Las Vegas, NV, 2012, pp. 1 – 8.,
- [103] G. iwanski, T. luszczky, P. pura, M. szypulski, –Standalone DFIG based power system supported by energy storage or auxiliary power unit”, Eighth International Conference and Exhibition on Ecological Vehicles and Renewable Energies (EVER), Monte Carlo, Monaco, 2013.
- [104] A. M. Dizqah, A. Maher, K. Busawon, and A. Kamjoo, —Amultivariable optimal energy management strategy for standalone DC microgrids”, IEEE Transactions on Power Systems, vol. 30, no. 5,pp. 2278-2287, September 2015.
- [105] J. C. Y. Hui, A. Bakhshai, and P. K. Jain, —A energy management scheme with power limit capability and an adaptive maximum power point tracking for small standalone PMSG wind energy systems”, IEEE Transactions on Power Electronics, vol. 31, no. 7, pp.4861-4875, July 2016.
- [106] S. Mirjalili, S. M. Mirjalili, and A. Lewis, "Grey wolf optimizer," Advances in Engineering Software, vol. 69, pp. 46-61, 2014.
- [107] S. Mirjalili , "How effective is the grey wolf optimizer in training multi-layer perceptrons" ,Applied Intelligence, pp.1-12, 2015.
- [108] L.I. Wong,M.H. Sulaiman, M. Ruslim, M.S. Hong, "Grey wolf optimizer for solving economic dispatch problems" ,IEEE International Conference on Power and Energy (PECon), 2014, Malaysia, vol . 3,pp. 1-5.
- [109] B. Yang , X. Zhang, T. Yu, H. Shu, Z. Fang, —Grouped grey wolf optimizer for maximum power point tracking of doubly-fed induction generator based wind turbine” Energy Conversion and Management, vol. 133, pp. 427–443, 2017.
- [110] S. Soued,M. A. Ebrahim, H. S. Ramadan, M. Becherif, –Optimal blade pitch control for enhancing the dynamic performance of wind power plants via metaheuristic optimisers”, IET Electric Power Applications, vol. 11, pp. 1432-1440, Sep. 2017.
- [111] T. Zhou and W. Sun, –Optimization of battery–supercapacitor hybrid energy storage station in wind/solar generation system”, IEEE Transactions on Sustainable Energy, vol. 5, no. 2,pp. 408-415, April 2014.
- [112] J. Wang and F. Yang , –Optimal capacity allocation of standalone wind/solar/battery hybrid power system based on improved particle swarm optimisation algorithm”, IET Renewable Power Generation, vol. 7, no.. 5, pp. 443–448, March 2013.

- [113] M.N. Uddin, I.K. Amin, N. Rezaei ; M. Marsadek, —grey wolf optimization based power management strategy for battery storage of DFIG-WECS in standalone operating mode”, IEEE Industry Applications Society Annual Meeting (IAS), Portland, OR, USA, Sep. 2018.
- [114] J.M. Kwon, —Composite energy storage system with photovoltaic power generation and uninterruptible power supply function”, International Journal of Photoenergy, Hindawi Publishing Corporation, June 2013.
- [115] R. Pena, G.M. Asher, J.C. Clare, —Adoubly fed induction generator using back to back PWM converters supplying an isolated load from a variable speed wind turbine”, Proceedings of Industrial Electronics, Electrical Power Applications, pp. 380–387, 1996.
- [116] I. Munteanu, A. I. Bratu, N-A. Cutululis, E. Ceangă, —Optimal control of wind energy systems- Towards a global approach”, Ch. 2, Springer-Verlag London Limited, UK, 2008.
- [117] M.M.I. Chy, M.N. Uddin, —Development and implementation of a new adaptive intelligent speed controller for IPMSM drive” IEEE Transactions on Industry Applications”, vol. 45, no. 3, pp. 1106-1115, May-June 2009.
- [118] S. Heier, Grid Integration of Wind Energy Conversion Systems, New York, Wiley, 1998.
- [119] M. E. Haque, M. Negnevitsky, K.M. Muttaqi, —Anovel control strategy for a variable speed wind turbine with a permanent magnet synchronous generator”, IEEE Transactions on Industry Applications, vol. 46, no. 1,pp. 331-339, February 2010.
- [120] <http://www.ieso.ca/en/Document-Library>.
- [121] S. M. R. Kazmi , H. Goto , H. J. Guo , O. Ichinokura, —Review and critical analysis of the research papers published till date on maximum power point tracking in wind energy conversion system”, IEEE Energy Conversion Congress and Exposition, Atlanta, GA, USA, Sept. 2010.
- [122] L. Xiong, J. Wang, X. Mi, M. W. Khan, —Fractional order sliding mode based direct power control of grid-connected DFIG”, IEEE Transactions on Power Systems, vol. 33, no. 3, pp.3087-3096, May 2018.
- [123] R.H. Park, —Two-reaction theory of synchronous machines generalized method of analysis-part I”, Transactions of the American Institute of Electrical Engineers, vol. 48, no. 3, pp. 716-727, July 1929.
- [124] L. Zhou, A. Swain, A. Ukil, —Q-learning and dynamic fuzzy q-learning based intelligent controllers for wind energy conversion systems”, IEEE Innovative Smart Grid Technologies - Asia (ISGT), May 2018, Singapore.
- [125] M. Valikhani and C. Sourkounis, —Adaptive intelligent controller for rotor resistance variations in DFIG system”— 22nd Mediterranean Conference on Control and Automation (MED), Palermo, Italy,pp. 882-887 June 2014.

Appendix -A

DFIG Parameters

Parameters	Real-time machine data
Rated turbine power	450 W
Equivalent blade radius	1.8 m
Rated generator power	480 VA
Grid voltage(rms)	120 V
Grid frequency	60 Hz
Number of pole pairs	2
Winding resistance	8.1 Ω
Leakage inductance	0.03 H
Magnetizing inductance	0.477 H
dc bus capacitance	4.2 mF
Rated dc bus voltage	308 V

Appendix –B

Matlab-Simulink Blocks for Simulation

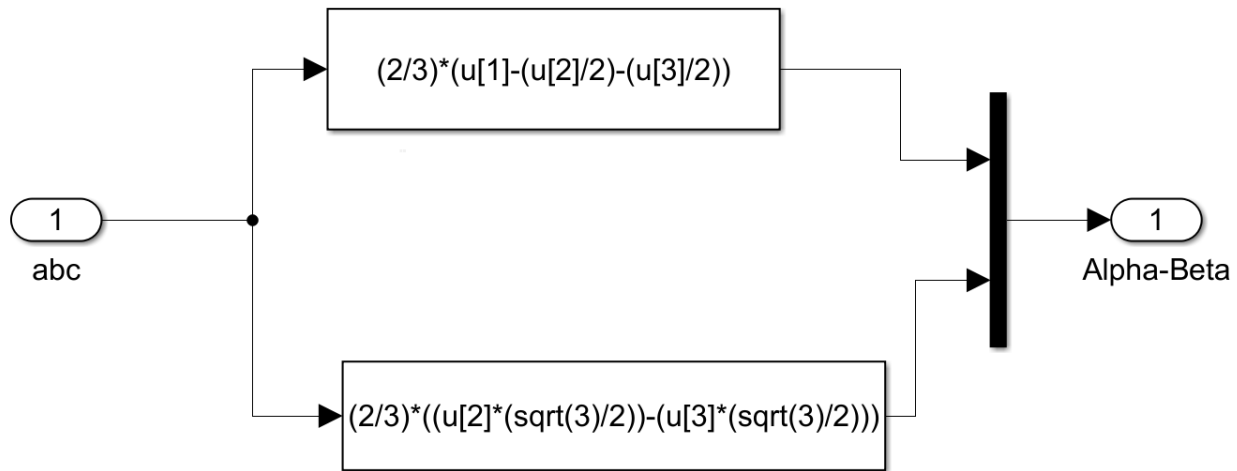


Fig. B.1. abc to alpha-beta vector rotator

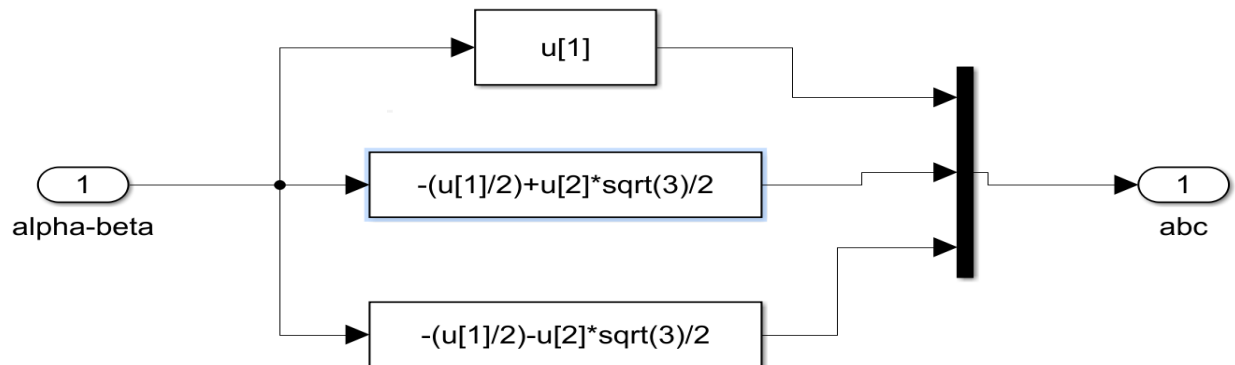


Fig. B.2. alpha-beta to abc vector rotator

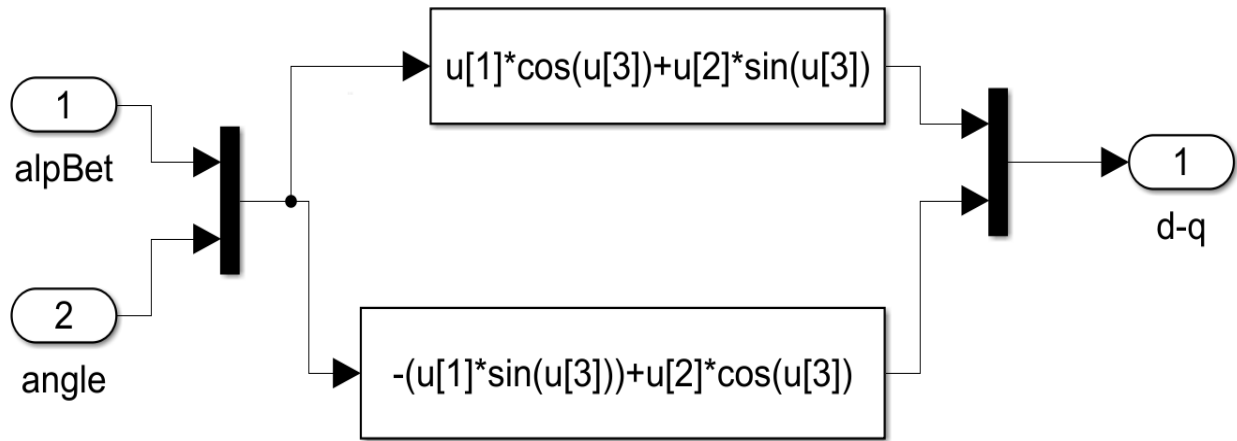


Fig. B.3. alpha-beta to d-q vector rotator

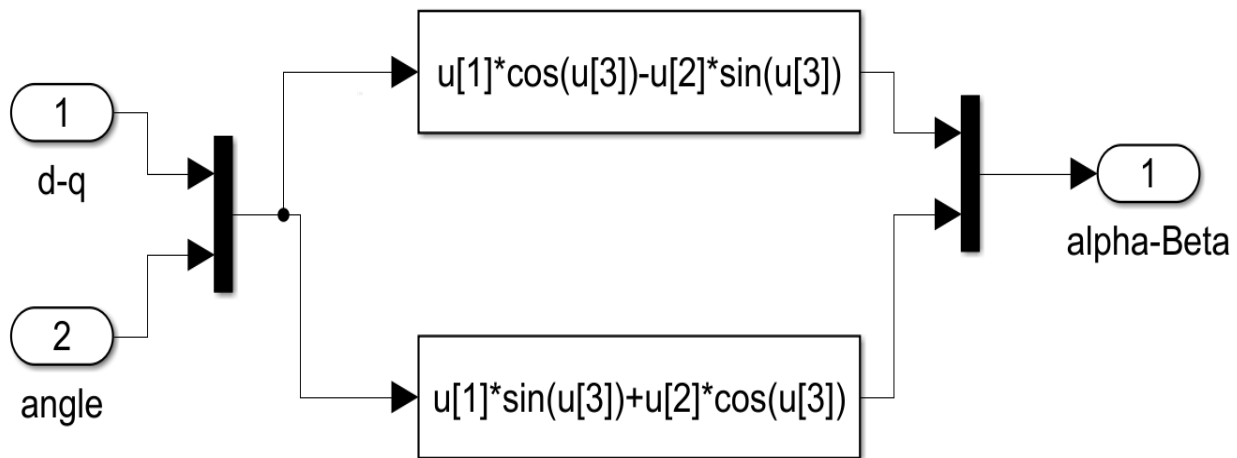


Fig. B.4. d-q to alpha-beta vector rotator

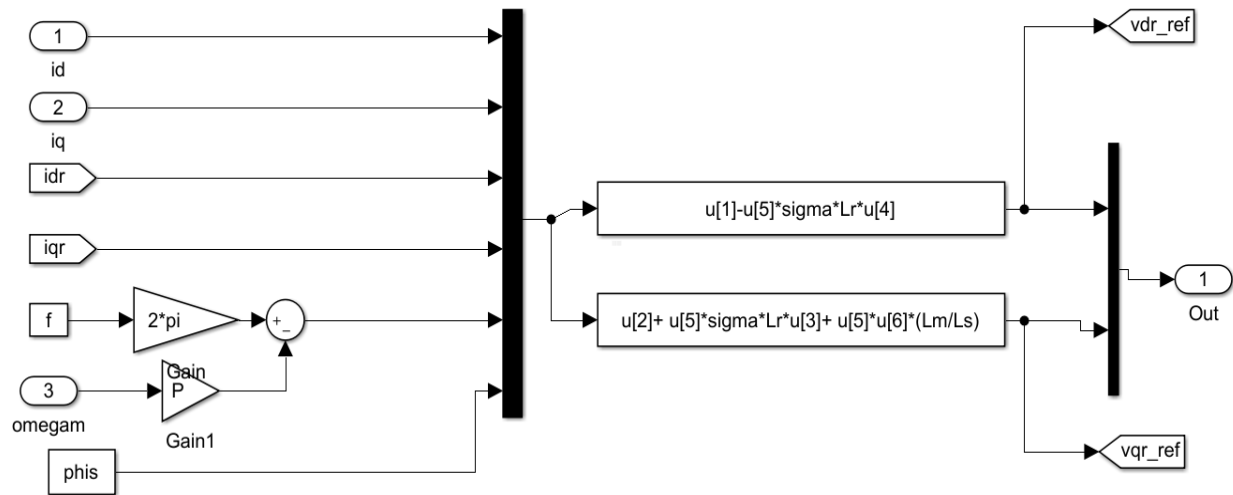


Fig. B.5. Cross-coupling term cancellation

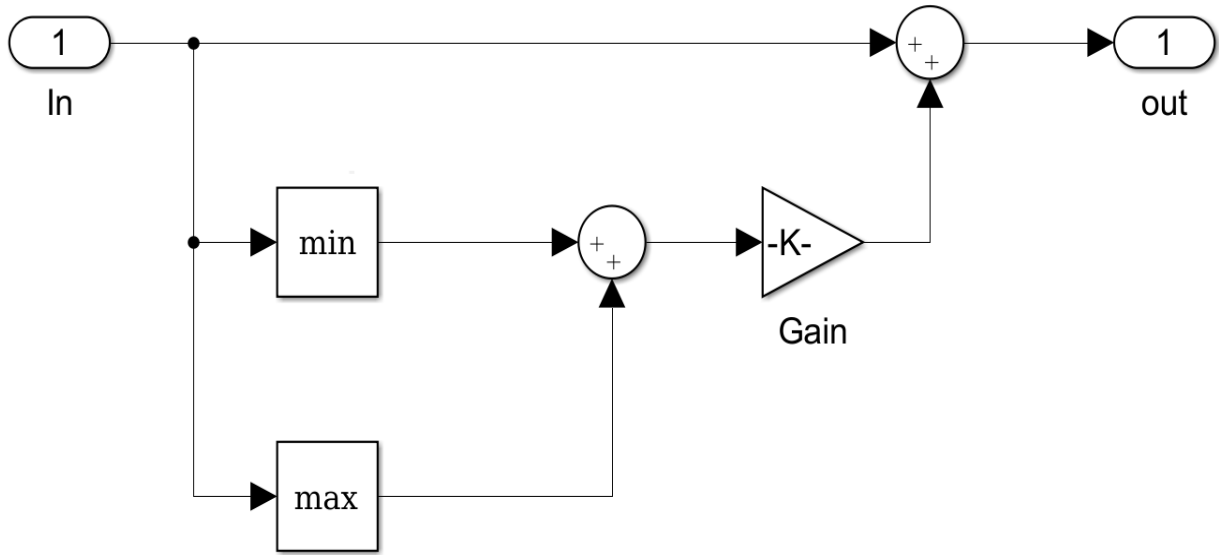


Fig. B.6. 3rd harmonic injection

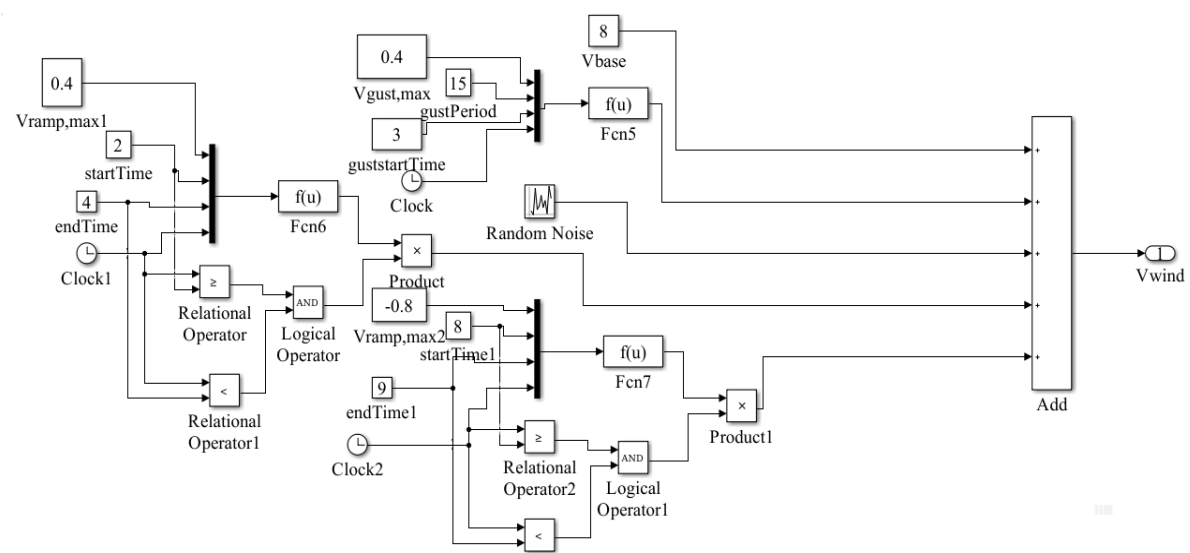


Fig. B.7. Wind model

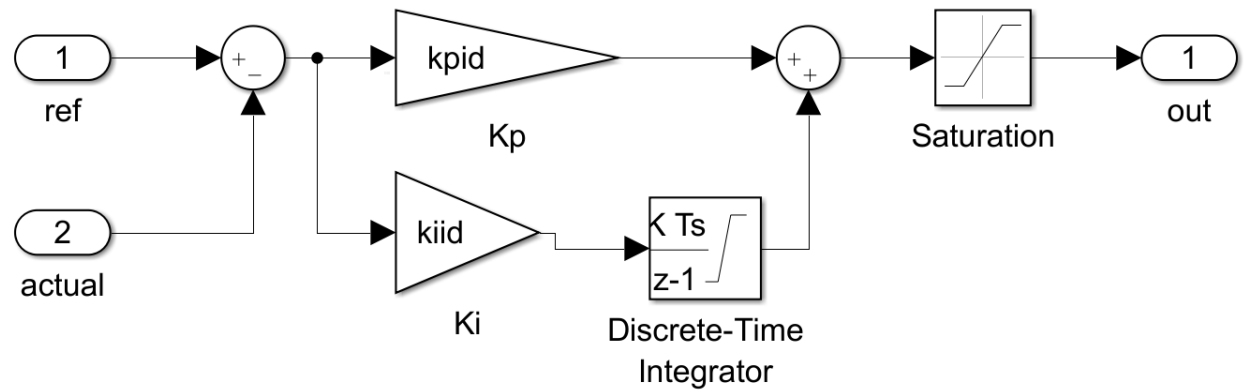


Fig. B.8. PI controller

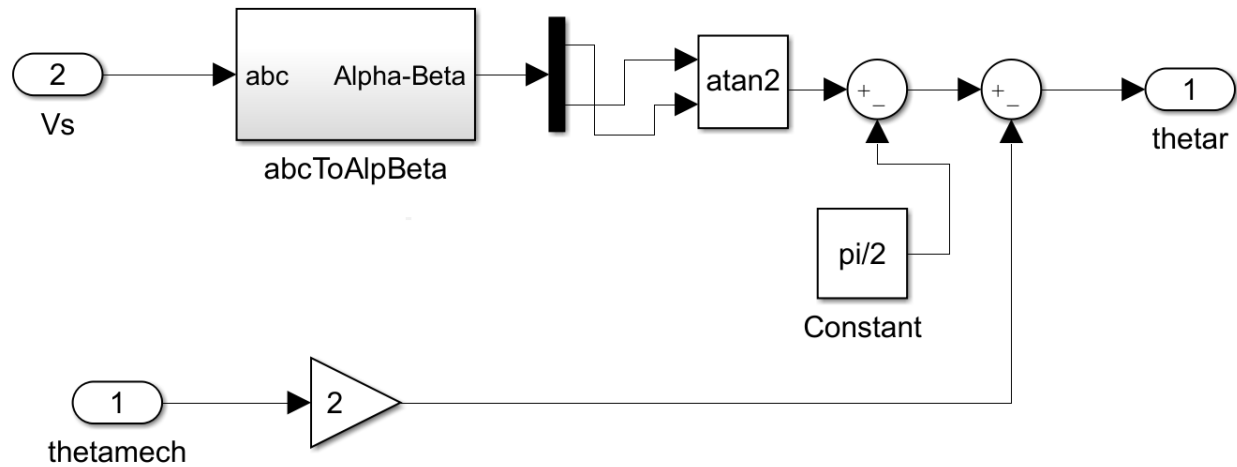


Fig. B.9. Grid angle calculator

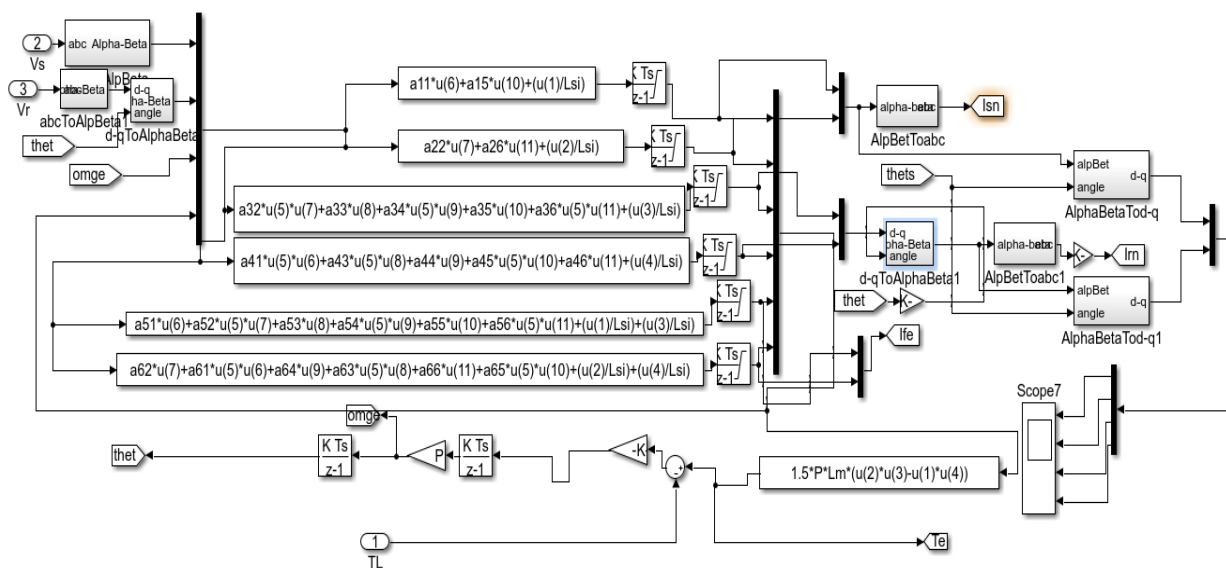


Fig. B.10. Model of DFIG with core resistance

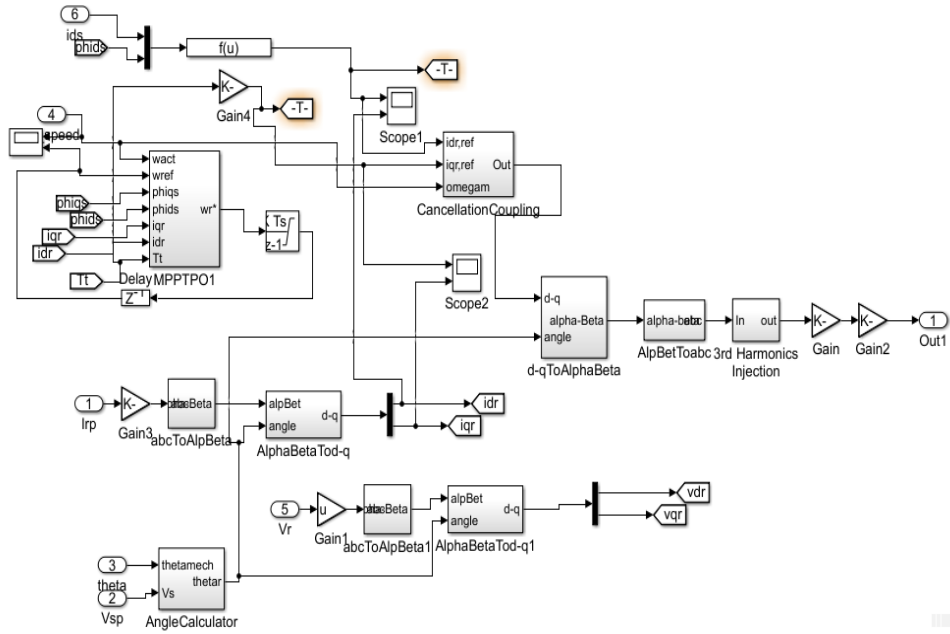


Fig. B.11. RSC pulse generator for nonlinear control of DFIG

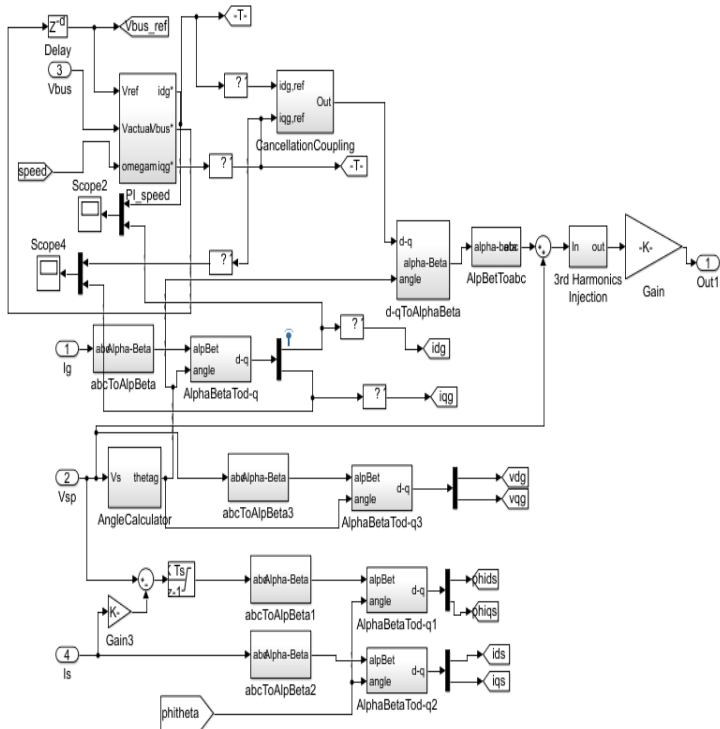


Fig. B.12. GSC pulse generator for nonlinear control of DFIG

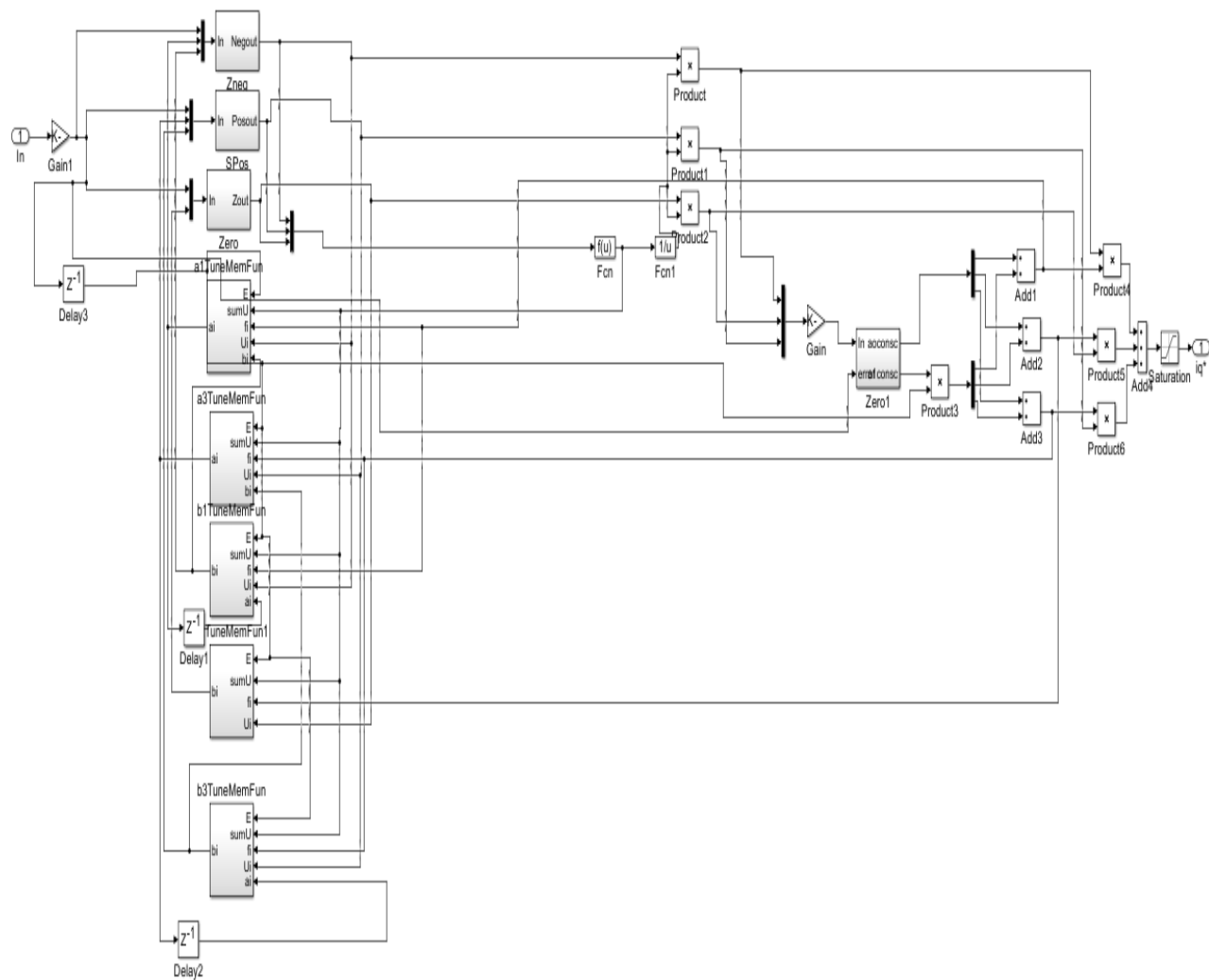


Fig. B.13. ANFIS controller

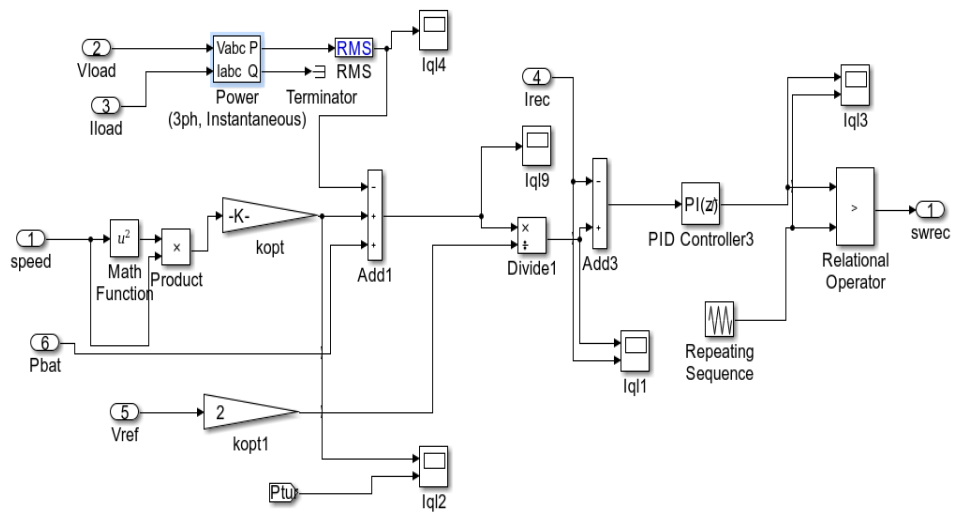


Fig. B.14. Boost converter control for standalone DFIG.

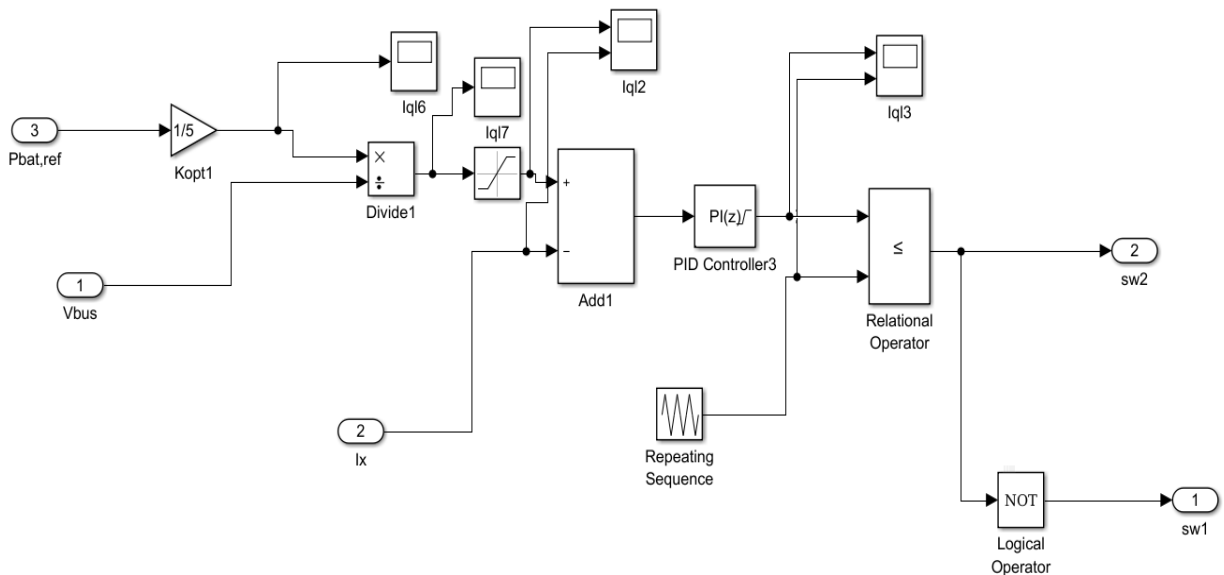


Fig. B.15. Bidirectional buck-boost converter control for standalone DFIG.

Appendix –C

Coding for the Simulink Block

Code for Simulink model initialization

```

%%% DFIG Machine Parameters %%%
%%% Rotor Parameters referred to the stator %%%

f=60;                                %Stator frequency
Ps=2e6;                               %Rated Stator power
n=1800;                               %Rated rotational speed(rpm)
Vs=690;                               %Rated stator voltage(V)
Is=1760;                             %Rated stator current(amp)
Tm=12732;                            %Rated torque(Nm)
Cs=1000e-6;

P=2;                                  %Pole pair
u=1/3;                                %stator to rotor turns ratio
Vr=2070;                             %Rotor voltage nonreached
smax=1/3;                            %maximum slip
Rs=2.6e-3;
Lsi=0.087e-3;
Lm=2.5e-3;
Rr=2.9e-3;
Ls=Lm+Lsi;
Lr=Lm+Lsi;
Vr_stator=Vr*smax*u;
ws=377;
J=127/2;
D=1e-3;
sigma=1-(Lm^2/(Ls*Lr));
phis=Vs*sqrt(2/3)/(2*pi*f);
fsw=4e3;

tca=(sigma*Lr)/Rr;
tcb=0.0005;
wna=5*1/(tca);
wnb=1/tcb;
kpid=(2*wna*sigma*Lr)-Rr;
kpiq=kpid;
kiid=(wna^2)*Lr*sigma;
kiiq=kiid;
kpspd=(2*wnb*J)/P;
kispd=(wnb^2)*J/P;
Ts=1/fsw/10;

%%% Grid Side Converter %%%
Cf=80e-3;
R=20e-6;
L=40e-6;
Rg=20e-6;
Lg=40e-6;
kpg=1/(1.5*Vs*sqrt(2/3));
kqg=-kpg;
kpv=-10000;

```

```

kiv=-300000;

%%% PI regulator grid side %%%
tig=Lg/Rg;
wig=60*2*pi;
kpidg=(2*wig*Lg)-Rg;
kiidg=kpidg;
kpiqg=2*wig*Lg;
kiiqg=kpiqg;

%%% Three blade Wind Turbine %%%
Radius=42;
beta=0;
N=100;
c1=0.5;
c2=116;
c3=0.4;
c4=5;
c5=21;
Vbus=1150;
%%%DFIG Coefficient%%%%%
Rf=5000;
a11=-Rs/Lsi;
a15=-Rf/Lsi;
a22=a11;
a26=a15;
a32=-Lm/Lsi;
a33=-Rr/Lsi;
a34=-Lr/Lsi;
a35=-Rf/Lsi;
a36=Lm/Lsi;
a41=-a32;
a43=-a34;
a44=a33;
a45=-a36;
a46=a35;
a51=a11;
a52=a32;
a53=a33;
a54=a34;
a55=-Rf*((1/Lsi)+(1/Lsi)+(1/Lm));
a56=a36;
a61=-a52;
a62=a51;
a63=-a54;
a64=a53;
a65=-a56;
a66=a55;
%%ANFIS Tuning %%
tune=3e-8;
tunebus=2e-11;

```

Code for GWO model

```
function [y1,y2] = fcn(Ptur,Pload,Pbat,Vbus2,Vbus1,Ts)
SearchAgents_no=30;
lb=-200;
ub=200;
Max_iter=300;
dim=1;
Positions=zeros(30,dim);
for i=1:dim
    ub_i=ub(i);
    lb_i=lb(i);
    Positions(:,i)=rand(SearchAgents_no,1).* (ub_i-lb_i)+lb_i;
end
Alpha_pos=zeros(1,dim);
Alpha_score=inf; %change this to -inf for maximization problems

Beta_pos=zeros(1,dim);
Beta_score=inf; %change this to -inf for maximization problems

Delta_pos=zeros(1,dim);
Delta_score=inf; %change this to -inf for maximization problems

%Initialize the positions of search agents

Convergence_curve=zeros(1,Max_iter);

l=0;% Loop counter

% Main loop
while l<Max_iter
    for i=1:size(Positions,1)

        % Return back the search agents that go beyond the boundaries of the search
        space
        Flag4ub=Positions(i,:)>ub;
        Flag4lb=Positions(i,:)<lb;

        Positions(i,:)=(Positions(i,:).*(~(Flag4ub+Flag4lb)))+ub.*Flag4ub+lb.*Flag4lb;

        %Pcap=1.1e-3*Vbus2*(Vbus2-Vbus1)/Ts;
        % Calculate objective function for each search agent
        fitness=(Ptur+Positions(i,1)-Pload).^2;

        % Update Alpha, Beta, and Delta
        if fitness<Alpha_score
            Alpha_score=fitness; % Update alpha
            Alpha_pos=Positions(i,:);
        end

        if fitness>Alpha_score && fitness<Beta_score
            Beta_score=fitness; % Update beta
            Beta_pos=Positions(i,:);
        end
    end
end
```

```

if fitness>Alpha_score && fitness>Beta_score && fitness<Delta_score
    Delta_score=fitness; % Update delta
    Delta_pos=Positions(i,:);
end
end

a=2-1*((2)/Max_iter); % a decreases linearly from 2 to 0

% Update the Position of search agents including omegas
for i=1:size(Positions,1)
    for j=1:size(Positions,2)

        r1=rand(); % r1 is a random number in [0,1]
        r2=rand(); % r2 is a random number in [0,1]

        A1=2*a*r1-a; % Equation (3.3)
        C1=2*r2; % Equation (3.4)

        D_alpha=abs(C1*Alpha_pos(j)-Positions(i,j)); % Equation (3.5)-part 1
        X1=Alpha_pos(j)-A1*D_alpha; % Equation (3.6)-part 1

        r1=rand();
        r2=rand();

        A2=2*a*r1-a; % Equation (3.3)
        C2=2*r2; % Equation (3.4)

        D_beta=abs(C2*Beta_pos(j)-Positions(i,j)); % Equation (3.5)-part 2
        X2=Beta_pos(j)-A2*D_beta; % Equation (3.6)-part 2

        r1=rand();
        r2=rand();

        A3=2*a*r1-a; % Equation (3.3)
        C3=2*r2; % Equation (3.4)

        D_delta=abs(C3*Delta_pos(j)-Positions(i,j)); % Equation (3.5)-part 3
        X3=Delta_pos(j)-A3*D_delta; % Equation (3.5)-part 3

        Positions(i,j)=(X1+X2+X3)/3;% Equation (3.7)

    end
end
l=l+1;
Convergence_curve(l)=Alpha_score;
end
y1=(1/7)*Alpha_pos(:,1);

y2=Convergence_curve;

```

Appendix –D

Real-time Simulink model

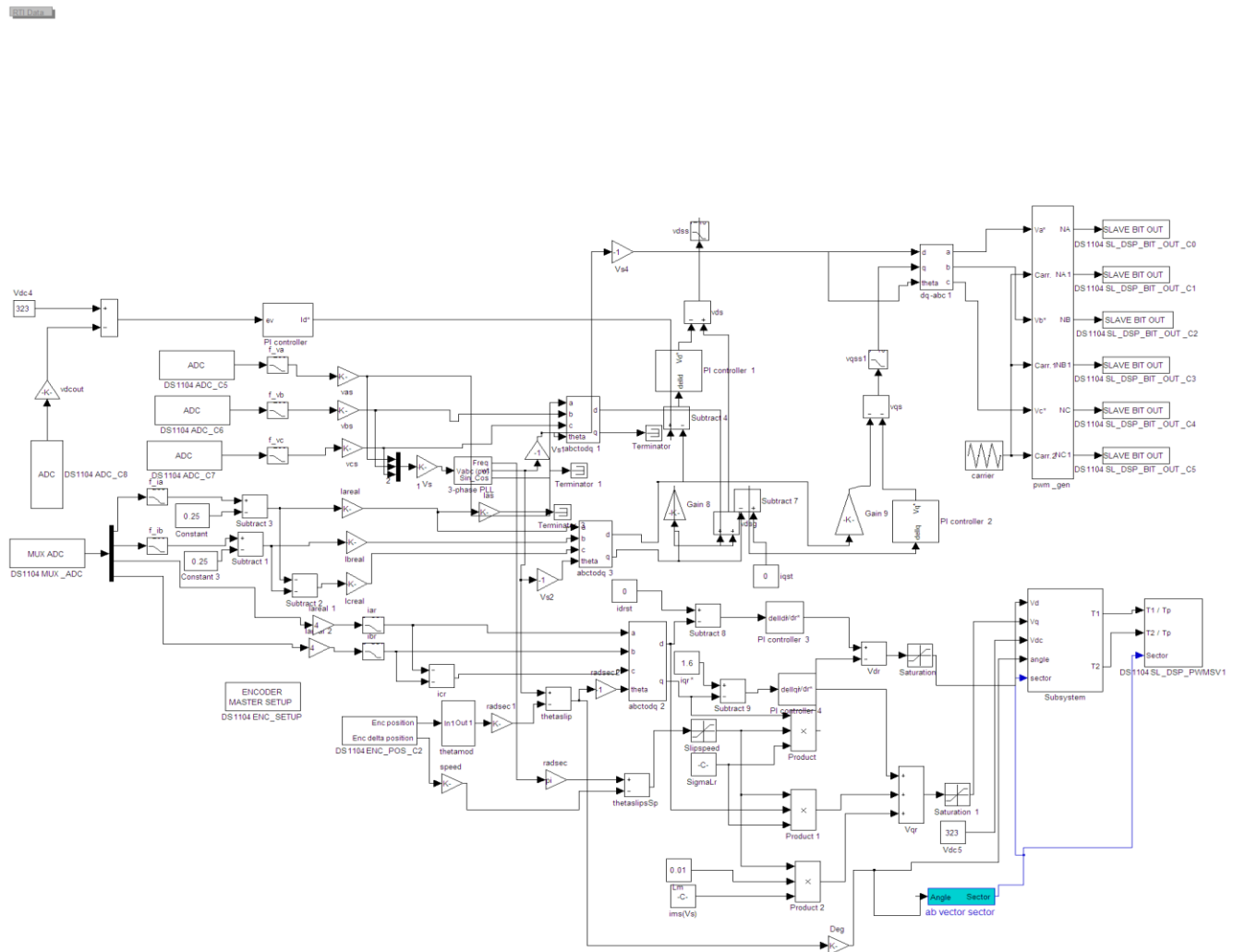
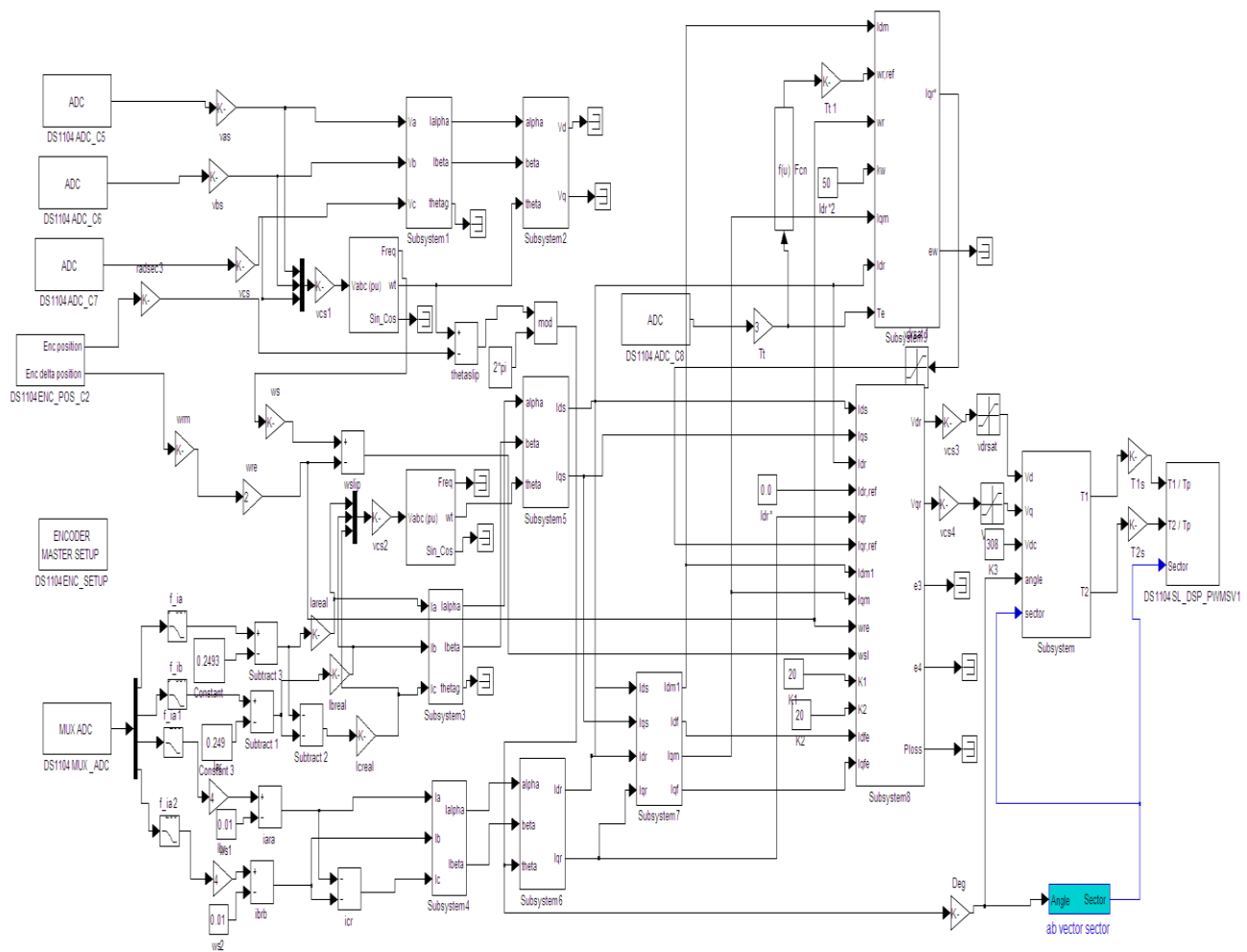


Fig. B.16. Real-time Simulink model for the adaptive step size based MPPT control in DFIG-WECS



RSC of DFIG-WECS

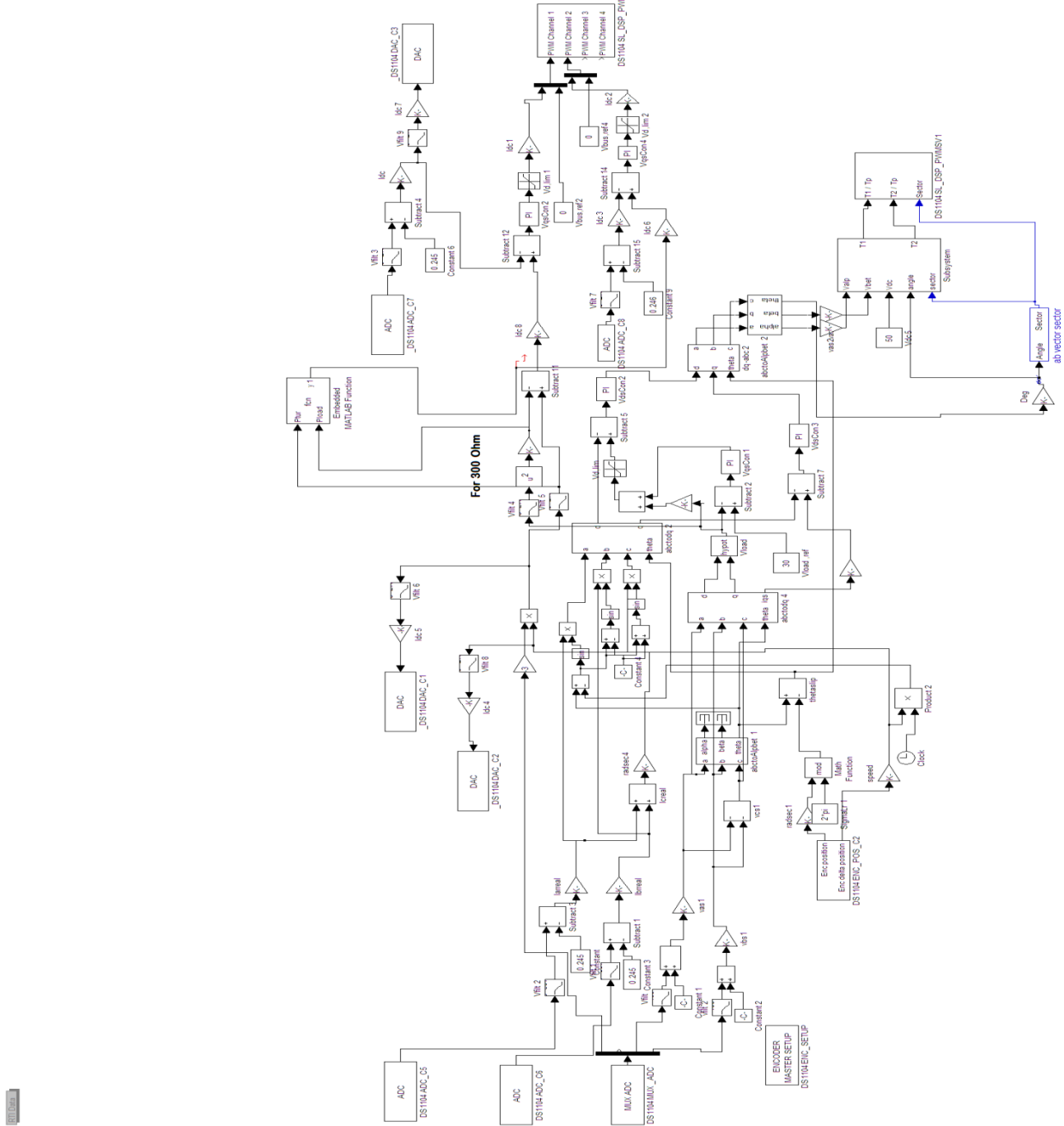


Fig. B.18. Real-time Simulink model for the GWO based battery power control for standalone operation of DFIG-WECS